

JNMT

Journal of Nuclear Medicine Technology

FEATURED IMAGE

^{68}Ga -DOTATATE PET/CT for Neuroblastoma Staging: Utility for Clinical Use.
Ata Ur Rehman Maaz et al. See page 265.



What Member Benefits Do You Value?

Basic numbers show your dues **value** but **benefits** of SNMMI membership are more than just a dollar amount! Stay a **member** of your professional **community** and the society **dedicated** to **supporting** you at every stage of your **career**. Join us for another **membership** year—Renew today!

Community Knowledge & Influence

SNMMI's **14,000+** members form a knowledge center of nuclear medicine and molecular imaging professionals, involved in peer-to-peer learning, in-person and virtual networking opportunities, and advocacy efforts for our community.

Continuing Education

Members can earn all the CME/CE credits needed to maintain certification requirements with **FREE** webinars, Journal exams, and other **complimentary** education products.

Publication & Research

Membership comes with a complimentary subscription to *The Journal of Nuclear Medicine (JNM)* and *Journal of Nuclear Medicine Technology (JNMT)*—a **\$770 publication package**.

Awards & Recognition

SNMMI provides more than **\$400,000 annually** through grants, awards, and scholarships along with opportunities to showcase professional expertise as a speaker, presenter, and author to a global audience.

...And exclusive discounts offering up to 40% off event registrations, products, and services

www.snmmi.org/renew

SNMMI Value Initiative
SOCIETY OF NUCLEAR MEDICINE & MOLECULAR IMAGING

Pass the NMTCB CT Exam. We GUARANTEE it!

Because MIC is all about outcomes.

Our
30th
Year!

We guarantee you'll pass the NMTCB CT Exam or *your money back!*

- Technologists must complete 35 hours of didactic education related to CT during the 3 year period prior to applying for the CT Exam.
- NMTCB has approved MIC's **CT Registry Review Program** along with **Sectional Anatomy & Imaging Strategies** to **completely satisfy that 35-hour CT didactic requirement!**
- Excellent companion for technologists in hybrid imaging.

There's no better time to participate in

MIC's Self-Study CE

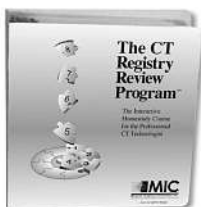
- Prepare for **CT certification**
- Satisfy NMTCB's **prerequisite**
- Ensure the **highest standards**

Ask for the CNMT discount when you enroll in both courses!

Technologists and their managers agree:
"MIC's courses really work!"

The CT Registry Review Program™

Pass the CT Exam after completing this course or we will refund your entire tuition!

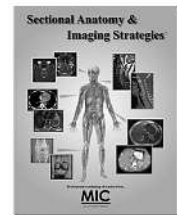


- Learn **essential** and **advanced** topics on the NMTCB and ARRT CT Exam.
- Prior training in CT is recommended.
- Pass the NMTCB or ARRT Exam in CT or your money back!
- 22 Credits • 8 StudyModules

5th
Ed!

Sectional Anatomy & Imaging Strategies™

Learn the essentials of sectional imaging in a convenient self-study format!



- Patient positioning, artifact reduction, image orientation, slice thickness, etc., for each clinical area.
- Explains sectional imaging with over 1,000 images and figures. The perfect companion to **The CT Registry Review Program**.
- 18 Credits • 6 StudyModules

A Proud Member of...

SNMMI

Call today for your
Free Info Kit
800-589-5685
or visit www.MICinfo.com



Medical Imaging Consultants, Inc.
1037 US Highway 46, Suite G2 • Clifton, NJ 07013 • 800-589-5685
...for your perfect image.™



Achieve the True Mark of **Quality & Safety** for Your Facility with IAC

A leader in accreditation for 30 years and counting, **IAC accreditation clearly indicates a 'seal of approval'** to current and prospective patients — proof that the facility has undergone a rigorous evaluation, by clinical experts, of all aspects of the operations deemed relevant to providing quality patient care.

IAC's quality solutions and resources provide facilities with a foundation to create and achieve realistic patient care goals:



The **IAC Quality Improvement (QI) Tool** allows facilities to assess their case studies and final reports, receive a quantitative report targeting opportunities for continuous improvement and satisfy a component of the MIPS Improvement Activity score.



Free access to the IAC **Online Accreditation** application including the capability to upload cases to a HIPAA-compliant, secure medical image sharing service. Trained, clinical staff are dedicated to guiding you through the process via phone, live chat or e-mail.



The IAC website offers **helpful resources** including a robust calendar of CE courses and free access to live special topic webinars, accreditation webinars and webcasts offering CE credit. Plus sample and guidance documents, accreditation checklist and more!

What can **IAC accreditation** do for ***your*** facility?

VASCULAR TESTING
ECHOCARDIOGRAPHY
NUCLEAR/PET
MRI . CT . DENTAL CT



CAROTID STENTING
VEIN CENTER
CARDIAC ELECTROPHYSIOLOGY
CARDIOVASCULAR CATHETERIZATION

EDITOR'S PAGE

- 197** Once Again—The SNMMI “Nailed It”!
Kathy S. Thomas

CONTINUING EDUCATION

- 199** Thyroid Follicular Epithelial Cell–Derived Cancer: New Approaches and Treatment Strategies
Julie Bolin
- 209** Brain Imaging Techniques: Improving the Quality
Rani M. Noble

PRACTICAL PROTOCOL TIP

- 215** ^{18}F -FDG PET/CT Brain Imaging
Rani M. Noble

CONTINUING EDUCATION

- 217** PET/MRI, Part 2: Technologic Principles
Geoffrey M. Currie, Peter Kamvosoulis, and Stewart Bushong

IMAGING

- 226** Experiences and Perceptions of Nuclear Medicine Technologists in the Assessment of Myocardial Perfusion Image Quality
Lucky R. Chiyepeya, Madri Jansen van Rensburg, and Mboyo-Di-Tamba Vangu
- 232** Estimation of Chest Wall Attenuation of ^{123}I Emissions in Substernal Goiter: A Phantom Study
Matthew Alfano, John Weaver, Richard Mazurek, and Alan Siegel
- 235** Correlation of Lesional Uptake Parameters and Ratios with miPSMA Score and Estimating Normal Physiologic Concentration: An Exploratory Analysis in Metastatic Castration-Resistant Prostatic Carcinoma Patients with ^{68}Ga -PSMA-11 PET/CT
Ashwini Kalshetty, Biju Menon, Sutapa Rakshit, Atanu Bhattacharjee, and Sandip Basu
- 241** Effect of Diet on Physiologic Bowel ^{18}F -FDG Uptake
Bahar Moasses-Ghafari, Babak Fallahi, Armaghan Fard Esfehiani, Mohammad Eftekhari, Khaled Rahmani, Arash Eftekhari, and Parham Geramifar
- 246** U.S. Diagnostic Reference Levels and Achievable Administered Activities for Adult Renal Scintigraphy: An Analysis of the Intersocietal Accreditation Committee Nuclear Laboratories
Kevin P. Banks, Rutger S. Gunther, Mary B. Farrell, Justin G. Peacock, Maria Costello, and Leonie L. Gordon
- 250** Accuracy Assessment of SUV Measurements in SPECT/CT: A Phantom Study
Fatin Halim, Hizwan Yahya, Khairul Nizam Jaafar, and Syahir Mansor

- 256** Improved Accuracy of Amyloid PET Quantification with Adaptive Template–Based Anatomic Standardization
Yuma Tsubaki, Takayoshi Kitamura, Natsumi Shimokawa, Go Akamatsu, and Masayuki Sasaki, for the Japanese Alzheimer's Disease Neuroimaging Initiative

BRIEF COMMUNICATION

- 262** Interobserver Agreement in the Diagnosis of Parkinson Disease with Cardiac ^{123}I -Metaiodobenzylguanidine Scintigraphy
Robert W. Foley, Stewart L. Redman, Isabel J. Laurence, Richard N. Graham, and David Little
- 265** ^{68}Ga -DOTATATE PET/CT for Neuroblastoma Staging: Utility for Clinical Use
Ata Ur Rehman Maaz, Jim O'Doherty, and Mehdi Djekidel

EDUCATORS' FORUM

- 269** Online Learning Strategies and Practical Tips for Nuclear Medicine Instructors
Sara L. Johnson

SPECIAL CONTRIBUTION

- 275** Nuclear Medicine and Molecular Imaging in Nodal Staging and Surveillance of Ocular Melanoma: Case Reports and Review of the Literature
Kenneth S. Zurcher, Odette M. Houghton, Joanne F. Shen, Mahesh Seetharam, Michael C. Roarke, and Ming Yang

TEACHING CASE STUDIES

- 281** Imaging Biomarkers in Lung Cancer with ^{68}Ga -DOTATATE, ^{18}F -Fluoride, and ^{18}F -FDG PET/CT Scans and the Theranostics Paradigm
Mehdi Djekidel, Ghulam Syed, and Aladdin Kanbour
- 284** Effect of COVID-19 on ^{18}F -FDG PET/CT: Is There a Need to Consider COVID-19 Status Before Planning ^{18}F -FDG PET/CT for Oncologic Evaluation?
Anwin Joseph Kavanal, Santosh Ranjan Jena, Rajender Kumar, Chandan Krushna Das, Sunil Kumar, and Bhagwant Rai Mittal
- 286** Reactive Axillary Lymphadenopathy to COVID-19 Vaccination on ^{18}F -FDG PET/CT
Mathew V. Smith and Ming Yang
- 288** Follicular Thyroid Carcinoma with Unusual Radioiodine-Refractory Breast Metastasis Mimicking Primary Breast Malignancy
Tarun Kumar Jain, Venkata Subramanian Krishnaraju, Bhagwant Rai Mittal, Ashwani Sood, Rajender Kumar, Rashi Garg, and Sunil Kumar
- 290** Antiseptic-Mediated Colloid Labeling as a Potential Source of Abnormal Liver and Spleen Uptake with $^{99\text{m}}\text{Tc}$ -Dimercaptosuccinic Acid
Veronica Krull, Madison R. Kocher, William J. Rieter

DEPARTMENTS

- 8A** Message from the President
- 292** Letters to the Editor
- 293** Book Reviews
- 11A** Technologist News

Quality in Nuclear Medicine Online Program

The **Quality in Nuclear Medicine Online Program** is designed to assist learners in understanding the skill requirements vital to their quality of practice, including:

- Demonstrating the ability to evaluate images through performance of technical analysis, demonstrated anatomy, pathophysiology, and overall image quality.
- Ability to triage and understand the disease processes being evaluated and how nuclear medicine diagnostic studies may drive care and treatment.
- Understanding their role in achieving a high-quality interpretable study by applying quality principles and using proper imaging techniques beyond basic protocols.



▶ Learning Modules:

- Introduction to Quality
- Defining the Patient Experience: Using Data to Tell the Story
- Work-Life Balance
- Implementing a Quality Program in Nuclear Medicine: The Role of Accreditation in Quality
- The Importance of Quality Control: Appropriate Use and Quality Diagnostic Reports
- Defining a Quality Technologist: Did I Do That? Avoidable Mishaps
- Using Data to Measure Quality and Drive Change
- The Importance of Quality in Gastrointestinal Imaging
- The Importance of Quality in Therapeutic Procedures
- The Importance of Quality in Skeletal Imaging
- The Importance of Quality in Thyroid Imaging
- The Importance of Quality in Lung V/Q Imaging

▶ Fees:

The Quality in Nuclear Medicine Online Program is complimentary for SNMMI members.

- Physician (AMA) Members: Free
- Physician (AMA) Non-Members: \$299
- Technologist (VOICE) Members: Free
- Technologist (VOICE) Non-Members: \$199
- Pharmacist (ACPE) Members: Free
- Pharmacist (ACPE) Non-Members: \$249
- Physicists (AMA) Members: Free
- Physicists (AMA) Non-Members: \$249

This 10.25-hour course will offer the following continuing education credits: Technologists (VOICE), Pharmacists (ACPE), Physicians and Physicists (AMA PRA Category 1 Credit™). This is also available as a non-credit activity for Students.

JNMT Journal of NUCLEAR MEDICINE TECHNOLOGY

The Official Publication of SNMMI-TS

Publications Committee

Chairperson

JESSICA WILLIAMS, CNMT, RT(N), FSNMMI-TS

Ex-Officio Member

TINA M. BUEHNER, PhD, CNMT, FSNMMI-TS

DANNY A. BASSO, MS, CNMT, NCT,
FSNMMI-TS

ERIN B. BELOIN, CNMT, RT(CT)

AMANDA COFFEY, CNMT

GEOFFREY M. CURRIE, PHD BPHARM
MMRS CNMT

MARY BETH FARRELL, MS, CNMT, NCT,
FSNMMI-TS

KRYSTLE W. GLASGOW, CNMT, NMTCB(CT),
NMAA

TOMMY LIEU, RTNM, CNMT

ELEANOR S. MANTEL, CNMT, RT(N),
FSNMMI-TS

MATTHEW C. McMAHON, MS, CNMT, RT(CT)

FRANCES L. NEAGLEY, BA, CNMT, FSNMMI-TS

CYBIL J. NIELSEN, MBA, CNMT, FSNMMI-TS

LISA L. PATRICK, RT(N), NCT, CT, PET

KIMBERLY RAMOS, CNMT

PAUL S. RILEY, Jr., MPH, CNMT

ELIZABETH C. ROMERO, RT(N)(CT), FSNMMI-TS

KIRAN K. SOLINGAPURAM SAI, PHD

KATHY S. THOMAS, MHA, CNMT, PET,
FSNMMI-TS

JOYCE K. ZIMMERMAN, CNMT, MBA,
FSNMMI-TS

Associate Director of Communications

SUSAN ALEXANDER

Senior Publications & Marketing Service Manager

STEVE KLEIN

Senior Copyeditor

SUSAN NATH

Editorial Production Manager

PAULETTE MCGEE

Editorial Project Manager

MARK SUMIMOTO

Director of Communications

REBECCA MAXEY

CEO

VIRGINIA PAPPAS

The *JOURNAL OF NUCLEAR MEDICINE TECHNOLOGY* (ISSN 0091-4916 [print]; ISSN 1535-5675 [online]) is published quarterly by the SNMMI, 1850 Samuel Morse Dr., Reston, VA 20190-5316; phone: (703) 708-9000; fax: (703) 708-9018. Periodicals postage paid at Reston, VA, and at additional mailing offices.

POSTMASTER: Send address changes to the *Journal of Nuclear Medicine Technology*, 1850 Samuel Morse Dr., Reston, VA 20190-5316.

EDITORIAL COMMUNICATIONS should be sent to the editor, Kathy S. Thomas, MHA, CNMT, PET, FSNMMI-TS, JNMT Office, SNMMI, 1850 Samuel Morse Dr., Reston, VA 20190-5316; phone: (703) 326-1185; fax: (703) 708-9018. To submit a manuscript, go to <http://submit-tech.snmjournals.org>.

BUSINESS COMMUNICATIONS concerning permission requests should be sent to the publisher, SNMMI, 1850 Samuel Morse Dr., Reston, VA 20190-5316; phone: (703) 708-9000; home page address: <http://tech.snmjournals.org>. Subscription requests, address changes, and missed issue claims should be sent to Membership Department, SNMMI, at the address above. Notify the Society of change of address and telephone number at least 30 days before date of issue by sending both the old and new addresses. Claims for copies lost in the mail are allowed within 90 days of the date of issue. Claims are not allowed for issues lost as a result of insufficient notice of change of address. For information on advertising, contact Team SNMMI (Kevin Dunn, Rich Devanna, and Charlie Meitner; (201) 767-4170; fax: (201) 767-8065; TeamSNMMI@cunnasso.com). Advertisements are subject to editorial approval and are restricted to products or services pertinent to nuclear medicine. Closing date is the 25th of the second month preceding the date of issue.

INDIVIDUAL SUBSCRIPTION RATES for the 2021 calendar year are \$237 within the United States and Canada; \$252 elsewhere. CPC IPM Sales Agreement No. 1415131. Sales of individual back copies are available for \$58 at <http://www.snmmt.org/subscribe> (subscriptions@snmmi.org; fax: (703) 667-5134). Individual articles are available for sale online at <http://tech.snmjournals.org>.

MISSION: SNMMI-TS is dedicated to the advancement of molecular and nuclear medicine technologists by providing education, advocating for the profession, and supporting research to achieve clinical excellence and optimal patient outcomes. **VISION:** To be recognized as the leader in molecular imaging and therapy. To be dedicated to the advancement of the profession through adoption of emerging technologies.

COPYRIGHT © 2021 by the Society of Nuclear Medicine and Molecular Imaging, Inc. All rights reserved. No part of this work may be reproduced or translated without permission from the copyright owner. Individuals are asked to fill out a permission-request form at <http://tech.snmjournals.org/misc/permission.dtl>. Because the copyright on articles published in the *Journal of Nuclear Medicine Technology* is held by the Society, each author of accepted manuscripts must sign a statement transferring copyright (available for downloading at <http://tech.snmjournals.org/site/misc/ifora.xhtml>).

The ideas and opinions expressed in *JNMT* do not necessarily reflect those of the SNMMI or the Editors of *JNMT* unless so stated. Publication of an advertisement or other product mentioned in *JNMT* should not be construed as an endorsement of the product or the manufacturer's claims. Readers are encouraged to contact the manufacturer with any questions about the features or limitations of the products mentioned. The SNMMI does not assume any responsibility for any injury or damage to persons or property arising from or related to any use of the material contained in this journal. The reader is advised to check the appropriate medical literature and the product information currently provided by the manufacturer of each drug to be administered to verify the dosage, the method and duration of administration, and contraindications.

JNM^T Journal of NUCLEAR MEDICINE TECHNOLOGY

Editor

Kathy S. Thomas, MHA, CNMT, PET, FSNMMI-TS

Battle Ground, Washington

Associate Editors

Sarah A. Frye, MBA, CNMT, PET, NCT, CCRP
*St. Louis University
St. Louis, Missouri*

Sara G. Johnson, MBA, CNMT, NCT,
FSNMMI-TS
*VA Hospital San Diego
San Diego, California*

Sara L. Johnson, MEd, CNMT, NMTCB (RS),
ARRT(N)(CT)
*Hillsborough Community College
Tampa, Florida*

April Mann, MBA, CNMT, NCT, RT(N),
FSNMMI-TS
*Hartford Healthcare Corporation
Hartford, Connecticut*

Jennifer Prekeges, MS, CNMT, FSNMMI-TS
*Bellevue College
Bellevue, Washington*

Jessica Williams, CNMT, RT(N), FSNMMI-TS
*HCA Healthcare
London, England*

Associate Editor, Continuing Education

Mary Beth Farrell, MS, CNMT, NCT, FSNMMI-TS
*Intersocietal Accreditation Commission
Langhorne, Pennsylvania*

Associate Editor, Book Reviews

Frances L. Neagley, BA, CNMT, FSNMMI-TS
San Francisco, California

Consulting Editors

Norman Bolus, MSPH, MPH, CNMT,
FSNMMI-TS
*University of Alabama
Birmingham, Alabama*

Patrick M. Colletti, MD
*University of Southern California
Los Angeles, California*

George H. Hinkle, RPh, MS, BCNP
*The Ohio State University
Columbus, Ohio*

Carl K. Hoh, MD
*University of California San Diego
San Diego, California*

Alexander W. Scott, II, PhD, DABR,
DABSNM
*Cedars-Sinai Medical Center
Los Angeles, California*

Michael E. Spieth, MD
*Rochester General Hospital
Rochester, New York*

Jennifer R. Stickel, PhD
*Colorado Associates in Medical Physics
Golden, Colorado*

Alan D. Waxman, MD
*Cedars-Sinai Medical Center
Los Angeles, California*

Consulting Editors (International)

Geoffrey M. Currie, BPharm,
MMedRadSc (NucMed),
MAppMngt (Hlth), MBA, PhD
*Charles Sturt University
Wagga Wagga, Australia*

John D. Thompson, PhD, MSc, BSc (HONS)
*University of Salford
Greater Manchester, United Kingdom*

As a Gold Standard
professional, you want
to continually



THE AMERICAN REGISTRY
OF RADIOLOGIC
TECHNOLOGISTS®

IMPROVE YOUR SKILLS

"The process was easy
to navigate and a much
needed refresher."



CQR helps
you become
even better.

Questions about CQR?

Visit ARRT's CQR Resource Center at arrt.org/cqr

Priorities for the Coming Year

Dusty M. York, CNMT, PET, RT(N)(CT)

As nuclear medicine technologists (NMTs) working in hospitals, clinics, private practices, academic organizations, research, or industry, we are faced with critically important decisions every day. The very nature of our job requires us to be highly trained and specialized professionals. Over the last decade, our scope of practice has changed and the entry-level curriculum has expanded; yet all of us, as nuclear medicine professionals, have continued to evolve and adapt to what is needed to ensure that we continue to provide the best patient care and outcomes.

As a clinical coordinator, I am acutely aware of how important clinical preceptors are to the success of the program and the students. The time commitment and the knowledge shared by clinical preceptors are unpaid and, in some cases, not acknowledged. Preceptors volunteer their time to train students and help to guide and shape these individuals into successful NMTs. The SNMMI-TS knows the efforts of these individuals is incredible, and sometimes the preceptors do not get all the training they would like or need to develop in their role. The SNMMI-TS has started work to create a program that will provide education to clinical preceptors, focused in 5 key areas: (1) education and training, (2) role as a facilitator—how attitudes motivate students, (3) assessment of clinical performance, (4) remediation, and (5) record keeping, confidentiality, and responsibilities.

A pressing issue for the SNMMI-TS is ensuring NMTs have the training they need to perform radiopharmaceutical therapy procedures. While the administration of therapies is part of the NMT scope of practice, the continuous approval of new therapies and trends makes it necessary to ensure that NMTs have the most current and cutting-edge education in this space. The SNMMI-TS is currently working to develop a radiopharmaceutical therapy supplement to the *Journal of Nuclear Medicine Technology* (JNMT), due out next summer. The supplement will focus on five therapies—I-131, Xofigo, Lu-DOTA, Lu-PSMA, and Azedra—and will include information on patient selection; clinical, technical, and regulatory considerations; protocols; radiation safety; dosimetry; imaging; billing; coding; and how to make the therapy a success. In addition, the SNMMI-TS is developing a comprehensive educational module for each therapy. Upon completion of these modules, technologists will be awarded a “badge” that can be displayed on their curriculum vitae, LinkedIn, and

other social media and professional platforms. The priority is to ensure that NMTs are trained and prepared to perform radiopharmaceutical procedures.

While in 2020 there was a decline in state legislation issues, 2021 is making up for lost time. Many state legislators are making moves and working to introduce new bills ahead of the fall session. The SNMMI-TS and the State Technologist Advocacy Group (State TAGs) are aggressively monitoring what is happening in each state and will continue their efforts to pursue licensure in every state and work to ensure that NMTs are protected and recognized under any new potential bill. Most recently, in California Assemblyman Freddie Rodriguez introduced *A.B 1273*, Interagency Advisory Committee on Apprenticeship: the Director of Consumer Affairs and the State Public Health Officer. Our SNMMI-TS Advocacy Committee acted quickly and submitted an *opposition letter* before the public hearing with the Health Committee. The harmful piece of legislation is now scheduled to go to California’s Senate for vote this summer, so we are calling on our members to act quickly to oppose it. Legislation like this bill, and so many others that have been introduced over the last several years, is the exact reason why the SNMMI-TS’s advocacy efforts are crucial to the sustainability of the profession.

Finally, as I look towards the 2022 Mid-Winter Meeting scheduled for Orlando, FL, in January, I am hopeful that we will be able to come together face-to-face. This coming year, 2022, marks the 5th and final year of the SNMMI-TS strategic plan. While there have been many accomplishments this year, we are eager to plan and embark on what the future of nuclear medicine and molecular imaging has in store for the SNMMI-TS. This coming January the SNMMI-TS leadership, board, and key committees will come together to begin the planning and development of the new strategic plan. This new plan will guide the SNMMI-TS through the next five years and beyond.

The field is growing rapidly, and I am excited to be part of such a dynamic and future-driven organization.



Dusty M. York, CNMT,
PET, RT(N)(CT)

Once Again—The SNMMI “Nailed It”!

Kathy S. Thomas, MHA, CNMT, PET, FSNMMI-TS

Editor, *JNMT*

At the time of this writing, elite athletes from around the world are demonstrating excellence in their chosen sport with only a virtual audience to support them. Yet, through the advances of modern technology, the world can still cheer them on and share in the many victories and successes of the XXXII Summer Olympic Games.

In a smaller way, the same celebration was enjoyed by nuclear medicine professionals worldwide as we gathered together once again in a virtual setting to share the latest in nuclear medicine and molecular imaging at the Society of Nuclear Medicine and Molecular Imaging's (SNMMI) 2021 Annual Meeting.

Similar to the virtual event in 2020, the 2021 virtual annual meeting included the opportunity to participate in live continuing education and scientific presentations, explore the latest advances presented as scientific posters in the exhibit hall, and visit with sponsoring commercial sponsors. Then, in the evenings (or mornings, depending on your time zone!), we could relax and share information learned from the day's educational sessions, participate in the Knowledge Bowl, or maybe just compare protocols or techniques and catch up with friends from around the world in the Drink and Think sessions.

The annual meeting is also an opportunity to celebrate the excellence of technologists, scientists, and physicians presenting abstracts and posters. During this year's Technologist Business meeting, the Technologist Best Abstract Awards as well as the *Journal of Nuclear Medicine Technology (JNMT)* 2020 Best Paper Awards were presented. The *JNMT* 2020 Best Paper awardees are selected from manuscripts written in the previous year by a technologist as the first author in the following categories: Scientific Papers (1st, 2nd, and 3rd place), Continuing Education Article, and Educators' Forum Article. Take a moment to review the awards and photos of this year's best paper awards in this issue.

Although we could not meet in person, I'm sure those who participated in the virtual annual meeting will agree—it was a complete success! The SNMMI staff—which we know are the backbone of this success story—as well as the speakers and technical staff absolutely “Nailed It” and deserve gold

medals for their dedication to excellence in making our meeting such a successful event.

In this issue, three continuing education articles offer a wide diversity of topics. First, nuclear medicine continues to play a vital role in treating thyroid cancer, one of the original theranostic studies in nuclear medicine. Julie Bolin discusses the latest approaches and treatment strategies in follicular thyroid

cancer (1). Next, Rani Noble takes us back to basics to share techniques to improve the quality of brain imaging (2). Finally, Geoff Currie continues the MRI series with an overview of technological principles in MRI and PET/MRI (3).

The need to translate nuclear medicine technology lessons to an online platform has been a challenge for our educators. In the Educators' Forum, Sara Johnson shares strategies and practical tips for effective online instruction, including careful course design and implementation and effective communication (4).

As the COVID-19 pandemic continues to ravage the world, key image findings continue to be shared among imaging professionals, including the need to consider COVID-19 status before scheduling a PET/CT scan (5) and the visual results noted on a PET/CT scan following a COVID-19 vaccination (6).

For those interested in refining their adult dynamic renal scintigraphy protocols, don't miss the recent practice-based survey performed to establish a national U.S. reference value for diethylenetriaminepentaacetic acid and mercaptoacetyl-triglycine (7).

Phantom studies are used to assess and validate the accuracy of measurements in imaging. In this issue, 2 phantom studies are presented to estimate chest wall attenuation from ^{123}I (8) and the accuracy of SUV measurements in SPECT/CT data (9).

Be sure to take some time to explore the diverse scientific and teaching case studies and the review summarizing the newly published book *Pharmacology Primer for Medications in Nuclear Medicine and Medical Imaging* (10) in this issue. I'm sure that you will find topics of interest specific to your clinical setting.



**Kathy S. Thomas,
MHA, CNMT, PET,
FSNMMI-TS**

As always, I value your comments and suggestions. Please contact me at ksstomas0412@msn.com with your ideas to enhance the content and value of *JNMT*.

REFERENCES

1. Bolin J. Thyroid follicular epithelial cell-derived cancer: new approaches and treatment strategies. *J Nucl Med Technol.* 2021;49:199–208.
2. Noble R. Brain imaging techniques: improving the quality. *J Nucl Med Technol.* 2021;49:209–214.
3. Currie GM, Kamvosoulis P, Bushong S. PET/MRI, part 2: technologic principles. *J Nucl Med Technol.* 2021;49:217–225.
4. Johnson SL. Online learning strategies and practical tips for nuclear medicine instructors. *J Nucl Med Technol.* 2021;49:269–274.
5. Kavanal AJ, Jena SR, Kumar R, et al. Effect of COVID-19 on ^{18}F -FDG PET/CT: is there a need to consider COVID-19 status before planning ^{18}F -FDG PET/CT for oncologic evaluation? *J Nucl Med Technol.* 2021;49:284–285.
6. Smith MV, Yang M. Reactive axillary lymphadenopathy to COVID-19 vaccination on ^{18}F -FDG PET/CT. *J Nucl Med Technol.* 2021;49:286–287.
7. Banks KP, Gunther RS, Farrell MB, Peacock JG, Costello M, Gordon LL. U.S. diagnostic reference levels and achievable administered activities for adult renal scintigraphy: an analysis of the Intersocietal Accreditation Committee Nuclear Laboratories. *J Nucl Med Technol.* 2021;49:246–249.
8. Alfano M, Weaver J, Mazurek R, Siegel A. Estimation of chest wall attenuation of ^{123}I emissions in substernal goiter: a phantom study. *J Nucl Med Technol.* 2021;49:232–234.
9. Halim F, Yahya H, Jaafar KN, Mansor S. Accuracy assessment of SUV measurements in SPECT/CT: a phantom study. *J Nucl Med Technol.* 2021;49:250–255.
10. Nielsen C. Pharmacology primer for medications in nuclear medicine and medical imaging [book review]. *J Nucl Med Technol.* 2021;49:293.

Thyroid Follicular Epithelial Cell–Derived Cancer: New Approaches and Treatment Strategies

Julie Bolin

Nuclear Medicine Technology Program, GateWay Community College, Phoenix, Arizona

Thyroid follicular epithelial cell–derived cancer includes papillary carcinoma, follicular carcinoma, Hürthle cell carcinoma, poorly differentiated thyroid cancer, and anaplastic thyroid carcinoma. Although the incidence of thyroid cancer has increased over the past 30 years, there has not been a significant increase in patient mortality. Use of increasingly sensitive detection methods such as high-resolution imaging has enabled earlier detection and better characterization of the thyroid malignancies. In the past several years, researchers have evaluated genetic mutations promoting thyroid carcinogenesis and oncogenesis. The identification of genetic mutations is important in understanding tumor initiation and progression. Additionally, these identified mutations may also serve as potential diagnostic or prognostic indicators and therapeutic molecular targets.

Key Words: anaplastic thyroid carcinoma; follicular thyroid carcinoma; papillary thyroid carcinoma; mitogen activated protein kinase; ATC; FTC

J Nucl Med Technol 2021; 49:199–208

DOI: 10.2967/jnmt.120.257105

Thyroid cancer is the twelfth most common type of cancer in the United States. According to the National Cancer Institute, over 850,000 people were living with thyroid cancer in the United States in 2017, and it was estimated that there would be 52,890 new cases of thyroid cancer in 2020 (1). Women are disproportionately affected across all age groups, with thyroid cancer having a 3 times higher incidence in women than in men. Thyroid cancer is more common in adults over 30 y old, with the peak incidence occurring in women in their 40s–50s and men in their 60s–70s (2). Thyroid cancer rarely affects children and adolescents; however, it accounts for 1.4% of pediatric malignancies (3). The incidence of thyroid cancer has also increased worldwide but may be variable because of variations in health-care access, use of population-level screening, ethnic or racial differences, varying exposure to ionizing radiation, and variations in iodine intake (excess or deficiency) (4,5). The rise in thyroid carcinoma incidence, particularly small papillary carcinomas, is largely due to the use of increasingly sensitive detection methods such as high-resolution imaging and ultrasensitive

thyroglobulin assays, which allow for the detection of previously undetectable thyroid cancers (6–8). Improved technology has allowed for not only an earlier detection of small carcinomas but also a better characterization of the lesions, prompting revisions in clinical management.

THE BASICS

Thyroid cancer includes 6 main types: papillary, follicular, Hürthle cell, medullary, poorly differentiated, and anaplastic. Clinicians often categorize the 6 main types of thyroid cancer on the basis of the origination cell type (follicular epithelial cell vs. parafollicular C cell) and preservation of cell type (differentiated, poorly differentiated, undifferentiated), as these characteristics relate to diagnosis, prognosis, and treatment (8). Follicular cells, also called thyroid epithelial cells or thyrocytes, line the colloid follicles and concentrate iodine for thyroid hormone synthesis. These cells give rise to papillary, follicular, Hürthle cell, poorly differentiated, and anaplastic thyroid cancers (9). The parafollicular or C cells are neuroendocrine cells that are scattered throughout the thyroid follicles and are responsible for the synthesis, storage, and secretion of calcitonin. Parafollicular cells give rise to medullary thyroid cancer (9). This continuing education article will focus only on follicular epithelial cell–derived thyroid cancers, which include papillary, follicular, Hürthle cell, poorly differentiated, and anaplastic carcinomas.

PRESERVATION OF CELL TYPE

Differentiated thyroid cancer represents most (90%–95%) types of thyroid cancer and includes papillary, follicular, and Hürthle cell carcinomas (HCCs) (6). Cellular differentiation is a central aspect in the histopathologic classification for thyroid follicular epithelial cell–derived cancers and refers to the process by which a cell becomes specialized to perform a specific function. Differentiated thyroid cancers maintain the characteristics and behavior of normal follicular epithelial cells in thyroid tissue. These cells retain many of the physiologic functions of thyroid cells, including thyroid-stimulating hormone (TSH, also called thyrotropin) stimulation of growth, iodine uptake (expression of sodium iodine symporter), and thyroid hormone production (9). Differentiated thyroid cancers maintain radioactive iodine (RAI) avidity, which permits the use of RAI scintigraphy and treatment as part of the disease management strategy. As a general rule,

Received Sep. 17, 2020; revision accepted Apr. 14, 2021.

For correspondence or reprints, contact Julie Bolin (julie.bolin@gatewaycc.edu).

Published online July 9, 2021.

COPYRIGHT © 2021 by the Society of Nuclear Medicine and Molecular Imaging.

differentiated cancers tend to be less aggressive than undifferentiated cancers (9).

Poorly differentiated thyroid cancer (PDTC) was at one time considered a variant of differentiated thyroid cancer; however, the World Health Organization began recognizing it as a distinct pathologic entity in 2004 because the clinical and histologic features occupy an intermediate position between differentiated thyroid cancer and undifferentiated thyroid cancer (10–13). PDTC occurs de novo; however, there is a theory that PDTC may also transform from differentiated thyroid cancers through the accumulation of genetic abnormalities (11,14). This theory is supported by the frequent cooccurrence of PDTC and differentiated thyroid cancer in the same tumor specimen and the overlap of genetic mutations (11). When PDTC and well-differentiated thyroid cancer are present in the same tissue sample, it is important to note the presence of PDTC, as prognosis and treatment strategies may be guided by the PDTC component (10). Given that PDTCs are often resistant to RAI therapy, these cancers present a therapeutic challenge (11,12). Outcome statistics for PDTCs are worse than for differentiated thyroid cancers. In PDTCs, approximately 50% of patients survive after 10 y, whereas in differentiated thyroid cancers, particularly papillary thyroid carcinoma (PTC), 95% of patients survive after 10 y (13).

Undifferentiated thyroid cancer includes anaplastic thyroid carcinoma (ATC), a very rare form of thyroid carcinoma accounting for less than 1% of all thyroid carcinomas (15).

Undifferentiated thyroid cancer may occur de novo or may transform from a previously differentiated thyroid cancer (more commonly PTC, but also follicular thyroid carcinoma [FTC] and PDTC) (12,14). A signature attribute of many advanced tumors is cellular dedifferentiation, whereby cancerous cells maintain little to no resemblance to the normal cells from which the cancer originated. In the context of thyroid cancer, loss of RAI avidity most commonly develops from cellular dedifferentiation, resulting in the impairment of the sodium iodine symporter function (14,15). Loss of iodine avidity excludes the use of RAI scintigraphy and treatment. As thyroid cancer cells dedifferentiate, their glucose metabolism increases, allowing for evaluation with ^{18}F -FDG PET/CT (16). Overall outcomes and survival statistics are poor for undifferentiated thyroid cancer, with a mean survival of 0.5 y after diagnosis (15).

Figure 1 illustrates the cellular differentiation stage for follicular epithelial cell–derived thyroid carcinomas and how it relates to radioiodine scintigraphy/treatment and overall prognosis.

OVERVIEW OF FOLLICULAR EPITHELIAL CELL–DERIVED THYROID CANCERS

PTC

PTC is the most commonly occurring form of differentiated thyroid cancer and accounts for 80%–85% of all thyroid

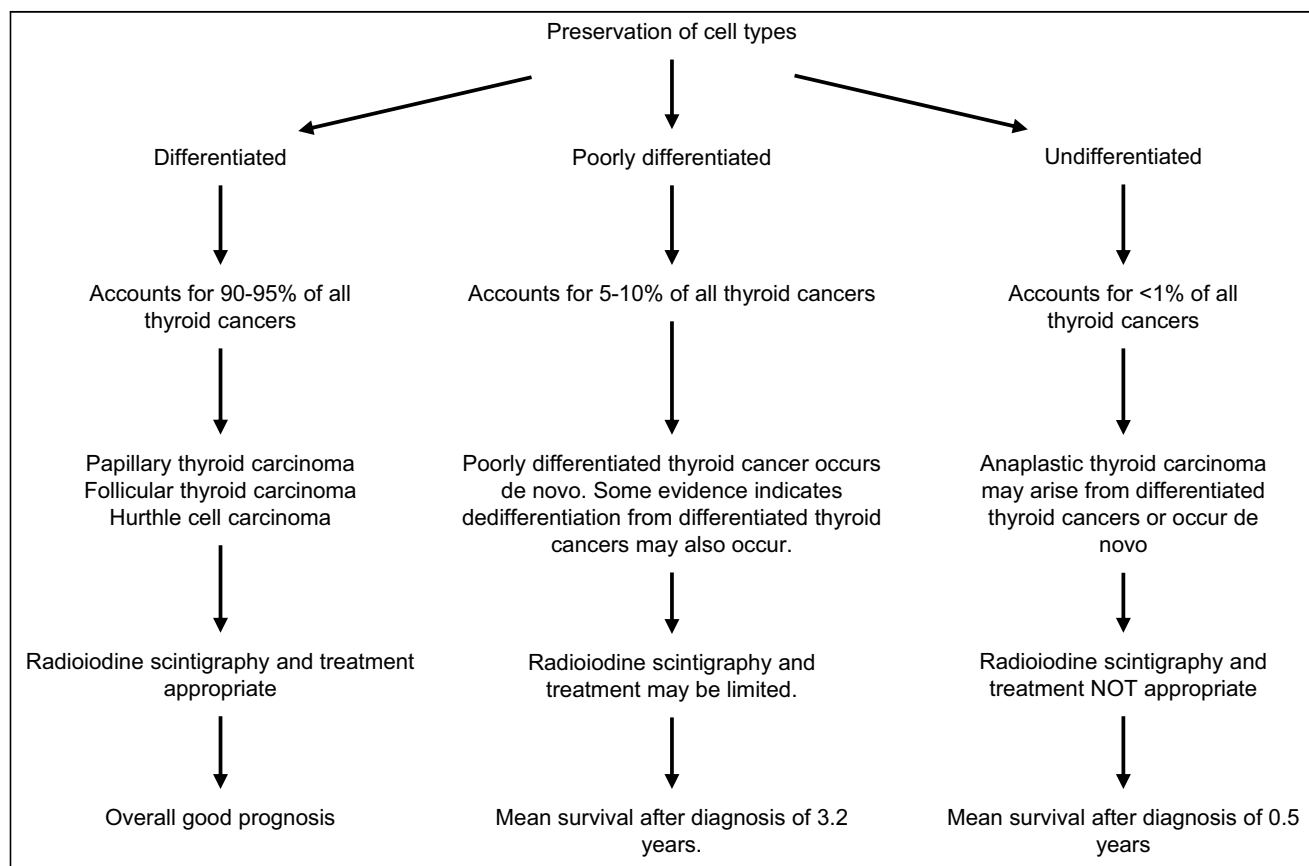


FIGURE 1. Cellular differentiation and diagnostic/prognostic implications.

cancer (17). Patients are often asymptomatic but may have cervical lymphadenopathy, hoarseness, and dysphagia. Risk factors for PTC include radiation exposure, particularly during childhood, a family history of thyroid malignancy, and inherited conditions such as familial adenomatous polyposis or Cowden syndrome (18). PTC most often affects middle-aged women. Thyroid carcinoma accounts for 1.4% of pediatric malignancies, with PTC being the most common thyroid carcinoma affecting children (3).

In 2017, the World Health Organization recognized 15 histologic subtypes of PTC: conventional/classic, papillary microcarcinoma (<1 cm in diameter), encapsulated, follicular, diffuse sclerosing, tall cell, columnar cell, cribriform-morular, hobnail, PTC with fibromatosis/fasciitislike stroma, oncocytic, solid/trabecular, spindle cell, clear cell, and Warthin-like variant (12,13). Conventional/classic, papillary microcarcinoma, encapsulated, follicular, diffuse sclerosing, and tall cell are the most common and best-documented histologic subtypes (12,13). Because histologic subtypes relate to biologic aggressiveness and prognosis, these distinctions are valuable in terms of disease management strategies and recommendations. The papillary microcarcinoma and encapsulated variants are considered the least biologically aggressive. The tall cell and hobnail variants have the potential to be more aggressive than the conventional/classic variant, and as a result, patients with these tumors may require a more aggressive disease management strategy than do those with conventional/classic papillary cancer of the same stage (12).

In addition to the histologic subtype, PTC tumors range in size and extent of the primary lesion (17). Although there may be microcarcinomas (<1 cm in diameter) and intrathyroidal lesions (>1.5 cm in diameter) that are confined to the thyroid capsule, it is not uncommon for patients to have multifocal disease, extrathyroidal extension, and cervical lymph node metastasis (17). Up to 27% of patients have cervical lymph metastasis at the initial presentation (17). Children, more commonly than adults, present with lymph node involvement or metastasis to distant sites such as the lungs (3). Overall, patients with PTC typically have a good prognosis. Increased risk for recurrence or poor prognosis is often related to age (persons > 55 y old at diagnosis), increased vascular invasion, invasion into the adjacent neck structures, and distant metastasis (17).

FTC

FTC is the second most common type of thyroid cancer after PTC and accounts for 10% of differentiated thyroid cancers (19). Unlike PTC, FTC is rarely associated with previous radiation exposure but may be associated with iodine deficiency. FTC typically occurs in a slightly older age group than PTC (40–60 y) and is also less common in children (20). Minimally invasive FTC is limited to microscopic capsular or vascular invasion, whereas widely invasive tumors may have multiple foci and extensive, widespread invasion (21). Given that vascular invasion is common with FTC,

metastatic disease may be noted even when the primary thyroid lesion is small. Distant metastatic spread to the lungs or bones is found more commonly with FTC than with PTC (19–21). Poor prognosis is often related to tumor size, degree of vascular and capsular invasion, and age (20).

HCC

HCC accounts for 3% of all thyroid cancers. Previously, HCC was classified as an oxyphilic variant of FTC; however, data from genetic and molecular analysis suggest that HCC is a distinct entity (22,23). Just as with FTC, HCC occurs in a slightly older age group than PTC. Unlike FTC, HCC has more of a propensity to spread to cervical lymph nodes and has a higher risk of distant metastatic disease, particularly skeletal and pulmonary metastasis (24). Another important distinction relevant for patient management is that although metastatic lesions in FTC often concentrate RAI, HCC metastatic foci are often RAI-refractory (23,25).

PDTC

PDTC has not been studied as commonly as other follicular epithelial cell–derived thyroid cancers, partly because of its overall rarity but also because it was not classified as an independent thyroid cancer histotype until 2004 (11). According to the Turin proposal, the presence of PDTC is determined by the presence of carcinoma of follicular cell derivation, architectural patterns (solid/trabecular/insular architecture), and high-grade features such as nuclear pleomorphism, tumor necrosis, or a high mitotic rate (11–14). PDTC more commonly occurs in women 60–70 y old and is associated with aggressive characteristics such as extrathyroidal extension, regional lymph node metastasis, and distant metastasis. Just as with other forms of follicular epithelial cell–derived thyroid cancers, the most common sites of distant metastasis include the lungs and bones; however, less common metastatic sites also include the liver, skin, ovaries, and retroperitoneal space (11). Although PDTC accounts for only 4%–7% of all thyroid cancers, it represents the main cause of death from nonanaplastic follicular cell–derived thyroid cancer (11).

ATC

ATC is the most aggressive and rarest thyroid cancer. Although ATC accounts for only 1%–2% of all thyroid cancer cases, it is responsible for 14%–39% of deaths related to thyroid malignancy (26). ATC occurs primarily in the geriatric population and is more common in persons 60–70 y old. Patients with ATC often have a large, palpable thyroid mass associated with hoarseness, dyspnea, dysphagia, and vocal cord paralysis (26). The extent of disease may be restricted to the neck region or may include distant metastasis to the lungs, bone, or brain. Although ATC may develop as a singular entity, it may also evolve from or coexist with differentiated thyroid cancer (12,13,26). Given that ATC is a type of undifferentiated thyroid cancer, these cells will not maintain the characteristics and behavior of normal follicular epithelial cells and thus will not concentrate RAI.

GENETIC CHANGES INVOLVED IN THYROID CARCINOGENESIS

Table 1 defines abbreviations used in discussing the genetics of thyroid carcinogenesis.

MAPK Pathway

In recent years, there have been multiple studies evaluating the genetic alterations and molecular mechanisms underlying thyroid carcinogenesis and their prevalence in follicular epithelial cell–derived thyroid carcinomas. An understanding of these mutations may explain the diverse clinical characteristics of thyroid follicular epithelial cell–derived carcinomas and provide diagnostic information relative to treatment. Mutations in both oncogenes and tumor suppressor genes acquired along the path of tumor progression allow cancerous cells to evade the normal control of cell cycle and apoptotic processes and promote the transition from localized to metastatic disease. Oncogenic activation of the mitogen MAPK is considered the most common molecular alteration in thyroid cancer and is believed to initiate carcinogenesis (6). The MAPK pathway is a key molecular signaling pathway responsible for the regulation of several diverse cellular functions, including cellular growth, proliferation, and angiogenesis. In the normally functioning cell, the MAPK pathway is triggered by the binding and activation of receptor tyrosine kinases, which transmit growth signals from the plasma membrane to the nucleus (6). Oncogenic alterations in the MAPK pathway influence processes that are crucial for cancer development and progression. In oncogenic cells, the MAPK pathway is driven by mutations including *RET/PTC*, *RAS*, and *BRAF* (6). These driver mutations are initiating mutations and occur early in thyroid carcinogenesis (14).

RET/PTC Rearrangements

RET protooncogene rearrangements are most commonly found in PTC (termed *RET/PTC* rearrangements) and lead to the constitutive activation of the *RET* tyrosine kinase domain and subsequent activation of the MAPK signaling pathway (27). *RET/PTC* rearrangements are found in 20%–70% of PTCs and are more commonly associated with pediatric thyroid cancers (27). Although 13 *RET/PTC* rearrangements have been found, *RET/PTC1* and *RET/PTC3* are the most

common. *RET/PTC1* is more prevalent in sporadic PTC, and *RET/PTC3* is highly prevalent in radiation-induced PTC. *RET/PTC* rearrangements are also found in the follicular variant of PTC and in FTC (15). The prognostic significance of *RET/PTC* rearrangements is not fully established. *RET/PTC1* does not correlate with clinical pathologic features of PTC; however, *RET/PTC3* is associated with aggressive characteristics and poor prognostic factors, including greater primary tumor size, cellular variations, and a more advanced stage at diagnosis (15,27).

RAS Mutations

The *RAS* oncogene mutations play an important role in thyroid oncogenesis through the regulation of 2 important signaling pathways: the MAPK cascade, which is responsible for cellular proliferation, and the phosphatidylinositol 3-kinase (PI3K)/protein kinase B (AKT) pathway, which is important

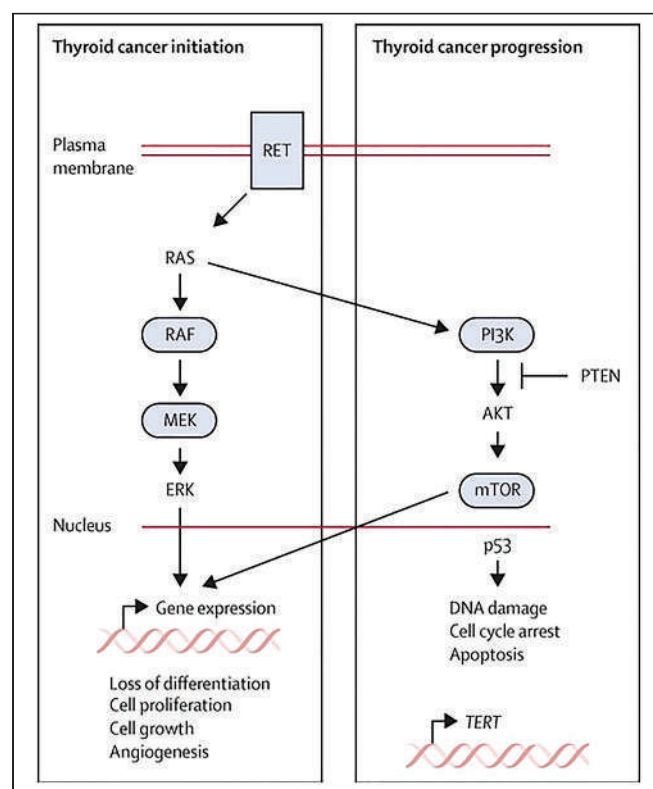


FIGURE 2. Key molecular signaling pathways involved in thyroid cancer initiation and progression. (Left) MAPK pathway, which is activated by mutations in *RET*, *RAS*, and *BRAF*. (Right) Pathways involved in tumor progression, including PI3K/AKT, p53 tumor suppressor, and *TERT*. Blue boxes represent molecular targets for therapies approved by Food and Drug Administration. ERK = extracellular-signal-regulated kinase; MEK = mitogen/extracellular-signal-regulated kinase; mTOR = mammalian target of rapamycin; PTEN = phosphatase and tensin homolog mutation; p53 = Tp53 or tumor protein; RAF = rapidly accelerated fibrosarcoma; RAS = rat sarcoma point mutations; RET = rearrangement during transfection; TERT = telomerase reverse transcriptase. (Reprinted with permission of (6).)

TABLE 1
Genetic Abbreviations

Name	Abbreviation
Mitogen-activated protein kinase	MAPK
Rearrangement during transfection/ papillary thyroid cancer mutations	<i>RET/PTC</i>
Rat sarcoma point mutations	<i>RAS</i>
B-rapidly accelerated fibrosarcoma	<i>BRAF</i>
Telomerase reverse transcriptase promoter	<i>TERT</i>
Tumor protein	<i>Tp53</i>
Phosphatase and tensin homolog deleted from chromosome 10	<i>PTEN</i>

for cell survival (Fig. 2) (6,15). Oncogene activation in the 3 *RAS* protooncogenes (*HRAS*, *KRAS*, and *NRAS*) is found in most human cancers, including thyroid cancer. *RAS* mutations occur in almost every type of thyroid cancer and in benign follicular adenomas: 20%–25% of benign follicular adenomas, 10%–20% of PTCs, 30%–45% of follicular-variant papillary thyroid cancers, 30%–35% of FTCs, 20%–40% of PDTCs, and 10%–20% anaplastic thyroid cancers (ATCs) (9,28). *RAS* mutation alone is most likely associated with limited aggressiveness of thyroid cancer; however, *RAS* may coexist with other mutations such as *TERT* or *PTEN*, both of which have been implicated in aggressive clinicopathologic behavior (28,29).

BRAF Mutations

Although more than 40 point mutations have been documented in *BRAF*, the most frequent mutation is *T1799A BRAF*, resulting in V600E protein kinase (6). *BRAF V600E* is exclusive to PTC, PTC-derived PDTC, and ATC. The *BRAF V600E* mutation occurs in about 40%–45% of all PTCs and in about 60% of *BRAF*-associated PTCs (30). *BRAF V600E* mutation is noted in the potentially more aggressive PTC variants, including multinodular/diffuse forms of the follicular variant of PTC (15). *BRAF V600E* mutation causes constitutive activation of the *BRAF* kinase and MAPK signaling pathway and has been associated with aggressive clinicopathologic features such as extrathyroidal invasion, lymph node metastasis, vascular invasion, and a primary tumor of advanced stage (15). In *BRAF*-associated PTC, both vascular endothelial growth factor and platelet-derived growth factor are upregulated (31,32). Vascular endothelial growth factor and platelet-derived growth factor are potent stimulators of angiogenesis, a process that is vital to carcinogenesis. *BRAF* mutations have also been implicated in the loss of cellular differentiation resulting in decreased expression of sodium iodide symporter, TSH receptor, and thyroglobulin, thereby creating a situation for iodine-refractory disease (6,9,14). Although *BRAF* mutations have been implicated in aggressive behavior, there is no clear consensus. Frequently, classic PTC and papillary microcarcinomas have associated *BRAF* mutations. Despite these mutations, classic PTC and papillary microcarcinomas maintain an excellent prognosis. Isolated *BRAF* mutations may not substantially contribute to risk stratification and increased specific disease mortality. Cancer evolution is triggered by the sequential accumulation of mutations that bestow metastatic potential. *BRAF* mutations are frequently associated with *TERT* mutations. Thyroid cancers displaying both *BRAF V600E* and *TERT* mutations exhibit more aggressive clinicopathologic behavior than do thyroid cancers displaying only *BRAF* mutations (29).

NON-MAPK GENETIC MUTATIONS

***TERT* Mutations**

A genetic alteration in *TERT* has been associated with increased aggressiveness and poor patient prognosis.

Telomerase is the enzyme involved in telomere elongation, whose main function is preservation of chromosome integrity and genomic stability. Telomeres are repetitive DNA sequences at the ends of chromosomes acting as protective caps. Telomeres are continually shortened with each successive generation. When telomeres reach a critically short length, the chromosomes participate in breakage–fusion–breakage cycles resulting in cell crisis and apoptosis (29). Therefore, telomeres allow a cell to replicate only a certain number of times. Since cancer cells seek to grow at an unconstrained rate, the shortened telomeres and subsequently restricted replication present a significant problem. In cancer cells, telomere length is maintained by telomerase, which functions to elongate telomeric DNA by using its 2 components: an RNA template and a reverse transcriptase (29). Mutations in *TERT* are sufficient to restore the activity of the telomerase complex (15). Most adult differentiated cells do not express or have very low expression of telomerase; however, telomerase is significantly expressed in 90% of human cancers, including differentiated, poorly differentiated, and undifferentiated thyroid cancers (29). By expressing higher levels of reverse transcriptase, and therefore allowing for increased telomerase activity, carcinoma cells prevent critically short telomeres and apoptosis, meaning the oncogenic changes bestow an extended life or immortality.

Independent of its function in telomere length maintenance, *TERT* mutations have also been associated with metastatic capability and cellular dedifferentiation (15,29). Studies have indicated that *TERT* may encourage metastasis through the activation of the epithelial–mesenchymal transition. This transition is a process by which epithelial cells lose their normal characteristics such as intercellular adhesion and lack of motility and acquire mesenchymal cell properties such as reduced intercellular adhesion, increased motility, invasiveness, and apoptosis resistance (29). Activation of the epithelial–mesenchymal transition process is triggered by various stimuli resulting in the silencing of intracellular adhesion molecules such as epithelial cadherin and the upregulation genes promoting the mesenchymal shift (29). The epithelial–mesenchymal transition is also suggested to promote the dedifferentiation process, resulting in poorly differentiated or undifferentiated cancers (29).

***Tp53* Mutation**

Alterations in several tumor suppressor genes have been associated with thyroid oncogenesis, but the most widely studied is the *Tp53* gene. p53 (also known as Tp53) is a key tumor suppressor protein known as the “guardian of the genome” because of its functions in maintaining genomic integrity through control of cell division, apoptosis, DNA repair, and angiogenesis (15). Cancer cells with a *Tp53* mutation have evolved the ability to bypass the cell cycle checkpoints, to favor antiapoptotic pathways, and to proliferate uncontrollably. The amount of p53 in normal cells is maintained at a very low level; however, *Tp53* mutations and p53 overexpression are frequent in several human cancers and occur in well-differentiated thyroid cancers (40% of

PTCs and 22% of oncocytic FTCs), as well as in a high proportion of PDTC and ATCs (particularly those originating from PTC), which indicates that *Tp53* mutations promote the transition from differentiated to undifferentiated thyroid cancer (15). *Tp53* mutations are most noted in the later stages of oncogenesis and occur simultaneously with a substantial increase in cellular proliferation (15). *Tp53* mutations have been noted in cancers with *BRAF* mutations and *RET/PTC* rearrangements and are believed to promote extrathyroidal extension and distant metastasis (15).

Figure 2 illustrates key molecular signaling pathways involved in thyroid cancer initiation and progression. Table 2 reviews genetic mutations associated with thyroid carcinogenesis.

ASSESSMENT AND TREATMENT

Thyroid cancers of follicular epithelial cell origin exhibit highly variable clinical manifestations ranging from microcarcinomas with very low tumor-specific morbidity or mortality to very aggressive thyroid carcinomas such as anaplastic carcinoma. Diagnostic workup and standard treatments such as the use of surgery, RAI therapy, and TSH suppression therapy are individualized to the patient and the clinical objectives. Despite the increased incidence of thyroid carcinoma in the past 30 years, there has not been a substantial increase in mortality (6,7,33). This has sparked a discussion in the medical community about the potential for overdiagnosis and overtreatment. In 2015, American Thyroid Association (ATA) guidelines for medical management of adults with thyroid nodules and differentiated thyroid cancer

emphasized a distinction between low-risk and high-risk patient groups, with physicians identifying patients who require more aggressive treatment while sparing patients with a low risk from unnecessary diagnostic procedures and treatments (33,34). The 2015 ATA guidelines are not inclusive of all proper approaches or methods and were met with controversy by the medical community. In 2018, the Martinique Working Group, comprising representatives from the ATA, the European Association of Nuclear Medicine, the European Thyroid Association, and the Society of Nuclear Medicine and Molecular Imaging, published an authoritative report called “The Martinique Principles,” which highlighted controversies in the medical management of thyroid cancer (35). Although the current article will not highlight the spectrum of expert opinions presented by members of the Martinique Working Group, it should be stated that there is still debate within the medical community regarding disease management strategies.

Treatment decisions for patients with differentiated thyroid cancer are based on strategies for risk assessment that consider symptom manifestation, histology, tumor size, tumor invasiveness, lymph node involvement, distant metastasis, and diagnostic imaging. Cervical lymph node sonography, which provides information on the size, number, and location of thyroid lesions and on vascularity, lymph node involvement, and adjacent tissue invasion, is widely used as the primary imaging tool when determining surgery and treatment options (6). The 2015 ATA guidelines recommend preoperative sonography for patients undergoing surgery for confirmed or suspected thyroid malignancy (33,34). Preoperative

TABLE 2
Genetic Mutations and Associated Prognostic Significance

Genetic mutation	Cancers displaying genetic mutation	Prognostic significance
<i>BRAF</i>	PTC (<i>BRAF V660E</i>), PDTC, ATC	No clear consensus on prognostic significance; linked to extrathyroidal invasion, lymph node metastasis, vascular invasion, advanced tumor stage in primary tumor, and multifocality; linked to cellular dedifferentiation; linked to loss of iodine avidity; upregulates platelet-derived growth factor; upregulates vascular endothelial growth factor
<i>PTEN</i>	Differentiated thyroid cancers, PDTC	Uncontrolled cell growth and proliferation
<i>RAS</i>	PTC, PTC-FV, FTC, PDTC, ATC	<i>RAS</i> mutations alone likely associated with limited aggressiveness
<i>RET/PTC</i> rearrangements	PTC (adult and pediatric), PTC-FV, FTC	Not fully established; <i>RET/PTC1</i> does not correlate with clinical pathologic features; <i>RET/PTC3</i> is associated greater primary tumor size, cellular variations, and more advanced stage at diagnosis
<i>TERT</i>	90% of human cancers, differentiated thyroid cancers, PDTC, ATC	Restores telomerase complex activity (prevents apoptosis); promotes epithelial mesenchymal transition, which promotes metastasis and cellular dedifferentiation
<i>Tp53</i>	PTC, FTC, PDTC, ATC	Extrathyroidal extension; distant metastasis; potentially promotes cellular dedifferentiation

BRAF = B-rapidly accelerated fibrosarcoma mutation; *PTEN* = phosphatase and tensin homolog mutation; *RAS* = rat sarcoma point mutation; PTC-FV = follicular variant of papillary thyroid cancer; *RET/PTC* = rearrangement during transfection/papillary thyroid cancer (*RET/PTC*) mutation; *TERT* = telomerase reverse transcriptase mutation.

cervical lymph node sonography identifies 20%–30% of suggestive lymph nodes; identifying such nodes may change the surgical plan and allow for a more complete initial surgical dissection (6,33). For patients with papillary microcarcinomas 1 cm or smaller and with no evidence of lymph node metastasis, nonsurgical management may be possible (6,7,34). If surgery is indicated, a hemithyroidectomy is potentially an option for unifocal tumors smaller than 4 cm and with no evidence of lymph node metastasis or invasion into adjacent neck structures; however, a total thyroidectomy may be indicated if the disease management team believes RAI therapy will be used or if structural changes dictate surgical preferences (6,7,33).

In addition to sonography, the 2015 ATA guidelines advocate for the presurgical use of cross-sectional imaging with CT and MRI when there is sonographic evidence of extrathyroidal extension, significant cervical lymphadenopathy, tumor adherence to neck structures, or patient symptoms such as hoarseness and dysphagia, as these situations are potentially high-risk (33,34). Use of iodinated contrast medium in these patients may delay RAI imaging and therapy for several months; however, the complete surgical excision of all thyroid tissue and locoregional metastasis is a critical element in patient management (33). Rarely, additional preoperative imaging is required for differentiated thyroid cancer, unless there is suspicion of widespread or distant metastasis. ^{18}F -FDG PET/CT may be indicated for initial staging in these cases but is more commonly used for postsurgical evaluation in RAI-refractory disease (5).

After surgery, the disease management team will determine the need for RAI ablation, TSH suppression therapy, or both. The 2015 ATA guidelines identify high, intermediate, and low risk for thyroid cancer recurrence and include clinical symptoms, postsurgical thyroglobulin levels, and pathologic features in the determination of risk of recurrence (6,34). The extent of surgery will influence the acceptable ranges for thyroglobulin, as patients who had a hemithyroidectomy will have a higher thyroglobulin level because of the remaining thyroid tissue, which is likely benign (7).

TSH Suppression Therapy

In patients who have had a partial or total thyroidectomy, thyroid hormone replacement may be used not only to replace endogenous thyroid hormone but also to inhibit tumor progression or recurrence because TSH encourages cellular proliferation in differentiated thyroid cancer cells. TSH suppression therapy significantly reduces recurrence and thyroid cancer–related mortality (6,36). The goal of TSH suppression therapy is to reduce TSH to below the reference range (0.4–4.5 mIU/L). The appropriate TSH concentration as determined by the disease management team may vary among patients given the extent of surgery and the distinction between low-risk and high-risk status. Reducing TSH concentrations to 0.1 mIU/L can improve outcomes for high-risk patients; however, this reduction requires doses of thyroid hormone replacement that may induce subclinical

hyperthyroidism (6). Potential adverse effects include osteoporosis in postmenopausal women, angina, and atrial fibrillation (6). In patients with low-risk thyroid cancer, a more conservative approach with the goal of thyroid hormone replacement therapy to maintain TSH at or slightly below the lower limit of normal (0.1–0.5 mIU/L) may be appropriate (36). Patients who undergo a lobectomy instead of total thyroidectomy may not require TSH suppression therapy if their TSH serum levels are maintained at the lower limit of normal (0.5–2.0 mIU/L) (36).

Figure 3 illustrates the negative-feedback loop for thyroid hormone synthesis. The hypothalamic–pituitary axis regulates TSH release through a negative-feedback loop. TSH-releasing hormone stimulates anterior pituitary thyrotrophs to secrete TSH. When TSH binds to the TSH receptor on thyroid follicular cells, it stimulates iodine uptake, thyroid hormone (triiodothyronine, tetraiodothyronine) secretion, and thyroid gland growth and differentiation. Of the thyroid hormones released, approximately 80% are in the form of tetraiodothyronine and 20% in the form of triiodothyronine (37). Triiodothyronine has a short half-life but is most active on the nuclear receptor, whereas tetraiodothyronine has a long half-life but is less active in binding to the nuclear receptor. Because tetraiodothyronine becomes deiodinated and converted into triiodothyronine by most tissues (especially the liver and kidneys), tetraiodothyronine acts as a reservoir for triiodothyronine (37). Serum levels of thyroid hormone exert negative-feedback control on TSH-releasing hormone and TSH. High thyroid hormone levels decrease TSH secretion, whereas low thyroid hormone levels stimulate TSH synthesis

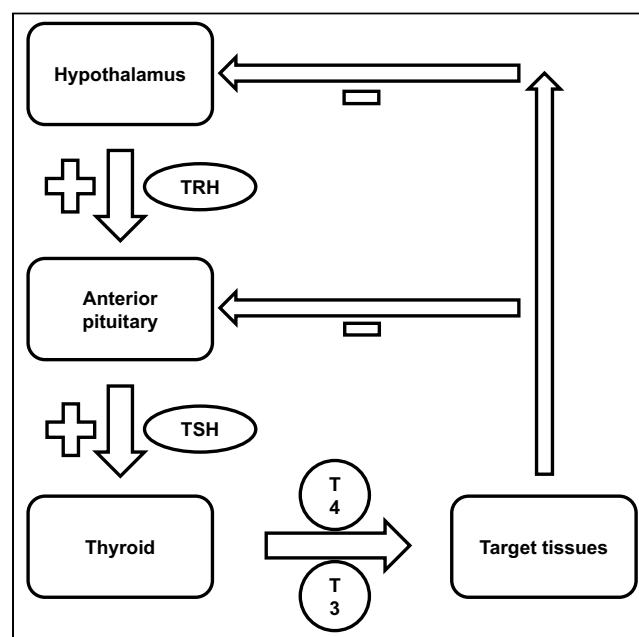


FIGURE 3. Thyroid hormone synthesis negative-feedback loop. Arrow with plus sign indicates stimulation. Arrow with minus sign indicates inhibition. T3 = triiodothyronine; T4 = tetraiodothyronine; TRH = TSH-releasing hormone.

and secretion. As this relates to thyroid cancer, patients who have had a total thyroidectomy require TSH suppression therapy for 2 reasons: to replace endogenous thyroid hormone and to suppress TSH. TSH suppression is an important aspect of treatment because TSH may stimulate cellular proliferation in differentiated thyroid cancer cells.

RAI Therapy

In previous years, many clinicians routinely recommended RAI therapy for all patients with differentiated thyroid cancer, except in patients with papillary microcarcinoma. However, the 2015 ATA guidelines proposed a more conservative approach based on specific histopathologic features that could modulate risk of recurrence or disease-specific mortality, disease follow-up implications, potential adverse effects, and physician and patient preferences (6,7,34). The goals of RAI therapy are remnant ablation, adjuvant therapy, and treatment of known residual or recurrent disease.

Remnant ablation eliminates residual clusters of presumably normal or benign thyroid tissue, which incorporates iodine and produces thyroglobulin, thereby complicating efforts to use thyroglobulin serum assays and RAI scintigraphy to identify persistent disease or recurrence (6). Potential benefits to remnant ablation include improved initial staging and the clinical use of RAI whole-body scintigraphy and thyroglobulin serum assays as a follow-up for cancer recurrence. However, use of RAI whole-body scintigraphy is not used as common as it once was because of the increased sensitivity of cervical lymph node sonography (6), which is cheaper by comparison, is more widely available, has no associated radiation exposure, has no potential side effects, and does not require discontinuation of thyroid hormone replacement therapy or use of TSH α injections (6). Cervical lymph node sonography combined with postoperative serum thyroglobulin (either with the patient taking thyroid hormone replacement or after TSH stimulation) are very sensitive methods for detecting persistent disease or a thyroid remnant, for predicting the potential for disease recurrence, and for tailoring future diagnostic and therapeutic approaches (6,33). Postoperative whole-body RAI scintigraphy may still be indicated when the extent of a thyroid remnant or residual disease cannot be accurately determined from cervical lymph node sonography and surgical reports or when the results of whole-body RAI scintigraphy may alter treatment decisions. If remnant ablation is deemed appropriate for low- to intermediate-risk patients, lower dose ranges for ^{131}I NaI (1,110 MBq, or 30 mCi) may be preferred over high doses, depending on the size of the remnant (7,33).

Use of RAI for initial adjuvant therapy destroys microscopic foci that may or may not be present in the thyroid remnant or elsewhere in the body after surgical resection. The goals of adjuvant therapy are to reduce the risk of disease recurrence and improve long-term outcomes. Given that patients are selected for adjuvant therapy with regard to risk of recurrence instead of known disease, some patients who receive adjuvant therapy may have been adequately treated

by their primary surgery (35). For patient selection and RAI dose determination, clinicians evaluate several factors, such as the likelihood of improved clinical outcomes, potential side effects, the results of postsurgical follow-up RAI scintigraphy, thyroglobulin assays, the extent of thyroid surgery, and the preferences of the patient and disease management team (35). If RAI is indicated as adjuvant therapy for patients without known distant metastasis, a dose range of up to 5,550 MBq (150 mCi) is generally recommended but should be tailored to the specific patient on the basis of individual risk, the lowest activity needed for effective treatment, and specific recommendations from the disease management team (33).

The third use of RAI therapy is for patients with known iodine-avid metastatic disease or for recurrence. Typical doses are 3,700–7,400 MBq (100–200 mCi) and may be based on the observations and experience of the disease management team or estimated by dosimetry, with a goal of limiting excess radiation exposure to the bone marrow and avoiding hematopoietic toxicities (7,33). Just as with adjuvant RAI therapy, there may be multiple factors that account for the determined dose. Dose-related impairment of testicular function and transient ovarian failure have been observed after RAI therapy. General recommendations include avoidance of pregnancy for at least 6 mo after treatment, or longer if additional RAI therapy may be indicated. For men who may receive multiple RAI treatments, consideration of sperm banking may be necessary if there is an anticipated cumulative ^{131}I -sodium iodide dose greater than 14 GBq (378 mCi) (38).

For patients with iodine-refractory disease, RAI therapy is less likely to provide benefit. The Martinique Working Group described 5 common clinical scenarios that may indicate an iodine-refractory state: no RAI uptake on a diagnostic whole-body scan, no RAI uptake on a scan obtained several days after RAI therapy administration, lack of RAI uptake in all tumor foci, progression of differentiated thyroid cancer metastasis despite RAI uptake, and progression of differentiated thyroid cancer metastasis despite cumulative ^{131}I NaI doses of more than 22.2 GBq (600 mCi) (35). Potential treatments for iodine-refractory disease include external radiation therapy, chemotherapy, and targeted molecular therapy.

Targeted Molecular Therapy for Advanced Differentiated Thyroid Cancer

Table 3 defines abbreviations used in discussions of targeted molecular therapy for advanced differentiated thyroid cancer.

Both papillary and follicular carcinomas are well-differentiated thyroid cancers and are considered highly treatable by conventional treatments, which include surgery, RAI ablation, and TSH suppression therapy. Although HCC is also considered differentiated and may also be treated with conventional treatments, it may prove more RAI-resistant than PTC and FTC. A small percentage of patients with differentiated thyroid cancer develop iodine-refractory metastatic disease, thereby limiting treatment options (39). Although

TABLE 3
Targets in Molecular Therapy

Abbreviation	Definition
FGF	Fibroblast growth factor
FLT-3	Type III receptor tyrosine kinase
KIT	Type of receptor tyrosine kinase and type of tumor marker
MEK	Mitogen/extracellular signal-regulated kinase
mTOR	Mammalian target of rapamycin
PDGF α	Platelet-derived growth factor α
PDGFR β	Platelet-derived growth factor receptor β
PPAR γ	Peroxisome proliferator-activated receptor γ
RET	Rearrangement during transfection
RET/PTC	Rearrangement during transfection/papillary thyroid cancer
VEGFR	Vascular endothelial growth factor receptor

conventional treatments may also be used in PDTC, many cases are RAI-resistant (14). Thyroid cancers that are no longer responsive to RAI therapy are still candidates for other forms of treatment, including standard chemotherapy and targeted therapy. Targeted therapy and chemotherapy differ in their mechanism of cancer treatment. Targeted drug therapy specifically prohibits the action of key proteins involved in cancer-specific activities, whereas traditional chemotherapy affects all rapidly proliferating cells, including normal cells. Targeted drug therapy is an active area of cancer research, and currently there are 2 approved drugs that target the MAPK cascade. The U.S. Food and Drug Administration approved 2 multikinase inhibitors for the treatment of advanced differentiated thyroid cancer refractory to RAI treatment: sorafenib (approved in 2013) and lenvatinib (approved in 2015). Multikinase inhibitors block the effect of tyrosine kinases that are overactive in the MAPK pathways. Sorafenib is a kinase inhibitor that inhibits multiple intracellular and cell-surface kinases (KIT, FLT-3, RET, RET/PTC, VEGFR 1-3, and PDGFR- β) (40) that are implicated in tumor cell signaling, angiogenesis, and apoptosis. Lenvatinib is also a kinase inhibitor that inhibits the vascular endothelial growth factor receptors as well as other kinases (FGF receptors, PDGF α , KIT, and RET) associated with pathogenic angiogenesis, tumor growth, and cancer progression (39,41). In addition to the multikinase inhibitors, selective kinase inhibitors are also therapeutic options for advanced differentiated thyroid carcinoma. In May 2020, the Food and Drug Administration approved a highly selective kinase inhibitor, selpercatinib, for the treatment of iodine-refractory RET-positive advanced thyroid cancer (39,42).

A promising use of kinase inhibitors in iodine-refractory differentiated thyroid cancer is the resensitization to RAI. *BRAF V600E* mutations coincide with reduced sodium iodine symporter expression, thereby inhibiting RAI uptake (39). In a study conducted by Rothenberg et al., 10 patients with iodine-refractory thyroid cancer received a *BRAF* inhibitor for 25 d. Six of the 10 patients demonstrated uptake of RAI

and could be retreated with RAI (39,43). RAI resensitization has also been documented in a phase II trial with an MEK inhibitor, selumetinib, in patients expressing *BRAF* or *RAS* mutation (39). Figure 2 illustrates the key molecular signaling pathways involved in thyroid cancer initiation and progression. MEK is a downstream protein in the RAS/RAF/MEK MAPK signaling cascade. Selumetinib inhibits overstimulation of this pathway. Of the 20 patients in the trial (9 with *BRAF* mutation and 5 with *NRAS* mutation), 12 demonstrated RAI uptake in response to selumetinib use. Eight of the 12 patients could be treated with RAI. Of the 8 patients who received another RAI treatment, 5 had *NRAS* mutations and one had a *BRAF* mutation (39).

Treatment for Undifferentiated Thyroid Carcinoma

Anaplastic thyroid cancer is a diagnostic and therapeutic challenge because it is very rare, advances quickly, and is not iodine-avid, which prevents the use of RAI for evaluation and treatment. In these cases, ^{18}F -FDG PET is useful for evaluation and follow-up after treatments. Initial treatment includes surgical resection and airway management (often a tracheostomy) followed by external-beam radiation therapy with or without use of doxorubicin, taxanes, or cisplatin (6,39,44). Patients who have unresectable cancer but without distant metastasis are generally treated with palliative chemoradiation (6). Genetic marker analysis has led to the development of therapeutic agents that target specific molecular pathways associated with ATC. For example, clinical trials with *BRAF* inhibitors (e.g., dabrafenib), MEK inhibitors (e.g., trametinib and lenvatinib), mTOR inhibitors, or PPAR γ inhibitors may be appropriate for patients with ATC (39,44). MEK is a key protein in the MAPK signaling cascade, whereas mTOR is a key protein in the PI3K-AKT pathway. PPAR γ acts as a tumor suppressor gene, upregulating important enzymes that control the cell cycle (6,44).

CONCLUSION

Thorough evaluation of decades' worth of data on thyroid carcinoma incidence, treatment, and outcomes have called into question the most appropriate management of patients with follicular epithelial cell-derived thyroid carcinoma. The 2015 ATA guidelines called for a more conservative approach for low-risk malignancies but take into account physician and patient preferences. However, given the lack of consensus on the recommendations for a reduction in the extent of surgery and RAI therapy, the preferences of the disease management team may vary among institutions. The controversy regarding the 2015 ATA guidelines for diagnostic and therapeutic use of RAI prompted a collegial discussion among members of the greater nuclear medicine community and resulted in an authoritative paper, "The Martinique Principles." These principles helped to define common terminology for the goals of RAI therapy (ablation, adjuvant treatment, or treatment of known residual or recurrent disease), reiterated the importance of evaluating multiple factors when determining the appropriateness of RAI therapy, and

acknowledged the limitations of current scientific literature. Most importantly, the Martinique Working Group established a platform for evaluating current practices, exchanging ideas, and critiquing the literature that will help guide future research and optimize thyroid cancer diagnosis and management.

Genetic and molecular evaluation of thyroid carcinoma has identified 2 key signaling pathways primarily involved in carcinogenesis and oncogenesis. The MAPK pathway is implicated in loss of differentiation, cell growth, cell proliferation, and angiogenesis, whereas the PI3K-AKT pathway promotes tumor progression. Many genetic alterations coexist, and as these mutations accumulate, the MAPK and PI3K-AKT pathways are activated. The use of molecular analysis to classify malignancies and predict tumor progression will evolve as more molecular markers are developed. This advancement will likely lead to new prognostic tools and potential therapeutic agents for improved patient management and treatment strategies.

DISCLOSURE

No potential conflict of interest relevant to this article was reported.

REFERENCES

1. Cancer stat facts: thyroid cancer. Surveillance Epidemiology, and End Results website. <https://seer.cancer.gov/statfacts/html/thyro.html>. Accessed June 30, 2021.
2. Thyroid cancer risk factors. American Cancer Society website. <https://www.cancer.org/cancer/thyroid-cancer/causes-risks-prevention/risk-factors.html>. Accessed June 30, 2021.
3. Verburg FA, Van Santen HM, Luster M. Pediatric papillary thyroid cancer: current management challenges. *Onco Targets Ther*. 2016;10:165–175.
4. Salehiniya A, Pakzad R, Hassanipour S, Mohammadian M. The incidence and mortality of thyroid cancer and its relationship with HDI in the world. *World Cancer Res J*. 2018;5:e1091.
5. Lubitz CC, Sosa JA. The changing landscape of papillary thyroid cancer: epidemiology, management, and the implications for patients. *Cancer*. 2016;122:3754–3759.
6. Cabanillas ME, McFadden DG, Durante C. Thyroid cancer. *Lancet*. 2016;388:2783–2795.
7. Nabhan F, Ringel MD. Thyroid nodules and cancer management guidelines: comparisons and controversies. *Endocr Relat Cancer*. 2017;24:R13–R26.
8. What is thyroid cancer? American Cancer Society website. <https://www.cancer.org/cancer/thyroid-cancer/about/what-is-thyroid-cancer.html>. Accessed June 30, 2021.
9. Younis E. Oncogenesis of thyroid cancer. *Asian Pac J Cancer Prev*. 2017;18:1191–1199.
10. Cherkaoui GS, Guensi A, Taleb S, et al. Poorly differentiated thyroid carcinoma: a retrospective clinicopathological study. *Pan Afr Med J*. 2015;21:137.
11. Landa I, Ibrahimovic T, Boucai L, et al. Genomic and transcriptomic hallmarks of poorly differentiated and anaplastic thyroid cancers. *J Clin Invest*. 2016;126:1052–1066.
12. Lam AK. Pathology of endocrine tumors update: World Health Organization new classification 2017—other thyroid tumors. *AJSP: Reviews & Reports*. 2017;22:209–221.
13. Kakudo K, Bychkov A, Bai Y, et al. The new 4th edition World Health Organization classification for thyroid tumors, Asian perspectives. *Pathol Int*. 2018;68:641–664.
14. Soares P, Lima J, Preto A, et al. Genetic alterations in poorly differentiated and undifferentiated thyroid carcinomas. *Curr Genomics*. 2011;12:609–617.
15. Penna GC, Vaisman F, Vaisman M, Sobrinho-Simões M, Soares P. Molecular markers involved in tumorigenesis of thyroid carcinoma: focus on aggressive histotypes. *Cytogenet Genome Res*. 2016;150:194–207.
16. Prante O, Maschauer S, Fremont V, et al. Regulation of uptake of ^{18}F -FDG by a follicular human thyroid cancer cell line with mutation-activated K-Ras. *J Nucl Med*. 2009;50:1364–1370.
17. Limaie F, Rehman A, Mazzoni T. Papillary thyroid carcinoma. National Center for Biotechnology Information website. <https://www.ncbi.nlm.nih.gov/books/NBK536943/>. Published January 6, 2021. Accessed June 30, 2021.

18. Schmidbauer B, Menhart K, Hellwig D, Grosse J. Differentiated thyroid cancer: treatment—state of the art. *Int J Mol Sci*. 2017;18:292.
19. Cipriani NA, Nagar S, Kaplan SP, et al. Follicular thyroid carcinoma: how have histologic diagnoses changed in the last half-century and what are the prognostic implications? *Thyroid*. 2015;25:1209–1216.
20. Gimm O, Dralle H. Differentiated thyroid carcinoma. In: *Surgical Treatment: Evidence-Based and Problem-Oriented*. Zuckschwerdt; 2001:1–15.
21. Stenson G, Nilsson IL, Mu N, et al. Minimally invasive follicular thyroid carcinomas: prognostic factors. *Endocrine*. 2016;53:505–511.
22. Besic N, Schwarzbartl-Peve A, Videgar-Kralj B, Crnic T, Gazic B, Marolt Music M. Treatment and outcome of 32 patients with distant metastases of Hürthle cell thyroid carcinoma: a single-institution experience. *BMC Cancer*. 2016;16:162.
23. Ahmadi S, Stang M, Jiang XS, Sosa JA. Hürthle cell carcinoma: current perspectives. *Onco Targets Ther*. 2016;9:6873–6884.
24. De Melo AS, De Oliveira Rodrigues MF, Marchiori E. Metastatic Hürthle cell cancer. *QJM*. 2019;112:453–454.
25. Cannon J. The significance of Hürthle cells in thyroid disease. *Oncologist*. 2011;16:1380–1387.
26. Perri F, Di Lorenzo G, Della Vittoria Scarpati G, Buonerba C. Anaplastic thyroid carcinoma: a comprehensive review of current and future therapeutic options. *World J Clin Oncol*. 2011;2:150–157.
27. Romei C, Elisei R. RET/PTC translocations and clinico-pathological features in human papillary thyroid carcinoma. *Front Endocrinol (Lausanne)*. 2012;3:54.
28. Xing M. Clinical utility of RAS mutations in thyroid cancer: a blurred picture now emerging clearer. *BMC Med*. 2016;14:12.
29. Donati B, Ciarrocchi A. Telomerase and telomeres biology in thyroid cancer. *Int J Mol Sci*. 2019;20:2887.
30. Zatelli MC, Trasforini G, Leoni S, et al. BRAF V600E mutation analysis increases diagnostic accuracy for papillary thyroid carcinoma in fine-needle aspiration biopsies. *Eur J Endocrinol*. 2009;161:467–473.
31. Yu XM, Lo CY, Chan WF, Lam KY, Leung P, Luk JM. Increased expression of vascular endothelial growth factor C in papillary thyroid carcinoma correlates with cervical lymph node metastases. *Clin Cancer Res*. 2005;11:8063–8069.
32. Wang Y, Ji M, Wang W, et al. Association of the T1799A BRAF mutation with tumor extrathyroidal invasion, higher peripheral platelet counts, and over-expression of platelet-derived growth factor-B in papillary thyroid cancer. *Endocr Relat Cancer*. 2008;15:183–190.
33. Tuttle RM. Controversial issues in thyroid cancer management. *J Nucl Med*. 2018;59:1187–1194.
34. Haugen BR, Alexander EK, Bible KC, et al. 2015 American Thyroid Association management guidelines for adult patients with thyroid nodules and differentiated thyroid cancer: The American Thyroid Association Guidelines Task Force on thyroid nodules and differentiated thyroid cancer. *Thyroid*. 2016;26:1–133.
35. Tuttle RM, Ahuja A, Avram AM, et al. Controversies, consensus, and collaboration in the use of ^{131}I therapy in differentiated thyroid cancer: a joint statement from the American Thyroid Association, the European Association of Nuclear Medicine, the Society of Nuclear Medicine and Molecular Imaging, and the European Thyroid Association. *Thyroid*. 2019;29:461–470.
36. Lee YM, Jeon MJ, Kim WW, et al. Optimal thyrotropin suppression therapy in low-risk thyroid cancer patients after lobectomy. *J Clin Med*. 2019;8:1279.
37. Pirahanchi Y, Toro F, Jialal I. Physiology, thyroid stimulating hormone. National Center for Biotechnology Information website. <https://www.ncbi.nlm.nih.gov/books/NBK499850/>. Updated May 9, 2021. Accessed June 30, 2021.
38. Sodium iodide I 131 solution therapeutic for oral use. U.S. Food and Drug Administration website. https://www.accessdata.fda.gov/drugsatfda_docs/label/2012/016515s0101bl.pdf. Updated January 2012. Accessed June 30, 2021.
39. Faugeras L, Pirson AS, Donckier J, et al. Refractory thyroid carcinoma: which systemic treatment to use? *Ther Adv Med Oncol*. 2018;10:1758834017752853.
40. Nexavar (sorafenib) tablets, oral. U.S. Food and Drug Administration website. https://www.accessdata.fda.gov/drugsatfda_docs/label/2010/021923s008s0091bl.pdf. Updated October 2010. Accessed June 30, 2021.
41. Lenvima (lenvatinib) capsules, for oral use. U.S. Food and Drug Administration website. <http://www.lenvima.com/pdfs/prescribing-information.pdf>. Updated December 2020. Accessed June 30, 2021.
42. Retevmo (selpercatinib). Eli Lilly and Company website. <https://uspl.lilly.com/retevmo/retevmo.html#section-1.3>. Updated January 2021. Accessed June 30, 2021.
43. Rothenberg SM, Daniels GH, Wirth LJ. Redifferentiation of iodine-refractory BRAF V600E-mutant metastatic papillary thyroid cancer with dabrafenib-response. *Clin Cancer Res*. 2015;21:5640–5641.
44. Sun XS, Sun SR, Guevara N, et al. Chemoradiation in anaplastic thyroid carcinomas. *Crit Rev Oncol Hematol*. 2013;86:290–301.

Brain Imaging Techniques: Improving the Quality

Rani M. Noble, CNMT, RT(N)

Nuclear Medicine Department, HonorHealth, Phoenix, Arizona

CE credit: For CE credit, you can access the test for this article, as well as additional *JNMT* CE tests, online at <https://www.snmilearningcenter.org>. Complete the test online no later than September 2024. Your online test will be scored immediately. You may make 3 attempts to pass the test and must answer 80% of the questions correctly to receive 1.0 CEH (Continuing Education Hour) credit. SNMMI members will have their CEH credit added to their VOICE transcript automatically; nonmembers will be able to print out a CE certificate upon successfully completing the test. The online test is free to SNMMI members; nonmembers must pay \$15.00 by credit card when logging onto the website to take the test.

Image quality is a factor of the utmost importance in nuclear medicine. Regardless of what type of scan is being done, technologists should be diligent in how images are being acquired. With respect to brain imaging, there can be challenges that the technologist must understand how to navigate and overcome. This continuing education article, focusing mainly on brain SPECT (particularly with ^{123}I -ioflupane) and brain ^{18}F -FDG PET/CT, will help technologists better understand how artifacts occur and how imaging techniques can affect image quality.

Key Words: quality; brain; techniques; artifacts

J Nucl Med Technol 2021; 49:209–214

DOI: 10.2967/jnmt.120.257592

There are many variables that can affect the quality of imaging. These range from technical or mechanical problems to patient and technologist issues. It is imperative that technologists obtain sufficient training to be competent in quality-imaging techniques regardless of the type of nuclear medicine scan being done. Errors in following the imaging protocol, a lack of understanding of the isotope being used, and not performing instrumentation quality control (QC) tests can affect image quality and, in turn, cause image misinterpretation and an incorrect outcome for patients.

To help technologists gain up-to-date information on the best practices for brain imaging, this article covers the proper techniques to achieve high-quality results for various types of SPECT and PET/CT brain scans. It also reviews important aspects of the various isotopes that are used.

DEFINITION OF A QUALITY IMAGE

A high-quality image produces the best possible resolution and contrast to allow for an accurate diagnosis (1). Several factors go into ensuring that a high-quality nuclear medicine image is produced. These differ according to the

imaging device being used, the patient being imaged, the isotope being used, and the technologist's capability (1). Issues that can impact the integrity of the image include suboptimal camera QC, poor spatial resolution, nonuniformity, incorrect energy resolution, inadequate patient preparation, poor technologist education or understanding of protocols, instrument artifacts, patient artifacts, inadequate patient dose, incorrect camera parameters, and mistakes in image interpretation (1). The technologist must not neglect considering all such variables. If they can be avoided, every image will be of high quality. It is especially important that protocols be standardized throughout institutions and that technologists be capable of overcoming imaging challenges when they arise.

PATIENT PREPARATION

The first step to ensuring proper imaging technique is to prepare the patient. Depending on the protocol for the particular type of scan, the patient may need to stop taking certain medications and fast for a specific time.

For ^{123}I -ioflupane (DaTscan; GE Healthcare) SPECT, patients will need to stop taking any medication that might bind to the dopamine transporter (2), as such binding may impact the ability of ^{123}I -ioflupane to fully bind to the dopamine transporter. Patients will also need to be prepped with an iodine solution, 400 mg of potassium perchlorate, a single dose of potassium iodide, or a single dose of Lugol solution. Single doses are equal to 100 mg of iodine and prevent any free ^{123}I from being taken up by the thyroid gland (2).

Brain perfusion SPECT does not require as much patient preparation as some other scans. For 24 h before the scan, patients must avoid substances that can affect brain perfusion, such as alcohol, caffeine, and stimulants; cigarette smoking needs to be stopped the day of the examination (3). The technologist follows the preinjection protocol that allows for the best possible cerebral uptake. This protocol entails placing the patient in a dimly lit, quiet room; obtaining intravenous access; waiting 10–15 min for the patient to relax; making sure the patients does not read or speak for about 5 min before and after the injection; and injecting the radiopharmaceutical while the patient's are eyes open (closed eyes can cause

Received Sep. 26, 2020; revision accepted Mar. 18, 2021.
For correspondence or reprints, contact Rani M. Noble (raninoble@yahoo.com).

Published online July 9, 2021.

COPYRIGHT © 2021 by the Society of Nuclear Medicine and Molecular Imaging.

hypometabolism of the occipital lobe and a false-positive finding of dementia with Lewy bodies) (3,4).

Preinjection and postinjection preparation for brain ^{18}F -FDG PET/CT is similar to that for brain perfusion SPECT in that patients need to be in a calm, dimly lit room and intravenous access established about 10 min before injection of the tracer. If the injection is done any sooner, false uptake can occur in the pain center of the brain. To prevent uptake in the hearing area of the brain, the technologist should also not talk with the patient during the injection. After receiving the injection, the patient needs to keep the eyes open but avoid speaking, reading, or any considerable movement during the 30-min uptake period (5). In addition, the patient needs to fast for 4–6 h before the scan, including no alcohol, drugs, or caffeine (drinking water is acceptable), and the blood glucose level needs to be checked. The acceptable level varies by institution; most commonly, if the level is greater than 150–200 mg/dL, the scan will be rescheduled for a later date when a lower level can be achieved (5).

MECHANICAL ARTIFACTS

There are several types of mechanical artifacts that can decrease image quality. It is essential that camera QC testing be performed on a regular schedule to avoid any chance of a decline in image quality. QC testing may differ among camera manufacturers; technologists need to be familiar with the routine testing required for the cameras they use.

One of the main QC procedures is daily uniformity testing. This can be either extrinsic or intrinsic, depending on the recommendation of the manufacturer, and is done mainly to make sure the detector's response to a source is within the defined limits. Uniformity testing can identify multiple different issues that degrade image quality, such as issues with the photomultiplier tubes, spatial linearity, and energy, and can reveal generalized degradation of uniformity in images (6).

Spatial-resolution, linearity, and center-of-rotation testing is also needed. Again, the specific protocol varies among manufacturers. Spatial-resolution and linearity testing help determine long-term, rather than acute, degradation of camera resolution (6) and will indicate whether something was adjusted incorrectly during maintenance. Center-of-rotation testing is important for SPECT imaging. If the center of rotation is not in a straight line across the axial direction and does not have the sine wave shape across the other axis, the center of rotation may have shifted and not be centered accurately, causing blurring and resolution degradation (6). It is important that the center of rotation be tested for each zoom and collimator.

High-count flood imaging, another QC procedure that checks for nonuniformity around the central axis of rotation, should be performed only during acceptance testing or if damage to a collimator is suspected (6). The filtered backprojection that is used during reconstruction of the flood image helps showcase any ring artifacts (6).

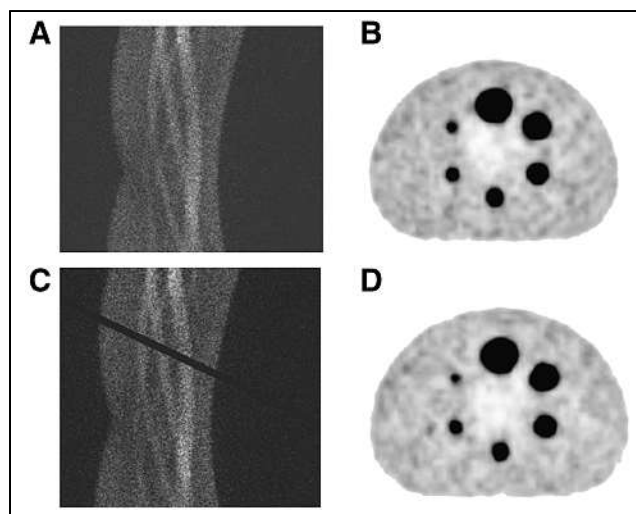


FIGURE 1. Two-dimensional PET sinograms (A and B) and corresponding reconstructed transverse PET images (C and D, respectively) of ^{18}F -filled phantom. Black band in C (suggestive of faulty detector) is virtually undetectable in D (11).

Neglecting to perform scheduled camera maintenance and QC tests can cause a considerable loss of image quality. The manufacturer should be notified if any of the QC results fall outside the reference limits it sets. If a camera with undesirable QC values continues to be used, patient images can show inaccurate findings and degraded quality and resolution, potentially affecting patient care and treatment (Fig. 1).

TECHNOLOGIST-TRIGGERED ARTIFACTS

Technologists need to have adequate training in the nuclear medicine procedures they perform. A lack of understanding about the procedure can lead to technologist-triggered artifacts that can, in turn, result in uninterpretable images. Some such errors include poor image processing, lack of patient education or preparation, neglecting to monitor for patient motion, use of the incorrect dose, and improper operation of the camera (Fig. 2).

Avoiding these errors is especially important in brain imaging. A mistake such as not positioning the detectors at the correct distance from the patient can impact image quality. For example, the radius of the detectors relative to the patient for a ^{123}I -ioflupane scan should be between 11 and 15 cm (2). A larger radius can cause blurring (Fig. 3). The technologist needs to be familiar with how many counts are adequate for the scan being done, as well as the correct scan length. ^{123}I -ioflupane scans require a minimum of 1.5 million counts for the entire scan (2). The scan time for PET/CT depends on the type of camera. Brain SPECT requires 60 or more stops, and the scan length should be limited to 30–45 min (7) to reduce patient discomfort and motion. Insufficient counts or camera stops can produce suboptimal images that may be uninterpretable.

Constant monitoring of the imaging facility by the technologist and management can reveal practices and performance

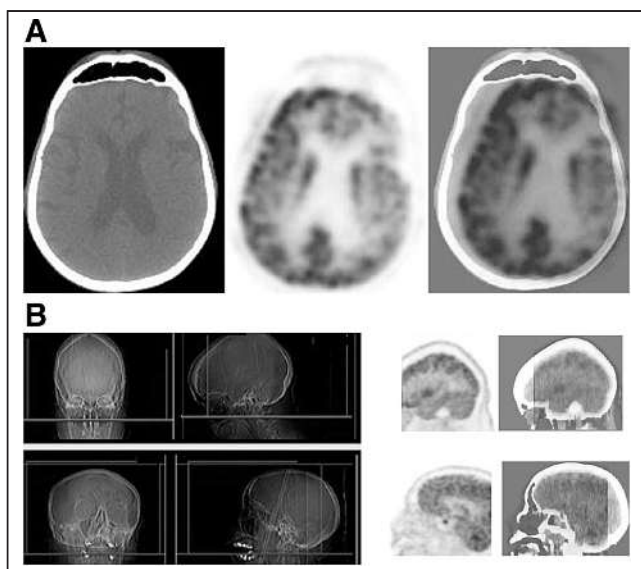


FIGURE 2. (A) Brain ^{18}F -FDG PET/CT images with technologist-caused motion artifact due to misplacing of region-of-interest box on scout images. (B) Transaxial and sagittal lateral radiographs (left), PET images (middle), and PET/CT images (right) of head. Artifact causes false reduction in uptake in left hemicortex and results in part of brain being cut off in final images (12).

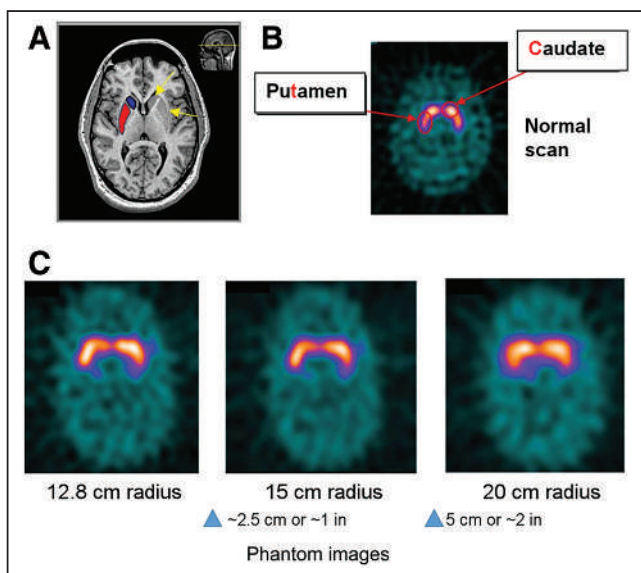


FIGURE 3. (A and B) Brain MRI (A) and PET (B) scans showing location of caudate nucleus and putamen within brain. These are main focus of ^{123}I -ioflupane scans and need to be fully included in images. (C) PET phantom scans showing how important it is to keep detector radius within 11- to 15-cm range. More distance between patient and detector will increase blurring (9). Arrows in A point to left caudate and left putamen; blue indicates right caudate and red indicates location of right putamen. Scans in A and B are of a patient.

that need improvement. One option for improving quality within the imaging facility is to use data analysis to examine performance. A previously published practice guideline laid out a useful 10-step process to help facilities improve the

quality of performance within their lab (8). The 10 steps of quality improvement include identifying a potential problem or area of concern, gathering information and understanding the full extent of the problem, stating the goal and setting goal targets, designing a data collection strategy, collecting data, analyzing those data, sharing the results of the data, implementing the needed changes, recollecting data, and analyzing. Following these 10 steps can identify suboptimal performance and provide an opportunity for improvement. A step-by-step checklist plan such as this one—that helps reduce technologist-triggered artifacts and imaging mistakes—can reduce the number of patients who need to be rescanned.

PATIENT POSITIONING

Patient positioning is one of the more critical steps in a protocol. A head holder should be used for brain imaging. Before getting onto the imaging table, patients should be encouraged to void to prevent interruption of the scan. Patients also need to remove eyeglasses, hats, earrings, and any other items that can interfere with the images. The technologist should help the patient get as comfortable as possible on the table, such as by providing a knee bolster to alleviate pressure on the lower back or a blanket for warmth. A body strap can be used to secure the patient in a comfortable position on the table, and straps across the forehead or chin can also be used to help prevent motion during imaging (9).

The canthomeatal line is a standard positioning line used for most brain scans. It is an imaginary line extending from the lateral canthus to the center of the auditory meatus and should be perpendicular to the imaging table. Basing the patient positioning on this imaginary line will help ensure that the entire brain is included in the imaging field. However, it is more important that the patient be in a comfortable position than for this line to be perpendicular to the imaging table. In such a case, proper orientation of the patient's brain can be achieved during processing, and the interpreting physician should be told that the patient was difficult to position (Fig. 4).

PRECAUTIONS

Technologists need to take into consideration the type of patient and the type of brain scan and remain flexible about

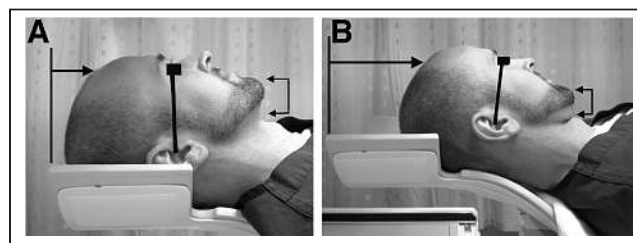


FIGURE 4. (A) Correct positioning of head during brain imaging. Canthomeatal line should be positioned as perpendicularly to imaging table as possible to eliminate head tilt and resulting artifacts. (B) Incorrect head positioning. Patient's head is tilted and not placed fully in head holder (13).

applying extra care and precautions if needed. For example, because patients might move during ^{123}I -ioflupane imaging, securing and immobilizing the head are extremely important. Extra time should be taken to ensure proper head placement, and chin and head straps should be used to ensure that the patient remains still during the entire scan. Another example is a brain ^{18}F -FDG PET/CT scan being performed on a patient who might be cognitively impaired and not able to remember instructions about remaining still on the imaging table. These instructions may need to be repeated several times during the scan.

Another important precaution technologists can take is to monitor and give special attention to patients with neurologic defects (10), who might find it difficult to complete a brain scan. Monitoring will ensure that the patient is comfortable and still throughout the entire scan. Straps across the forehead and chin may help keep the patient's head correctly positioned and motion-free during the scan. Monitoring is especially important for patients with epilepsy and can include continuous recording if the patient is being scanned as part of a preoperative evaluation.

It is not uncommon for patients to need a mind-altering drug, such as a sedative, to help them tolerate a scan. If sedation is needed for a brain PET/CT scan, it should be given as late as possible after the uptake period (5). If needed for a

^{123}I -ioflupane scan (and depending on the sedation), it should be given anywhere from 30 min to immediately before imaging to provide ample time for the sedation to take effect (2). If needed for a brain SPECT scan, it should be given 5 min after injection of the radiopharmaceutical (10). Sedation can be helpful for patients who are claustrophobic, have difficulty lying still, have dementia, or are uncooperative.

IMAGE INTERPRETATION

Image quality should be checked before image interpretation. Cine or sinogram images should be checked for motion and head alignment. Target-to-background ratio and other artifacts such as contamination, attenuation, patient motion, and undesired radiopharmaceutical uptake should be assessed. If there are difficulties with patient motion, images can be acquired in list mode and then reconstructed into a shorter-interval acquisition in the case of movement at the last minute. Precaution needs to be taken when levels of contrast are selected, as some color scales can be misleading during interpretation of results (5). Another consideration for interpretation criteria is the extent of normal variability between patients. Radiologists should familiarize themselves with a reference database (2). The general distribution of the radiotracer and symmetry between hemispheres should be observed.

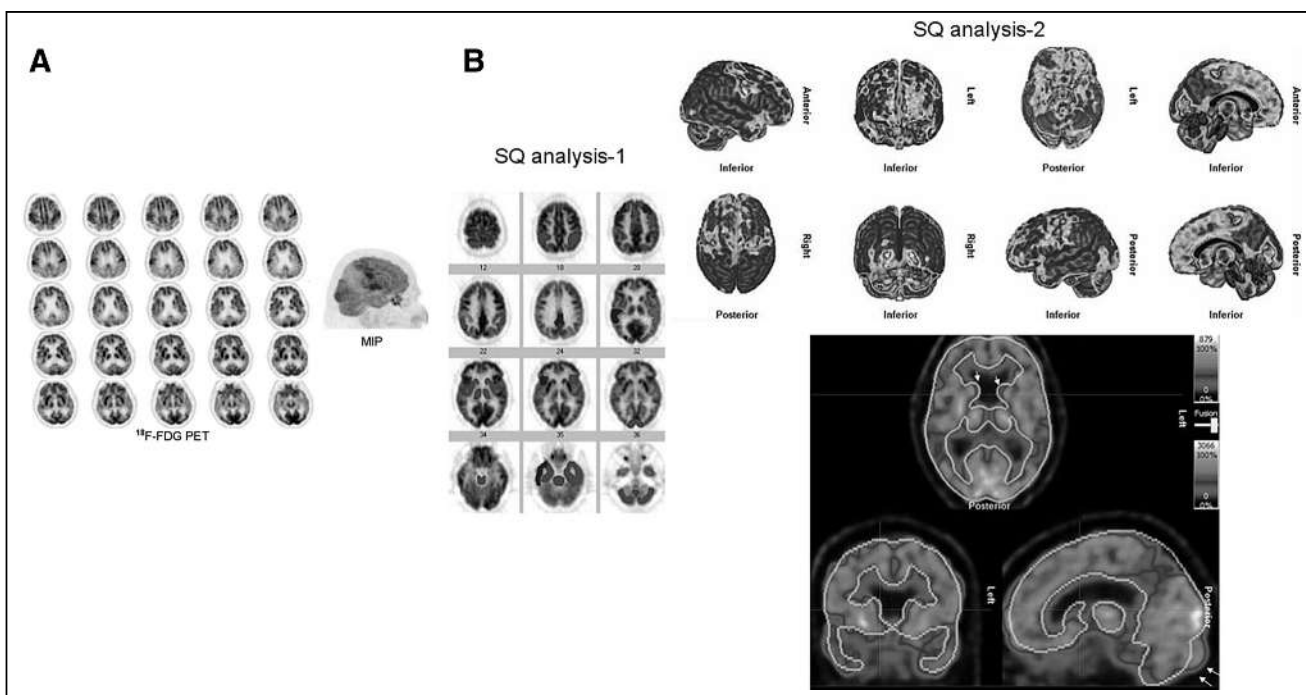


FIGURE 5. ^{18}F -FDG PET brain images showing bilateral hypometabolism in temporal, parietal, and frontal lobes, and maximum-intensity projection (MIP) showing cerebral cortical hypometabolism localization. (B) Semiquantitative (SQ) analysis showing reduction in metabolism in patient's frontal and temporal lobes and in posterior cingulate cortices and temporoparietal junctions. Semiquantitative analysis, however, does not show hypometabolism in patient's parietal lobes and undervalues reduction of metabolism in left temporal lobe (12). In B, SQ1 uses NeuroQ software; it presents reduced metabolism in bilateral frontal lobes, posterior cingulate cortices, temporoparietal junctions, bilateral temporal lobes with right being greater than left, and mildly in left basal ganglia. SQ2 uses Hermes BRASS software. This software furnishes greater matching results to visual analysis in cerebral cortex. This does not apply to basal ganglia, however. This program exhibits inferior registration of various parts of brain, which includes caudate heads.

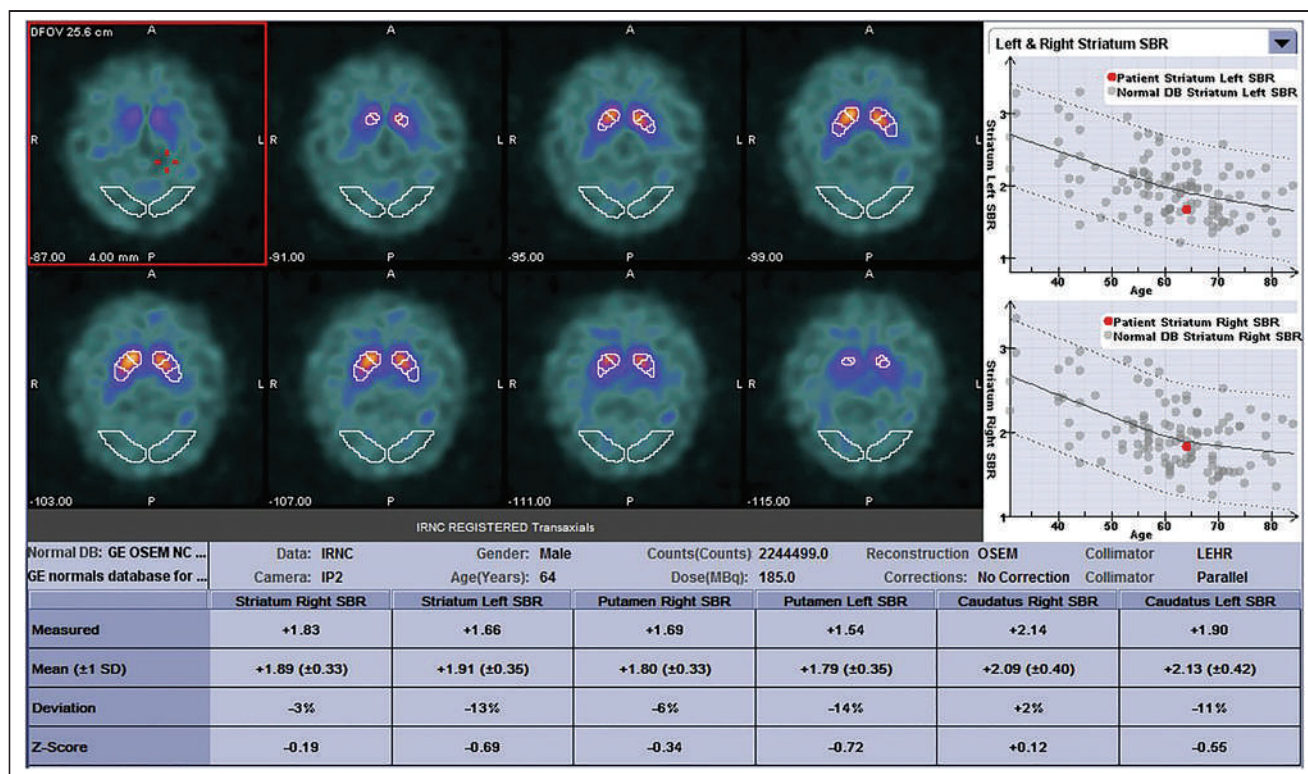


FIGURE 6. Screenshot showing results of DaTQUANT, semiquantitative analysis software used for ^{123}I -ioflupane scans. Scans show how results would be displayed with ROIs placed (14). A = anterior; DB = database; IP2 = type of operating system in Siemens cameras, computer software; IRNC = iterative reconstruction without attenuation correction; LEHR = low-energy high-resolution; NC = normal control; OFOV = operational field of view; OSEM = ordered-subsets expectation maximization; P = posterior; SBR = striatal binding ratio.

Qualitative or semiquantitative analysis can be done for brain image interpretation. Brain PET/CT scans will differ from routine oncologic PET/CT scans because an SUV is not used; however, quantitative analysis can still be done. Absolute glucose metabolism can be measured to calculate the arterial ^{18}F -FDG concentration–against–time curve. This calculation would require serial sampling of arterial blood (Fig. 5) (5).

Semiquantitative analysis can complement visual interpretation for ^{123}I -ioflupane scans. To be interpretable, the semiquantitative data need to be compared with a reference database (2). However, the reference database will need further clarification regarding what makes it “normal.” Not using an automated system for regions of interest can cause interobserver variability, resulting in region-of-interest placement errors and false interpretations (2). Automated ROI placement systems help reduce that variability. Several different studies have shown accurate diagnoses from interpretations based on only semiquantitative information. However, these results were only for experienced readers (2). There is no information on whether inexperienced readers would have the same outcome, but semiquantitative information may benefit those readers with less experience (Fig. 6) (2).

CONCLUSION

Quality imaging starts at the technologist level. Understanding brain imaging and how to accomplish high-quality

images is very achievable. Brain imaging is a critical part of the nuclear medicine field, and high-quality images can help in the diagnosis of crucial conditions. Every step of the protocol should be followed, from patient preparation, education, and positioning to camera operation and image interpretation. Images that are submitted for interpretation should be of the best quality obtainable. Achieving this level of quality may mean having to overcome challenges that arise during the imaging process. If care is taken to understand a protocol completely, these challenges can be overcome and high-quality images obtained.

ACKNOWLEDGMENT

I thank Mary Beth Farrell for editorial assistance, mentorship, and continued support.

REFERENCES

1. Image quality and quality control in diagnostic nuclear medicine. International Atomic Energy Agency website. <https://www.iaea.org/resources/rpop/health-professionals/nuclear-medicine/diagnostic-nuclear-medicine/image-quality-and-quality-control>. Accessed June 28, 1958.
2. Djang DSW, Janssen MJR, Bohnen N, et al. SNM practice guideline for dopamine transporter imaging with ^{123}I -ioflupane SPECT 1.0. *J Nucl Med*. 2012;53:154–163.
3. Kapucu OL, Nobili F, Varrone A, et al. EANM procedure guideline for brain perfusion SPECT using $^{99\text{m}}\text{Tc}$ -labelled radiopharmaceuticals, version 2. *Eur J Nucl Med Mol Imaging*. 2009;36:2093–2102.
4. Brown RK, Bohnen N, Wong K, et al. Brain PET in suspected dementia: patterns of altered FDG metabolism. *Radiographics*. 2014;34:684–701.

5. Waxman AD, Herholz K, Lewis D. Society of nuclear medicine procedure guideline for FDG PET brain imaging. Society of Nuclear Medicine and Molecular Imaging website. <http://s3.amazonaws.com/rdcms-snmml/files/production/public/docs/Society%20of%20Nuclear%20Medicine%20Procedure%20Guideline%20for%20FDG%20PET%20Brain%20Imaging.pdf>. Published February 8, 2009. Accessed June 28, 2021.
6. Murphy PH. Acceptance testing and quality control of gamma cameras, including SPECT. *J Nucl Med.* 1987;28:1221–1227.
7. Parker JA, Graham LS, Royal HD, et al. The SNM procedure guideline for general imaging 6.0. Society of Nuclear Medicine and Molecular Imaging website. http://s3.amazonaws.com/rdcms-snmml/files/production/public/docs/General_Imaging_Version_6.0.pdf. Published January 14, 1996. Revised September 12, 2010. Accessed June 28, 2021.
8. Farrell MB, Abreu SH. A practical guide to quality improvement in nuclear medicine. *J Nucl Med.* 2012;40:211–219.
9. Grabher BJ. Brain imaging quality assurance: how to acquire the best brain images possible. *J Nucl Med Technol.* 2019;47:13–20.
10. Juni JE, Waxman AD, Devous MD Sr, et al.; Society for Nuclear Medicine. Procedure guideline for brain perfusion SPECT using 99mTc radiopharmaceuticals 3.0. *J Nucl Med Technol.* 2009;37:191–195.
11. Zanzonico P. Routine quality control of clinical nuclear medicine instrumentation: a brief review. *J Nucl Med.* 2008;49:1114–1131.
12. Sarikaya I, Sarikaya A, Elgazzar A. Current status of ¹⁸F-FDG PET brain imaging in patients with dementia. *J Nucl Med Technol.* 2018;46:362–367.
13. Covington MF, McMillan NA, Avery RJ, Kuo PH. The semicolon sign: dopamine transporter imaging artifact from head tilt. *J Nucl Med Technol.* 2013;41:105–107.
14. Booi J, Dubroff J, Pryma D, et al. Diagnostic performance of the visual reading of 123I-ioflupane SPECT images with or without quantification in patients with movement disorders or dementia. *J Nucl Med.* 2017;58:1821–1826.

¹⁸F-FDG PET/CT Brain Imaging

Rani M. Noble, CNMT, RT(N)

RATIONALE

¹⁸F-FDG PET/CT imaging assists in evaluating metabolism and brain function. ¹⁸F-FDG brain imaging can help with various clinical indications, including dementia, seizure disorders, and new or recurrent brain tumors. PET imaging performed with ¹⁸F-FDG can exemplify pathologic conditions before morphologic presentation is seen with CT and MRI.

CLINICAL INDICATIONS

- Diagnosis, staging, or detection of recurrent tumor.
- Tumor grading and directing biopsy.
- Evaluation of known dementia, including the diagnosis of Alzheimer disease and Parkinson disease.
- Seizure localization.
- Huntington disease.
- Differentiation of radiation necrosis versus tumor recurrence.

CONTRAINDICATIONS

- Blood glucose levels that are above the range of 150–200 mg/dL.
- Pregnancy or breastfeeding: refer to local institutional policy for pregnancy assessment/exclusion.
- Patients unable to remain still for imaging (30–60 min).

PATIENT PREPARATION/EDUCATION

- The patient should fast 4–6 h before the injection, except for hydration with water.
- Parenteral feeding or fluid given intravenously containing dextrose should be withheld for 4–6 h before the examination.
- The patient should avoid caffeine, alcohol, and other medications that can affect cerebral glucose metabolism for 24 h.
- A focused history should include current or past head trauma, mental status, psychiatric examinations, drug use, stroke, epilepsy, and transient ischemic attacks. Additional information should include: history of diabetes; prior brain surgeries; any current neurologic

medication and when last taken; and results of any previous brain imaging (CT, MRI, PET, or SPECT)

- Study should be scheduled 4–6 wk after radiation therapy where appropriate.

PROTOCOL/ACQUISITION INSTRUCTIONS

- Verify blood glucose level before dose administration. Refer to the institution's policy; however, most commonly, the glucose level should not exceed 150–200 mg/dL.

Preinjection

- Obtain intravenous access.
 - Place patient in a dimly lit, quiet room, seated for 20–30 min before injection of the radiopharmaceutical.
 - Instruct patients to keep eyes open (eyes should be closed only if the scan is being done for comparison and the eyes were closed previously); and to relax, not speak, and avoid any major movements.

Postinjection

- The patient should continue to relax in a quiet room for 30–60 min (per institutional guidelines).
 - A restless uptake period should be noted for the interpreting physician.
 - Before imaging, the patient should void the bladder for greater comfort.

IMAGING

- Remove any metal before positioning the patient supine on the imaging table.
- With the head in a head holder, use the canthomeatal line to position the head vertical with the imaging table.
 - As patient comfort is of greater importance, if the patient cannot tilt the head to achieve the required angle, proper orientation can be performed during image processing.
- Use straps across the forehead and chin to help minimize patient motion during imaging.
- Acquire images in either 2-dimensional (2D) or 3-dimensional (3D) mode.

- If acquiring in 2D mode, scan time will be 20 min per bed position.
- If acquiring in 3D mode, scan time will be 6 min per bed position.
- Refer to manufacturer's recommendations for 2D or 3D acquisition protocol.

IMAGE PROCESSING

- Pixel size: 2–4 mm; images reconstructed into transaxial slices. Images displayed in transaxial, coronal, and sagittal projections.
- Hanning or Shepp-Logan filters are frequently used with filtered backprojection.
- Iterative reconstruction should follow manufacturer's recommendations for iterations, subsets, and smoothness.

PRECAUTIONS

- Proper instructions for breastfeeding should be provided. Have patient withhold breastfeeding for 24 h.
- Supervision of patients should be constant; interaction should be kept to a minimum.

- If sedation is required, it should be done after the uptake period, as close to the imaging time as possible. Appropriate patient transportation should be arranged in the case of sedation.

CONSIDERATIONS

- For PET/CT, follow the manufacturer's recommendations for CT acquisition parameters.
- When imaging for epilepsy, electroencephalography monitoring may be indicated, and monitoring should start 2 h before injection to confirm the patient is not in a postictal state. Monitoring should continue for 20 min after ^{18}F -FDG injection.

REFERENCES

1. Farrell MB, Mantel ES, Basso DA, et al. PET: Brain imaging with ^{18}F -FDG. In: *Quick Reference Protocol Manual for Nuclear Medicine Technologists*. Society of Nuclear Medicine and Molecular Imaging; 2014:136–138.
2. Mettler F, Guiberteau M. *Essentials of Nuclear Medicine Imaging*. 6th ed. Elsevier; 2012.
3. Waxman A, Herholz K, Lewis D, et al. *Society of Nuclear Medicine Procedure Guideline for FDG PET Brain Imaging*. Society of Nuclear Medicine and Molecular Imaging; 2009.

PET/MRI, Part 2: Technologic Principles

Geoffrey M. Currie^{1,2}, Peter Kamvosoulis³, and Stewart Bushong²

¹*School of Dentistry and Health Science, Charles Sturt University, Wagga Wagga, Australia;* ²*Department of Radiology, Baylor College of Medicine, Houston, Texas;* and ³*Magnetic Resonance Department, New York–Presbyterian/Weill Cornell Medical Center, New York, New York*

CE credit: For CE credit, you can access the test for this article, as well as additional JNMT CE tests, online at <https://www.snmilearningcenter.org>. Complete the test online no later than September 2024. Your online test will be scored immediately. You may make 3 attempts to pass the test and must answer 80% of the questions correctly to receive 1.0 CEH (Continuing Education Hour) credit. SNMMI members will have their CEH credit added to their VOICE transcript automatically; nonmembers will be able to print out a CE certificate upon successfully completing the test. The online test is free to SNMMI members; nonmembers must pay \$15.00 by credit card when logging onto the website to take the test.

The challenges of hybridizing PET and MRI as a simultaneous modality have been largely overcome in recent times. PET hybridized with MRI has seen the emergence of PET/MRI systems in the clinical setting, and with it comes a responsibility to adapt appropriate facility design, safety practices, protocols and procedures, and clinical opportunity. This article provides an insight into the considerations and challenges associated with PET/MR technology. Given that the nature of PET is well established among the readership of this journal, the article provides an introduction to the foundations of MRI instrumentation and emphasis on specific technologic aspects of PET/MR systems. This article is the second in a 4-part integrated series sponsored by the PET/MR and Publication Committees of the Society of Nuclear Medicine and Molecular Imaging–Technologist Section, building on the previous article (part 1), which was on establishing a facility. In subsequent parts, PET/MRI will be explored on the basis of protocols and procedures (part 3) and applications and clinical cases (part 4).

Key Words: PET/MR; PET; MRI; PET/MRI

J Nucl Med Technol 2021; 49:217–225

DOI: 10.2967/jnmt.120.261862

Although the merits of SPECT, PET, CT and MRI have been widely recognized and reported in both research and clinical practice, the synergistic hybridization of imaging modalities has revolutionized diagnostic imaging. SPECT/CT and PET/CT are in widespread practice, merging the advantages of the high-resolution anatomic information of the CT with the physiologic and molecule-level functional information from the nuclear medicine modalities. More recently, PET/MRI hybrid systems have emerged, although PET/MR was devised and patented in the 1990s (1). The first integrated PET/MRI systems emerged in 2010, and by 2015 there were about 110 PET/MRI systems globally (~160 in

2020), with Siemens representing nearly 80% of the market, ahead of Philips and GE Healthcare (2). For clarification and consistency, the terms *PET/MR* and *PET/MRI* are not used interchangeably in this article. *PET/MR* is used in reference to the technology and principles, whereas *PET/MRI* refers to the application of that technology in imaging. The use of MRI versus MR throughout should be self-explanatory. Furthermore, the term *imaging system* is used in preference to the more archaic use of the term *scanner*.

A working knowledge of PET is assumed in this discussion but can be refreshed in the previously published work of Turkington (3). The general principles of MRI are outlined below. This is also not a forum for debating the relative merits of PET/MRI against PET/CT. Nonetheless, it would be remiss not to highlight the motivations for PET/MRI (1,4–7). First, PET/MRI produces a reduced patient radiation dose. This is particularly important in pediatric patients, women of childbearing age, and the numerous patients who undergo sequential scanning to monitor response to therapy or recurrence. Compared with PET/CT, PET/MRI can reduce the dose to just 25%, given that 75% of the patient radiation dose is associated with CT. An example would be the reduction in a pediatric whole-body PET/CT scan from 19.5 to 4.6 mSv for PET/MRI. Second, soft-tissue visualization and contrast on MRI are superior to those on CT, enhancing lesion detection and diagnostic accuracy in numerous conditions. MRI adds important complementary functional information to the PET scan, further enhancing outcomes. The opportunity from PET/MRI for multiparametric imaging increases radiomic feature extraction and diagnostic utility. Third, PET/MR offers genuinely simultaneous imaging, which has a positive impact on coregistration, especially in organs that move (e.g., heart and lungs), in lesions that experience physiologic motion (e.g., lung tumors), in organs that change (e.g., filling of the urinary bladder), or in patients who move during scanning (e.g., from pain or anxiety). The simultaneous imaging also allows better synchronization of respiratory and cardiac gating between PET and MRI data, as well as allowing application of motion correction to the PET data. The correction for motion increases lesion detection and quantitative

Received Dec. 19, 2020; revision accepted Feb. 11, 2021.
For correspondence or reprints, contact Geoffrey M. Currie (gcurrie@csu.edu.au).

Published online March 15, 2021.

COPYRIGHT © 2021 by the Society of Nuclear Medicine and Molecular Imaging.

accuracy. Fourth, there is also a reported efficiency when PET and MRI are required, because they are acquired simultaneously. In the absence of PET/MRI, PET/CT is sequential and then requires the additional time of the stand-alone MRI. Finally, image reconstruction offers the chance to correct partial-volume artifacts on the PET images using the MRI coregistration. The net impact of this approach is resolution recovery or enhanced spatial resolution of the PET data.

Despite these advantages, replacing PET/CT with PET/MR is associated with several challenges, such as detector function in a magnetic field, attenuation correction, scatter correction, artifacts, and truncation of the field of view. These challenges are especially true when one is considering truly integrated PET/MR with simultaneous acquisition (1,4,5,7).

FOUNDATIONS OF MRI

For the MRI novice, the basic foundations allow a working knowledge of the principles of MRI. For some, the superficial introduction outlined below will provide sufficient insight. Others will yearn for deeper understanding beyond the scope and word limit of this article. Such insight can be sourced from several key textbooks (8,9). Rather than exploring Newtonian and quantum physics, a simpler model of MRI is offered.

MR Signal

Some nuclei spin on their own axis, which allows them to be thought of as small magnets. Hydrogen is one such nuclei—indeed, the one that produces the strongest magnet. Consider the distribution of hydrogen in the human body. It is clear that hydrogen imaging would be both biologically useful for some tissues and sufficiently abundant in distribution to allow quality imaging. The dispersion of hydrogen in objects is random and fairly uniform, which means the small magnets in opposite alignments cancel one another out to produce a net zero magnetic vector (Fig. 1A). If a magnetic field is applied to the object, then the hydrogen atoms align parallel with the magnetic field and the object has a net magnetic vector; it has become polarized (Fig. 1B) (8–10). In reality, not all

hydrogen atoms (let us refer to them as proton dipoles) become aligned with the magnetic field. Approximately 1 per million of proton dipoles realign with the magnetic field, but this is sufficient to create polarization (8). Although a simple schematic representation such as Figure 1 suggests that the atoms have aligned uniformly, in reality they wobble. The wobble is known as precession (Fig. 1C), and the frequency of the precession is called the Larmor frequency and depends on the strength of the magnetic field (8–10). For hydrogen, a 1.5-T MRI system produces 63.9 MHz of precession whereas 3 T produces 127.8 MHz of precession (8,9). Indeed, this might be better expressed as a gyromagnetic ratio of MHz of precession per T. This is important because each dipole nucleus has a unique gyromagnetic ratio. For hydrogen (^1H) it is 42.6 MHz/T, whereas others include ^{19}F at 40.1 MHz/T, ^{31}P at 17.2 MHz/T, ^{23}Na at 11.3 MHz/T, and ^{13}C at 10.7 MHz/T.

Excitation

Consider the patient in an MRI system. In the presence of the magnetic field, proton dipoles align with the magnetic field to produce a net magnetic vector (Fig. 1B). This is also referred to as the equilibrium magnetization state. The magnetic field causes each dipole to randomly precess (Fig. 2A). If a pulse of radiofrequency is emitted at the Larmor frequency, it will change the energy state of the hydrogen nuclei (excitation) (8–10). This is achieved using the radiofrequency coil, which pulses at resonance and causes the net magnetic vector to flip to negative on the z-axis. Despite this, the precession remains perpendicular to the z-axis, but instead of being random, the precession of each dipole becomes in phase (Fig. 2B) (8–10). This is referred to as phase coherence and generates the optimal MR signal. The net magnetism returns to the equilibrium magnetism state (relaxation) (8–10). This creates a moving magnetic field, and electric current can then be generated in a radiofrequency receiver coil (Fig. 2C) (8–10). The time for the signal to return to equilibrium is called relaxation time, and the signal produced is referred to as free induction decay (FID) (8–10).

Relaxation

Relaxation time is associated with 2 independent processes, T_1 and T_2 , that occur simultaneously (8–10). T_1 relaxation is also known as longitudinal relaxation because it describes the rate at which the magnetism returns to equilibrium. T_2 relaxation is also known as transverse relaxation because it describes the rate at which phase-coherent precession dephases. T_1 is the time required to return to 63% of the equilibrium value after exposure to a 90° radiofrequency pulse (8–10). Conversely, T_2 is the time required to

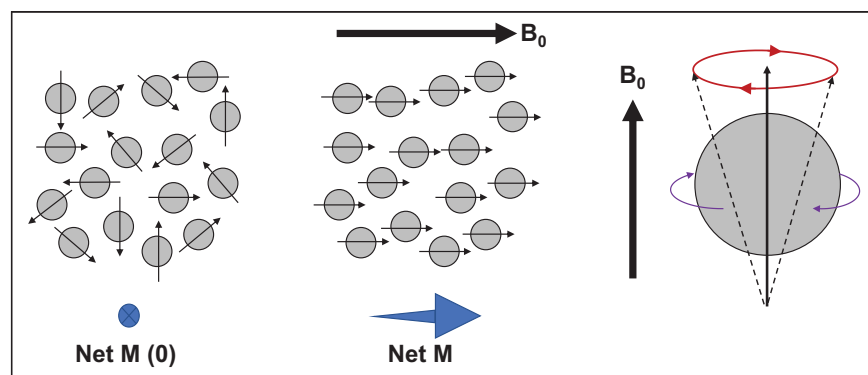


FIGURE 1. Nucleus spin creates polarity with random distribution, producing net magnetic vector (M) of zero (left). Application of strong magnetic field (B_0) creates alignment of proton dipoles, producing net M aligned with B_0 (middle). Although proton dipoles spin on their axis (purple arrows) to produce small magnets, movement in presence of magnetic field is gyromagnetic (red arrows) and termed precession (right).

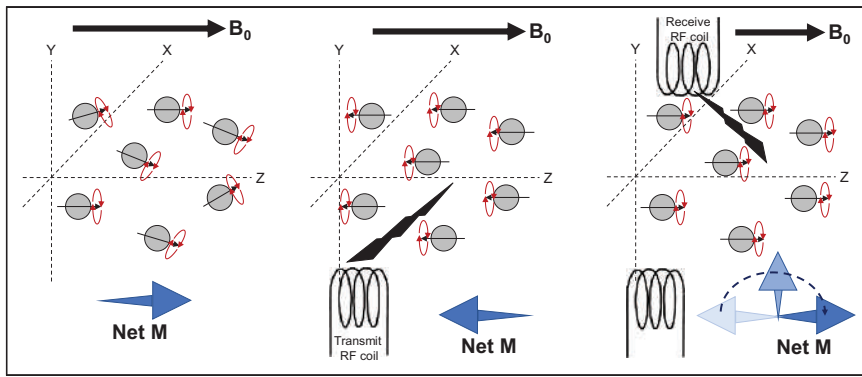


FIGURE 2. Nucleus spin creates polarity with magnetic field (B_0) and positive alignment of proton dipoles with z-axis, producing net magnetic vector (M) and random precession (left). Radiofrequency (RF) transmission causes aligned proton dipoles to flip to negative on z-axis and causes precession to come into phase (middle). Relaxation results in reversion of net M , producing FID signal at RF receiver coil (right).

dephase the signal to 37% of its original value. The role of contrast medium is to alter the relaxation times (Fig. 3) (8–10). Relaxivity measures the degree to which a given amount of contrast agent shortens T_1 or T_2 , which means higher relaxivity produces better enhancement (11).

Image Formation

The FID signal intensity decreases over time as a harmonic oscillation (Fig. 4A) (8). Figure 4A represents signal intensity over time, but this can be converted to the frequency domain via Fourier transformation to produce a nuclear MR spectrum

collected at multiple projections, which can then be reconstructed using tomographic principles previously described (12).

Pulse Sequences

Although this provides a simple explanation of the MRI process, in reality, FID is not a simple imaging option because of the weak signal (8–10). A 1-pulse sequence would need to be repeated several hundreds of times to generate an adequate signal (8,9). The time between each radiofrequency pulse is called the repetition time

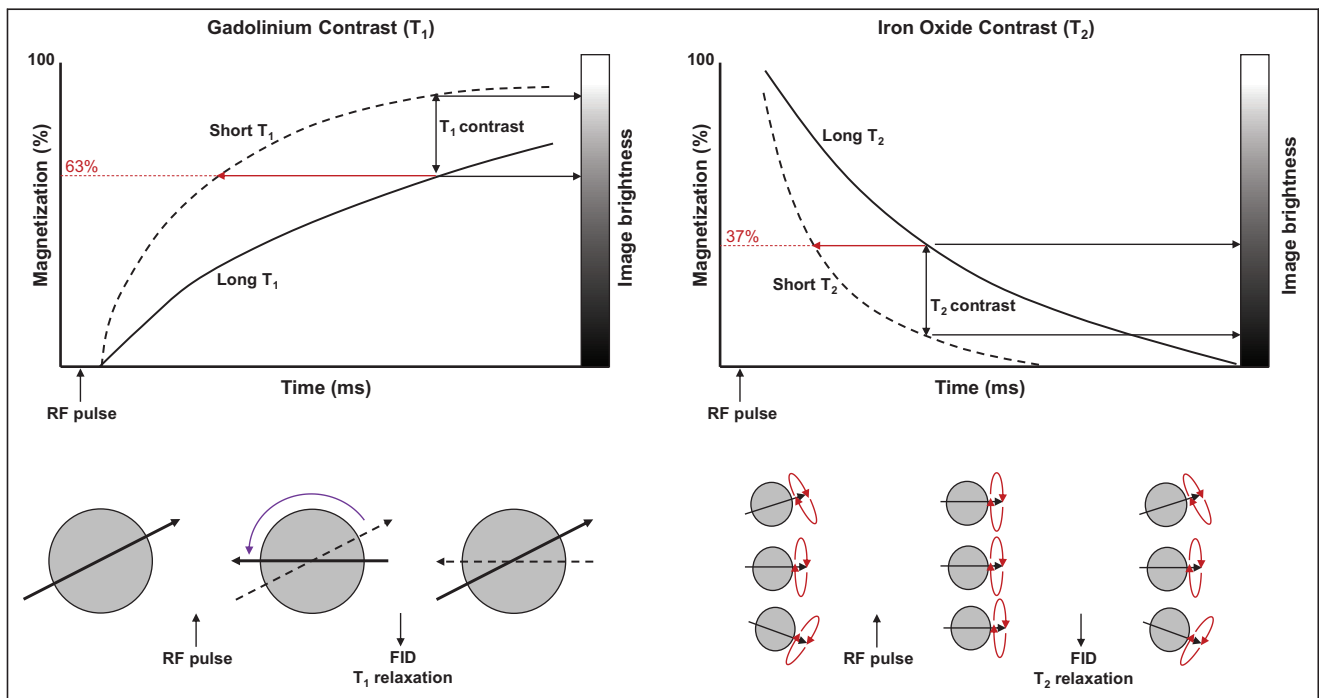


FIGURE 3. Schematic representation of principle of T_1 and T_2 contrast enhancement by altering relaxation times. T_1 plot (top left) shows effect of shortening relaxation time with gadolinium contrast and resultant positive enhancement of contrast. Likewise, T_2 plot (top right) shows effect of shortening relaxation time with iron oxide contrast and resultant negative enhancement of contrast. (Adapted with permission of (11).) RF = radiofrequency.

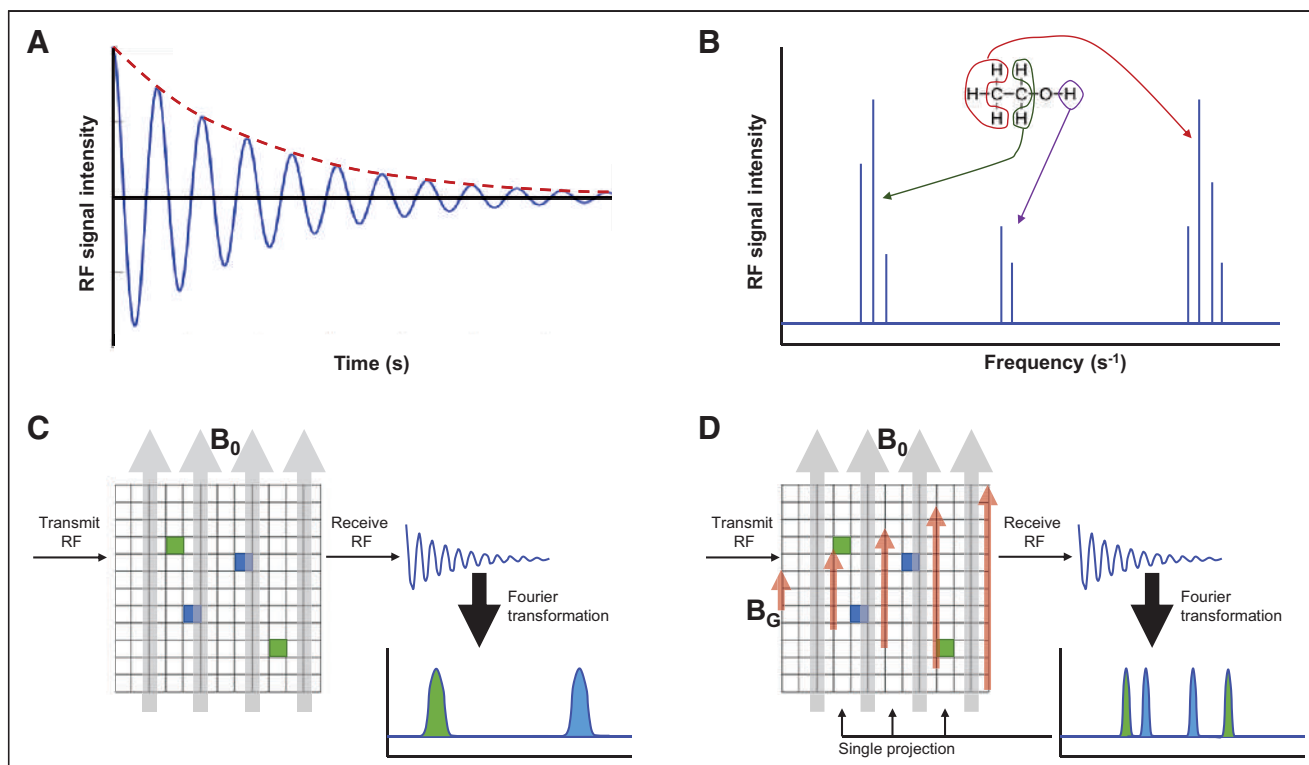


FIGURE 4. (A) FID with decreasing harmonic oscillation. (B) Fourier transformation of FID creates frequency-domain nuclear MR spectrum. For MRI, clusters represent different tissues, as is schematically represented here for nuclear MR spectroscopy, with each cluster representing a different molecular array of hydrogen (as depicted with red, green, and purple hydrogen atoms). (C) In static magnetic field (B_0), nuclear MR spectrum identifies different tissues but not spatial location. (D) Application of gradient magnetic field (B_G), depicted in red, allows spatial identification for that gradient projection. Rotating gradient magnetic field allows multiple projections to be collected and reconstructed. RF = radiofrequency.

(TR), and if sufficient time elapses between each radiofrequency pulse, equilibrium allows the amplitude of successive FIDs to be equal (8,9). A short TR means equilibrium has not been reached and successive FIDs will have smaller amplitudes (partial saturation) (8,9).

Alternatively, multiple pulse sequences can be used. If the 90° radiofrequency pulse is followed by a 180° radiofrequency pulse, an echo signal of the FID can be generated by the rephasing (8,9). The echo signal is termed spin echo and is stronger than the FID signal; it is measured at the peak echo time (8,9). Echo time after the 180° radiofrequency pulse is equal to the time between the 90° radiofrequency pulse and the 180° radiofrequency pulse (8,9). A multiecho spin-echo pulse sequence could be used in which a subsequent 180° radiofrequency pulse follows the previous one, producing another spin echo (8,9). An image can be generated from each of the spin echoes (primary and secondary) at the respective echo time to produce images of differing characteristics. The inversion-recovery pulse sequence starts with a 180° radiofrequency pulse and follows it with a 90° radiofrequency pulse that inverts the net magnetism (8,9). There are a large variety of sequences used in MRI, and the details are beyond the scope of this article; however, those interested are encouraged to do

further research on gradient echo sequences, dual-echo sequences, fluid-attenuated inversion-recovery sequences, diffusion-weighted sequences, short- τ inversion recovery sequences, and Dixon chemical shifts.

PET/MR TECHNOLOGY

System Design

One of the principal barriers to hybrid PET/MRI systems is the incompatibility of the technology. The traditional PET system design using photomultiplier tubes (PMTs) is susceptible to even small magnetic fields and, thus, incompatible with the large magnetic fields associated with MRI (1,4–7). Furthermore, the electronics associated with signal processing in PET can create interference in the MR signal (4–7). This limitation gives rise to several solutions or configurations. The first is to have separate PET and MRI systems linked by a single patient table, with each gantry positioned and shielded sufficiently to not interfere with the other (e.g., Philips Ingenuity TF) (Fig. 5A). Alternatively, the detectors themselves could reside within the MRI system and be coupled by optical fibers to PMTs residing outside the magnetic field (Fig. 5B). This design may adopt a split-magnet design allowing the optical fibers to be shorter and the magnet bore wider. The genuinely integrated option would modify

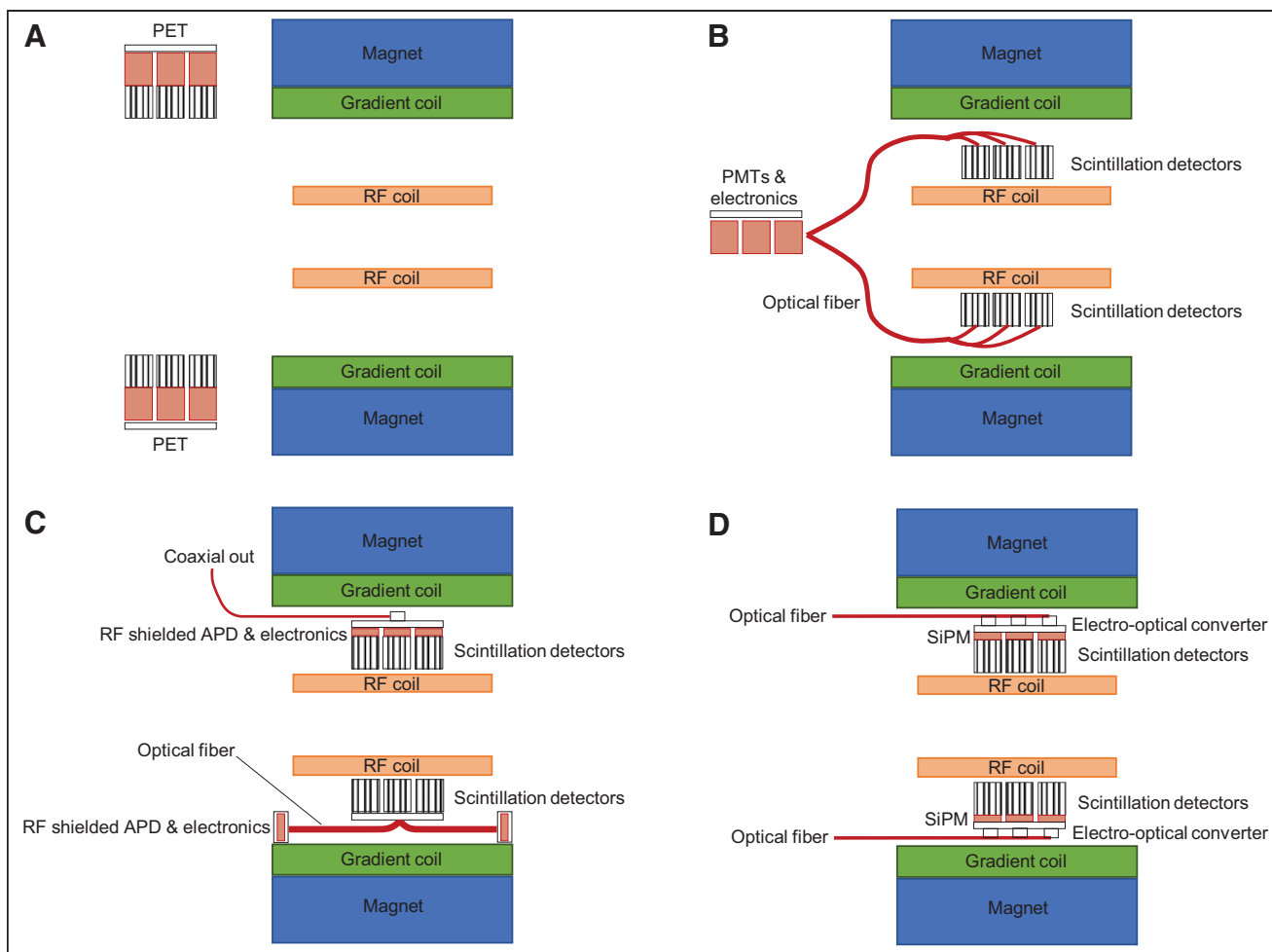


FIGURE 5. (A) Separate but linked PET/MR without option for simultaneous acquisition. (B) Integrated and simultaneous PET/MR housing radiofrequency (RF)-sensitive PMTs and electronics outside gantry. (C) Two versions of integrated PET/MR using RF-shielded APDs and electronics. Top half of schematic represents RF-shielded APD inside gantry, whereas bottom half uses optical fiber to connect to RF-shielded APDs at edge of MR field of view. (D) Integration of RF-compliant SiPM with optical fiber output obviates RF shielding of PET components.

detector composition to eliminate susceptibility from and to the magnetic field (e.g., Siemens Biograph mMR, GE Healthcare Signa PET/MR, and United Imaging uPMR 790 PET/MR). Clearly, the integrated system is required to take advantage of simultaneous PET and MRI. One approach is to couple the scintillation detector directly or by optical fibers to avalanche photodiodes (APDs) in radiofrequency shielding (Fig. 5C). Alternatively, silicon photomultiplier (SiPM) detectors can be coupled to the scintillation detector (Fig. 5D).

Commercial Systems

There are 4 commercially available clinical PET/MRI systems on the market. The Signa PET/MR is an integrated system with a 3-T MR component with PET (time of flight) that uses SiPM detectors directly coupled to lutetium-based crystals. The GE Healthcare MR750w wide-bore (70 cm) MRI system can be retrofitted with an SiPM PET insert to produce a 6-cm-bore PET/MR device. The Biograph mMR PET/MR

is an integrated system with a 3-T MR component with PET that uses APD detectors and lutetium oxyorthosilicate crystals. The uPMR 790 PET/MR is an integrated system with a 3-T MR component with PET that uses SiPM detectors directly coupled to lutetium yttrium oxyorthosilicate (LYSO) crystals. The Ingenuity TF PET/MR is a sequential system with a 3-T MR component colocated and sharing an imaging system bed with a LYSO and PMT-based PET system.

Detectors

The traditional PET PMT was based on the coupling of bismuth germinate oxide scintillation crystal detectors to PMTs. More recently, the detectors have been upgraded to lutetium-based scintillators such as lutetium oxyorthosilicate and LYSO. Lutetium oxyorthosilicate and LYSO have faster scintillation decay, which makes them more effective in high-count-rate conditions, in additional lines of response for 3-dimensional scanning, in longer axial fields of view, and in time of flight (1,4,6,13). Lutetium oxyorthosilicate

and LYSO have typically been coupled to PMTs. PMTs offer signal amplification but are susceptible to magnetic fields and are bulky, both being significant issues for integrating PET into an MRI gantry. APDs are silicon semiconductors that not only are able to operate within the magnetic field but also are compact (1,4,6,7,13). Unfortunately APDs are thermally sensitive, which requires thermal stabilization. Furthermore, the signal gain is very low compared with a traditional PMT, which requires additional electronic signal amplification (1,4,7,13). Both these requirements have been met successfully in traditional sequential PET/CT imaging system design and with some difficulties in PET/MR design. For example, the additional electronics for signal boosting is MR-sensitive, the thermal control creates bulk, and the low signal gain prohibits time of flight.

SiPMs are an alternative to the PMT and APDs, although technically, they are a type of APD (1,7,13). SiPMs are a silicon semiconductor detector operating in Geiger mode and are also referred to in the literature as solid-state photomultipliers and multipixel photon counters (Fig. 6A) (1,7,13). In the SiPM, the detector matrix comprises thousands of pixels that operate as a photon counter in Geiger mode. The pixels are known as single-photon avalanche diodes, and each individual single-photon avalanche diode can be counted independently and simultaneously with other single-photon avalanche diodes (Fig. 6B) (1,13). This approach results in high resolution, high sensitivity, high signal gain, low noise, fast timing, less magnetic susceptibility, and time-of-flight capability (1,13).

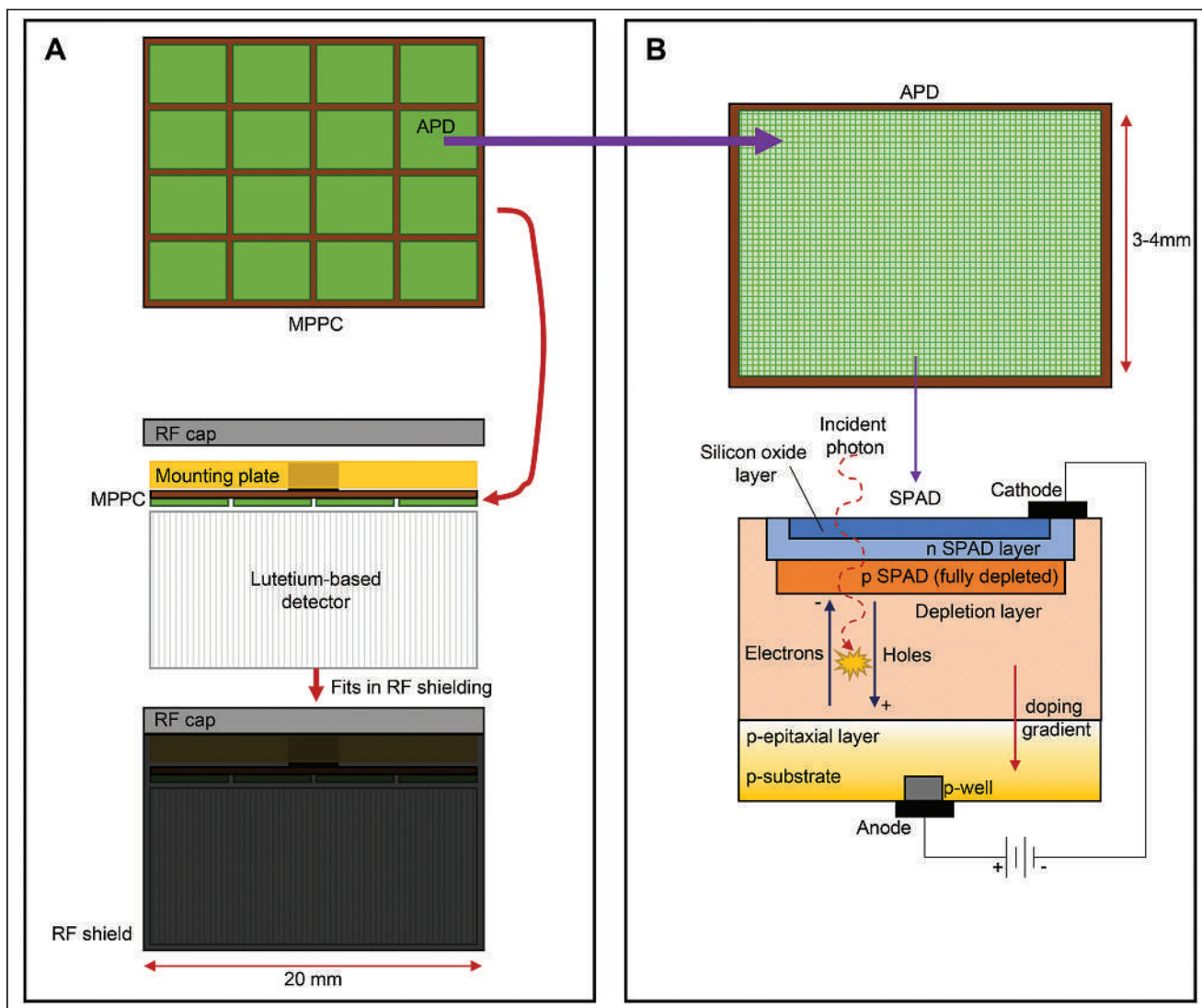


FIGURE 6. (A) Multipixel photon counter (MPPC) array comprises multiple APDs and is mounted to lutetium-based detector, which is housed in lightproof radiofrequency (RF) shield. These small individual MPPC units (2 cm) make up PET detector system. (B) APD (in this case, Geiger-mode APD) comprises pixels (single-photon avalanche diode, or SPAD). Layers of SPAD use silicon dioxide layer through which incident photons interact in depletion layer. Excitation causes electron holes that migrate to positive and negative doped layers to produce signal.

CHALLENGES OF PET/MR

Even with the technical issues addressed, PET/MR comes with several challenges. Physical space, shielding, and planning are a major challenge but have been detailed in the first article in this series (*14*) and will not be duplicated here. The time cost associated with imaging protocols and procedures will only briefly be discussed below since it will be detailed in part 3 of this series of articles.

Time Cost

Although PET/MRI is considered simultaneous in nature, MRI radiofrequency-pulse sequences tend to be longer than PET bed positions (*1*). A 3-min bed position, for example, may be insufficient for all MRI sequences to be completed, although recent developments have seen the emergence of 4–5 MRI sequences in a 3-min PET bed position. This discrepancy is exacerbated in whole-body imaging typical of oncology studies. The solution under development is fast MRI protocols. These have shown some early success but have several barriers to overcome, including noise reduction. Nonetheless, multiple sequences for whole-body MRI over 20–40 min have a higher time cost than the multiple-bed-position PET covering the same anatomy in 10–20 min (*1*). An important consideration in this discussion is the actual applications of PET/MRI, which will be discussed in detail in part 4 of this series. Many of the clinical applications or clinical scenarios in which PET/MRI provides a tangible benefit over PET/CT may require only a single bed position—neurologic PET/MRI, cardiac PET/MRI, or head and neck oncology imaging, for example.

Attenuation Correction

A distinct advantage of PET/CT is the ability to perform accurate attenuation correction using a rapid CT acquisition immediately before or after the PET image is acquired. This was a significant advance over the previous methods using $^{68}\text{Ge}/^{68}\text{Ga}$ sources to produce transmission scans before the patient is administered the PET radionuclide dose. PET/MRI has no option for producing a transmission scan for attenuation correction because there is no correlation between the attenuation coefficient and MR signal intensity (*1,5,6,15*). A variety of approaches have been adopted to create an MR-based proxy for the attenuation map; each continues to be constrained by limitations. The challenge of accurate attenuation mapping using MRI is complicated by additional attenuation associated with MR hardware and coils in the field of view (*1,6*). Furthermore, attenuating structures on the PET image may be positioned outside the acquisition field; an arms-down chest PET/MRI study, for example, may truncate the MR signal from the arms and, thus, be unable to estimate attenuation from the truncated tissues (*1,6*). The advantage of PET/MRI attenuation correction over PET/CT, if it can be performed accurately, is the reduced patient radiation dose and the simultaneous acquisition that can overcome mismatches between sequentially performed PET and CT attenuation mapping (*1*).

Simple segmentation and classification of different tissue types using the T_1 signal can be constrained by the lack of bone signal and associated attenuation correction (*1,5,7,15*). Moreover, some tissues, such as lung, can have different attenuation coefficients from one person to the next (*1*). Another simple approach may be suitable for tissues with uniform attenuation (e.g., the brain) using estimation methods and an attenuation formula (*1*). This method was used for brains before PET/CT, but the additional influence of MRI coils requires careful mapping of the coil template in the estimated attenuation corrections (*1,15*). It is possible to also revert to previous PET system designs in which a rotating rod source ($^{68}\text{Ge}/^{68}\text{Ga}$) is used for a transmission scan (*1,15*). Obviously, this approach adds to the time associated with the transmission scan, produces noisy attenuation maps, and remains inferior to CT-based attenuation correction.

Current approaches to attenuation correction on integrated PET/MRI use a 3-dimensional Dixon approach that provides in-phase and out-of-phase datasets for water and fat (*6*). In essence, this allows segmentation of air, fat, muscle, and lung tissue for attenuation coefficients but lacks accommodation for bone (*6*). Bone is classified as soft tissue from an attenuation coefficient perspective in this approach. The underestimation of attenuation associated with this bone non-classification can produce substantial errors in quantitation of both bone and adjacent soft tissue. This could be overcome with the addition of atlas-based methods, but these have limitations around variations from normal anatomy not uncommon in pathologic patients (*15*). A different approach incorporates ultrashort-echo signals to delineate bone and add to the standard T_1 tissue segmentation. The ultrashort-echo-time approach can also be combined with a Dixon sequence (MRI sequence based on chemical shift designed for fat suppression) to produce classes of very short T_2 tissues for segmentation (*5,6,15*). This approach has particular potential in lung imaging.

An important area of development for PET/MRI is pseudo-CT attenuation maps (Fig. 7). There are several limitations in estimating an attenuation map from MRI for PET/MRI that convolutional neural networks (CNNs) may overcome (*16*). Deep CNNs can produce an attenuation map that closely models the CT-based grounded truth (*17,18*). Others have integrated the Dixon method with a CNN to generate pseudo-CT for pelvic PET/MRI, with promising results of less than 2% variation from the CT map (*19*). More accurate attenuation maps also resulted from the use of deep CNN combined with zero-echo-time Dixon pseudo-CT (*20*). CNN approaches can produce pseudo-CT attenuation maps from the PET sinogram, and this approach was used successfully (<1% error) on ^{18}F -FDG brain scans (*21*).

The ability to accurately correct for attenuation is essential for accurate quantitation of PET data (*1,6*). Indeed, the accuracy of relative quantitation markers such as SUV will be undermined if the integrity of attenuation correction is sacrificed.

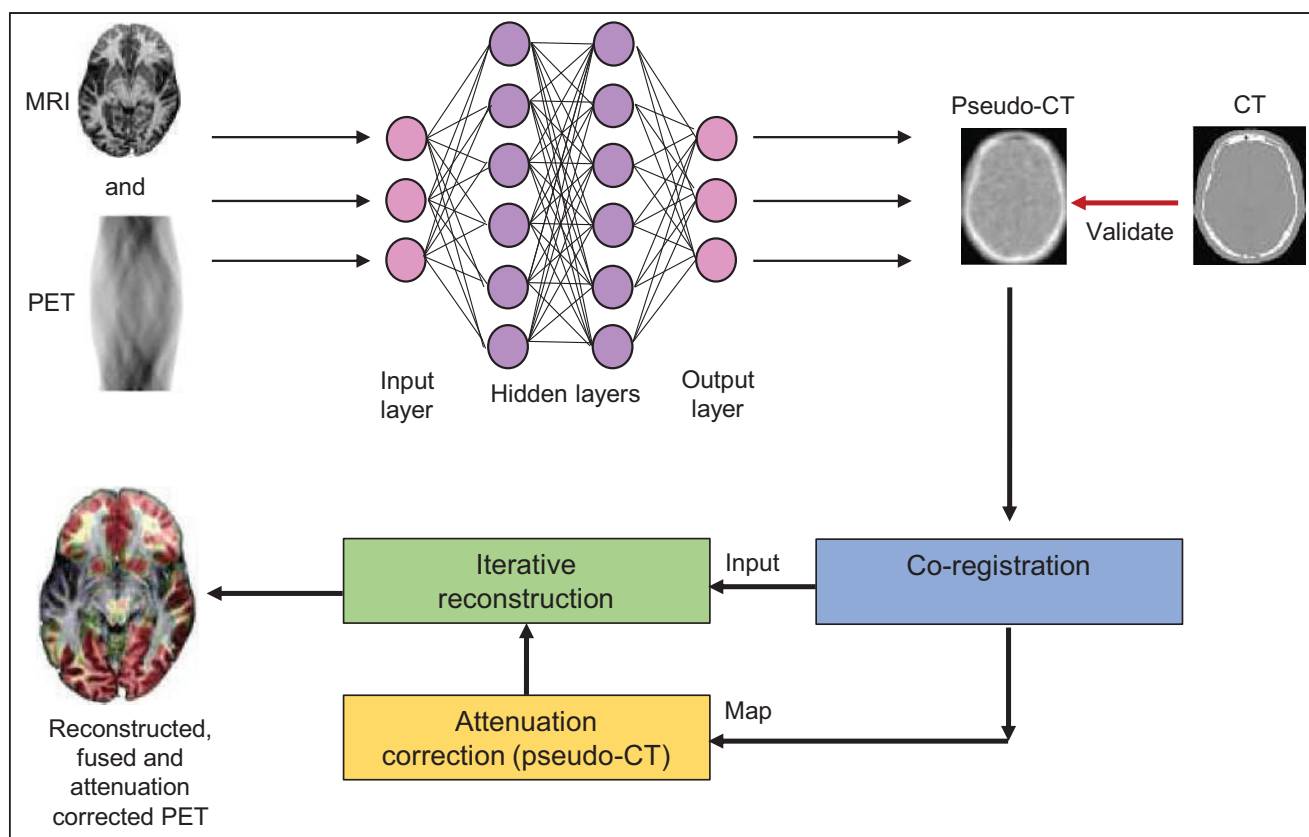


FIGURE 7. Model for potentially using CNN for improved pseudo-CT attenuation correction in PET/MRI. (Adapted from (16).)

Artifacts

Both PET and MRI are vulnerable to artifacts, and this vulnerability can undermine not only image quality but also quantitative accuracy. PET/MRI, combined, adds a layer of complexity to potential artifacts. The most common artifact that raises concern is cross-talk between PET and MRI, but this has been largely overcome by the new detector designed previously. It is possible that mechanical misalignment can cause coregistration inaccuracies (6). Imperfect attenuation correction remains a concern for artifact production, and this can be exacerbated by the administration of contrast by interfering with tissue segmentation (6). MRI is susceptible to signal voids associated with items such as implants, and these may also produce attenuation artifacts on the PET scan (6). As already discussed, artifacts can be produced in the PET data by attenuation from the MRI hardware and coils and by truncation of the field of view.

CONCLUSION

Although hybrid imaging with PET/MR plays a role in several clinical situations, there are several technical considerations required in the design and operation of the imaging systems. Specifically, modifications to conventional imaging systems that accommodate integration of the 2 modalities without image-degrading cross talk require deep understanding before the technology can be adopted. Such understanding will have translational benefits to

procedural and clinical applications of PET/MRI. Specific design features of PET/MRI help guide the facility planning detailed in part 1 of this series. The integration of PET/MRI affords the opportunity for enhanced protocols and clinical applications which will be explored in more detail in parts 3 and 4 of this series, respectively. Understanding the principles of PET, MRI, and integrated PET/MRI systems provides the foundation for safe, effective, and optimal adoption of PET/MR technology.

DISCLOSURE

No potential conflict of interest relevant to this article was reported.

REFERENCES

1. Vandenberghe S, Marsden PK. PET-MRI: a review of challenges and solutions in the development of integrated multimodality imaging. *Phys Med Biol*. 2015;60:R115–R154.
2. Fendler WP, Czernin J, Herrman K, Beyer T. Variations in PET/MRI operations: results from an international survey among 39 active sites. *J Nucl Med*. 2016;57:2016–2021.
3. Turkington TG. Introduction to PET instrumentation. *J Nucl Med Technol*. 2001;29:4–11.
4. Wehrl HF, Sauter AW, Judenhofer MS, Pichler BJ. Combined PET/MR imaging: technology and applications. *Technol Cancer Res Treat*. 2010;9:5–20.
5. Herzog H. PET/MRI: challenges, solutions and perspectives. *Z Med Phys*. 2012;22:281–298.
6. Quick HH. Integrated PET/MR. *J Magn Reson Imaging*. 2014;39:243–258.

7. Disselhorst JA, Bezrukov I, Kolb A, Parl C, Pichler BJ. Principles of PET/MR imaging. *J Nucl Med*. 2014;55(suppl):2S–10S.
8. Bushong SC, Clarke G. *Magnetic Resonance Imaging: Physical Principles and Biological Principles*. 4th ed. Elsevier; 2015.
9. Hashemi RH, Bradley WG, Lisanti CJ. *MRI: The Basics*. 2nd ed. Lippincott Williams & Wilkins; 2004.
10. van Geuns RJM, Wielopolski PA, de Bruin HG, et al. Basic principles of magnetic resonance imaging. *Prog Cardiovasc Dis*. 1999;42:149–156.
11. Currie GM. Pharmacology, part 5: CT and MRI contrast media. *J Nucl Med Technol*. 2019;47:189–202.
12. Currie G, Hewis J, Bushong S. Tomographic reconstruction; a non-mathematical overview. *J Med Imaging Radiat Sci*. 2015;46:403–412.
13. Gundacker S, Heering A. The silicon photomultiplier: fundamentals and applications of a modern solid-state photon detector. *Phys Med Biol*. 2020;65:17TR01.
14. Kamvosoulis P, Currie G. PET/MR, part 1: establishing a PET/MRI facility. *J Nucl Med Technol*. 2021;49:120–125.
15. Martinez-Möller A, Nekolla SG. Attenuation correction for PET/MR: problems, novel approaches and practical solutions. *Z Med Phys*. 2012;22:299–310.
16. Currie GM. Intelligent imaging: artificial intelligence augmented nuclear medicine. *J Nucl Med Technol*. 2019;47:217–222.
17. Hwang D, Kim KY, Kang SK, et al. Improving the accuracy of simultaneously reconstructed activity and attenuation maps using deep learning. *J Nucl Med*. 2018;59:1624–1629.
18. Hwang D, Kang SK, Kim KY, et al. Generation of PET attenuation map for whole-body time-of-flight ^{18}F -FDG PET/MRI using a deep neural network trained with simultaneously reconstructed activity and attenuation maps. *J Nucl Med*. 2019;60:1183–1189.
19. Torrado-Carvajal A, Vera-Olmos J, Izquierdo-Garcia D, et al. Dixon-VIBE Deep Learning (DIVIDE) pseudo-CT synthesis for pelvis PET/MR attenuation correction. *J Nucl Med*. 2019;60:429–435.
20. Leynes AP, Yang J, Wiesinger F, et al. Zero-Echo-Time and Dixon Deep Pseudo-CT (ZeDD CT): direct generation of pseudo-CT images for pelvic PET/MRI attenuation correction using deep convolutional neural networks with multiparametric MRI. *J Nucl Med*. 2018;59:852–858.
21. Liu F, Jang H, Kijowski R, Zhao G, Bradshaw T, McMillan AB. A deep learning approach for ^{18}F -FDG PET attenuation correction. *EJNMMI Phys*. 2018;5:24.

Experiences and Perceptions of Nuclear Medicine Technologists in the Assessment of Myocardial Perfusion Image Quality

Lucky R. Chipeya¹, Madri Jansen van Rensburg¹, and Mboyo-Di-Tamba Vangu²

¹Department of Medical Imaging and Radiation Sciences, University of Johannesburg, Johannesburg, South Africa; and ²Division of Nuclear Medicine, Department of Radiation Science, University of Witwatersrand, Johannesburg, South Africa

Nuclear medicine technologists (NMTs) are experts in the acquisition of myocardial perfusion (MP) images, in addition to the many other types of images acquired in nuclear medicine departments. NMTs are expected to ensure that images are of optimal quality in order to facilitate accurate interpretation by nuclear medicine physicians (NMPs). However, ensuring optimal image quality is a shared responsibility between NMTs and NMPs. The shared responsibilities have resulted in inconsistencies in the assessment of MP image quality among NMTs in different departments. Little is known about the perceptions and experiences of NMTs on the assessment of MP image quality. Therefore, the focus of this research study was NMTs. The aim of this qualitative study was to explore and describe the perceptions and experiences of NMTs on the assessment of MP image quality. The research question was, "How do NMTs perform the responsibility of ensuring MP image quality?" **Methods:** The study followed a qualitative explorative approach using focus groups as a means of collecting data. Nineteen NMTs from 4 academic hospitals were purposefully selected to participate. A semistructured questionnaire was used to conduct the focus groups. The collected data were managed using a computer-aided qualitative data analysis software program to formulate codes, categories, and themes. **Results:** Two overarching themes emerged from the data: the management of MP images, and the resources required to support NMTs. NMTs differed in their management of MP images because of the prevailing circumstances in their respective departments. In addition, the results suggested that NMTs' level of involvement in the assessment of MP image quality was influenced by the availability of resources required for processing and assessing image quality. **Conclusion:** Despite the shared responsibility in the assessment of MP image quality with NMPs, NMTs considered themselves as playing a major role. However, resources to facilitate the assessment of image quality are considered necessary and should be available to support NMTs in submitting images of optimal quality for interpretation.

Key Words: technologists; myocardial perfusion imaging; quality; artifacts.

J Nucl Med Technol 2021; 49:226–231

DOI: 10.2967/jnmt.120.255125

Myocardial perfusion imaging (MPI) is one of the most common imaging procedures requested in nuclear medicine

departments (NMDs) (1,2). The primary indication for MPI is to assess the relative distribution of coronary blood flow in patients with suspected or known obstructive coronary artery disease (3,4). MPI has emerged not only as a diagnostic technique but also as a robust prognostic tool able to provide data about myocardial perfusion (MP), ventricular function, and viability in a single test (5). It is therefore important that MP images be acquired and diagnosed accurately in order to decrease the risk of misdiagnosis (6).

The diagnostic accuracy of MP images is compromised by artifacts associated with localized subdiaphragmatic radiopharmaceutical concentrations in the abdominal viscera, such as the liver, stomach, and bowel (2,7), and patient motion is the most common artifact on MP images (8–10). Further, artifacts may also arise from γ -camera limitations, electrocardiography gating irregularities, and inadequate counts (8,9). Other artifacts are caused by nuclear medicine technologists (NMTs) during imaging, such as through incorrect patient positioning (8). It is important that artifacts be identified because unidentified artifacts and pitfalls have deleterious effects on the reconstructed data (11). Therefore, the quality of images should be reviewed and technical abnormalities recognized and corrected when possible by NMTs (12) during and after acquisition of images.

NMTs should be aware of sources of potential error in MPI and take appropriate steps to correct them if they occur (2,8). Before image acquisitions, NMTs perform daily uniformity and energy-peaking tests on γ -cameras; other quality control tests, such as tests of sensitivity, resolution, linearity, and center of rotation, are performed weekly (9). In addition, before the commencement of MPI, NMTs verify the integrity of electrocardiography leads by ensuring that electrical contacts are secure; otherwise, the signal can be randomly interrupted (13). If not placed properly, the R-wave gating device will not trigger on the R wave but on a different portion of the trace (13). Therefore, quality control programs are adhered to for optimizing diagnostic accuracy and ensuring consistent high-quality MP images (14).

Errors identified during image acquisition, such as extracardiac activity, require the NMT to stop the procedure temporarily, apply an appropriate intervention, such as delaying the imaging in order to allow the extracardiac activity to move away from and stop obscuring the heart, and restarting the acquisition. The NMT can also intervene after an imaging

Received Aug. 10, 2020; revision accepted Feb. 22, 2021.
For correspondence or reprints, contact Lucky R. Chipeya (lchipeya@uj.ac.za).

Published online April 5, 2021.

COPYRIGHT © 2021 by the Society of Nuclear Medicine and Molecular Imaging.

acquisition by using software to correct errors such as minor motion. However, in the case of major motion that cannot be corrected by software, the NMT repeats the acquisition. The NMT also uses attenuation correction software to rectify attenuation errors. The attenuation might result from inadequate counts due to variable radiation attenuation from different projection angles (13). During processing, reconstruction, and display, computer software tools help to shape and transform the images to make them more amenable to visual and quantitative analysis (15). But several user-dependent technical errors may occur during the processing phase of MP images because the user must choose the short-axis, horizontal long-axis, and vertical long-axis limits (8).

The responsibilities of NMTs in the assessment of MP image quality vary widely among different departments and countries (6,16). However, NMTs should review MP images to ensure that the required information has been obtained, is processed properly, and is of optimal quality (16). The assessment of image quality, including processing, reconstruction, and display, is within the scope of practice of NMTs (17–19). Nuclear medicine physicians (NMPs) also assess the quality of the MP images before interpretation (12). Although both NMTs and NMPs have responsibilities toward ensuring MP image quality, very little is known about the perceptions and experiences of NMTs during the assessment of MP image quality. The aim of this study was therefore to explore and describe these perceptions and experiences.

MATERIALS AND METHODS

The Research Ethics and Higher Degrees Committee of the Faculty of Health Sciences at the University of Johannesburg approved this study, and all participants individually gave written informed consent to take part in it. Further, all participants gave written permission for an audio recording to be made of the focus group discussions. Anonymity was ensured, and code names were used during discussions. It was anticipated that the participants would mention each other's names during discussions; therefore, code names were allocated at the beginning of each focus group discussion and the participants were given time to familiarize themselves with their code names.

The research study adopted a qualitative phenomenologic approach. The use of focus group discussions traded on group dynamics because the social and psychologic aspects of group behavior are used to foster the ability of the participants to get involved, speak their minds, and reflect on the views of others (20,21). In addition, focus groups are appropriate for quickly exploring topics about which little is known (22).

A purposive sampling method was adopted to select and recruit NMTs whose knowledge and work experience (23) in MPI and other nuclear medicine imaging procedures were sufficient to extract useful information. The experience of the NMTs ranged from 2 to 28 y. The focus groups were divided into 3 cohorts according to the NMD in which the NMTs worked. There were 19 NMTs in total: 7 from NMD 1, 6 from NMD 2, and 6 from NMD 3.

All the NMDs are affiliated with teaching hospitals and are accredited to teach resident NMPs and student NMTs. Consultant NMPs supervise the resident NMPs in all aspects of ensuring MP image quality and interpreting images. Likewise, during clinical placements, student NMTs are monitored by supervisory NMTs

regarding all aspects of acquiring MP images and performing quality control tests. Further, resident NMPs learn how MP images are acquired. When the NMTs submit MP images to the reporting rooms, either the resident NMPs or the consultant NMPs view the images. Therefore, the NMPs are the final referees of MP image quality, despite the NMTs' judgments.

Focus group discussions were conducted at convenient times, at venues remote from the work areas and away from disruptions (24). An interview guide was used for consistency and to direct the discussions toward significant and relevant issues pertaining to the purpose of the research study. The questions were semistructured, allowed the participants to contribute as much detailed information as they could, and permitted the researcher to probe through follow-up questions (25). The interview guide was divided into 3 areas, namely; engagement, exploration, and exit questions (26). All discussions were audio-recorded (27,28) and transcribed verbatim. Member checking was used to verify the transcriptions (24), with the participants confirming their accuracy.

Thematic analysis is the search for, and extraction of, general patterns found in data through multiple readings of data (30,31). This study used thematic analysis because it is not confined to any preexisting theoretic frameworks and can be applied to different situations (29). A qualitative data analysis software program, ATLAS.ti (version 7; Scientific Software Development GmbH), was used to manage the study data (20,32). The transcripts were uploaded into the project documents of the hermeneutic unit of ATLAS.ti, and codes, categories, and themes were developed.

Open coding was used to group similar codes to form categories under themes. During the coding, the researcher examined the data corpus as facilitated by ATLAS.ti using the NCT model (Noticing things, Collecting things, and Thinking about things), a model adapted for computer-assisted analysis (33). The final stage of the analysis was the linking of quotations to categories, and a structure was then formed from which the presentation of the results was drawn.

RESULTS

The main findings included 2 overarching themes, the management of MP images and resources to support NMTs. The first theme was developed from 3 categories, namely the assessment of MP image quality, the role of NMTs in MP image quality, and NMTs' perceptions on NMPs' assessments of MP image quality. The second theme was developed from 5 categories, namely processing workstations, user manuals, colleagues or NMPs, training, and medical imaging application specialists.

The Management of MP Images (Theme 1)

Our study confirmed the findings of Johansson et al. (16) that the extent of NMTs' responsibilities toward MP image quality varied. In NMD 1, the NMTs assessed MP image quality by processing, reconstructing, and displaying the final images. The final images were saved and submitted to the NMPs together with the raw images (unprocessed) for interpretation. In NMD 2, the NMTs followed the same procedure as the NMTs in NMD 1 but did not save the final images; instead, they submitted only the raw images to the NMPs. In NMDs 3 and 4 (both referred to hereafter as NMD 3 because they had similar procedures), the NMTs assessed MP image quality during acquisition, but once acquisition

was completed, the images were automatically submitted to the NMPs as raw images.

NMTs' Extent of Involvement in Assessing MP Image Quality. All NMTs confirmed that they were involved in the assessment of MP image quality. They also expressed their extent of involvement. The NMTs from NMD 1 considered themselves privileged to be processing and reconstructing MP images that were considered ready for interpretation:

Once everything is done, in terms of processing, you send it to the nuclear medicine physician, and most of the time they take the very same data that we have actually processed. (NMT, NMD 1)

I have been privileged to have been processing myself and then having to hand [the images] over to physicians or [resident NMPs]. (NMT, NMD 1)

Further, the NMTs from NMD 1 revealed that the NMPs request that image acquisition be repeated if the image quality was compromised, such as because of an inadequate count density or because of motion:

They just report, but if eventually they also fail to improve the quality, then they would say that the patient needs to be repeated. (NMT, NMD 1).

Again if you can't correct the motion—yes, then you have to repeat. (NMT, NMD 1)

The NMTs from NMD 2 reported processing MP images for purposes of assessing image quality and not for interpretation by the NMPs. This processing was meant to ensure that the raw images were of adequate quality:

You check for quality: your bowel, liver activity, interferences. If it's not there, fine, that's the end of the story for you. The doctors will do the processing; I think of it as a personal preference. They just prefer it that way—not that we cannot process or whatever. (NMT, NMD 2)

Lastly, the NMTs from NMD 3 assessed the MP image quality differently from those from NMD 1 or NMD 2. They reported assessing the image quality on screen and then approaching the NMPs to confirm whether the quality was optimal:

The doctors normally process their own images, but I normally check for motion, check gut activity if it's there, or I can call the doctor to double check and then from there we decide. (NMT, NMD 3)

NMTs' View of Their Role in Ensuring MP Image Quality. The NMTs from NMD 1 believed they have an impact on image quality and should be involved in the entire process, thus having the opportunity to identify errors at any stage of image processing, reconstruction, or display:

I feel that the role of the [technologist] impacts a lot on the image quality since this is the person who actually interacts with the patient from day one. I'm doing the scan. (NMT, NMD 1)

If you don't play a role in processing the whole study, you won't be able to know what you need to improve on whatever you would have done. (NMT, NMD 1)

The NMTs from NMD 2 perceived themselves as having a major role in ensuring image quality; they advocated for NMTs to do their best in ensuring optimal image quality:

Generally, what I would say is if you can do a scan, the [technologist] has to have a major part to play in the quality—basically, looking at those artifacts, like bowel and liver. (NMT, NMD 2)

Being the [technologist], you would have to do your all, making sure you are processing and bringing best-quality images to [NMPs]. (NMT, NMD 2)

I think, as [technologists], we basically look at that static image ... to produce a really good image, whereas physicians are more looking at pathology. I think we need to be involved. (NMT, NMD 3)

NMTs' Perceptions on NMPs' Assessment of MP Image Quality. Because the NMTs believed that they play a major role in ensuring MP image quality, they advocated for NMPs to be relieved of quality assurance tasks in order to concentrate on reporting MP images and other imaging procedures. However, the NMTs suggested that the NMPs could be involved in quality assurance if the NMTs find it difficult to process and assess the quality of certain MP images:

We can take some of the workload in terms of processing, and [NMPs] can be more involved with other patients. Obviously, there will still be difficult patients, but the ones that are not too complicated—that, we can process. If there is a challenge, [NMPs] can still process themselves, so we help each other out. (NMT, NMD 3)

Further, the NMTs perceived that NMPs, particularly resident NMPs, need to learn how to process and assess MP images but then would reach a point at which their involvement is limited. In addition, the NMTs assumed that the number of resident NMPs in the department would influence their involvement in processing:

Obviously, the [resident NMPs] will also need to learn, they will also get to a point where—been there, done that—they just want the end result, so it will save time for them and for the patient. (NMT, NMD 2)

Now there are a lot of [resident NMPs]. So now I think they are giving them a chance to actually do it by themselves. (NMT, NMD 2)

The NMTs from NMD 3 revealed that workloads and staff shortages made it difficult for them to find time to process and assess MP image quality. They also have to complete other imaging procedures:

There is not enough time to go and sit for processing, meaning that, basically, you've got to process at the end of the day. Sometimes, the end of the day is even late hours, so that's

where the problem comes, now and then. I suppose that's where [NMPs] also see that, "I have to process here." (NMT, NMD 3)

It always comes down to not enough personnel; we are just not enough to have an extra person sitting and processing. You must scan other patients. (NMT, NMD 3)

The NMTs perceived that when NMPs decided to process and assess MP images themselves, they were taking that responsibility because the images submitted were of suboptimal quality:

The [technologists] are sort of partly to blame for what is sent—if you have to process that same type of scan and send it to the doctor—for it to come back again for rescan. (NMT, NMD 2)

Resources to Support NMTs (Theme 2)

In every NMD, there are several resources available to produce images of optimal quality. In addition, different studies will require different resources at any given time. The NMTs acknowledged the availability of resources to support them in the processing and assessment of MP image quality. These resources included processing workstations, user manuals, colleagues or NMPs, training, and medical imaging application specialists.

Processing Workstations. The NMTs reported that processing workstations were available for NMTs to use. However, access for NMTs differed among the departments, with the workstations being either in the imaging rooms, in the NMP reporting rooms, or in special rooms:

We don't have our own for [technologists] other than the one that we have in the [imaging] room. Others have their own processing stations. (NMT NMD 2)

We have 3 [γ -cameras] and 2 processing units—well, make it 4 processing stations, out of which only 2 processing stations can be used. (NMT NMD 1)

Despite the availability of processing workstations in the imaging rooms, the NMTs in NMD 2 and NMD 3 reported that these workstations were limited in what they could do:

But [the processing units in the rooms] are limited—like basic—just to see if there is any infracardiac activity or not. (NMT NMD 3)

The reporting room has got another software; we got another one. [The processing workstations are] almost the same, but there is some additional stuff on the reporting. (NMT NMD 2)

User Manuals. User manuals are usually supplied by vendors after the installation of γ -cameras or processing workstations and are used as references for computer commands. The NMTs acknowledged their availability and usefulness but differed in their use practically:

You can actually refer to the manuals, and you get the finer details of whatever you don't understand. (NMT, NMD 1)

I would rather just do things blindly without following the manuals, because some departments have been following certain protocols of doing things and then you'll have to know them. (NMT, NMD 3)

You need another degree just to understand [the user manual]. (NMT, NMD 3)

Colleagues and NMPs. The NMTs from NMDs 1 and 2 revealed that they frequently asked for a second opinion from colleagues, especially those with more experience, and if these colleagues were unable to assist, the NMPs were consulted. The NMTs from NMD 3 preferred consulting the NMPs from the onset:

I have my colleagues for second opinion. We go for the most experienced. (NMT, NMD 1)

The first person that I will contact is my colleague to ask for a second opinion: "How do you see this?" And then, if he/she agrees with me, I'm happy, but if I'm still doubting, I will go and ask the consultant's opinion. (NMT, NMD 2)

And if you have any queries, those ones you leave for the doctors. (NMT, NMD 3)

Training. The NMTs considered training as a major resource for support in the assessment of MP image quality. They received training during work-integrated learning as students and were taught by qualified NMTs and clinical tutors. During the focus group discussions, the NMTs opined that being taught by a colleague was the best option:

The colleague will show you how to process, and you practice by yourself until you gain confidence. (NMT, NMD 1)

I think we were happy the way we were trained because we were trained through a clinical tutor. (NMT, NMD 2)

Further, the NMTs believed it was important that, after qualifying, they be given ongoing opportunities to practice what they had learned so as not to forget it:

It has been part of our training. So it's just that when we come out and we are qualified, the departments that we go to don't really allow us to process, so we lose it. (NMT, NMD 3)

You can have a structure where you go for a course or program, 1-day program. You are taught how to do things, but when you don't practice it frequently, you easily forget it. (NMT, NMD 1)

Again, the NMTs echoed the need for training of qualified NMTs. Training was deemed especially necessary for NMTs who are not actively involved in ensuring MP image quality:

We are not doing a lot of processing, but when I went to another hospital for a month, they showed me how to process, so obviously, I needed a lot of training. (NMT, NMD 2)

Training needs to be redeveloped to fill the gap for all the qualified. We have clearly lost a bit of it. (NMT, NMD 3)

Medical Imaging Application Specialists. The NMTs revealed that after installation of new equipment, medical imaging application specialists were available to train them but did not have all the answers and were not readily available if the NMTs require assistance after the training period:

[Medical imaging application specialists] usually come on installation day, and if the department doesn't know the software or... the machine, they come and do everything, and they go, leave the manuals, and it's for you to remember what they said and how the things work. (NMT NMD 2)

You can often ask them the questions and they don't have answers because they don't have the clinical experience. (NMT, NMD 3)

They won't come, like, tomorrow, but they would like to come later on to see the progress. On your day 1 of the training session, you may not be able to ask a lot of questions because you don't know anything about this equipment. Once you start using the machine, you now start experiencing problems. (NMT, NMD 1)

DISCUSSION

The NMTs from the different NMDs expressed different and similar perceptions and experiences about processing MP images and assessing their quality. Because of the paucity of published literature on this topic, parallels are drawn from similar professions in the medical field, such as diagnostic radiography and nursing. These professions share some responsibilities with other professions, diagnostic radiographers with radiologists and nurses with physicians (34).

The NMTs from the different departments ensured that the MP images submitted to the NMPs for reporting were assessed for quality. However, those who assessed MP raw images were likely to miss artifacts that appear during processing and reconstruction. Artifacts may arise at any stage of MPI (9). In addition, processing is not a substitute for poor positioning techniques (35). Therefore, if NMTs process the MP images during the assessment of quality, they can identify artifacts that may arise during processing and they can see how positioning affects the resultant images. This capability would help NMTs realize the effects of acquisition parameters, patient positioning, and other variables during acquisition of the final images.

The NMTs' suggestion that they be more involved than NMPs in the processing and quality assessment of MP images, to allow the NMPs more time for reporting, was also expressed by diagnostic radiographers in a study by Brealey and Scuffham (36). This study found that training diagnostic radiographers on how to report examinations for patients referred from accident and emergency departments afforded radiologists the time to concentrate on other reporting duties. The same could be said of NMTs trained to process and assess MP images in order to release NMPs from image-quality responsibilities, allowing them to concentrate on MPI

reporting and other procedures. In the United Kingdom, adoption of an enhanced role for NMTs in stress testing enabled the nuclear cardiology service to effectively increase its capacity for stress sessions, thus allowing NMPs to focus on reporting, clinical research, and development of the clinical service (37).

If an organization develops adequate resources to help NMTs achieve the goal of ensuring optimal MP image quality (38,39), it would seem possible for them to assume responsibility for processing and assessing MP images. Such resources differed among the 3 NMDs. User manuals were available but were underutilized by the NMTs. Instead, the NMTs relied on following the protocols established locally by their departments, as was also reported by Sá Dos Reis et al. (40). Because such protocols were favored over user manuals and sometimes were adaptations or simplifications of the user manuals, these protocols should be optimized, with the manuals serving as a backup.

Support from colleagues in the workplace is important in any organization. Our finding that NMTs relied on colleagues as a first line of support was also reported by Choi (41), whose study found that team members of similar educational levels helped each other. However, a decision to first approach NMPs, rather than colleagues, for image-quality opinions could be due to lack of confidence in colleagues whose involvement in image-quality assessment is limited. It is therefore important that NMTs be adequately trained to submit images that are of optimal quality and will not need to be repeated.

It seemed acknowledged that medical imaging application specialists are made available to train NMTs on how to use new equipment. However, after the training session, these specialists were no longer available on site to respond to any challenges the NMTs might later experience. Instead, the specialists left behind user manuals as a reference, which the NMTs found difficult to use and did not often consult. NMDs could consider recalling the specialists for further training, especially once the NMTs have started using the new equipment. Nonetheless, since MP image processing and assessment of quality are part of formal clinical training for NMT students, it is important that after qualification, they have an opportunity to practice and update the acquired skills in order not to become obsolete. In another study, NMTs and radiation therapists advocated for more training on technologic developments, preferably facilitated by their respective departments (42). Therefore, ongoing in-house training and practice should be the norm. The NMPs and senior NMTs could conduct regular in-house training sessions on predetermined schedules.

Our findings are limited to the NMTs who participated in this study and therefore cannot be generalized beyond them, as is the nature of a phenomenologic research study. However, the useful information that emerged on the perceptions and experiences of NMTs in the assessment of MP image quality—a shared responsibility with NMPs—could elicit further research in this area.

CONCLUSION

The burden of MPI on the patient from the stress testing procedure, the length of stay, the cost, and the impact of the results should be taken seriously. Therefore, it is important that the MP images submitted by NMTs to NMPs for interpretation be of optimal quality. It is also important for NMTs to display confidence and assume ownership of MP image quality so that MP image processing, assessment of image quality, and reconstruction will be meticulously executed. To facilitate production of optimal MP images, resources should be available and effectively used by NMTs. Since ensuring optimal MP image quality is a shared responsibility between NMTs and NMPs, management of the MP images should be well coordinated with the NMTs. When followed carefully, clearly written protocols for the processing and reconstruction of MP images can improve this process. Therefore, such protocols are recommended.

DISCLOSURE

No potential conflict of interest relevant to this article was reported.

REFERENCES

1. Fragkaki C, Giannopoulou CH. Pitfalls in classical nuclear medicine: myocardial perfusion imaging. *J Phys Conf Ser*. 2011;317:012014.
2. Fathala A. Myocardial perfusion scintigraphy: techniques, interpretation, indications and reporting. *Ann Saudi Med*. 2011;31:625–634.
3. Henzlova MJ, Duval L. SPECT radionuclide myocardial perfusion imaging protocols. In: Heller GV, Hendel RC, eds. *Nuclear Cardiology: Practical Applications—The Sage Handbook of Nuclear Cardiology*. McGraw Hill; 2011:71–79.
4. Baggish AL, Boucher CA. Radiopharmaceutical agents for myocardial perfusion imaging. *Circulation*. 2008;118:1668–1674.
5. Acampa W, Zampella E, Assante R. State of the art in myocardial imaging. In: Rider H, Testanera G, Veloso JV, Vidović B, eds. *Myocardial Perfusion Imaging. A Technologist's Guide*. EANM; 2014:6–15.
6. Tilkemeier PL, Serber ER, Farrell MB. The nuclear cardiology report: problems, predictors and improvement—a report from ICANL. *J Nucl Cardiol*. 2011;18:858–868.
7. Hendel RC, Corbett JR, Cullom J, DePuey G, Garcia EV, Bateman TM. The value and practice of attenuation correction for myocardial perfusion SPECT imaging: a joint position statement from the American Society of Nuclear Cardiology and the Society of Nuclear Medicine. *J Nucl Cardiol*. 2002;9:135–143.
8. Burrell S, McDonald A. Artefacts and pitfalls in myocardial perfusion imaging. *J Nucl Med Technol*. 2006;34:193–211.
9. Mann A. Quality control for myocardial perfusion imaging. In: Heller GV, Hendel RC, eds. *Nuclear Cardiology: Practical Applications—The Sage Handbook of Nuclear Cardiology*. McGraw Hill; 2011:39–50.
10. Won KS, Song B. Recent trends in nuclear cardiology practice. *Chonnam Med J*. 2013;49:55–64.
11. Wheat JM, Currie GM. Recognising and dealing with artifact in myocardial perfusion SPECT. *Internet J Cardiovasc Res*. 2006;4:1–4.
12. Hendel C. Exercise and pharmacological stress testing. In: Heller GV, Hendel RC, eds. *Nuclear Cardiology: Practical Applications*. McGraw Hill Medical; 2011:53–69.
13. Nichols KJ, Kenneth J, Van Tosh A. Gated SPECT myocardial perfusion imaging quality assurance in current and future practice. *J Nucl Cardiol*. 2017;24:543–545.
14. Dorbala S, Ananthasubramaniam K, Armstrong JS, et al. Single photon emission computed tomography (SPECT) myocardial perfusion imaging guidelines: instrumentation, acquisition, processing, and interpretation. *J Nucl Cardiol*. 2018;25:1784–1846.
15. Gernamo G, Slomka P, Berman D. Computer aspects of myocardial imaging. In: Henkin R, ed. *Nuclear Medicine*. Elsevier; 2006:609–630.
16. Johansson L, Lomsky M, Gjerdtsson L, et al. Can nuclear medicine technologists assess whether a myocardial perfusion rest study is required? *J Nucl Med Technol*. 2008;36:181–185.
17. Health professions act, 1974 (act 56 of 1974): regulations defining the scope of the profession of radiography. Health Professions Council of South Africa website. https://www.hpcsa.co.za/Uploads/RCT/Rules%20and%20Regulations/REGULATIONS_PUBLISHED_FOR_COMMENT.pdf. Published August 21, 2020. Accessed June 23, 2021.
18. Society of Nuclear Medicine Technologists. Performance and responsibility guidelines for the nuclear medicine technologist. *J Nucl Med Technol*. 2003;31:222–229.
19. Society of Nuclear Medicine Technology Section Presidential Task Force. Scope of practice for the nuclear medicine technologist. *J Nucl Med Technol*. 2007;35(3):15A–17A.
20. Denscombe M. *The Good Research Guide for Small-Scale Social Research Projects*. McGraw-Hill Open; 2010:177.
21. Wagner C, Kawulich B, Garner M. *Doing Social Research: A Global Context*. McGraw-Hill Education; 2012:135.
22. Turner DW. Qualitative interview design: a practical guide for novice investigators. *Qual Rep*. 2010;15:754–760.
23. Matthews B, Ross L. *Research Methods: A Practical Guide for Social Sciences*. Pearson Education Limited; 2010:167.
24. Krueger RA, Casey MA. *Focus Groups: A Practical Guide for Applied Research*. Sage; 2009.
25. Nyumba TO, Wilson K, Derrick CJ, Mukherjee W. The use of focus group methodology: insights from two decades of application in conversation. *Methods Ecol Evol*. 2017;9:20–32.
26. How to conduct a focus group. Eliot and Associates website. 2005. https://datainnovationproject.org/wp-content/uploads/2017/04/4_How_to_Conduct_a_Focus_Group-2-1.pdf. Published 1005. Accessed July 28, 2021.
27. De Vos AS. *Research at Grass Roots: A Primer for the Caring Professions*. Van Schaik Publishers; 2002.
28. Klug N, Butow PN, Burns M, Dhillon HM, Sundaresan P. Unmasking anxiety: a qualitative investigation of health professionals—perspectives of mask anxiety in head and neck cancer. *J Med Radiat Sci*. 2020;51:12–21.
29. Winter RI, Patel R, Norman RI. A qualitative exploration of the help-seeking behaviors of students who experience psychological distress around assessment at medical school. *Acad Psychiatry*. 2017;41:477–485.
30. Clarke V, Braun V. Teaching thematic analysis: overcoming challenges and developing strategies for effective learning. *Psychologist*. 2013;26:120–123.
31. Yukhymenko MA, Brown SW, Lawless KA, Brodowska K, Mullin G. Thematic analysis of teacher instructional practices and student responses in middle school classrooms with problem-based learning environment. *Global Education Rev*. 2014;1:93–109.
32. Burnard P, Gill P, Stewart K, Treasure E, Chadwick B. Analysing and presenting qualitative data. *Br Dent J*. 2008;204:429–432.
33. Friesen S. *Qualitative Data Analysis with ATLAS.ti*. Sage; 2014:12.
34. Pongnapang N. Practical guidelines for radiographers to improve computed radiography image quality. *Biomed Imaging Interv J*. 2005;1:e12.
35. Culpán G, Culpán AM, Docherty P, Denton E. Radiographer reporting: a literature review to support cancer workforce planning in England. *Radiography (London)*. 2019;25:155–163.
36. Brealey SD, Scuffham PA. The effect of introducing radiographer reporting on the availability of reports for Accident and Emergency and General Practitioner examinations: a time-series analysis. *Br J Radiol*. 2005;78:538–542.
37. Vara A. Multidisciplinary approach and advanced practice. In: Ryder H, Testanera G, Veloso JV, Vidović B, eds. *Myocardial Perfusion Imaging. A Technologist's Guide*. EANM; 2014:35–41.
38. Halbesleben JRB, Neveu JP, Paustian-Underdahl SC, Westman M. Getting to the “COR”: understanding the role of resources in conservation of resources theory. *J Management*. 2014;40:1334–1364.
39. Nielsen K, Nielsen MB, Ogbornayad C, Käsälä M, Saarie E, Kerstin I. Workplace resources to improve both employee well-being and performance: a systematic review and meta-analysis. *Work and Stress*. 2017;31:101–120.
40. Sá Dos Reis C, Pascoal A, Mario R, de Oliveira MF, Alves J. Overview of the radiographers' practice in 65 healthcare centers using digital mammography systems in Portugal. *Insights Imaging*. 2017;8:345–355.
41. Choi JN. Collective dynamics of citizenship behaviour: what group characteristics promote group-level helping? *J Manage Studies*. 2009;46:1396–1420.
42. Aarts S, Cornelis F, Zevenboom Y, et al. The opinions of radiographers, nuclear medicine technologists and radiation therapists regarding technology in health care: a qualitative study. *J Med Radiat Sci*. 2017;64:3–9.

Estimation of Chest Wall Attenuation of ^{123}I Emissions in Substernal Goiter: A Phantom Study

Matthew Alfano, John Weaver, Richard Mazurek, and Alan Siegel

Department of Radiology, Dartmouth-Hitchcock Medical Center, Lebanon, New Hampshire

In patients with substernal goiter, the generally accepted theory is that thyroid uptake measurements with iodine isotopes are underestimated because of attenuation by the chest wall. The extent of this underestimation is not well known. In this study, we calculated the attenuation of ^{123}I emissions using a cadaver chest wall with a thyroid probe to better understand the potential severity of this underestimation. **Methods:** A 11.1-MBq capsule of ^{123}I was measured using a thyroid probe directly in a standard neck phantom and behind a cadaver chest wall that included the soft tissues and bony structures (sternum). **Results:** The calculated attenuation of the iodine capsule was 18% for the neck phantom and 35% for the cadaver chest wall. **Conclusion:** Thyroid uptake in cases of substernal goiter may be underestimated by standard techniques using a neck phantom. The composition of the chest wall can vary greatly, and the substernal extent of the goiter would be difficult to calculate with high accuracy on a routine basis. Comparison between the cadaveric specimen and the phantom does give us a rough estimation of the differences in attenuation. Our findings suggest that attenuation by the chest wall can be substantial. Knowledge of the extent of the substernal component of the thyroid gland may be useful if the uptake measurement is used to calculate doses for treating hyperthyroidism in patients with substernal goiter.

Key Words: endocrine; instrumentation; radionuclide therapy; radioactive iodine therapy; radioactive iodine uptake; substernal goiter

J Nucl Med Technol 2021; 49:232–234
DOI: 10.2967/jnmt.120.260810

Thyroid uptake measurements with radioactive isotopes are common in patients with suspected thyroid dysfunction. Such measurements can be particularly useful in hyperthyroidal patients for whom radioactive iodine therapy is planned (1). These measurements will indicate the fraction of administered radioisotope that is within the thyroid gland after a predetermined time. The most commonly used isotopes are ^{123}I and ^{131}I . The capsule of iodine is placed within a neck phantom and counted with a probe. After administration to the patient, the activity within the neck is then measured with the probe, typically 24 h later. Some laboratories also obtain

an early measurement at 4–6 h. Measurements are corrected for background and for physical decay (2).

For the uptake measurements, the thyroid probe is directed at the neck, the presumed location of the thyroid gland. In substernal goiter, a portion of the thyroid gland is in a low position, posterior to the sternum. If the probe is directed at the neck and the gland lies inferior to that point, the uptake measurement will be an underestimate. However, if the thyroid gland is known to be substernal, and the probe is aimed properly, the thyroid uptake measurement may still be incorrect because the attenuation by the neck phantom will not match the true attenuation created by the chest wall. There is no standard phantom for the chest wall.

The goal of our study was to estimate the sternal attenuation of ^{123}I emissions and the resulting level of error in a thyroid uptake measurement.

MATERIALS AND METHODS

Attenuation of the γ -emissions from ^{123}I (159 keV) through a cadaver chest wall was measured by direct counting with a thyroid probe (Biodex).

A 11.1-MBq capsule of ^{123}I was counted with the thyroid probe for 1 min and then placed into a standard neck phantom (Biodex) and counted again for 1 min (Figs. 1 and 2). For the phantom calculation, the probe was positioned 24 cm from the surface of the phantom, as is done in patient studies, meeting the 20–30 cm set by the 2009 practice guideline of the American College of Radiology, Society of Nuclear Medicine and Molecular Imaging, and Society for Pediatric Radiology (3). For counting without the phantom, the probe was positioned at 24 cm plus an additional 2 cm (26 cm total), which is the distance from the capsule holder within the phantom to the surface of the phantom. The capsule was then placed below the sternum of a female cadaver chest wall (Fig. 3). The probe count for 1 min was again obtained with the thyroid probe. Background activity (air) was counted for 1 min. Background was subtracted both from the capsule count and from the attenuated capsule count. The attenuation of the emissions was calculated by comparing the count through the phantom or through the chest wall with the count from the capsule alone: $\text{attenuation} = 1 - [(\text{capsule count in phantom or behind chest wall} - \text{background}) / (\text{capsule count} - \text{background})]$.

RESULTS

All counts are shown in Table 1. Calculated attenuation by the neck phantom was 18%. Attenuation through the cadaver chest wall was 35%.

Received Nov. 23, 2020; revision accepted Mar. 16, 2021.
For correspondence or reprints, contact Alan Siegel (alan.h.siegel@hitchcock.org).
Published online July 9, 2021.
COPYRIGHT © 2021 by the Society of Nuclear Medicine and Molecular Imaging.

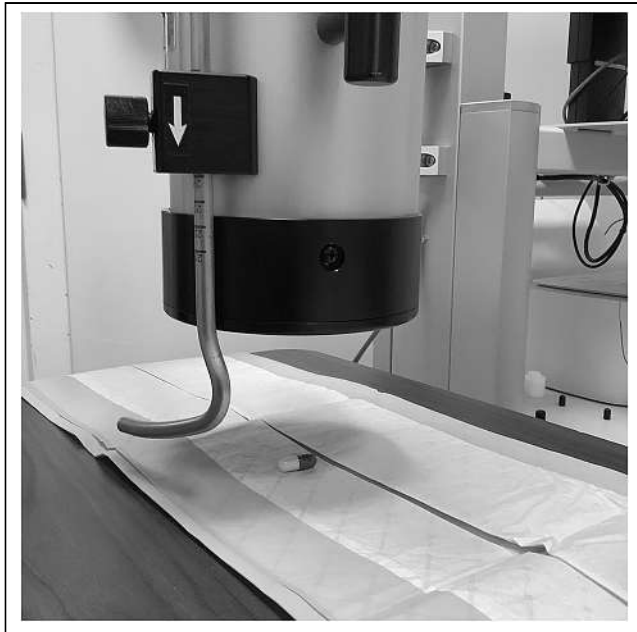


FIGURE 1. Demonstration of counting of capsule of iodine without attenuator. Probe is 26 cm from capsule (equivalent to 24 cm from surface of phantom, when used, plus 2 cm from surface to capsule).

DISCUSSION

Substernal goiter is the process wherein all or a portion of the thyroid gland extends into the mediastinum. It has been estimated to occur in 6% of individuals being evaluated for thyroidectomy (3,4). By including asymptomatic patients, the overall prevalence would be lower. Substernal goiter is often seen in elderly patients and is more common in women than men (6). Although substernal goiters are more often hypofunctioning, patients with hyperthyroidism may have a substernal component to their thyroid gland.

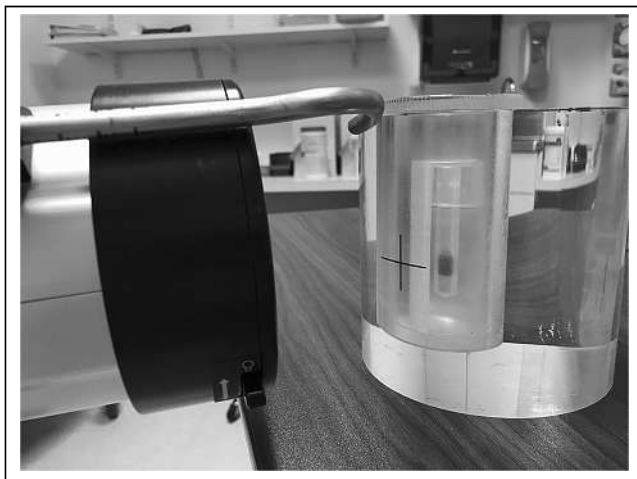


FIGURE 2. Demonstration of counting of iodine capsule within standard neck phantom using thyroid probe. Probe is 24 cm from surface of phantom. Same position is used for patient studies.



FIGURE 3. Demonstration of counting of iodine capsule attenuated by cadaver chest wall. Capsule is within sealed plastic bag below chest wall. Thyroid probe is 26 cm from capsule.

Measurement of thyroid uptake is a commonly performed procedure in which the fraction of ingested iodine within the thyroid gland is calculated after a specified period (usually 24 h and sometimes with the addition of a 4- to 6-h measurement). This test plays a role in characterizing a patient with hyperthyroidism. The measurement is often used to calculate the dose of ^{131}I for treating hyperthyroidism. There are several different ways that this calculation can be done.

We found that our neck phantom attenuated the capsule emissions by 18%—presumably, the approximate attenuation of ^{123}I emissions for an average-sized neck. For a cadaver

TABLE 1

Thyroid Probe Counts of 11.1-MBq Capsule of ^{123}I Without Attenuator, Within Neck Phantom, and Behind Cadaver Chest Wall

Object	Data
Background	115 counts/min
Capsule	1.581×10^6 counts/min
Capsule + neck phantom	1.290×10^6 counts/min
Capsule + chest wall	1.029×10^6 counts/min
Calculated attenuation	
Neck phantom	18%
Chest wall	35%

chest wall containing the sternum, the attenuation increased to 35%, essentially doubling.

The implication is that the thyroid uptake measurement is likely to be incorrect if a portion of the thyroid is substernal—a possibility that may be of consequence if the measurement is used to calculate ^{131}I doses for treating hyperthyroidism. Uptake measurements may be underestimated, leading to an increase in the calculated therapeutic dose. Administering doses of ^{131}I higher than necessary may lead to an increase in both short-term side effects and long-term unwanted consequences. It is even possible that, with uptake underestimation, the therapy will not be performed. This has a lower significance for the treatment of thyroid cancer with ^{131}I : most treated patients will have undergone thyroidectomy, and uptake measurements are used less frequently in this population.

How would this translate into therapy dose calculations? Presume that the thyroid has an uptake of 50% and the goal is to administer 370 MBq (10 mCi) for treatment of hyperthyroidism. The administered dose would be 740 MBq (20 mCi). In the situation of a normally positioned, cervical thyroid gland, no additional calculation is needed. The phantom simulates neck attenuation. In the second scenario, the thyroid gland is completely substernal. Uptake would be $[(1.00 - 0.35)/(1.00 - 0.18)]$, or 79% of what it would have been if the gland were normally positioned. The thyroid uptake would be measured as 0.50×0.79 , or 0.40. The administered dose would be 370 MBq (10 mCi)/0.40, or 925 MBq (25 mCi), rather than 740 MBq (20 mCi). If the thyroid uptake is lower, the effect is magnified. In the case of an uptake of 30%, the administered dose would rise from 370 MBq (10 mCi)/0.3, or 1,221 MBq (33 mCi), to 370 MBq (10 mCi)/(0.3 \times 0.79), or 1,554 MBq (42 mCi). This is a worst-case scenario. Most substernal glands are not completely behind the sternum, and measurement error would be less extreme.

Park et al., in an article (7) describing their study evaluating the ability of thyroid scintigraphy to detect intrathoracic glands, briefly mentioned that they measured 21% attenuation of ^{123}I photons through a fresh adult cadaver sternum. Details regarding how this was calculated were not provided.

There are several ways in which this analysis will differ from real-life scenarios. First, the thyroid gland is rarely located completely behind the sternum. The cadaver chest wall is an approximation of the chest wall of a living human. Its constituent tissue will not have identical attenuation coefficients. Finally, we used 1 cadaver specimen; chest walls in cadavers, as in living patients, come in many shapes and sizes. There is no phantom that can function as an exact representation of a patient. Our goal was to provide a rough idea of how severe the attenuation may be.

Another separate, though related, problem is that of improper aiming of the thyroid probe. The probe is a collimated device, and moving the target away from its center point will lower the count. It would be interesting to investigate the effect of malpositioning of a thyroid probe.

It is likely that many patients who undergo ^{131}I therapy will not have had their anatomy defined, and it will be unknown whether there is a substernal component of their thyroid gland. There are patients, however, in whom this is known. Patients may have had thyroid scintigraphy with a sternal marker performed before therapy. Some patients will have had a prior CT scan of their neck or chest. In this scenario, consideration might be given to lowering the treatment dose from what would have been administered otherwise. There are also CT-based methods to calculate the actual attenuation coefficient of the interceding chest wall using the thickness of the tissues, density calculation with Hounsfield units, and the mass attenuation coefficients of the tissues. The chest wall may include soft tissue, cortical bone, cancellous bone, marrow, and cartilage. It is highly doubtful that there would be benefit from this demanding calculation. We do not recommend actually performing a CT scan on hyperthyroid patients solely for this purpose. Our aim was to provide an understanding of the potential magnitude of the attenuation.

CONCLUSION

The standard neck phantom used in the routine calculation of radioactive thyroid uptake with ^{123}I will lead to an underestimation when a substernal goiter is present. The extent of error will differ from patient to patient, but on the basis of our evaluation, in the most extreme example the impact can be substantial. When it is known that the thyroid has a substernal component, practitioners should consider lowering therapeutic doses of ^{131}I when using uptake measurements for calculation.

DISCLOSURE

No potential conflict of interest relevant to this article was reported.

ACKNOWLEDGMENT

We thank James A. Reed III from the Department of Anatomy at the Geisel School of Medicine at Dartmouth for his assistance in this study.

REFERENCES

1. McDougall IR. The importance of obtaining thyroid uptake measurement in patients with hyperthyroidism. *Nucl Med Commun.* 1990;11:73–76.
2. Czepczyński R. Nuclear medicine in the diagnosis of benign thyroid diseases. *Nucl Med Rev Cent East Eur.* 2012;15:113–119.
3. Society of Nuclear Medicine and Molecular Imaging Practice Guideline: ACR-SNM-SPR guideline for the performance of thyroid scintigraphy and uptake measurements. 2009. http://s3.amazonaws.com/rndms-snm-mi/files/production/public/docs/Thyroid_Scintigraphy_1382732120053_10.pdf. Accessed August 5, 2021.
4. Huins CT, Georgalas C, Mehrzad H, Tolley NS. A new classification system for retrosternal goitre based on a systematic review of its complications and management. *Int J Surg.* 2008;6:71–76.
5. Newman E, Shaha A. Substernal goiter. *J Surg Oncol.* 1995;60:207–212.
6. Wang LS. Surgical management of a substernal goiter. *Formosan J Surg.* 2012;45:41–44.
7. Park HM, Tarver RD, Siddiqui AR, Schauwecker DS, Wellman HN. Efficacy of thyroid scintigraphy in the diagnosis of intrathoracic goiter. *AJR.* 1987;148:527–529.

Correlation of Lesional Uptake Parameters and Ratios with miPSMA Score and Estimating Normal Physiologic Concentration: An Exploratory Analysis in Metastatic Castration-Resistant Prostatic Carcinoma Patients with ^{68}Ga -PSMA-11 PET/CT

Ashwini Kalshetty^{1,2}, Biju Menon^{1,2}, Sutapa Rakshit^{1,2}, Atanu Bhattacharjee^{2,3}, and Sandip Basu^{1,2}

¹Radiation Medicine Centre, Bhabha Atomic Research Centre, Tata Memorial Centre Annexe, Mumbai, India; ²Homi Bhabha National Institute, Mumbai, India; and ³Department of Biostatistics, ACTREC, Tata Memorial Centre, Mumbai, India

The use of prostate-specific membrane antigen (PSMA)-based PET/CT has grown rapidly in recent years. This study estimated lesional uptake, normal physiologic concentrations, and temporal variation on delayed PET/CT of ^{68}Ga -PSMA-11 across different molecular imaging PSMA (miPSMA) expression scores in patients with metastatic castration-resistant prostatic carcinoma. **Methods:** We retrospectively studied 50 patients who were evaluated for ^{177}Lu -PSMA-targeted radioligand therapy and underwent ^{68}Ga -PSMA-11 PET/CT to determine disease status. Their mean age was 67.5 ± 8 y (52–84 y), and their average serum prostate-specific antigen level was $401 \pm 1,353$ ng/mL (0.098–9,235.13 ng/mL) at the time of scanning. They underwent standard ^{68}Ga -PSMA-11 PET/CT an average of 65 min after injection (60–90 min). Tumors ($n = 50$) were correlated with miPSMA expression score and uptake. Physiologic tracer distribution was estimated by placing a volume of interest 1 cm in diameter for smaller organs (submandibular, parotid, lacrimal, and tubarial glands; renal cortices; blood pool; and bowel) and 3 cm for larger organs (liver and spleen). SUV_{max} and SUV_{mean} were estimated for each region. Tumor-to-spleen (T/S), tumor-to-liver (T/L), and tumor-to-parotid (T/P) ratios were calculated for each lesion. For 16 patients who underwent a delayed scan an average of 135 min after injection (120–150 min), additional analysis evaluated the effect of the delay.

Results: Uptake was maximal in renal cortices, followed by salivary glands, bowel, spleen, liver, lacrimal glands, and blood pool. SUV_{max} averaged 37.7 ± 22.1 for renal cortices, 15.4 ± 7.3 for submandibular glands, 14.4 ± 7.1 for parotid glands, 9.4 ± 4.9 for spleen, 6.2 ± 3.7 for lacrimal glands, 5.9 ± 2.3 for liver, 5.3 ± 1.41 for tubarial glands, 13.8 ± 7.6 for bowel, and 2.4 ± 1.9 for blood pool. SUV_{max} averaged 10.33 ± 3.27 (6.46–17) for miPSMA expression score 2 and 38.21 ± 25.9 (7.68–119.08) for score 3. T/S and T/P ratios averaged 1.21 ± 0.44 (0.48–2.04) and 0.6 ± 0.18 (0.39–0.87), respectively, for score 2 and 5.05 ± 4.46 (1.25–20.89) and 3.15 ± 2.09 (1.06–9.45), respectively, for score 3. SUV_{max} for score 3 lesions averaged 18.85, which increased significantly to 26.24 on delayed imaging ($P = 0.0001$). However, T/L, T/S, and T/P ratios did not significantly change. Temporal variation in normal organs showed SUV_{max} to increase significantly on delayed scans for

salivary (submandibular and parotid) and lacrimal glands and renal cortices, whereas SUV_{mean} increased significantly for spleen; liver; and parotid, tubarial, and lacrimal glands and insignificantly for other organs. **Conclusion:** These data form a basis for a proposed consensus on standard reference ranges for quantitative ^{68}Ga -PSMA-11 PET/CT. The temporal variations should be kept in mind for delayed acquisitions; T/S, T/L, and T/P ratios might serve as better markers for such scenarios.

Key Words: ^{68}Ga -PSMA-11 PET/CT; miPSMA score; ^{177}Lu -PSMA-617; metastatic castration-resistant prostate carcinoma; peptide receptor radioligand therapy; PSA

J Nucl Med Technol 2021; 49:235–240

DOI: 10.2967/jnmt.120.261289

Prostate-specific membrane antigen (PSMA)-labeled radioligands for PET/CT imaging in patients with prostate carcinoma have brought about a major change in the management of the disease. Furthermore, the recent introduction of PSMA-targeted radionuclide therapy for castration-resistant prostatic carcinoma patients has opened new areas of application for the theranostic pair for diagnosis and treatment, upholding the great promise of precision oncology. The role of PET/CT targeting of PSMA expression is well documented for staging and for detecting recurrence even in those with low serum prostate-specific antigen levels (1). Because of the high sensitivity and specificity of PSMA PET/CT, its use is currently expanding at various stages during the course of the disease.

The recently published PROMISE study has set guidelines for standard miTNM staging on PET/CT (2). Qualitative image assessment systems such as the molecular imaging PSMA (miPSMA) expression score are proposed as robust tools for defining objectivity in interpretation and staging (2,3), though they have yet to be validated for routine clinical use and their reproducibility in larger samples are yet to be tested. The miPSMA expression score takes into account the visual intensity of lesions relative to normal

Received Dec. 2, 2020; revision accepted Mar. 26, 2021.

For correspondence or reprints, contact Sandip Basu (drsanb@yahoo.com).

Published online July 9, 2021.

COPYRIGHT © 2021 by the Society of Nuclear Medicine and Molecular Imaging.

tracer uptake in internal reference organs such as the liver or parotid glands. Confirmation of normal biodistribution with the known range objectively can serve as an in vivo method of quality control as well as validate the observations made in the proposed scoring system, and there is a relative paucity of data on this topic, especially the temporal variation in such uptake (4–6). In this study, we attempted first to reproduce the reference ranges of ^{68}Ga -PSMA-11 in a subset of prostate carcinoma patients and subsequently to observe the correlation of miPSMA expression scores with various objective parameters such as SUV_{max} , tumor-to-spleen (T/S) ratio, tumor-to-liver (T/L) ratio, and tumor-to-parotid (T/P) ratio to supplement subjective observations and correlate semiquantitative values with miPSMA scores.

MATERIALS AND METHODS

In total, 50 patients with metastatic castration-resistant prostatic carcinoma who were being investigated for the feasibility of ^{177}Lu -PSMA-targeted radioligand therapy and underwent ^{68}Ga -PSMA-11 PET/CT either for staging or restaging in the past 2 y were retrospectively analyzed. The institutional medical ethics committee approved this retrospective study, and the requirement to obtain informed consent was waived. From the patient's medical records, we noted various general and clinical data such as patient age, Gleason score, history of surgery, history of prior therapy (hormonal therapy, chemotherapy, radiotherapy, or ^{177}Lu -PSMA-targeted radioligand therapy), and recent prostate-specific antigen levels. The mean age of the patients was 67.5 ± 8 y (range, 52–84 y), and the mean serum prostate-specific antigen level was $401 \pm 1,353$ ng/mL (range, 0.098–9,235.13 ng/mL) at the time of PET/CT scanning. The Gleason score was categorized as per the International Society of Urological Pathology Consensus grading, into 5 groups (7). The overall patient characteristics are described in Table 1.

PET/CT Acquisition Protocol

After appropriate preparation and quality control testing of the radiotracer, ^{68}Ga -PSMA-11, the patients were administered an average dose of 103.23 ± 22.2 MBq (range, 74–166.5 MBq) and 2 mL of furosemide (10 mg/mL) intravenously. After the injection, the patients were asked to drink an oral contrast medium (10 mL of sodium amidotrizoate and meglumine amidotrizoate [Urografin; Bayer]) diluted in 1 L of water within 1 h for optimal contrast in the abdominal pelvic region. The patients were asked to void before imaging to reduce urinary bladder activity, and whole-body scans were acquired at 65 min, on average (range, 60–80 min), after injection of the radiotracer. A subgroup of 16 patients underwent delayed scanning 135 min after injection, on average (120–150 min), after consenting to the procedure.

The PET/CT scans were acquired using a Philips Gemini TF 16 PET/CT scanner. A CT surviue (90 kV, 20 mA) followed by a CT scan (100 mA; 120 kV; field of view, ~ 600 mm; CT slice thickness, 2.0 mm; standard resolution; collimation, 16×1.5 ; pitch, 0.813; matrix, 512×512) was performed for PET attenuation correction. After CT, whole-body PET was performed in 3-dimensional mode at 8–10 bed positions, with a 2-min emission per bed position, from the mid thighs to the base of the skull in the arms-up position.

TABLE 1
Patient Characteristics and Previous Therapies

Parameter	Data
Age (y)	
Mean \pm SD	67.5 ± 8
Range	52–84
Serum prostate-specific antigen (ng/mL)	
Mean \pm SD	$401 \pm 1,353$
Range	0.098–9,235.13
Gleason score	
Group 1	1
Group 2	6
Group 3	9
Group 4	17
Group 5	17
Surgery (prostatectomy \pm orchidectomy) (n)	
Yes	50 (100%)
No	0 (0%)
Hormonal treatment (n)	
Yes	46 (92%)
No	4 (8%)
Chemotherapy (n)	
Yes	39 (78%)
No	11 (22%)
External-beam radiation therapy (n)	
Yes	24 (48%)
No	26 (52%)
^{177}Lu -PSMA therapy (n)	
Yes	16 (32%)
No	34 (68%)
Initial staging (n)	
Yes	11 (22%)
No	39 (78%)
Restaging (n)	
Yes	45 (90%)
No	5 (10%)

Images were reconstructed using a standard iterative algorithm based on the 3-dimensional row-action maximum-likelihood algorithm. The ^{68}Ga -PSMA PET/CT data were evaluated in a dedicated Philips EBW workstation.

Volume-of-Interest Measurements

The physiologic tracer biodistribution was assessed in each patient by placing spherical volumes of interest. These had a diameter of 1 cm for smaller organs (renal cortex, submandibular glands, parotid glands, lacrimal glands, the newly described tubarial glands (8), blood pool [abdominal and thoracic aorta], and bowel) and 3 cm for larger organs (liver and spleen). SUV_{max} and SUV_{mean} for each organ were estimated (average of 2 measurements for smaller organs and 3 for larger). The schematics of measurement are illustrated in Figure 1.

For the first part of the study, in which the miPSMA score was correlated with SUV, only the most intense lesion per patient was selected. In the second part, in which temporal analysis was performed on a smaller cohort, additional lesions per patient were considered to observe the trend in the delayed imaging. These lesions were considered in the following order: primary, nodes, bone (1 or 2), and then other soft-tissue metastases. All these lesions were closer in intensity to the index lesions measured in the first part.

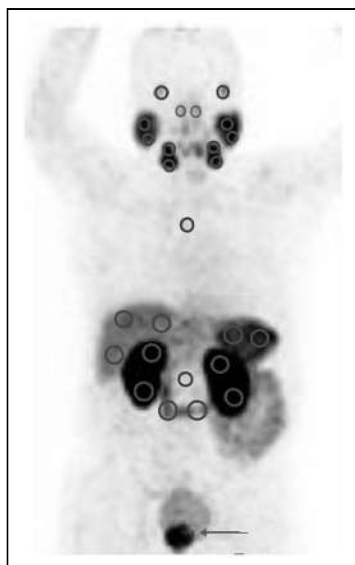


FIGURE 1. Schema for drawing volumes of interest adopted in this study. Arrow marks primary lesion in prostate.

In the subgroup of patients with additional delayed scans, we noted the same quantitative parameters in all regions in a similar manner. The lesions with maximum intensity in each scan was marked as the index lesion ($n = 50$). We used a fixed 1-cm volume of interest for measuring the SUV_{max} of such lesions. We measured additional lesions for the subgroup temporal analysis, amounting to total of 40 lesions. The miPSMA score was used for classifying the lesions as per the PROMISE trial (2).

We noted the SUV_{max} of all individual lesions against their grades. Apart from the directly measured

SUV_{max} of these lesions, we also estimated T/P, T/S, and T/L ratios. For the subgroup of patients who underwent additional delayed imaging, the temporal variation in these parameters was analyzed.

Statistical Analysis

Continuous data were represented as mean with SD. All data were verified for normal distribution. Groups with equal variance were tested for any significant difference between them using a paired t test. The unpaired t test was used for groups with unequal variance. A P value of less than 0.05 was considered significant.

RESULTS

Physiologic Uptake

The SUV_{max} and SUV_{mean} of the organs with physiologic uptake are represented as average values with their SD, shown in Table 2. The renal cortices showed the highest SUV_{max} and SUV_{mean} , followed by salivary glands, bowel, spleen, lacrimal glands, liver, and blood pool. The mean SUV_{max} was 37.72 ± 22.1 for the renal cortices, $15.44 \pm$

7.34 for the submandibular glands, 14.36 ± 7.05 for the parotid glands, 13.81 ± 7.6 for the bowel, 9.33 ± 4.98 for the spleen, 6.16 ± 3.68 for the lacrimal glands, 5.89 ± 2.32 for the liver, 5.3 ± 1.41 for the tubarial glands, and 2.36 ± 1.95 for the blood pool. A chart of the average SUV_{mean} and SUV_{max} for these regions is shown in Figure 2.

Tumor Lesions

When the lesions were classified as per the miPSMA expression score, we got primarily 2 categories, namely scores 2 and 3, as the patients at our center had been referred primarily to assess for ^{177}Lu -PSMA-targeted radioligand therapy feasibility and in that context had overt disease. The averages of SUV_{max} , T/S ratio, T/L ratio, and T/P ratio in each PSMA expression category were recorded. It appeared that score 3 lesions showed a mean of 3 times the PSMA expression of the parotid glands and 5 times than that of the spleen (Table 3). The presentation and the relative comparison of SUV_{max} , T/S ratio, T/L ratio, and T/P ratio for each category of lesions (scores 2 and 3) are illustrated in Figure 3. We performed unpaired t tests for these 2 scores of PSMA expression and found significant differences for all parameters (Table 3).

Temporal Variation in Uptake

The subgroup of 16 patients with paired early and delayed scan data also passed normality tests. Hence, paired t testing was performed.

Temporal Variation in Normal-Organ Physiologic Uptake

The paired t test assessed the variation in SUV_{mean} and SUV_{max} between the first and second scan groups. The average SUV_{mean} and SUV_{max} for most organs remained similar on delayed images. SUV_{max} was significantly increased in the salivary (submandibular and parotid) and lacrimal glands and in the renal cortices, whereas SUV_{mean} was significantly increased in the spleen and liver and in the parotid, tubarial, and lacrimal glands. The average SUV_{mean} and SUV_{max} in both studies, with their respective P values, are presented in Table 4.

Temporal Variation in Tumor Lesions

In total, 40 prominent lesions were identified in the subgroup of 16 patients who had dual-time-point imaging for evaluating the temporal variation in values. After applying paired t tests, we observed that SUV_{max} was significantly different from the baseline PET/CT scan (an increase on the delayed scan; $P = 0.0001$), whereas there was no significant difference in the T/S, T/L or T/P ratios. The results are in Table 5, and the temporal variation in the lesional parameters is plotted in Figure 4.

DISCUSSION

PSMA-based PET/CT imaging and theranostics have brought about a major change in the understanding and management of prostate cancer (9–17). The incorporation of semiquantitative and quantitative information continues to evolve and has the potential to enhance the fundamental

TABLE 2
 SUV_{mean} and SUV_{max} for Normal Organs

Organ	SUV_{mean}	SUV_{max}
Liver	3.98 ± 1.74	5.89 ± 2.32
Spleen	6.71 ± 3.8	9.33 ± 4.98
Kidneys	24.13 ± 15	37.72 ± 22.1
Submandibular glands	9.16 ± 4.56	15.44 ± 7.34
Parotid glands	9.51 ± 5.08	14.36 ± 7.05
Lacrimal glands	2.64 ± 1.46	6.16 ± 3.68
Blood pool	1.52 ± 1.22	2.36 ± 1.95
Bowel	7.7 ± 4.34	13.81 ± 7.6
Tubarial glands	2.7 ± 1.97	5.3 ± 1.41

Data are mean \pm SD.

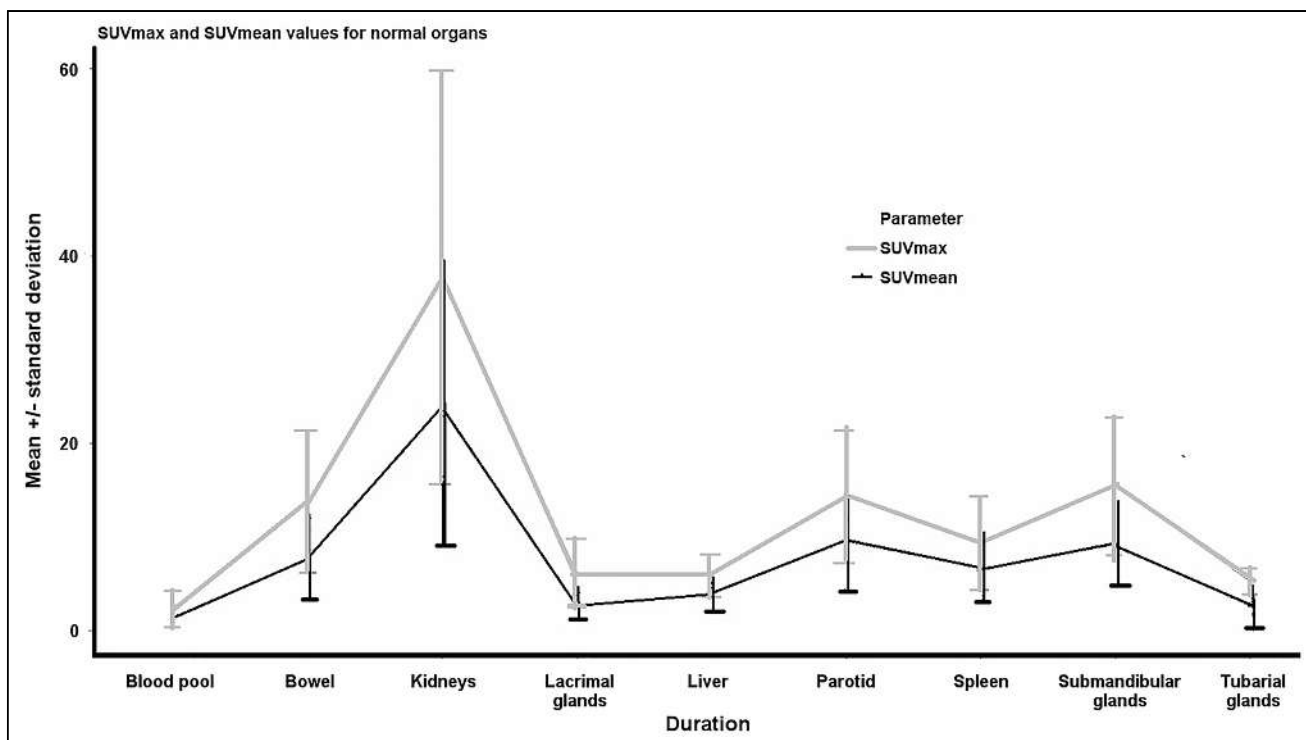


FIGURE 2. Average SUV_{max} and SUV_{mean} for different organs.

understanding of tumor heterogeneity, in vivo kinetics, and response to various therapies and hence can be a valuable supplement to visual interpretation and of paramount importance for undertaking clinical research (9,10,13,17). The present study analyzed ^{68}Ga -PSMA-11, the most common PET tracer used in prostate cancer diagnostics currently. Our results for the physiologic uptake align with some of the previously reported studies (4–6). Thus, we believe the present study results would allow a consistent pattern of reference range to be generated as a standard reference for future studies and research.

The miPSMA score as proposed by Eiber et al. (2) gives an elaborate description of miTNM staging on PSMA-based PET/CT. It is based on assigning a visual score from 0 to 3, with internal organs as reference points. When physiologic uptake is used as an internal reference for a scoring system, the ligand and biodistribution in the presence of high-volume disease have to be kept in mind and interpreted accordingly. The demonstration of SUV_{max} and its capacity to differentiate grades of lesions can elicit the incremental benefit of objective evidence to accurately assign the score.

Furthermore, to date, only a few studies have compared and addressed intra- and interpatient variability with ^{68}Ga - and ^{18}F -labeled PSMA ligands, with the recommendation of using the spleen as the reference organ for ^{18}F -PSMA-1007 (2,4–6). Besides these variations, other factors that also can influence uptake parameters, such as patient weight, injected dose, and wait duration, have not been conclusively studied. Hence, additionally, in the present study, we evaluated the effect of delayed imaging on SUV_{max} and SUV_{mean} in normal

organs, as well as SUV_{max} , T/S ratio, T/L ratio, and T/P ratio for tumor lesions.

In our study, the renal cortices showed the highest SUV_{max} and SUV_{mean} , followed by the salivary glands, bowel, spleen, lacrimal glands, liver, and blood pool. ^{68}Ga -PSMA-11 has been known to demonstrate high renal uptake, as stated in the literature, similar to the results obtained in our study (4–6). However, the maximum uptake in the kidneys was slightly higher in previous studies (4–6).

With respect to the temporal variation in normal physiologic uptake, SUV_{max} showed a significant increase on delayed scans in the salivary (submandibular and parotid) and lacrimal glands and in the renal cortices, whereas SUV_{mean} was significantly increased in the spleen and liver and in the parotid, tubarial, and lacrimal glands. In one

TABLE 3
Comparative Uptake Values and Ratios of Lesions

Parameter	Score of 2	Score of 3	P
Sample size (n)	11	39	
Average SUV_{max}	10.33 ± 3.27	38.2 ± 25.92	0.0009
SUV_{max} range	6.46–17.00	7.6–119.08	
Average T/S	1.21 ± 0.44	5.05 ± 4.46	0.0068
T/S range	0.48–2.04	1.25–20.89	
Average T/L	1.67 ± 0.46	6.98 ± 3.85	0.00004
T/L range	1.2–2.4	1.4–16.56	
Average T/P	0.61 ± 0.18	3.15 ± 2.09	0.00021
T/P range	0.39–0.87	1.06–9.45	

Data are mean \pm SD or range.

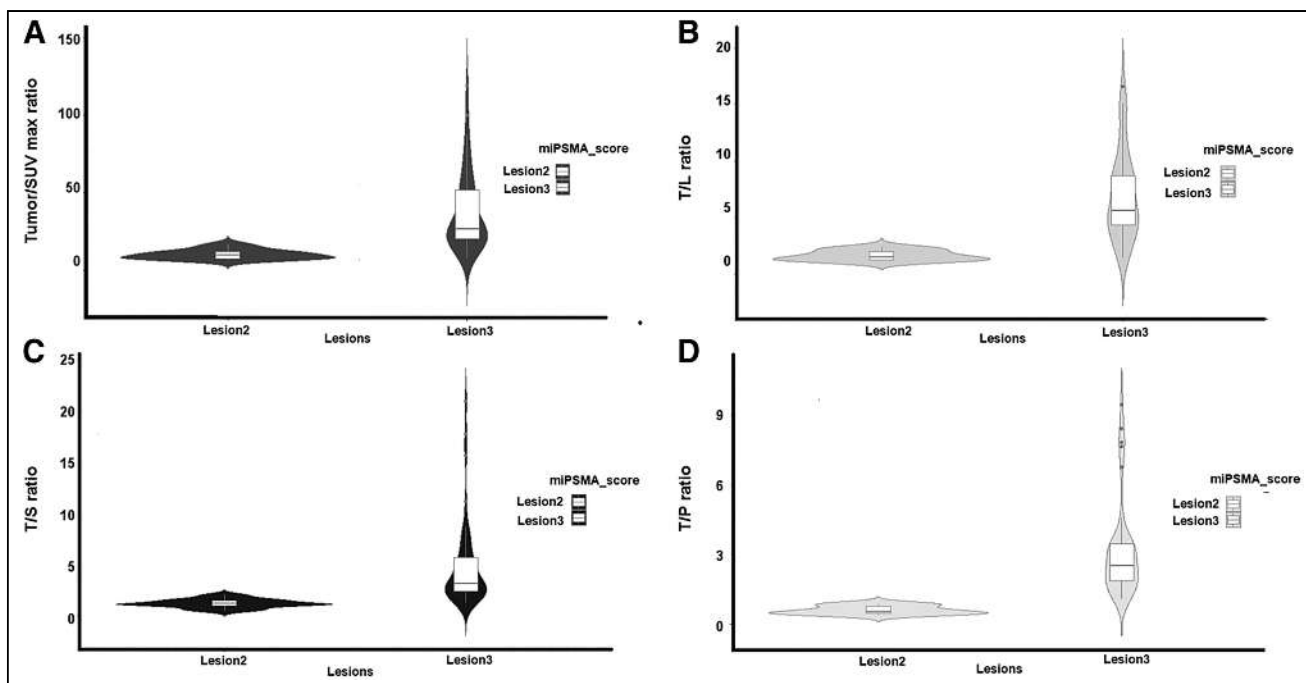


FIGURE 3. SUV_{max}, T/L ratio, T/S ratio, and T/P ratio for lesion2 and lesion3. Color version of this figure is available as supplemental file at <http://tech.snmjournals.org>.

TABLE 4
Comparative Temporal Variation of Mean SUV of Normal Organs with Their *P* Values

Organ	SUV _{mean}	SUV _{max}	SUV _{mean} delayed	SUV _{max} delayed	SUV _{mean} <i>P</i>	SUV _{max} <i>P</i>
Liver	3.6	5.9	3.1	6.7	0.0222	0.14
Spleen	6.5	9.4	5.8	9.1	0.0001	0.594
Kidneys	20.1	35.7	21.5	41.7	0.095	0.016
Submandibular glands	7.4	13.4	8.1	16.6	0.541	0.002
Parotid glands	7.1	12.9	8.5	14.1	0.047	0.037
Lacrimal glands	4.2	8.1	4.5	8.3	0.0267	0.01
Aorta	1.33	2.2	2.1	2.1	0.411	0.914
Bowel	5.5	9.7	5.4	10.9	0.41	0.44
Tubarial glands	2.87	5.55	3.3	6.06	0.02	0.08

previous study, no correlation was found between the uptake time and ^{68}Ga -PSMA-11 SUV_{peak} in the liver (4). The semi-quantitative measurements in our study have additionally demonstrated that the temporal variation in uptake is especially significant for lesions as well. Although the SUV_{max} of lesions as a standalone parameter varied significantly with time, the T/S and T/P ratios did not show a significant change. This observation would indicate that such temporal variations need to be kept in mind while interpreting images with delayed acquisitions and that T/S, T/L, or T/P ratio may be considered better parameters. The other area in which these values can have potential implications is treatment response assessment: the role of the quantitative parameters with receptor-based PET/CT continues to be in a development phase, and the various SUVs and ratios and their correlation with visual scoring can be useful for this purpose.

The limitations of this study are related to its retrospective nature, the limited number of cases, and its use of a

TABLE 5
Paired *t* Test Mean Values for Temporal Variation of Lesional Parameters Between Early and Delayed Images

Parameter	Early imaging	Delayed imaging	Paired <i>t</i> test <i>P</i>
SUV _{max}	18.85	26.24	0.0001
T/L ratio	5.9	6.65	0.45
T/S ratio	12.89	14.12	0.84
T/P ratio	9.36	9.05	0.62

single-center source. We did not study the effect of, or variations in, SUV normalized by lean body mass, which has been postulated to be a more robust parameter for quantitative analysis (18). Our study aimed to establish a reference range for normal organs; however, coexisting pathologies in reference organs, though rare in a given case scenario, are possible (e.g., splenic hemangioma). When present, they would need to be validated, and outliers can be

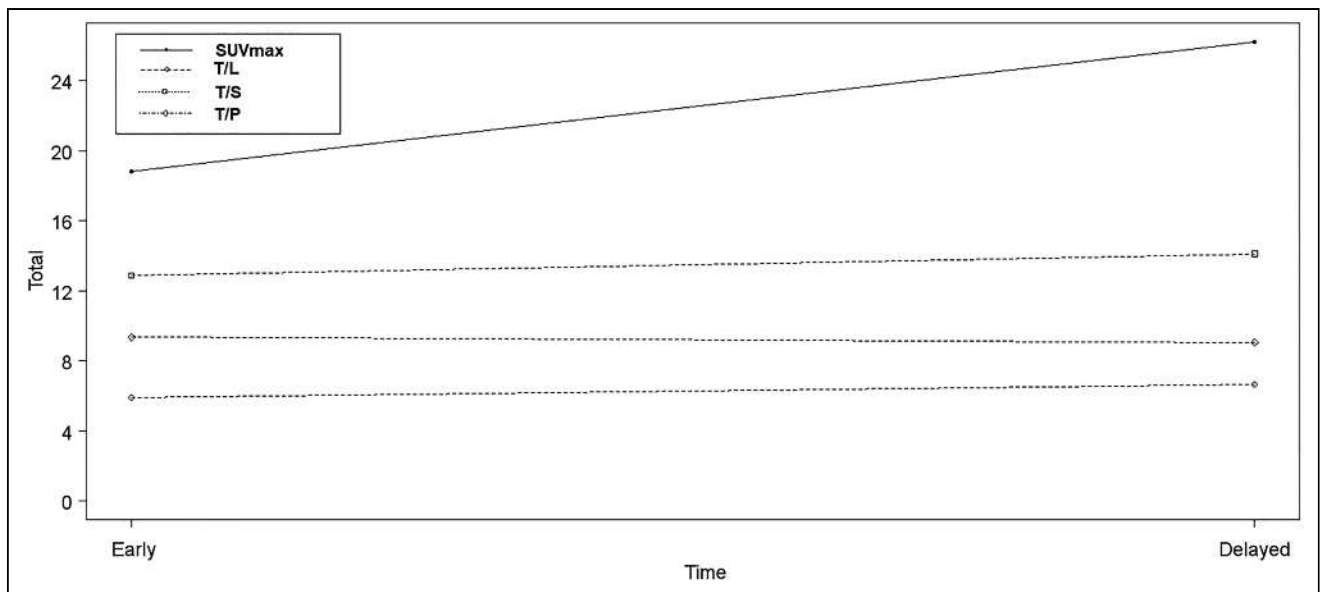


FIGURE 4. Comparison of SUV_{max}, T/L ratio, T/S ratio, and T/P ratio between scores 2 and 3.

identified. In the present study, the ratios were generated from a holistic perspective rather than a particular case in isolation. As standardization of such reference values becomes acceptable, we can get a general idea on distinguishing between normal and abnormal. We also have to mention that partial-volume effect was not considered in lesion selection in this analysis; the SUV and visual score of a very small lesion may be underestimated because of the partial-volume effect.

CONCLUSION

The reference ranges of normal organs (physiologic uptake) and tumor lesions for uptake and ratios for miPSMA scores of 2 and 3 were documented and established in the present study. On the basis of these data, a consensus on standard reference ranges can be generated for quantitative ⁶⁸Ga-PSMA-11 PET/CT. The temporal variation trends in lesions and reference organs should be kept in mind for delayed acquisitions. T/S, T/L, or T/P ratios serve as better markers for such scenarios.

DISCLOSURE

No potential conflict of interest relevant to this article was reported.

REFERENCES

- Fendler WP, Eiber M, Beheshti M, et al. ⁶⁸Ga-PSMA PET/CT: joint EANM and SNMMI procedure guideline for prostate cancer imaging—version 1.0. *Eur J Nucl Med Mol Imaging*. 2017;44:1014–1024.
- Eiber M, Herrmann K, Calais J, et al. Prostate cancer molecular imaging standardized evaluation (PROMISE): proposed miTNM classification for the interpretation of PSMA-ligand PET/CT. *J Nucl Med*. 2018;59:469–478.
- Rowe SP, Pienta KJ, Pomper MG, Gorin MA. PSMA-RADS version 1.0: a step towards standardizing the interpretation and reporting of PSMA-targeted PET imaging studies. *Eur Urol*. 2018;73:485–487.
- Ferreira G, Iravani A, Hofman MS, Hicks RJ. Intra-individual comparison of ⁶⁸Ga-PSMA-11 and ¹⁸F-DCFPyL normal-organ biodistribution. *Cancer Imaging*. 2019;19:23.
- Prasad V, Steffen IG, Diederichs G, Makowski MR, Wust P, Brenner W. Biodistribution of [⁶⁸Ga]PSMA-HBED-CC in patients with prostate cancer: characterisation of uptake in normal organs and tumour lesions. *Mol Imaging Biol*. 2016;18:428–436.
- Demirci E, Sahin OE, Ocak M, Akovali B, Nematyazar J, Kabasakal L. Normal distribution pattern and physiological variants of ⁶⁸Ga-PSMA-11 PET/CT imaging. *Nucl Med Commun*. 2016;37:1169–1179.
- Epstein JI, Egevad L, Amin MB, Delahunt B, Srigley JR, Humphrey PA; Grading Committee. The 2014 International Society of Urological Pathology (ISUP) Consensus Conference on Gleason Grading of Prostatic Carcinoma: definition of grading patterns and proposal for a new grading system. *Am J Surg Pathol*. 2016;40:244–252.
- Valstar MH, de Bakker BS, Steenbakkers RJHM, et al. The tubarial salivary glands: a potential new organ at risk for radiotherapy. *Radiother Oncol*. 2021;154:292–298.
- Demirci E, Kabasakal L, Şahin OE, et al. Can SUVmax values of Ga-68-PSMA PET/CT scan predict the clinically significant prostate cancer? *Nucl Med Commun*. 2019;40:86–91.
- Brito AET, Mourato FA, de Oliveira RPM, Leal ALG, Filho PJA, de Filho JLL. Evaluation of whole-body tumor burden with ⁶⁸Ga-PSMA PET/CT in the biochemical recurrence of prostate cancer. *Ann Nucl Med*. 2019;33:344–350.
- Miksch J, Bottke D, Krohn T, et al. Interobserver variability, detection rate, and lesion patterns of ⁶⁸Ga-PSMA-11-PET/CT in early-stage biochemical recurrence of prostate cancer after radical prostatectomy. *Eur J Nucl Med Mol Imaging*. 2020;47:2339–2347.
- Stone L. Predicting ⁶⁸Ga-PSMA-PET-CT positivity for recurrent disease. *Nat Rev Urol*. 2018;15:137.
- Verburg FA, Pfister D, Drude NI, Mottaghy FM, Behrendt FF. PSA levels, PSA doubling time, Gleason score and prior therapy cannot predict measured uptake of [⁶⁸Ga]PSMA-HBED-CC lesion uptake in recurrent/metastatic prostate cancer. *Nuklearmedizin*. 2017;56:225–232.
- Cem O, Torun N, Guler OC, Reyhan M, Yildirim BA, Yapar AF. Is there a correlation between Gleason score and maximum standardized uptake value in locally advanced prostate cancer patients? [abstract]. *J Clin Oncol* 2019 37(suppl):68.
- van Leeuwen PJ, Donswijk M, Nandurkar R, et al. Gallium-68-prostate-specific membrane antigen (⁶⁸Ga-PSMA) positron emission tomography (PET)/computed tomography (CT) predicts complete biochemical response from radical prostatectomy and lymph node dissection in intermediate- and high-risk prostate cancer. *BJU Int*. 2019;124:62–68.
- Jansen BHE, Kramer GM, Cysouw MCF, et al. Healthy tissue uptake of ⁶⁸Ga-prostate-specific membrane antigen, ¹⁸F-DCFPyL, ¹⁸F-fluoromethylcholine, and ¹⁸F-dihydrotestosterone. *J Nucl Med*. 2019;60:1111–1117.
- Onal C, Guler OC, Torun N, Reyhan M, Yapar AF. The effect of androgen deprivation therapy on ⁶⁸Ga-PSMA tracer uptake in non-metastatic prostate cancer patients. *Eur J Nucl Med Mol Imaging*. 2020;47:632–641.
- Gafita A, Calais J, Franz C, et al. Evaluation of SUV normalized by lean body mass (SUL) in ⁶⁸Ga-PSMA11 PET/CT: a bi-centric analysis. *EJNMMI Res*. 2019;9:103.

Effect of Diet on Physiologic Bowel ^{18}F -FDG Uptake

Bahar Moasses-Ghafari¹, Babak Fallahi², Armaghan Fard Esfehiani², Mohammad Eftekhari², Khaled Rahmani³, Arash Eftekhari⁴, and Parham Geramifar²

¹Kurdistan University of Medical Sciences, Sanandaj, Iran; ²Research Center for Nuclear Medicine, Shariati Hospital, Tehran University of Medical Sciences, Tehran, Iran; ³Social Determinants of Health Research Center, Kurdistan University of Medical Sciences, Sanandaj, Iran; and ⁴Diagnostic Radiology/Nuclear Medicine, Surrey Memorial Hospital and Jim Pattison Outpatient Care and Surgery Centre, Surrey, British Columbia, Canada

Intestinal ^{18}F -FDG uptake is variable in whole-body PET/CT. In cancer patients, particularly those suspected of relapse or metastasis, ^{18}F -FDG absorption might interfere with scan interpretation. This study evaluated the effect of diet on intestinal ^{18}F -FDG absorption.

Methods: In total, 214 patients referring for oncologic ^{18}F -FDG PET/CT participated. They were randomly divided into 2 groups and asked to follow either a routine diet (RD) or a low-carbohydrate, high-fat diet (LCHFD) for 24 h before the study. The small bowel and different parts of the colon (the cecum; the ascending, transverse, and descending segments; and the hepatic and splenic flexures) were evaluated and visually interpreted by nuclear medicine experts. Bowel uptake was graded through comparison with that in the liver as absent, mild, moderate, or severe. **Results:** Significantly higher ^{18}F -FDG uptake in the descending colon ($P = 0.001$) and small intestine ($P = 0.01$) was observed in the RD group than in the LCHFD group. After patients with bowel cancer were omitted from the statistical analysis, no significant differences in the final results were seen. **Conclusion:** An LCHFD for 24 h before ^{18}F -FDG PET imaging resulted in lower ^{18}F -FDG uptake in the descending colon and small bowel than did an RD, assisting the interpreting physician by reducing the intestinal activity interference for more accurate diagnostic interpretation.

Key Words: diet; bowel physiologic ^{18}F -FDG uptake; oncologic PET/CT imaging

J Nucl Med Technol 2021; 49:241–245

DOI: 10.2967/jnmt.120.257857

PET/CT is one of the most useful imaging modalities for metabolism studies at the cellular and molecular levels. Among imaging procedures, PET/CT is substantially superior for diagnosis, staging, restaging, and prognostic evaluation of oncologic patients. ^{18}F -FDG is the most common radioisotope used worldwide for PET/CT in malignant diseases (1), but a normal distribution of ^{18}F -FDG distribution based on glucose metabolism can also be seen in other organs, including brain, myocardium, kidneys, urinary bladder, and bowel (1,2).

Methods for suppressing myocardial ^{18}F -FDG uptake in oncologic patients have been previously reported (3–5). To our knowledge, however, no study has been conducted to determine the effects of diet on bowel ^{18}F -FDG uptake, the importance of which cannot be underestimated in the interpretation of PET/CT results for the abdomen and pelvis.

Previous researchers attempted to minimize physiologic ^{18}F -FDG uptake throughout the body by focusing mainly on reducing myocardial ^{18}F -FDG uptake through a low-carbohydrate high-fat diet (LCHFD) or prolonged fasting (4,5). The few studies that have been performed to control bowel ^{18}F -FDG uptake have focused on the effect of bowel preparation (6) and on classification of uptake and its potential interference with scan interpretation for abdominal–pelvic (mainly colon) cancer (7,8). Therefore, we decided to design a study to evaluate the effect of an LCHFD diet on intestinal ^{18}F -FDG uptake.

MATERIALS AND METHODS

In total, 214 patients older than 18 y (107 men and 107 women; age range, 18–84 y) with suspicion of, or proven, malignancies were enrolled. The protocol was evaluated and approved by the Institutional Research Ethics Committee, and the study plan was fully explained to the patients and written informed consent was obtained from all. PET/CT was requested at different stages of the disease. Exclusion criteria included a serum glucose level of more than 200 mg/dL at the time of radiotracer injection, failure to fast, known bowel disease, or pathologic bowel ^{18}F -FDG uptake interfering with physiologic bowel activity.

Patients were randomly assigned into 2 groups, with one group taking a routine diet (RD) and the other an LCHFD for 24 h before the ^{18}F -FDG PET/CT scan. All patients received the required details about their diet and were instructed to fast for at least 6 h before the study. Foods in the LCHFD included boiled eggs, grilled beef, fried chicken, and vegetables, and for 24 h before the study any carbohydrate-containing beverages or meals were avoided. PET/CT was performed on a Biograph TruePoint 6 (Siemens) approximately 60 min after intravenous administration of 392 ± 63 MBq (10.6 ± 1.7 mCi) of ^{18}F -FDG according to body weight (5.2 MBq/kg [0.14 mCi/kg]). The PET image reconstruction protocol included 4 iterations per 21 subsets, a 5-mm gaussian postsmoothing filter, and a 168×168 matrix, using the point-spread-function–based reconstruction algorithm TrueX. The protocol was set at 3 min/bed position as the default and 4 min/bed position in patients with a body mass

Received Sep. 30, 2020; revision accepted Mar. 26, 2021.
For correspondence or reprints, contact Parham Geramifar (pgeramifar@tums.ac.ir).

Published online July 9, 2021.

COPYRIGHT © 2021 by the Society of Nuclear Medicine and Molecular Imaging.

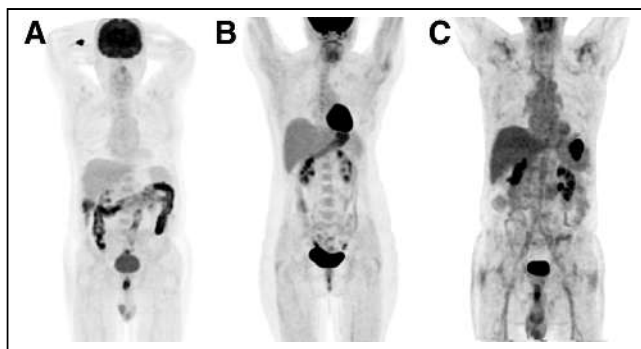


FIGURE 1. Grading bowel uptake by comparing it with that of liver as severe (more than liver) (A), moderate (equal to liver) (B), or mild (less than liver) (C).

index of more than 35. Low-dose CT (50 mA, 110 – 130 kV) was applied for attenuation correction.

^{18}F -FDG uptake was visually evaluated by 2 nuclear medicine physicians, who graded the uptake in the small intestine and different parts of the large bowel, including the ascending, transverse, and descending segments; the cecum; and the hepatic and splenic flexures. In cases of disagreement, a third specialist's opinion was the criterion for decision making. The intensity of uptake in the small intestine and in the various colon segments, in comparison to liver uptake (Fig. 1), was classified as absent, mild (less than liver), moderate (equal to liver), or severe (more than liver).

Statistical analyses were conducted using SPSS, version 22 (IBM), and an independent-sample t test, χ^2 test, or Fisher exact test was used to assess the relationship between the type of diet and the investigated outcome, including the intensity of ^{18}F -FDG uptake in the various bowel regions. A P value of less than 0.05 was considered statistically significant.

RESULTS

In total, 214 patients were enrolled, randomly divided into 2 groups. One group followed the RD, whereas the other thoroughly followed a 24-h LCHFD. Baseline data analysis of heart rate, blood pressure, and fasting blood sugar, besides

demographic characteristics consisting of sex, age, height, and weight, was done to ensure proper randomization of potential confounders in the study groups, and the demographic and baseline characteristics were balanced between the groups (Table 1).

The intensity of ^{18}F -FDG uptake in the different segments of colon is presented in the Table 2. Significantly higher ^{18}F -FDG uptake was observed in the descending colon and small intestine after the RD than after the LCHFD.

Thirty-four patients with a history of colon cancer were removed from the statistical analysis. The intensity of ^{18}F -FDG uptake in the descending colon and small intestine was lower in the LCHFD group than in the RD group, whereas no remarkable difference in ^{18}F -FDG uptake in other segments of the colon was noted between the 2 groups (Table 3).

As shown in Table 2, significantly higher ^{18}F -FDG uptake in the descending colon and small intestine was observed in the RD group than in the LCHFD group.

DISCUSSION

Epidemiologic studies have shown that colon cancer is the third most lethal cancer in the world, after prostate and lung cancer in men and after breast and lung malignancies in women (9,10).

The choice of colon cancer treatment depends on multiple factors, including the patient's basic health status and the size, location, and extent of the tumor. Surgery is the most commonly used therapy, depending on the size and extent of the tumor (9,10). PET/CT is an appropriate diagnostic tool for evaluating the regional or distant tumor extension and, accordingly, has a vital clinical effect on patients' management at different stages of the disease. In cases of suspected tumor recurrence or liver metastasis, PET/CT is effective in deciding the feasibility of surgery. PET/CT is also much more useful than conventional imaging in decision making during monitoring of the response to a given therapy.

Physiologic ^{18}F -FDG absorption in the small and large intestines can interfere with accurate interpretation and may

TABLE 1
Demographics and Baseline Characteristics of Subjects

Variable	RD	LCHFD	P
Age (y)	47.73 \pm 15.73	47.46 \pm 15.59	0.8
Weight (kg)	72.57 \pm 14.85	70.57 \pm 14.16	0.6
Height (cm)	167.90 \pm 9.79	166.67 \pm 9.66	0.9
Systolic blood pressure (mm Hg)	119.95 \pm 15.68	116.93 \pm 13.94	0.7
Diastolic blood pressure (mm Hg)	79.04 \pm 8.81	77.51 \pm 7.80	0.3
Fasting blood sugar (mg/dL)	95.21 \pm 18.73	93.69 \pm 17.13	0.6
Heart rate (bpm)	80.35 \pm 9.24	80.67 \pm 9.06	0.5
^{18}F -FDG injected dose (MBq [mCi])	390.72 \pm 67.34 (10.56 \pm 1.82)	394.79 \pm 61.42 (10.67 \pm 1.66)	0.6
Sex (n)			0.7
Male	55 (51.4%)	52 (48.6%)	
Female	52 (48.6%)	55 (51.4%)	

Data are mean \pm SD.

TABLE 2
¹⁸F-FDG Distribution Patterns in Bowel Regions

Pattern of ¹⁸ F-FDG distribution	¹⁸ F-FDG uptake								<i>P</i>
	None		Mild		Moderate		Severe		
	RD	LCHFD	RD	LCHFD	RD	LCHFD	RD	LCHFD	
Cecum	0	0	83 (77.57)	84 (78.50)	1 (0.93)	0	23 (21.50)	23 (21.50)	0.6
Ascending colon	66 (61.68)	72 (67.29)	17 (15.89)	23 (21.50)	19 (17.76)	9 (8.41)	5 (4.67)	3 (2.80)	0.1
Transverse colon	89 (83.18)	97 (90.65)	9 (8.41)	7 (6.54)	8 (7.48)	3 (2.80)	1 (0.93)	0	0.2
Descending colon	9 (8.41)	31 (28.97)	59 (55.14)	53 (49.53)	29 (27.10)	18 (16.82)	10 (9.34)	5 (4.67)	<0.001
Hepatic flexure	0	0	92 (85.98)	92 (85.98)	0	1 (0.93)	15 (14.02)	14 (13.08)	0.5
Splenic flexure	0	1 (0.93)	90 (84.11)	87 (81.31)	0	0	17 (15.89)	19 (17.76)	0.5
Small intestine	18 (16.82)	28 (26.17)	71 (66.36)	73 (68.22)	18 (16.82)	5 (4.67)	0	1 (0.93)	0.01

mask true lesions or, conversely, cause a misdiagnosis and false-positive results. Control of intestinal ¹⁸F-FDG uptake is expected to reduce possible false-positive and false-negative results.

After our previous study leading to success in suppressing myocardial ¹⁸F-FDG uptake by an LCHFD (5), we were encouraged to test the effect of diet on intestinal ¹⁸F-FDG absorption. Interestingly, the application of an LCHFD versus an RD resulted in a significant reduction in ¹⁸F-FDG uptake in the descending colon and small intestine. To the best of our knowledge, no study has yet been conducted on the effect of an LCHFD on intestinal absorption. Considering the significant prevalence of colon cancer and the role of PET/CT in its management, the results of such a study ought to be extremely valuable in improving the quality of images of the abdominopelvic cavity in particular. The goal of our study was to investigate the effect of diet on reducing ¹⁸F-FDG uptake in the bowel.

In this well-controlled randomized trial, we attempted to illustrate changes in ¹⁸F-FDG uptake in the intestinal system when an LCHFD was used for patients' preparation. The LCHFD might not be suitable for vegetarians, but because the focus of the assessment was on carbohydrate restriction along with an LCHFD, plant protein foods (e.g., soy) can be used as a substitute for animal proteins in the given food list.

A significant statistical relationship was found between diet and ¹⁸F-FDG distribution in the descending colon and small intestine, and diet can be an effective controllable factor to reduce bowel ¹⁸F-FDG uptake.

Of the patients in the LCHFD group, 78.5% had no ¹⁸F-FDG absorption or had only mild uptake in the descending colon, and 94.4% also had no ¹⁸F-FDG uptake or mild absorption in the small intestine. Moderate to severe ¹⁸F-FDG absorption (equal to or greater than the liver activity) was present in 36.4% of patients in the RD group but only 21.5% in the LCHFD group. In general, moderate to severe intestinal ¹⁸F-FDG absorption was reported in 16.8% of patients in the RD group and 5.6% in the LCHFD group (*P* = 0.01).

The results of the study showed that an LCHFD regimen for 24 h before the scan shifted the ¹⁸F-FDG uptake by the small intestine and descending colon from moderate or severe to mild or absent. In a 2015 study, background bowel ¹⁸F-FDG uptake was evaluated in 326 female breast cancer patients who underwent ¹⁸F-FDG PET for primary staging, none of whom had hypertension or diabetes. Colon absorption was categorized (as low or high) on the basis of visual and quantitative assessments, and the average SUV_{max} in 8 segments of the intestine (duodenum, jejunum, ileum, cecum, hepatic flexure, splenic flexure, descending colon, and sigmoid) was reported as total-bowel SUV_{max}. Age,

TABLE 3
¹⁸F-FDG Distribution Patterns in Bowel Regions after Exclusion of Patients with History of Colon Cancer

Pattern of ¹⁸ F-FDG distribution	¹⁸ F-FDG uptake								<i>P</i>
	None		Mild		Moderate		Severe		
	RD	LCHFD	RD	LCHFD	RD	LCHFD	RD	LCHFD	
Cecum	0	0	74 (76.29)	66 (79.52)	1 (1.03)	0	22 (22.68)	17 (20.48)	0.6
Ascending colon	61 (62.89)	56 (67.47)	14 (14.43)	18 (21.69)	17 (17.53)	6 (7.23)	5 (5.15)	3 (3.61)	0.1
Transverse colon	80 (82.47)	76 (91.57)	8 (8.25)	5 (6.02)	8 (8.25)	2 (2.41)	1 (1.03)	0	0.2
Descending colon	8 (8.25)	24 (28.92)	53 (54.64)	44 (53.01)	26 (26.80)	11 (13.25)	10 (10.31)	4 (4.82)	<0.001
Hepatic flexure	0	0	82 (84.54)	73 (87.95)	0	1 (1.20)	15 (15.46)	9 (10.84)	0.37
Splenic flexure	0	1 (1.20)	81 (83.51)	68 (81.93)	0	0	16 (16.49)	14 (16.87)	0.5
Small intestine	17 (17.53)	22 (26.51)	62 (63.92)	56 (67.47)	18 (18.56)	4 (4.82)	0	1 (1.20)	0.02

fasting blood sugar, body mass index, triglycerides, cholesterol, high-density lipoprotein, and low-density lipoprotein were considered cardiometabolic related factors. Total-bowel SUV_{max} had a positive relationship with age, body mass index, triglycerides, cholesterol, and low-density lipoprotein and a negative relationship with high-density lipoprotein. Multivariate analysis represented that body mass index and triglycerides were independent factors associated with bowel ¹⁸F-FDG uptake. According to these results, high bowel ¹⁸F-FDG uptake on the PET scan could be due to changes in lipid metabolism and an increased risk of cardiometabolic disease in nondiabetic and nonhypertensive patients (11), whereas in our study, the limited use of glucose and increased lipid levels in the diet resulted in a significantly reduced ¹⁸F-FDG uptake in the small intestine and descending colon.

The first study on factors potentially influencing intestinal ¹⁸F-FDG absorption was conducted in 1998. In that study, age, sex, and bowel habits had an effect on ¹⁸F-FDG absorption; no relationship, however, was found between free fatty acid level and bowel ¹⁸F-FDG uptake. Moreover, female sex, older age, and constipation were associated with higher ¹⁸F-FDG uptake (12).

Insulin increases glucose uptake by enterocytes and consequently increases bowel absorption in diabetic patients (13–15). However, a wide range of intestinal ¹⁸F-FDG uptake was observed in nondiabetic subjects. Another study concluded that hypoglycemic oral agents such as metformin were considered a factor causing higher ¹⁸F-FDG uptake, to a significant extent in the colon and to a lesser extent in the small intestine (13–18). Furthermore, a study in 2017 revealed that metformin consumption remarkably increased colonic ¹⁸F-FDG absorption, but this increased absorption was independent of an increase in energy expenditure or core body temperature. In other words, there was no relationship between maximal colonic ¹⁸F-FDG uptake and energy expenditure or core body temperature (19).

With discontinuation of metformin 48 h before the scan in the diabetic patients of this study, the effect of metformin interference on bowel ¹⁸F-FDG uptake was eliminated and only the effect of diet on bowel uptake was investigated.

Recently, the probability that intestinal bacteria have a role in luminal ¹⁸F-FDG uptake has been raised, and treatment with rifaximin before PET has been proposed to reduce luminal ¹⁸F-FDG uptake. Rifaximin is likely to cause different degrees of ¹⁸F-FDG uptake through changing the population of the intestinal bacteria and by the altering the flora and host metabolism (20). Another study evaluated the effect of administering *N*-butylscopolamine to decrease bowel artifacts during ¹⁸F-FDG PET. The results revealed that *N*-butylscopolamine could potentially improve the quality of PET images and their reporting as well (21).

The Randle cycle describes a biochemical mechanism that maintains a cellular fuel metabolism balance between glucose and free fatty acid oxidation by which glucose oxidation is decreased in the presence of free fatty acids. The significance

of the glucose–fatty acid cycle is that it may introduce a new aspect to more precise hormonal control by adding a nutrient-mediated modification (22). This fact has been proven in that the consumption of each nutrient (glucose vs. fatty acid) inhibited the use of the other in isolated myocardial and skeletal muscle (23), but no corresponding data exist to justify the effect of a nutrient shift on the smooth muscles of the intestine. The result of our previous study, about the factors affecting myocardial ¹⁸F-FDG uptake, demonstrated that in 107 patients with LCHFD, there was a significant statistical relationship between descending colon ¹⁸F-FDG absorption and myocardial ¹⁸F-FDG uptake ($P = 0.001$) (5). However, despite a meaningful shift in ¹⁸F-FDG absorption by the descending colon and small intestine, ¹⁸F-FDG did not show a significant shift from moderate or high to mild or absent uptake.

CONCLUSION

Management of physiologic bowel ¹⁸F-FDG uptake can play a key role in accurately identifying colon diseases by effectively deterring the occurrence of false-positive or false-negative results. Patient preparation using an LCHFD for 24 h before ¹⁸F-FDG PET imaging resulted in lower ¹⁸F-FDG uptake in the descending colon and small intestine and consequently better-quality images, in particular for precise characterization and interpretation of abdominopelvic findings.

DISCLOSURE

No potential conflict of interest relevant to this article was reported.

REFERENCES

- Bombardieri E, Aktolun C, Baum RP, et al. FDG-PET: procedure guidelines for tumour imaging. *Eur J Nucl Med Mol Imaging*. 2003;30:BP115–BP124.
- Israel O, Weiler-Sagie M, Rispler S, et al. PET/CT quantitation of the effect of patient-related factors on cardiac ¹⁸F-FDG uptake. *J Nucl Med*. 2007;48:234–239.
- Balink H, Hut E, Pol T, Flokstra F-J, Roef M. Suppression of ¹⁸F-FDG myocardial uptake using a fat-allowed, carbohydrate-restricted diet. *J Nucl Med Technol*. 2011;39:185–189.
- Kumar P, Patel CD, Singla S, Malhotra A. Effect of duration of fasting and diet on the myocardial uptake of F-18-2-fluoro-2-deoxyglucose (F-18 FDG) at rest. *Indian J Nucl Med*. 2014;29:140–145.
- Fallahi B, Moasses-Ghafari B, Fard-Esfahani A, et al. Factors influencing the pattern and intensity of myocardial ¹⁸F-FDG uptake in oncologic PET-CT imaging. *Iran J Nucl Med*. 2017;25:52–61.
- Soyka JD, Strobel K, Veit-Haibach P, et al. Influence of bowel preparation before ¹⁸F-FDG PET/CT on physiologic ¹⁸F-FDG activity in the intestine. *J Nucl Med*. 2010;51:507–510.
- Huebner RH, Park KC, Shepherd JE, et al. A meta-analysis of the literature for whole-body FDG PET detection of recurrent colorectal cancer. *J Nucl Med*. 2000;41:1177–1189.
- Yasuda S, Kobayashi K, Ono M, et al. Classification of physiological ¹⁸F-fluorodeoxyglucose uptake in the large intestine: a preliminary study. *Tokai J Exp Clin Med*. 2014;39:141–145.
- Marley AR, Nan H. Epidemiology of colorectal cancer. *Int J Mol Epidemiol Genet*. 2016;7:105–114.
- Siegel RL, Miller KD, Fedewa SA, et al. Colorectal cancer statistics, 2017. *CA Cancer J Clin*. 2017;67:177–193.
- Yoon H-J, Kim H-N, Yun Y, et al. Background intestinal ¹⁸F-FDG uptake is related to serum lipid profile and obesity in breast cancer patients. *PLoS One*. 2015;10:e0141473.

12. Yasuda S, Takahashi W, Takagi S, Fujii H, Ide M, Shohtsu A. Factors influencing physiological FDG uptake in the intestine. *Tokai J Exp Clin Med*. 1998;23:241–244.
13. Pénicaud L, Hitier Y, Ferre P, Girard J. Hypoglycaemic effect of metformin in genetically obese (fa/fa) rats results from an increased utilization of blood glucose by intestine. *Biochem J*. 1989;262:881–885.
14. Bailey CJ, Mynett K, Page T. Importance of the intestine as a site of metformin-stimulated glucose utilization. *Br J Pharmacol*. 1994;112:671–675.
15. Walker J, Jijon HB, Hugo D, Salehi P, Churchill T, Madsen KL. 5-aminoimidazole-4-carboxamide riboside (AICAR) enhances GLUT2-dependent jejunal glucose transport: a possible role for AMPK. *Biochem J*. 2005;385:485–491.
16. Gontier E, Fourme E, Wartski M, et al. High and typical ^{18}F -FDG bowel uptake in patients treated with metformin. *Eur J Nucl Med Mol Imaging*. 2008;35:95–99.
17. Oh J-R, Song H-C, Chong A, et al. Impact of medication discontinuation on increased intestinal FDG accumulation in diabetic patients treated with metformin. *AJR*. 2010;195:1404–1410.
18. Ozülker T, Ozülker F, Mert M, Özpaçacı T. Clearance of the high intestinal ^{18}F -FDG uptake associated with metformin after stopping the drug. *Eur J Nucl Med Mol Imaging*. 2010;37:1011–1017.
19. Bahler L, Holleman F, Chan M-W, Booij J, Hoekstra JB, Verberne HJ. ^{18}F -FDG uptake in the colon is modulated by metformin but not associated with core body temperature and energy expenditure. *PLoS One*. 2017;12:e0176242.
20. Franquet E, Palmer MR, Gifford AE, et al. Rifaximin suppresses background intestinal ^{18}F -FDG uptake on PET/CT scans. *Nucl Med Commun*. 2014;35:1026–1031.
21. Emmott J, Sanghera B, Chambers J, Wong WL. The effects of N-butylscopolamine on bowel uptake: an ^{18}F -FDG PET study. *Nucl Med Commun*. 2008;29:11–16.
22. Hue L, Taegtmeyer H. The Randle cycle revisited: a new head for an old hat. *Am J Physiol Endocrinol Metab*. 2009;297:E578–E591.
23. Wolfe RR. Metabolic interactions between glucose and fatty acids in humans. *Am J Clin Nutr*. 1998;67:519S–526S.

U.S. Diagnostic Reference Levels and Achievable Administered Activities for Adult Renal Scintigraphy: An Analysis of the Intersocietal Accreditation Committee Nuclear Laboratories

Kevin P. Banks¹, Rutger S. Gunther¹, Mary B. Farrell², Justin G. Peacock¹, Maria Costello², and Leonie L. Gordon³

¹U.S. Army Brooke Army Medical Center, San Antonio, Texas; ²Intersocietal Accreditation Commission, Ellicott City, Maryland; and

³Department of Radiology, Medical University of South Carolina, Charleston, South Carolina

The goal of this work was to determine U.S. diagnostic reference levels (DRLs) and achievable administered activities (AAAs) for adult renal scintigraphy. **Methods:** Under an Institutional Review Board–approved protocol, data were collected from the Intersocietal Accreditation Commission during one 3-y accreditation cycle encompassing 110 facilities. Elements included radiopharmaceutical, administered activity, practice type, and examination volume. DRLs and AAAs were calculated and compared with non-U.S. values and societal recommendations as available. **Results:** Ninety-three facilities provided data on ^{99m}Tc-mercaptoacetyltriglycine (^{99m}Tc-MAG3), and 15 provided data on ^{99m}Tc-diethylenetriaminepentaacetic acid (^{99m}Tc-DTPA) for adult renal scintigraphy exams. Analysis demonstrated a DRL of 392.2 MBq (10.6 mCi) for ^{99m}Tc-MAG3 and 531.7 MBq (14.4 mCi) for ^{99m}Tc-DTPA, with an AAA of 370 MBq (10 mCi) for ^{99m}Tc-MAG3 and 445.9 MBq (12.1 mCi) for ^{99m}Tc-DTPA. **Conclusion:** The resultant calculated novel U.S. DRLs and AAAs may serve as benchmarks that nuclear medicine facilities may use to refine renal scintigraphy protocols, reduce patient doses, and potentially guide future societal guideline recommendations.

Key Words: reference levels; renal scintigraphy; administered activity; ^{99m}Tc-MAG3; ^{99m}Tc-DTPA

J Nucl Med Technol 2021; 49:246–249

DOI: 10.2967/jnmt.120.261552

Given the potential for radiation-induced cancers and other health issues, it is the responsibility of imaging providers to tailor exams using ionizing radiation such that a diagnostic study is achieved with the lowest amount of radiation dose imparted to the patient. In nuclear medicine, the radiation dose is proportional to the administered radiopharmaceutical activity, and hence it is essential that the minimum activity needed for acceptable diagnostic quality be used.

Two metrics that have been identified to aid in this effort are the diagnostic reference level (DRL) and the achievable administered activity (AAA). The DRL, as defined by the

International Commission on Radiological Protection (ICRP), is the 75th percentile of dose associated with a diagnostic imaging study, whereas the AAA is defined as the 50th percentile (median) (1). In the field of nuclear medicine and molecular imaging, given the relationship between radiation exposure and the administered activity of the specific radiopharmaceuticals, these values are expressed in megabecquerels (MBq) or millicuries (mCi). The percentiles, and hence the underlying activities, are derived by surveying imaging facilities using various standard techniques and technologies.

Three surveys to date have identified the DRLs and AAAs for many U.S. nuclear medicine examinations, including myocardial perfusion imaging, planar and SPECT bone scintigraphy, hepatobiliary scintigraphy, lung perfusion scintigraphy, ¹²³I and ¹³¹I thyroid exams, brain and whole-body ¹⁸F-FDG PET/CT, and ¹⁸F-amyloid brain PET/CT (2–4). One of the less common nuclear medicine procedures, renal scintigraphy, can impart a moderate dose of 2.59 mSv when administering the standard adult radioactivity but does not have the benefit of well-established DRLs and AAAs. The only prior U.S. data were derived from a small survey with only 9 respondents and were limited to ^{99m}Tc-mercaptoacetyltriglycine (^{99m}Tc-MAG3); no data pertaining to ^{99m}Tc-diethylenetriaminepentaacetic acid (^{99m}Tc-DTPA) were gathered (5). The aim of this study was to accurately determine these values (based on accreditation surveys) for adult renal scintigraphy at U.S. nuclear medicine facilities and add them to the growing body of nuclear medicine reference levels so that facilities may use them to optimize protocols and potentially guide future societal guideline recommendations.

MATERIALS AND METHODS

Under an Institutional Review Board–approved protocol with the requirement to obtain informed consent waived, deidentified data regarding administered activities for adult renal scintigraphy were collected from the Intersocietal Accreditation Commission nuclear medicine accreditation program during one 3-y accreditation cycle from October 2015 through December 2018. The accreditation process requires nuclear laboratories to submit demographic and practice data. For each area for which the facility is seeking accreditation (e.g., lung, hepatobiliary, brain scintigraphy; oncologic PET/CT), the facility submits 2 example examinations along with information on the radiopharmaceutical used, the administered activities, the

Received Dec. 7, 2020; revision accepted Mar. 18, 2021.
For correspondence or reprints contact Kevin P. Banks (kevin.p.banks.civ@mail.mil).

Published online April 5, 2021.

COPYRIGHT © 2021 by the Society of Nuclear Medicine and Molecular Imaging.

TABLE 1

Practice Characteristics of 108 Facilities Included in
Intersocietal Accreditation Commission Accreditation Survey
Period of October 2015 to December 2018

Facility characteristic	Average	Maximum	Minimum
No. of general NM exams per year*	1,763	9,076	95
No. of genitourinary NM exams per year	86	697	3
Percentage of genitourinary NM of practice	5%	37%	0.50%

*All non-PET, non-MPS diagnostic exams. MPS = myocardial perfusion scintigraphy.
NM = nuclear medicine.

TABLE 2

Analysis of Administered Activities by Radiopharmaceutical

Parameter	^{99m} Tc-MAG3 (n = 182)	^{99m} Tc-DTPA (n = 24)
Minimum	140.6 (3.8)	206.1 (5.6)
25th percentile	303.4 (8.2)	386.7 (10.5)
50th percentile (AAA)	370 (10)	445.9 (12.1)
75th percentile (DRL)	392.2 (10.6)	531.7 (14.4)
Maximum	588.3 (15.9)	780.7 (21.1)

Data are megabecquerels followed by millicuries in parentheses.

final reports, and the standard operating procedure or protocol. For genitourinary nuclear medicine accreditation, the facility may choose to submit material from adult or pediatric examinations, and these may include any combination of diuretic renography, angiotensin-converting enzyme inhibitor renography, or renal cortical imaging exams. The cycle included 110 facilities applying for genitourinary nuclear medicine scintigraphy accreditation. Two provided information on only pediatric renal scintigraphy, and thus

information from 108 sites was included in the final dataset. Facility demographics showed most sites to be hospital-based ($n = 74$), and approximately one third were outpatient imaging centers ($n = 34$) with a wide range in volume for both general nuclear medicine studies and genitourinary scintigraphy studies (Table 1).

RESULTS

Most facilities used ^{99m}Tc-MAG3-based protocols; a small minority used ^{99m}Tc-DTPA, and a few used both. This resulted in ^{99m}Tc-MAG3 dose data being provided by 93 facilities and ^{99m}Tc-DTPA dose data by 15 facilities, with 182 ^{99m}Tc-MAG3 and 24 ^{99m}Tc-DTPA adult administered activities available for assessment. Additionally, there was one report using ^{99m}Tc-DMSA and one using ^{99m}Tc-glucuheptonate included in the submissions and discarded from the analysis. Two submitted adult diuretic renal scintigraphy reports failed to note the dose and were also excluded and 10 reports were excluded because they were for children. Minimum, average, and maximum administered activities were determined; DRLs and AAAs are presented in Table 2 and are later compared with the DRLs and AAAs of non-U.S. facilities, as available.

DISCUSSION

The priority for any imaging study is to achieve the diagnostic quality necessary to answer the clinical question. In the setting of exams using ionizing radiation, this priority must be carefully balanced with the patient radiation dose. In the absence of empiric experimental data, survey data and the resultant determined reference levels may be used to guide practitioners and professional societies. DRLs, indicating the 75th percentile for administered activities for a specific nuclear medicine procedure and radiopharmaceutical, can indicate whether the amount administered is unusually high and are viewed as the first step in optimizing patient dose (6). Facilities routinely exceeding the DRL may benefit from reviewing their technique to determine whether exams may be performed using a lower administered activity while maintaining adequate diagnostic quality. In contrast, the AAA, indicating the 50th percentile, is considered a goal for nuclear laboratories to strive for with prescribed administered activities. The overarching objective of both these metrics is to aid facilities in avoiding unnecessary patient radiation dose.

Several high-quality surveys of U.S. nuclear medicine facilities have identified the DRLs and AAAs for many radiopharmaceuticals and studies; however, renal scintigraphy either has not been

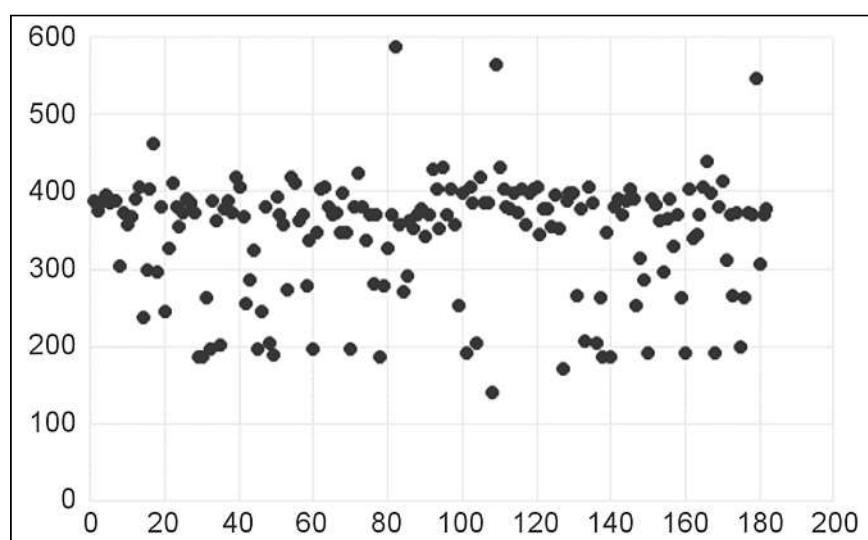


FIGURE 1. Distribution of 182 ^{99m}Tc-MAG3 administered doses. Vertical axis is activity (MBq). Horizontal axis is number of doses. Most values are close to 370 MBq (10 mCi).

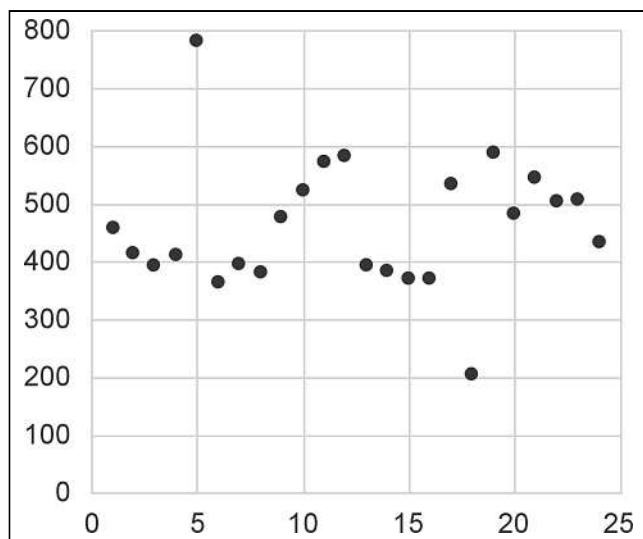


FIGURE 2. Distribution of 24 ^{99m}Tc -DTPA administered doses. Vertical axis is activity (MBq). Horizontal axis is number of doses. Nearly all fall within 370- to 555-MBq (10–15 mCi) range.

reviewed or has yielded too few data points to provide accurate values until now (2–4). Analysis of survey results from Intersocietal Accreditation Commission accreditation data revealed a U.S. DRL of 392.2 MBq (10.6 mCi) for ^{99m}Tc -MAG3 and a minimally lower AAA of 370 MBq (10 mCi), with nearly a third of values falling between these 2 values and another third being within 37 MBq (1 mCi) of either side of this range, indicating a narrow band of administered activities across most sites (Fig. 1). The same analysis revealed slightly greater values for ^{99m}Tc -DTPA, with a U.S. DRL of 531.69 MBq (14.4 mCi) and an AAA of 445.85 MBq (12.1 mCi) (Fig. 2).

Such values are available for Japan and much of Europe, providing an opportunity to compare and contrast with the

Intersocietal Accreditation Commission survey results. DRLs for Japan are 399.6 MBq (10.8 mCi) for both ^{99m}Tc -MAG3 and ^{99m}Tc -DTPA (7). In contrast, European researchers found a much lower ^{99m}Tc -MAG3 DRL of 99.9 MBq (2.7 mCi) to be the most common value reported from its survey of 36 countries, with the individual-country DRLs ranging from 99.9 to 370 MBq (2.7–10 mCi) (8). Most U.S. ^{99m}Tc -MAG3 administered activities fell below Japan's DRL, but all exceeded the European DRL. In contrast, most U.S. ^{99m}Tc -DTPA administered activities exceeded Japan's DRL (Fig. 3).

The American College of Radiology–Society for Pediatric Radiology practice parameter for renal scintigraphy allows for adult doses of up to 370 MBq (10 mCi) for ^{99m}Tc -MAG3 and 555 MBq (15 mCi) for ^{99m}Tc -DTPA (9). In contrast, whereas the SNMMI-EANM procedure standard allows for doses of up to 370 MBq (10 mCi) for both agents, it recommends lower administered activities of 37–185 MBq (1–5 mCi) for most applications (10). This lower range is supported by at least one study, which showed no increased interpretation benefit or relative function determination accuracy when comparing doses of 300–370 MBq (8.1–10 mCi) with doses of 37–185 MBq (1–5 mCi) (11). The Intersocietal Accreditation Commission survey analysis shows that administered activities in the United States generally are consistent across facilities at the upper range of the values endorsed by societal parameters and guidelines, with only a small portion of facilities using ^{99m}Tc -MAG3 administered activities well below both the DRL and AAA.

CONCLUSION

This practice-based survey of administered activities used by a large number of U.S. nuclear laboratories for the performance of adult dynamic renal scintigraphy has resulted in the first valid national reference levels for this nuclear medicine exam. Resultant DRLs of 392.2 MBq (10.6 mCi) for ^{99m}Tc -MAG3 and 531.7 MBq (14.4 mCi) for ^{99m}Tc -DTPA, with AAAs of 370 MBq (10 mCi) for ^{99m}Tc -MAG3 and 445.9 MBq (12.1 mCi) for ^{99m}Tc -DTPA, were identified. These values may serve as benchmarks that nuclear medicine facilities may use to refine their renal scintigraphy protocols and to guide future societal recommendations and organizational accreditation processes. Given that reference levels are dependent on the state of practice and the technology available at a particular point in time, future downward evolution of these values will be likely, based on improvements in equipment, techniques, and expertise.

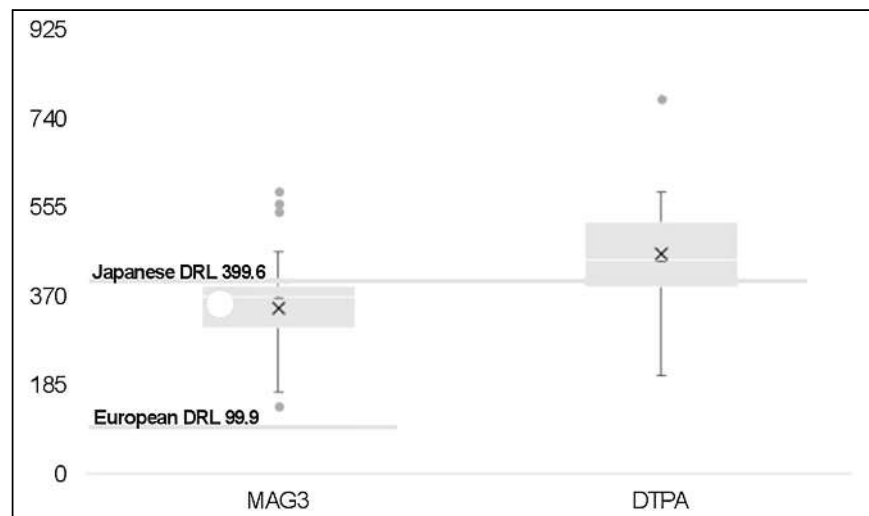


FIGURE 3. Box-and-whisker plot comparing minimum, maximum, and quartiles for U.S. ^{99m}Tc -MAG3 and ^{99m}Tc -DTPA administered activities (MBq) along with outliers vs. DRLs from Japan and Europe (^{99m}Tc -MAG3 only).

DISCLOSURE

Mary Farrell and Maria Costello are employees of the Intersocietal Accreditation Commission. Leonie Gordon is on the Intersocietal Accreditation Commission Board of Directors. No other potential conflict of interest relevant to this article was reported.

REFERENCES

1. Vano E, Miller DL, Martin CJ, et al. ICRP publication 135: diagnostic reference levels in medical imaging. *Ann ICRP*. 2017;46:1–144.
2. Alessio AM, Farrell MB, Fahey FH. Role of reference levels in nuclear medicine: a report of the SNMMI dose optimization task force. *J Nucl Med*. 2015;56:1960–1964.
3. Becker MD, Butler PF, Bhargavan-Chatfield M, et al. Adult gamma camera myocardial perfusion imaging: diagnostic reference levels and achievable administered activities derived from ACR accreditation data. *J Am Coll Radiol*. 2016;13:688–695.
4. Becker MD, Butler PF, Siam M, et al. U.S. PET/CT and gamma camera diagnostic reference levels and achievable administered activities for noncardiac nuclear medicine studies. *Radiology*. 2019;293:203–211.
5. Reference Levels and Achievable Doses in Medical and Dental Imaging: Recommendations for the United States. National Council on Radiation Protection and Measurements; 2012. NCRP report 172.
6. ACR–AAPM–SPR practice parameter for diagnostic reference levels and achievable doses in medical x-ray imaging. American College of Radiology website. <https://www.acr.org/-/media/ACR/Files/Practice-Parameters/Diag-Ref-Levels.pdf>. Published 2002. Revised 2018. Accessed July 13, 2021.
7. Watanabe H, Ishii K, Hosono M, et al. Report of a nationwide survey on actual administered radioactivities of radiopharmaceuticals for diagnostic reference levels in Japan. *Ann Nucl Med*. 2016;30:435–444.
8. Radiation protection n° 180: diagnostic reference levels in thirty-six European countries. European Commission website. <https://ec.europa.eu/energy/sites/ener/files/documents/RP180%20part2.pdf>. Published 2014. Accessed July 13, 2021.
9. ACR–SPR practice parameter for the performance of renal scintigraphy. American College of Radiology website. <https://www.acr.org/-/media/ACR/Files/Practice-Parameters/RenalScint.pdf>. Published 1995. Revised 2017. Accessed July 13, 2021.
10. Taylor AT, Brandon DC, De Palma D, et al. SNMMI procedure standard/EANM practice guideline for diuretic renal scintigraphy in adults with suspected upper urinary tract obstruction 1.0. *Semin Nucl Med*. 2018;48:377–390.
11. Taylor AT, Folks RD, Fazlur Rashman AKM, et al. ^{99m}Tc-MAG3: image wisely. *Radiology*. 2017;284:200–209.

Accuracy Assessment of SUV Measurements in SPECT/CT: A Phantom Study

Fatin Halim^{1,2}, Hizwan Yahya^{1,2}, Khairul Nizam Jaafar³, and Syahir Mansor^{1,3}

¹Oncological and Radiological Science Cluster, Advanced Medical and Dental Institute, SAINS@BERTAM, Universiti Sains Malaysia, Penang, Malaysia; ²Department of Nuclear Medicine, Penang Hospital, Penang, Malaysia; and ³Nuclear Medicine Unit, Advanced Medical and Dental Institute, Universiti Sains Malaysia, Penang, Malaysia

Advances in iterative image reconstruction enable absolute quantification of SPECT/CT studies by incorporating compensations for collimator–detector response, attenuation, and scatter. This study aimed to assess the quantitative accuracy of SPECT/CT based on different levels of ^{99m}Tc activity (low/high) using different SUV metrics (SUV_{mean}, SUV_{max}, SUV_{0.6 max}, and SUV_{0.75 max} [the average values that include pixels greater than 60% and 75% of the SUV_{max} in the volume of interest, respectively]). **Methods:** A Jaszczak phantom equipped with 6 fillable spheres was set up with low and high activity ratios of 1:4 and 1:10 (background-to-sphere) on background activities of 10 and 60 kBq/mL, respectively. The fixed-size volume of interest based on the diameter of each sphere was drawn on SPECT images using various metrics for SUV quantification purposes. **Results:** The convergence of activity concentration was dependent on the number of iterations and application of post-filtering. For the background-to-sphere ratio of 1:10 with a low background activity concentration, the SUV_{mean} metric showed an underestimation of about 38% from the actual SUV, and SUV_{max} exhibited an overestimation of about 24% for the largest sphere diameter. Meanwhile, bias reductions of as much as –6% and –7% for SUV_{0.6 max} and SUV_{0.75 max}, respectively, were observed. SUV_{max} gave a more accurate reading than the others, although points that exceeded the actual value were detected. At 1:4 and 1:10 background activity of 10 kBq/mL, a low activity concentration attained a value close to the actual ratio. Use of 2 iterations and 10 subsets without postfiltering gave the most accurate values for reconstruction and the best image overall. **Conclusion:** SUV_{max} is the best metric in a high- or low-contrast-ratio phantom with at least 2 iterations, 10 subsets, and no postfiltering.

Key Words: quantitative; SPECT/CT; SUV; ratio; phantom

J Nucl Med Technol 2021; 49:250–255
DOI: 10.2967/jnmt.120.259168

The development of multimodality γ -camera instrumentation (SPECT/CT), image reconstruction algorithms, and advanced compensation methods to correct photon attenuation, scattering, and resolution have rendered quantitative SPECT a feasible method that is comparable to the well-established quantitative PET (1).

Filtered backprojection (FBP) and ordered-subset expectation maximization are the 2 most commonly used algorithms in SPECT reconstruction (2). Although the FBP algorithm is simple and fast (3), it unnecessarily amplifies the high-frequency noise, which in turn will affect the quality of the final reconstructed SPECT image (4). Another limitation of FBP is that attenuation cannot be readily integrated and compensated for. Before or after reconstruction, the data should be corrected to compensate for attenuation in the FBP reconstruction, presenting a challenge for scholars (5).

Three-dimensional ordered-subset expectation maximization is a quantitative image reconstruction algorithm used in state-of-the-art SPECT/CT systems (6). Ordered-subset expectation maximization separates the measured datasets into various subsets and uses a single subset for every iteration, thus accelerating the algorithm by a factor equal to the number of subsets (7).

The quantitative accuracy of reconstructed SPECT images deteriorates because of several physical factors, namely photon attenuation, Compton scattering, and a spatially varying collimator response (2). The inclusion of collimator response, that is, resolution recovery, in the GE Healthcare systems (Discovery NM/CT 670 SPECT/CT device; Infinia SPECT/CT) will increase the accuracy of the final reconstructed images (8,9). Attenuation causes inconsistent projection information that may increase or decrease counts in the image, particularly near the detector plane (10). Meanwhile, the presence of scattered photons will result in less contrast and a loss of quantification accuracy in reconstructed images.

Different activity concentrations affect the quantification of SPECT/CT. On the basis of a study by Francis et al. (11), SUV increases with increased activity concentrations for the same size of sphere. Their study proved that radionuclide uptake values correspond to activity concentrations in organs or tissues.

The use of SUV in the quantification of SPECT/CT is gaining interest. SUV is defined as the concentration of radioactivity in the tissue normalized to the injected dose and body weight. SUV_{mean} is defined as the average SUV in the volume of interest (VOI), and SUV_{max} is defined as the maximum SUV in the VOI. In this study, we also included SUV_{0.6 max} and SUV_{0.75 max}, which are defined as the average values that include pixels greater than 60% and 75%, respectively, of the SUV_{max} in the VOI. Finally, we compared these 4 SUV metrics to see which gave the most accurate reading.

Received Oct. 27, 2020; revision accepted Feb. 8, 2021.

For correspondence or reprints, contact Syahir Mansor (syahir.mansor@usm.my).

Published online March 15, 2021.

COPYRIGHT © 2021 by the Society of Nuclear Medicine and Molecular Imaging.

Factors that potentially affect SUV measurements include spatial resolution and reconstruction parameters. For small objects, image resolution has a partial-volume effect on the measured SUV (12). Usually, SPECT collimators are equipped with a maximum permissible resolution to partially offset the limited detection performance (13). Any changes in reconstruction parameters, such as matrix size, filtering, field-of-view size, and iteration number, will have a significant effect on SUV calculation in clinical cases.

In this study, we aimed to assess the quantitative accuracy when different levels of activity concentration (low/high) with different reconstruction parameters are used for various SUV metrics (SUV_{mean} , SUV_{max} , $SUV_{0.6\ max}$, and $SUV_{0.75\ max}$).

MATERIALS AND METHODS

Phantom Studies

Quantitative ^{99m}Tc -SPECT/CT acquisitions of a Jaszczak phantom containing 6 spheres of various diameters (9.9, 12.4, 15.6, 19.7, 24.8, and 31.2 mm) were performed on a Discovery NM/CT 670 SPECT/CT device (GE Healthcare) equipped with a low-energy, high-resolution collimator. For the first experiment, the background compartment was filled with an activity concentration of about 60 kBq/mL, with sphere-to-background ratios of 10:1 and 4:1. For the second experiment, the background compartment was filled with an activity concentration of about 10 kBq/mL, again with sphere-to-background ratios of 10:1 and 4:1.

Data Acquisition and Reconstruction

SPECT acquisitions were reconstructed using the ordered-subset expectation maximization on a GE Healthcare Xeleris workstation with a $128 \times 128 \times 128$ voxel grid. The acquisition voxel size was $4.42 \times 4.42 \times 4.42$ mm. A CT scan with an energy of 120 kVp and a tube current of 205 mAs was used for attenuation correction. CT-based attenuation correction and dual-energy window scatter correction were systematically applied in SPECT reconstructions. Both experiments were acquired using 20 s per view for a total of 60 views per camera head with no zoom application ($\times 1$ multiplication), and images were reconstructed using 2, 10, and 20 iterations with 10 fixed subsets with and without the gaussian filter. SPECT/CT data were reconstructed in an isotropic voxel size of $128 \times 128 \times 128$ with a dimension of 4.42×4.42 mm and a slice thickness of 4.42 mm. All images were reconstructed using the ordered-subset expectation maximization algorithm with attenuation correction, scatter correction, and resolution recovery. We utilized the gaussian postprocessing filter using a 4-mm full width at half maximum.

Image Analysis

The reconstructed data were processed using A Medical Image Data Examiner (AMIDE, version 1.0.4) freeware tool (14). The VOI was drawn for 6 spheres based on the CT images and then fused onto the SPECT images. This tool was used to obtain the total number of counts in the VOI on the SPECT images. The SUV was calculated from the activity concentration (kBq/mL) divided by the total administered activity (kBq) within the phantom background chamber and normalized to the weight (g) of the solution in the phantom. SUV_{mean} , SUV_{max} , $SUV_{0.6\ max}$, and $SUV_{0.75\ max}$ metrics were used for each sphere in different phantom contrast ratios and activity

concentrations, similar to the study conducted by Lee et al. (15). Calculation of $SUV_{0.6\ max}$ and $SUV_{0.75\ max}$ was based on an assumption about the average values of all regional voxels, with values being within 60% and 75%, respectively, of the maximal voxel value. The statistical variance or noise was determined using the coefficient of variation. For each measurement, the coefficient of variation for each sphere was calculated by dividing the SD by the mean reading for each sphere.

Statistical Analysis

Statistical analysis was performed using SPSS (version 24; IBM Corp.) software. An independent-sample *t* test was used to verify whether significant differences existed between high and low background activity concentrations and between 1:4 and 1:10 ratios. Meanwhile, a sample *t* test was used to compare the SUVs with the reference values for different factors, such as the different activity concentrations, ratios, SUV metrics, and reconstructions. In this study, multiple metric SUVs were tested to find the value nearest the reference value, and the results were proven through 1-way ANOVA.

RESULTS

From Figure 1, high iteration numbers increased the contrast along with the noise of an image. The use of a postprocessing filter suppressed the noise but caused an oversmoothing effect

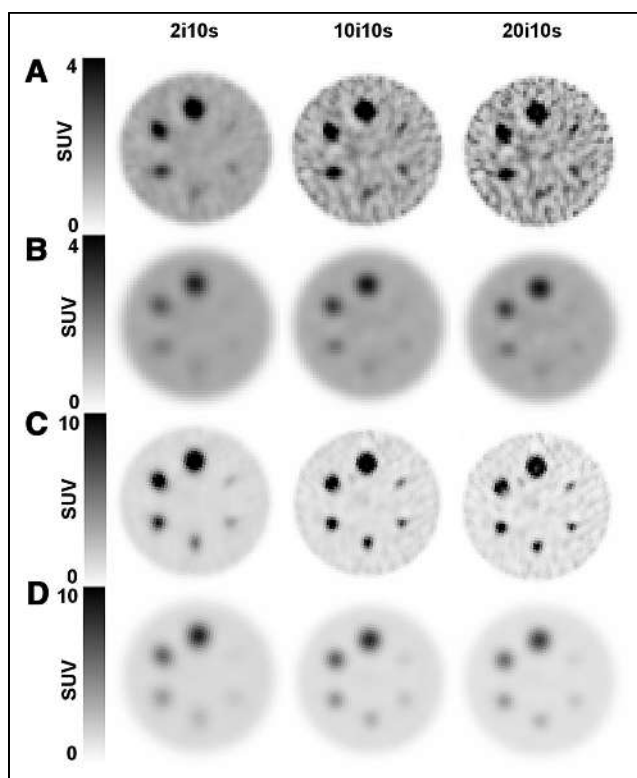


FIGURE 1. SUV images from phantom study without (A and C) and with (B and D) 4-mm gaussian postprocessing filter. Reconstructed images were achieved using 3-dimensional ordered-subset expectation maximization with 2, 10, and 20 iterations and 10 subsets (2i10s, 10i10s, and 20i10s, respectively) and with background-to-sphere ratios of 1:4 and 1:10 with high activity concentration.

(low contrast) on the image (Figs. 1B and 1D). Use of a filter reduced the contrast between the sphere and background, resulting in less qualitative enhancement of the images. However, the smoothing effect caused by the filter introduced additional blurring to the image and hence eliminated details of the structure within the image.

Descriptive Analysis

All SUV metrics (SUV_{mean} , SUV_{max} , $SUV_{0.6\ max}$, and $SUV_{0.75\ max}$) for the different activity concentrations and ratios were plotted on a graph against the function of sphere size and background. On the basis of the plotted graph, the SUV at a low activity concentration (10 kBq/mL) was over-estimated compared with the actual value. Meanwhile, a high activity concentration (60 kBq/mL) underestimated the

SUV for the sphere-to-background ratios of 1:4 and 1:10 (Fig. 2, Supplemental Figs. 1–3; supplemental materials are available at <http://jnmt.snmjournals.org>). A sphere-to-background ratio of 1:4 showed a higher accuracy at a low activity concentration (Supplemental Fig. 1) than at a high activity concentration (Fig. 2).

The various diameters of spheres inside the Jaszczak phantom (9.9, 12.4, 15.6, 19.7, 24.8, and 31.2 mm) were analyzed across the activity concentrations and sphere-to-background ratios of 1:4 and 1:10. The results showed that at the sphere-to-background ratio of 1:4 with a high activity concentration, SUV_{mean} , SUV_{max} , $SUV_{0.6\ max}$, and $SUV_{0.75\ max}$ increased with the increase in sphere diameter (Fig. 2).

When we focused on the largest sphere, SUV_{mean} decreased by about 38% from the actual SUV at a low activity

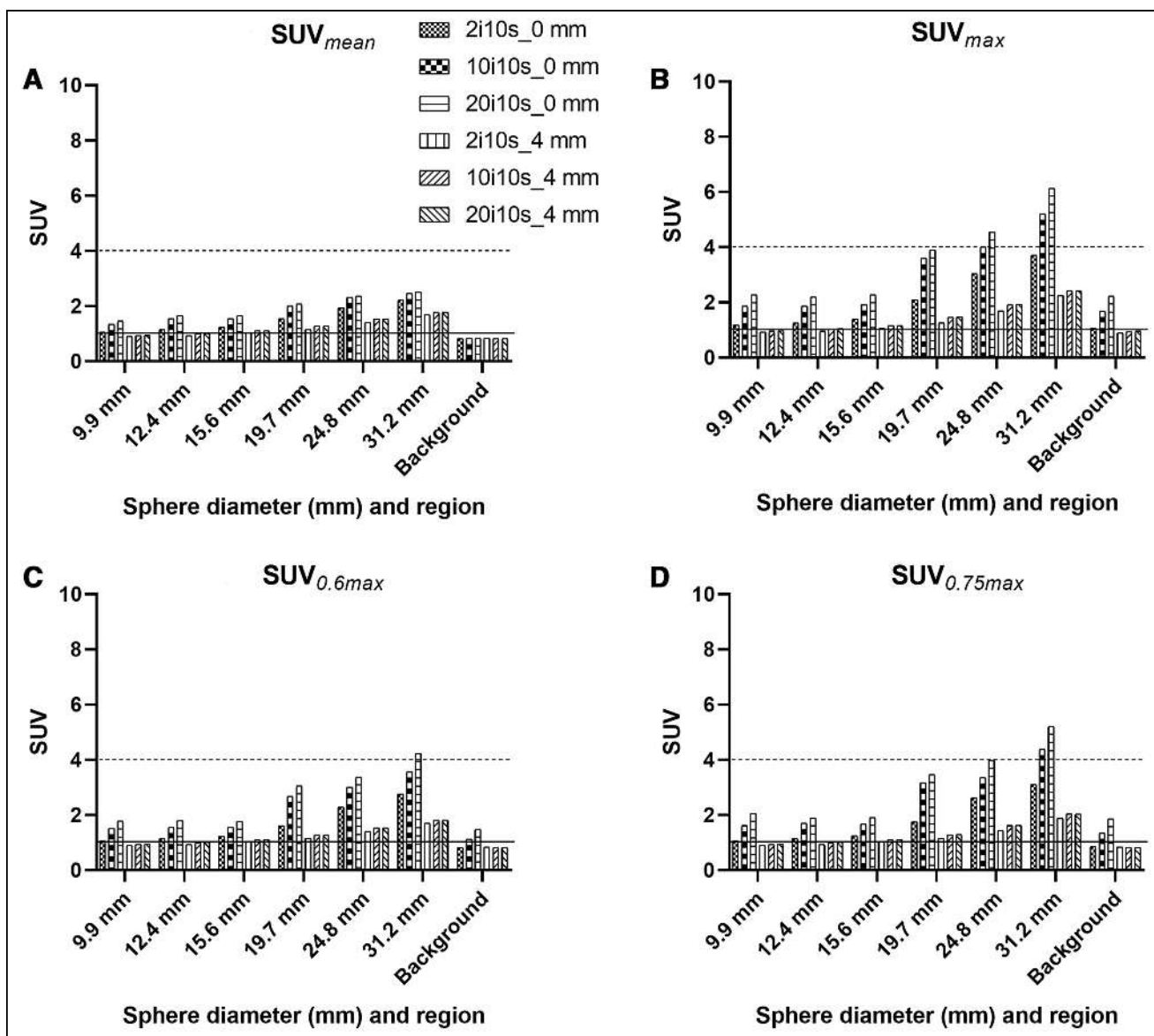


FIGURE 2. Sphere-to-background ratio of 1:4 with high activity concentration. Dotted lines show true SUV for respective spheres and background.

concentration, whereas SUV_{max} increased by about 24%. Given that $SUV_{0.6\ max}$ and $SUV_{0.75\ max}$ showed no major variations, reduction biases of about -6% and -7% were observed, respectively.

In this experimental work, a fixed subset of 10 was used for the reconstruction parameter, whereas the increase in iterations from 2 to 10 and 20 indicated an overestimation of SUV when the filter was not utilized. Compared with not using filters, using filters underestimated SUVs regardless of differences in iteration number, SUV threshold, sphere diameter, activity concentration, and sphere-to-background ratio. Such a result was due to the filter function of simultaneously removing noise while reducing the counts in the final reconstructed images.

A coefficient of variation was used to demonstrate noise level and can be calculated by dividing the SD by the average activity concentration and multiplying by 100. Figure 3 shows the noise for various reconstructions for the 3 largest

spheres in the phantom. The higher the iteration number, the higher the coefficient of variation (Fig. 3; Supplemental Fig. 4). However, when using filters, the coefficient of variation values were the same for all 3 iterations used.

Statistical Analysis

All data were analyzed using SPSS software. The P values for different SUV metrics at sphere-to-background ratios of 1:4 and 1:10 with different activity concentrations showed a significant difference. Theoretically, the true mean value at the 1:4 sphere-to-background ratio is 4 for all spheres inside the phantom, whereas the true mean value at the 1:10 ratio is 10. The SUV_{max} at a low activity concentration was the nearest to the theoretic value for both ratios.

One-way ANOVA was conducted to determine whether SUVs differed for groups with various SUV metrics. SUV was classified into 4 groups: SUV_{mean} , SUV_{max} , $SUV_{0.6\ max}$, and $SUV_{0.75\ max}$. There were statistically significant differences

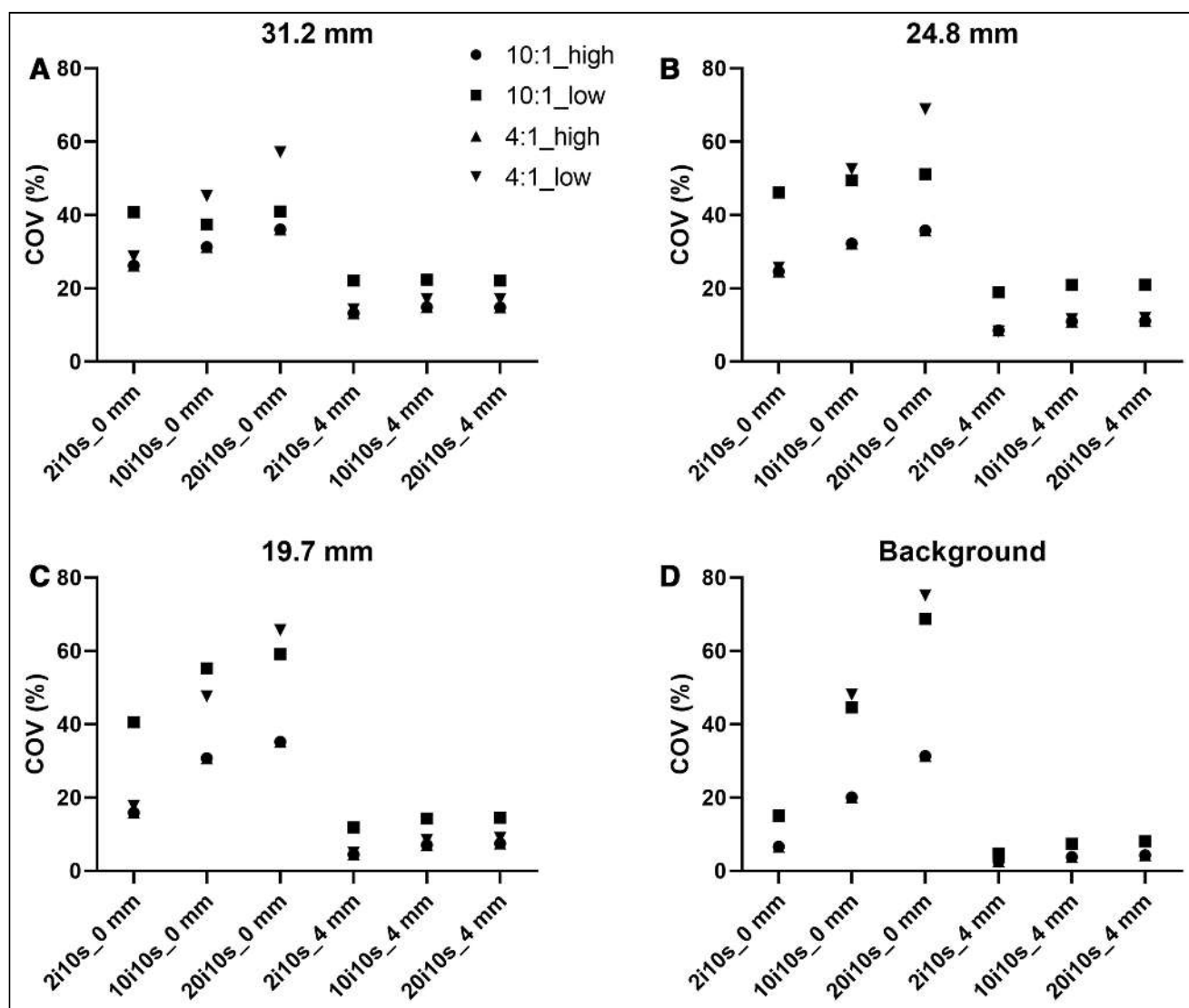


FIGURE 3. Noise (percentage coefficient of variation [COV]) for various reconstructions for 3 largest spheres and background. i = iterations; s = subsets.

between different SUV metrics—differences for which the P value was less than 0.001. Dunnett T3 post hoc analysis revealed that SUV_{mean} was statistically significant ($P < 0.05$) when compared with the other 3 groups, but no other group differences were statistically significant between SUV_{max} , $SUV_{0.6 \text{ max}}$, and $SUV_{0.75 \text{ max}}$.

The varying spheric sizes inside the phantom represent lesion in the patient's body. Significant differences were observed for all sphere sizes, with true mean values of 4 and 10, except for the 24.8-mm sphere at a low activity concentration and at a sphere-to-background ratio of 1:4 ($P = 0.104$).

The effects of different reconstruction iterations on the true mean value of the phantom showed a significant difference from the true mean (4 and 10) under different reconstruction methods, except for 2 iterations and 10 subsets without postfiltering at a low activity concentration for sphere-to-background ratios of 1:4 ($P = 0.595$) and 1:10 ($P = 0.268$).

DISCUSSION

Two different background activity concentrations (60 and 10 kBq/mL) were used in this study. These backgrounds were intended to compare the 2 concentrations to obtain an accurate reading relative to the theoretic value. Increasing the activity concentration retained the SUV based on the ratios. However, the results showed that the SUV was closest to the actual value in a low activity concentration. When we observed the phantom images at different concentrations and sphere-to-background ratios, we determined that the spill-in effect appeared at a low activity concentration at a 1:4 sphere-to-background ratio for the smallest sphere diameter (9.9 mm). This effect is known as the partial-volume effect, which is caused by the limited partial resolution of the imaging system (16,17).

In the comparison of the 4 SUV-based graphs in Figure 2 and Supplemental Figures 1–3, SUV_{mean} showed an underestimation from the real SUV, whereas SUV_{max} exhibited an overestimation. Given that $SUV_{0.6 \text{ max}}$ and $SUV_{0.75 \text{ max}}$ showed no considerable difference, $SUV_{0.75 \text{ max}}$ was closer to the theoretic value.

Supplemental Figure 1 indicates that a low activity concentration with a low sphere-to-background ratio may be disastrous if the SUV_{max} metric is used. Given the high background value, proper background subtraction is an important measure in quantification. The number of iterations is the primary variable affecting image quality. Although a high number of iterations will generally result in a high spatial resolution, the noise level will also increase. A high number of iterations will also hasten image convergence.

The algorithm cannot fully converge if the iteration number is inadequate, which will eventually result in a blurry image with inadequate contrast. Meanwhile, if the number of iterations is extremely large, then the reconstructed image shows oversharpening, with an elevated level of noise (Fig. 1). The

selection of reconstruction parameters, such as iteration number, filtering, attenuation correction, scatter correction, and resolution recovery, is important to produce good-quality images with minimal noise.

In this study, images were reconstructed using 10 subsets with 2, 10, and 20 iterations. Reconstruction using 2 iterations, 10 subsets, and no postfiltering at a low activity concentration for both sphere-to-background ratios was found to be most suitable based on the SUV obtained from this study. This result indicates that the obtained value approached the true theoretic value.

The postprocessing filter reduced noise but also produced a smoothing effect on the final reconstructed images. Filters can have a major effect on the quality of clinical images due to their degree of smoothing. Proper filter selection and appropriate smoothing allow physicians to interpret the results and make an accurate diagnosis (18). Gaussian smoothing produces a low image resolution and thus reduces the accuracy of the SUV.

In this experimental study, when we applied the 4-mm gaussian filter, the accuracy of SUV dramatically decreased, and not a single value under various ratios and spheres reached the true theoretic value. Thus, the filter choice can affect the quantitative value of SPECT/CT images.

Clinical bone SPECT/CT studies usually have high sensitivity but low specificity. This imaging procedure typically reconstructs images using 3 or 5 iterations and 8–10 subsets with postsmoothing using a gaussian or Butterworth filter (19). For quantitative analysis, the filter selected must allow for the best compromise between image quality and noise. Given that SUV_{max} is most accurate at various ratios and at a low or high activity concentration, it should be considered for use in clinical settings.

In nuclear medicine imaging, quantification offers a great advantage. Although SUV may have initially been a framework for PET imaging, it is now found equally ideal for SPECT imaging. The use of SUV in SPECT imaging offers a wide range of radiopharmaceuticals and applications. In this study, we compared different SUV metrics by creating various factors to determine the accuracy of SUV readings. SUV_{max} demonstrated the reading that correlated most accurately with the clinical setting commonly used for SUV reporting.

CONCLUSION

The concentration of the activity ratio (high or low activity concentration) plays a role in determining an accurate SUV. On the basis of the analysis, a low activity concentration under both ratios provided a more accurate value than a high activity concentration. SUV_{max} was the closest to the actual theoretic values. From the aspect of reconstruction, the use of 2 iterations and 10 subsets without postfiltering is optimal for accurate quantification and overall image quality when there is a compromising noise level.

DISCLOSURE

This study was supported by Universiti Sains Malaysia (USM); under short-term grant (304/CIPPT/6315160) and under fundamental research grant scheme (203/CIPPT/6711730). No other potential conflict of interest relevant to this article was reported.

REFERENCES

1. Bailey DL, Willows KP. An evidence-based review of quantitative SPECT imaging and potential clinical applications. *J Nucl Med.* 2013;54:83–89.
2. Alzimami KS, Sassi SA, Spyrou NM. A comparison between 3D OSEM and FBP image reconstruction algorithms in SPECT. In: Ao S-I, Gelman L, eds. *Advances in Electrical Engineering and Computational Science*. Springer Netherlands; 2009: 195–206.
3. Zeng GL. A filtered backprojection algorithm with characteristics of the iterative landweber algorithm. *Med Phys.* 2012;39:603–607.
4. Ramírez J, Górriz JM, Gómez-Río M, et al. Effective emission tomography image reconstruction algorithms for SPECT data. In: *Computational Science—ICCS 2008*. Springer; 2008:741–748.
5. Meysam T, Marian N. Quantitative evaluation of the effect of attenuation correction in SPECT images with CT-derived attenuation. Spie Digital Library website. <https://www.spiedigitallibrary.org/conference-proceedings-of-spie/10948/2512120/Quantitative-evaluation-of-the-effect-of-attenuation-correction-in-SPECT/10.1117/12.2512120.short?SSO=1>. Accessed August 19, 2021.
6. Katua AM, Ankrah AO, Vorster M, van Gelder A, Sathekge MM. Optimization of ordered subset expectation maximization reconstruction for reducing urinary bladder artifacts in single-photon emission computed tomography imaging. *World J Nucl Med.* 2011;10:3–8.
7. Hudson HM, Larkin RS. Accelerated image reconstruction using ordered subsets of projection data. *IEEE Trans Med Imaging.* 1994;13:601–609.
8. Ismail FS, Mansor S. Impact of resolution recovery in quantitative ^{99m}Tc SPECT/CT cardiac phantom studies. *J Med Imaging Radiat Sci.* 2019;50:449–453.
9. Knoll P, Kotalova D, Köchle G, et al. Comparison of advanced iterative reconstruction methods for SPECT/CT. *Z Med Phys.* 2012;22:58–69.
10. Frey EC, Humm JL, Ljungberg M. Accuracy and precision of radioactivity quantification in nuclear medicine images. *Semin Nucl Med.* 2012;42:208–218.
11. Francis H, Amuasi JH, Kwame KA, Vangu MD. Quantitative assessment of radionuclide uptake and positron emission tomography-computed tomography image contrast. *World J Nucl Med.* 2016;15:167–172.
12. Adams MC, Turkington TG, Wilson JM, Wong TZ. A systematic review of the factors affecting accuracy of SUV measurements. *AJR.* 2010;195:310–320.
13. Ritt P, Vija H, Hornegger J, Kuwert T. Absolute quantification in SPECT. *Eur J Nucl Med Mol Imaging.* 2011;38(suppl 1):S69–S77.
14. Loening AM, Gambhir SS. AMIDE: a free software tool for multimodality medical image analysis. *Mol Imaging.* 2003;2:131–137.
15. Lee JR, Madsen MT, Bushnell D, Menda Y. A threshold method to improve standardized uptake value reproducibility. *Nucl Med Commun.* 2000;21:685–690.
16. Soret M, Bacharach SL, Buvat I. Partial-volume effect in PET tumor imaging. *J Nucl Med.* 2007;48:932–945.
17. Du Y, Madar I, Stumpf MJ, Rong X, Fung GS, Frey EC. Compensation for spill-in and spill-out partial volume effects in cardiac PET imaging. *J Nucl Cardiol.* 2013;20:84–98.
18. Lyra M, Ploussi A. Filtering in SPECT image reconstruction. *Int J Biomed Imaging.* 2011;2011:693795.
19. Van den Wyngaert T, Strobel K, Kampen WU, et al. The EANM practice guidelines for bone scintigraphy. *Eur J Nucl Med Mol Imaging.* 2016;43:1723–1738.

Improved Accuracy of Amyloid PET Quantification with Adaptive Template–Based Anatomic Standardization

Yuma Tsubaki¹, Takayoshi Kitamura², Natsumi Shimokawa¹, Go Akamatsu³, and Masayuki Sasaki¹
for the Japanese Alzheimer's Disease Neuroimaging Initiative

¹Department of Health Sciences, Graduate School of Medical Sciences, Kyushu University, Fukuoka, Japan; ²Department of Health Sciences, School of Medicine, Kyushu University, Fukuoka, Japan; and ³National Institute of Radiological Sciences, National Institutes for Quantum and Radiological Science and Technology, Chiba, Japan

Amyloid PET noninvasively visualizes amyloid- β accumulation in the brain. Visual binary reading is the standard method for interpreting amyloid PET, whereas objective quantitative evaluation is required in research and clinical trials. Anatomic standardization is important for quantitative analysis, and various standard templates are used for this purpose. To address the large differences in radioactivity distribution between amyloid-positive and amyloid-negative participants, an adaptive-template method has been proposed for the anatomic standardization of amyloid PET. In this study, we investigated the difference between the adaptive-template method and the single-template methods (use of a positive or a negative template) in amyloid PET quantitative evaluation, focusing on the accuracy in diagnosing Alzheimer's disease (AD).

Methods: In total, 166 participants (58 healthy controls [HCs], 62 patients with mild cognitive impairment [MCI], and 46 patients with AD) who underwent ¹¹C-Pittsburgh compound B (¹¹C-PiB) PET through the Japanese Alzheimer's Disease Neuroimaging Initiative study were examined. For the anatomic standardization of ¹¹C-PiB PET images, we applied 3 methods: a positive-template-based method, a negative-template-based method, and an adaptive-template-based method. The positive template was created by averaging the PET images for 4 patients with AD and 7 patients with MCI. Conversely, the negative template was created by averaging the PET images for 8 HCs. In the adaptive-template-based method, either of the templates was used on the basis of the similarity (normalized cross-correlation [NCC]) between the individual standardized image and the corresponding template. An empiric PiB-prone region of interest was used to evaluate specific regions where amyloid- β accumulates. The reference region was the cerebellar cortex, and the evaluated regions were the posterior cingulate gyrus and precuneus and the frontal, lateral temporal, lateral parietal, and occipital lobes. The mean cortical SUV ratio (mcSUVr) was calculated for quantitative evaluation. **Results:** The NCCs of single-template-based methods (the positive template or negative template) showed a significant difference among the HC, MCI, and AD groups ($P < 0.05$), whereas the NCC of the adaptive-template-based method did not ($P > 0.05$). The mcSUVr exhibited significant differences among the HC, MCI, and AD groups with all methods ($P < 0.05$). The mcSUVr area under the curve by receiver operating characteristic analysis between the positive group (MCI and AD) and the HC group did not significantly

differ among templates. With regard to diagnostic accuracy based on mcSUVr, the sensitivity of the negative-template-based and adaptive-template-based methods was superior to that of the positive-template-based method ($P < 0.05$); however, there was no significant difference in specificity between them. **Conclusion:** In quantitative evaluation of AD by amyloid PET, the adaptive-template-based anatomic standardization method had greater diagnostic accuracy than the single-template-based methods.

Key Words: Alzheimer's disease; amyloid PET; anatomic standardization; adaptive-template method

J Nucl Med Technol 2021; 49:256–261

DOI: 10.2967/jnmt.120.261701

Dementia is a brain disease showing disturbance of multiple higher cortical functions (1). The most common type of dementia is Alzheimer's disease (AD). It accounts for more than 50% of cases of primary disease causing dementia in Japan (2). The number of affected patients is expected to reach approximately 5.0 million by 2025 (2,3).

The cause of AD is thought to be neuronal degeneration induced by the accumulation of amyloid- β plaques and phosphorylated tau protein. Such an accumulation is considered to begin before the onset of cognitive impairment (4). Amyloid PET noninvasively visualizes amyloid- β plaques in the brain. The standard method of interpreting amyloid PET scans is visual binary reading, and objective quantitative evaluation is required in research and clinical trials. Anatomic standardization (i.e., spatial normalization) is essential for the quantitative evaluation of amyloid PET; for this process, a standard brain template is required. The standard templates are defined in the standard space (e.g., Montreal Neurologic Institute standard space), and various types of templates, such as an MRI T1-weighted template and an ¹⁸F-FDG PET template, have been used for anatomic standardization (5). Although MRI-based methods are common for anatomic standardization of brain PET, PET-based methods have also been used in numerous studies for practical reasons (6,7). Amyloid PET demonstrates the activity distribution patterns that differ between amyloid-positive and amyloid-negative images. To account for the difference in activity distributions, Akamatsu et al. developed an adaptive-template-based method, which

Received Dec. 12, 2020; revision accepted Mar. 1, 2021.

For correspondence or reprints, contact Masayuki Sasaki (msasaki@hs.med.kyushu-u.ac.jp).

Published online April 5, 2021.

COPYRIGHT © 2021 by the Society of Nuclear Medicine and Molecular Imaging.

involves the use of multiple templates, both positive and negative (8). In the adaptive-template-based method, the template that is most similar to the subject image is selected and used for anatomic standardization. In some studies, the adaptive-template-based method has been used for amyloid PET anatomic standardization (9,10). However, the difference between the adaptive-template-based method and the single-template-based methods in amyloid PET quantitative evaluation has not been well elucidated.

In this study, the influence of the different anatomic standardization methods (the adaptive-template-based method and the single-template-based methods) on amyloid PET quantitative evaluation was investigated, focusing on diagnostic accuracy for AD.

MATERIALS AND METHODS

Participants

We retrospectively analyzed the data from 166 participants who underwent ^{11}C -Pittsburgh compound B (^{11}C -PiB) PET examination through the Japanese Alzheimer's Disease Neuroimaging Initiative (J-ADNI) study (11). The J-ADNI study is a multiinstitutional research project on AD led by the Ministry of Health, Labor, and Welfare and by the New Energy and Industrial Technology Development Organization in Japan. (12). The J-ADNI study was approved by the ethics committee of each institution for data acquisition, and written informed consent was obtained. The data used in this study were provided by the National Bioscience Database Center and were retrospectively analyzed. In addition, the requirement for written informed consent was waived. This study was approved by the ethics committee of Kyushu University, Fukuoka, Japan (approval 30-174).

All participants were native Japanese speakers, and their mean age was 70.5 ± 6.3 y (range, 60–84 y). The participants consisted of 58 healthy controls (HCs), 62 patients with mild cognitive impairment (MCI), and 46 patients with AD as shown in Table 1. The diagnoses of MCI and probable AD were based on the clinical criteria of the National Institute of Neurologic and Communicative Disorders and the Alzheimer's Disease and Related Disorders Association. The Mini-Mental State Examination–Japanese (MMSE-J), the Clinical Dementia Rating Scale–Japanese (CDR-J), and the Wechsler Memory Scale–R, Logical Memory II, corrected for education (WMS-R), were used to classify the early stages of dementia. The HCs scored 24–30 on the MMSE-J, 0 on the CDR-J, and above the cutoff on the WMS-R. The MCI patients scored 24–30 on the MMSE-J, 0.5 on the CDR-J, and below the cutoff on the WMS-R. The AD patients scored 20–26 on the MMSE-J, 0.5 or 1 on the CDR-J, and below the cutoff on the WMS-R.

Imaging Protocol for ^{11}C -PiB PET

^{11}C -PiB PET was performed using 10 different PET camera models by 3 vendors as presented in Table 2 (13). PET images were reconstructed with data from 50 to 70 min after ^{11}C -PiB injection (555 ± 185 MBq). For attenuation correction, the segmented attenuation correction method by a 6-min transmission scan or a CT-based method was used, depending on scanner type, including stand-alone PET scanners and hybrid PET/CT scanners. Of the ^{11}C -PiB PET images, 88 were classified as visually positive, 68 as visually negative, and 10 as visually equivocal by 3 expert nuclear medicine physicians (14). All physicians had specialized in

TABLE 1
Participant Characteristics

Characteristic	HC	MCI	AD
Sex (n)			
Male	30	30	21
Female	28	32	25
Age (y)			
Mean \pm SD	66.4 \pm 4.5	71.4 \pm 5.5	74.4 \pm 6.3
Range	60–80	60–82	62–84
NINCDS-ADRDA	—	—	Probable AD
MMSE-J			
Mean \pm SD	29.3 \pm 1.1	26.7 \pm 1.8	22.2 \pm 1.8
Range	24–30	24–30	20–26
CDR-J	0	0.5	0.5 or 1.0
WMS-R	Above cutoff	Below cutoff	Below cutoff
Visually positive (n)	14	41	43
Visually negative (n)	44	21	3

NINCDS-ADRDA = National Institute of Neurologic and Communicative Disorders and Alzheimer's Disease and Related Disorders Association.

neuroimaging for more than 15 y. The results of the visual interpretation were based on the official judgment of the J-ADNI PET Core (14). In this study, the equivocal images were analyzed with the positive images (98 images).

Workflow of Quantitative Evaluation Method

The positive and negative templates were created in a previous study (8). Eleven typical positive images (4 AD and 7 MCI patients with high ^{11}C -PiB accumulation) were averaged to generate the positive template, and 8 typical negative images (8 HCs) were averaged to generate the negative template (8).

Figure 1 presents the workflow of the quantitative evaluation method (8). These processes were performed using the PMOD software, version 3.7 (PMOD Technologies LLC). First, the PET images were anatomically standardized to either the positive or the negative template. In the adaptive-template-based method, the PET images were standardized to both templates, and the template most similar to the subject image, according to the normalized cross-correlation (NCC), was selected. Second, the transformation vector of the anatomic standardization was recorded. Third, regions of interest were inversely transformed to individual PET images using a transformation vector. We calculated SUV ratio (SUVR) using the empirical PiB-prone region of interest, which was generated to evaluate regions where amyloid- β specifically accumulates (8).

The NCC was calculated to evaluate similarities between anatomically standardized images and the respective templates (8). In addition, the SUVR in 5 brain regions (posterior cingulate gyrus and precuneus, frontal lobe, lateral temporal lobe, lateral parietal lobe, and occipital lobe) was calculated; the reference region was the cerebellar cortex. The average SUVRs of the 5 regions were referred to as mean cortical SUVR (mcSUVR).

Statistical Analysis

JMP 13 (SAS Institute Inc.), was used for statistical analysis. The Steel–Dwass test was used to analyze the significance of differences between NCC and mcSUVR in the 3 groups (HC, MCI, and AD).

TABLE 2
PET Scanners and Reconstruction Parameters for ^{11}C -PiB PET in J-ADNI Study

Scanner vendor	Scanner model	Algorithm	Iterations	Subsets
GE Healthcare	Advance	Iterative (FORE + OSEM)	6	16
	Discovery ST Elite	Iterative (VUE Point plus)	2	40
Shimadzu	Eminence Sophia G/X	FORE + DRAMA	4	NA
	Eminence Sophia B/L	FORE + DRAMA	4	NA
	Eminence G/X	FORE + DRAMA	4	NA
	Headtome V	Iterative (FORE + OSEM)	4	16
Siemens	ECAT Accel	Iterative (FORE + OSEM)	6	16
	ECAT Exact HR+	Iterative (FORE + OSEM)	4	16
	Biograph 6	Iterative (FORE + OSEM)	4	16
	Biograph 16	Iterative (FORE + OSEM)	4	14

FORE = Fourier rebinning; OSEM = ordered-subsets expectation maximization; NA = not available; DRAMA = dynamic row-action maximum-likelihood algorithm.

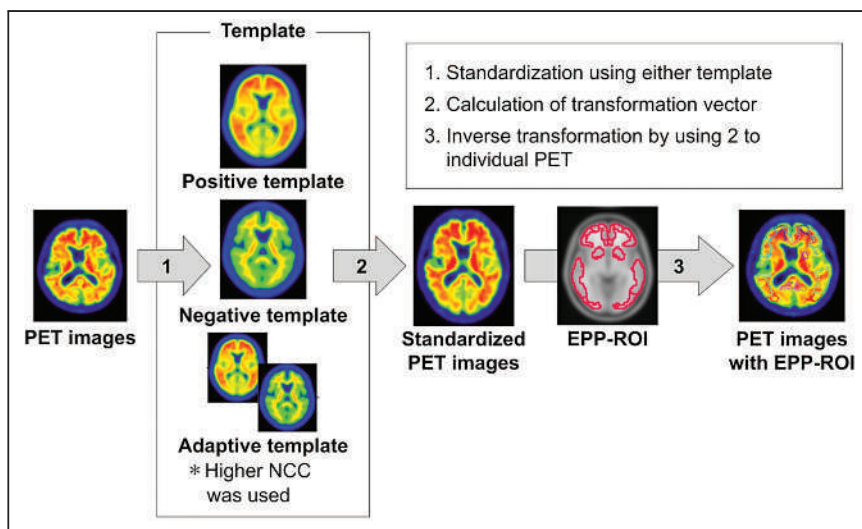


FIGURE 1. Workflow of PET-only quantitative evaluation method. First, PET images are anatomically standardized to either template using positive-template method, negative-template method, or adaptive-template method. Second, transformation vector used for standardization is calculated. Third, empirical PiB-prone region of interest (EPP-ROI) is inverse-transformed to individual PET image using transformation vector.

The McNemar test was used to analyze significance regarding diagnostic ability. The significance level was set to a P value of less than 0.05. The cutoff for differential diagnosis was obtained according to the method of maximizing Youden index (sensitivity + specificity – 1).

RESULTS

Concordance Rate Between Visual Evaluation and Used Template

Table 3 presents the concordance rate between the visual evaluation and the template that was used. When the adaptive template was used, the concordance of the adopted template with visual evaluation was 89.2%, and the association coefficient was 0.803.

NCC in Relation to Different Templates

The results of the NCCs are presented in Figure 2. When the negative template was used, the mean NCCs of the HC, MCI, and AD groups were 0.754 ± 0.122 , 0.654 ± 0.143 , and 0.580 ± 0.106 , respectively. NCCs significantly differed among the 3 groups ($P < 0.05$). HCs who were visually negative had the highest NCC. When the positive template was used, the mean NCCs were 0.548 ± 0.130 for HCs, 0.701 ± 0.142 for MCI patients, and 0.777 ± 0.098 for AD patients. The results differed significantly among the 3 groups ($P < 0.05$): NCCs were higher for positive participants (MCI and AD) than for HCs. When the adaptive-template-based method was used, the mean NCCs were 0.778 ± 0.102 for HCs, 0.791 ± 0.072 for MCI patients, and 0.803 ± 0.050 for AD

patients. All 3 groups exhibited high NCCs, which did not differ significantly.

The mcSUVR in Different Anatomic Standardization Methods

The mcSUVRs obtained using the different anatomic standardization methods are presented in Figure 3. When the positive template was used, mcSUVRs were 1.48 ± 0.33 for HCs, 1.86 ± 0.46 for MCI patients, and 2.12 ± 0.45 for AD patients. When the negative template was used, they were 1.35 ± 0.26 for HCs, 1.68 ± 0.42 for MCI patients, and 1.93 ± 0.44 for AD patients. On the other hand, the mcSUVRs of HCs, MCI patients, and AD patients were 1.37 ± 0.33 , 1.80 ± 0.50 , and 2.10 ± 0.47 , respectively, when the adaptive template was used. The difference in mean mcSUVR among the 3 groups was greatest for the adaptive template. mcSUVR differed

TABLE 3
Visual Evaluation of Participants

Visual evaluation	Clinical diagnosis	No. of participants	No. of images		
			Positive template	Negative template	Adaptive template
Positive	HC	14	58	0	7
	MCI	41	62	0	35
	AD	43	46	0	38
	Total	98	166	0	80
Negative	HC	44	0	58	51
	MCI	21	0	62	27
	AD	3	0	46	8
	Total	68	0	166	86
Concordance rate			59.0%	41.0%	89.2%
Coefficient of association			not	not	0.80

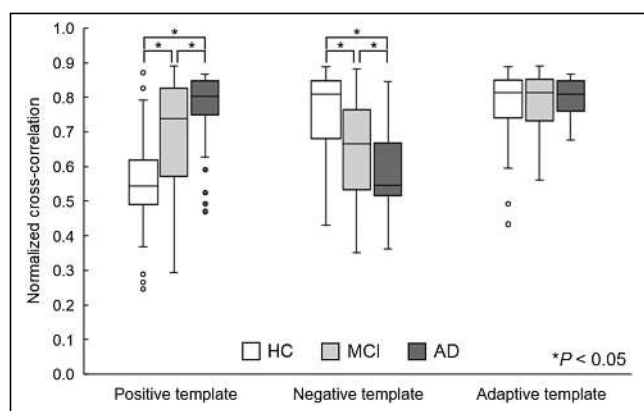


FIGURE 2. NCC results. $*P < 0.05$.

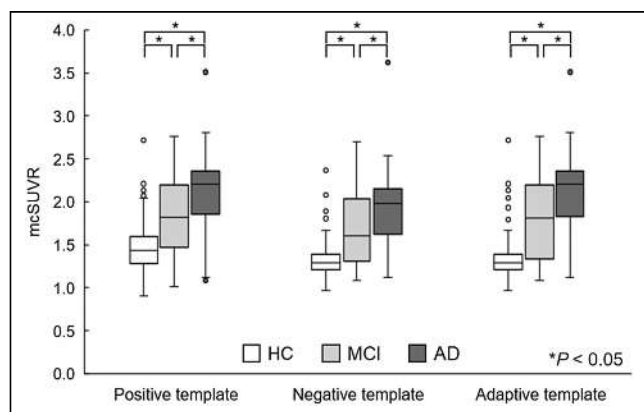


FIGURE 3. mcSUVR results. $*P < 0.05$.

significantly among groups for all methods ($P < 0.05$), although the difference was greatest when the adaptive-template-based method was used.

Diagnostic Ability in Different Anatomic Standardization Methods

Figure 4 and Table 4 show the results of receiver-operating-characteristic analysis for differentiating positive (MCI and AD) from negative (HC). The areas under the curve did not

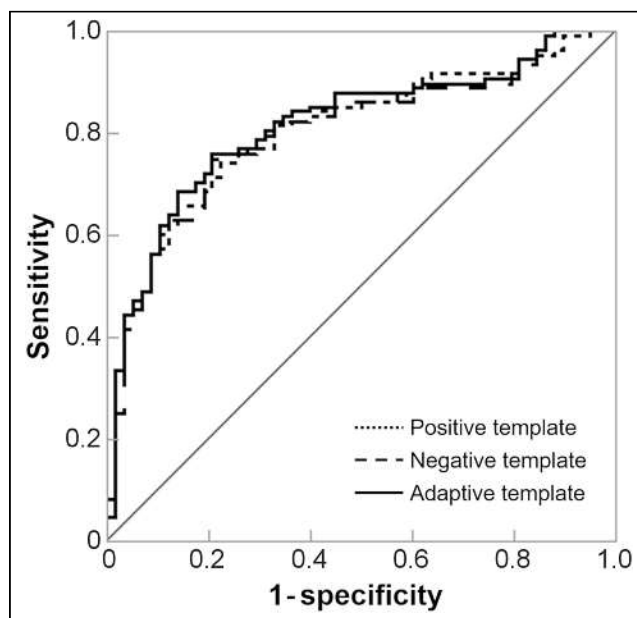


FIGURE 4. mcSUVR receiver-operating-characteristic curves for each template. Areas under curve for positive template-based method, negative template-based method, and adaptive template-based method were 0.806, 0.801, and 0.815, respectively.

significantly differ among the anatomic standardization methods; however, the area under the curve for the adaptive-template-based method was slightly larger than that for the single-template-based methods. The diagnostic ability of each method is presented in Table 4. The adaptive-template-based and negative-template-based methods exhibited significantly higher sensitivity than did the positive-template-based method ($P < 0.05$). Neither specificity nor accuracy differed significantly among methods; however, the accuracy of the adaptive-template-based method was the highest.

DISCUSSION

In this study, we examined the influence of the different anatomic standardization methods on ^{11}C -PiB PET

TABLE 4
Diagnostic Ability

Template	AUC	Cutoff	Sensitivity	Specificity	Accuracy
Positive	0.806	1.80	0.657	0.862	0.729
Negative	0.801	1.40	0.750*	0.793	0.765
Adaptive	0.815	1.40	0.759*	0.793	0.771

* $P < 0.05$ (difference from positive template).

AUC = area under curve.

quantitative evaluation, focusing on diagnostic accuracy for AD. The adaptive-template method was useful in improving the diagnostic performance of AD, as the mcSUVR difference among groups was greater with this method than with the single-template methods.

The adaptive-template method exhibited high agreement (89.2%) with visual classification. The mcSUVR of the HC, MCI, and AD groups differed significantly for all standardization methods. For the differential diagnosis, the adaptive-template-based method was most accurate.

The adaptive-template-based method exhibited higher NCCs in all groups than did the single-template-based methods. Lundqvist et al. and Bourgeat et al. examined ^{18}F -flutemetamol PET and ^{11}C -PiB PET, respectively (9,10). They reported that the template most similar to visual evaluation adopted by using a cross-correlation coefficient and normalized mutual information enhanced the quantitative accuracy. Therefore, the adaptive-template method is considered to be a successful adaptation of an individual PET image.

mcSUVR differed significantly among the 3 groups ($P < 0.05$), with the mcSUVR of the adaptive-template-based method being the largest (Fig. 3). For sensitivity and accuracy based on mcSUVR, the adaptive-template method outperformed the single-template methods. This improved performance is probably due to the fact that we calculated the cutoff to maximize accuracy. The negative and adaptive templates had the same cutoffs, whereas the positive template had a higher cutoff (Table 4). This cutoff (1.8) is high, compared with a previous study (1.5) (15), and may include a large number of false-negative cases (low sensitivity). The specificities of the templates did not differ significantly, although the specificity of the positive template was higher. The receiver-operating-characteristic curves did not significantly differ among the 3 methods, although the area under the curve for the adaptive-template-based method was superior to those for the single-template-based methods.

Edison et al. reported that the use of a conventional MRI-based template and a single PET template yielded comparable results in the ^{11}C -PiB PET quantitative analysis (16). Moreover, several studies have demonstrated that the use of multiple PET templates for anatomic standardization improved quantitative accuracy. Bourgeat et al. reported no significant difference between the SUVRs using the adaptive PET atlas approach and the MRI-based SUVR, although the SUVR

obtained using the single mean PET atlas was significantly different from the MRI-based SUVR (10). Kang et al. developed a deep learning-based approach to generate multiple adaptive ^{11}C -PiB PET templates (17). This approach also significantly enhanced the quantitative accuracy of PET-based anatomic standardization (17). Our results suggested that the adaptive-template-based method can provide sufficient accuracy for amyloid PET anatomic standardization, although only 2 templates (positive and negative) were used.

This study had some limitations. First, the number of participants was small. Thus, further examination of a larger number of participants is needed to yield more robust results. Second, 2 templates were examined in this study. In the adaptive-template-based method, increasing the number of templates with various types of accumulation has the potential to improve the accuracy of anatomic standardization. Third, the PET data were acquired more than 10 y ago. Because recent PET scanners can provide higher-resolution images, the difference between positive and negative images might be clearer. Therefore, we expect the adaptive-template-based method to be effective for current PET images as well.

CONCLUSION

We have examined the influence of different anatomic standardization methods on amyloid PET quantitative evaluation, focusing on diagnostic accuracy for AD. The adaptive-template-based method slightly improved diagnostic accuracy in comparison with the single-template-based methods.

DISCLOSURE

This study was supported by JSPS KAKENHI grant 16K19882. No other potential conflict of interest relevant to this article was reported.

ACKNOWLEDGMENT

Data used in the preparation of this article were obtained from the J-ADNI database deposited in the National Bioscience Database Center (NBDC) Human Database, Japan (Research ID: hum0043.v1, 2016). As such, the investigators within J-ADNI contributed to the design and implementation of J-ADNI or provided data but did not participate in the analysis or writing of this report. A complete listing of J-ADNI investigators can be found at <https://humandbs.biosciencedbc.jp/en/hum0043-v1>.

REFERENCES

1. International statistical classification of diseases and related health problems. World Health Organization website. <https://icd.who.int/browse11/l-m/en/#/http%3a%2f%2fid.who.int%2f%2fid%2fentity%2f546689346>. Updated May 2021. Accessed July 2, 2021.
2. Akatsu H, Takahashi M, Matsukawa N, et al. Subtype analysis of neuropathologically diagnosed patients in a Japanese geriatric hospital. *J Neurol Sci*. 2002;196:63–69.
3. Ninomiya T. Research on future projection of the population of the elderly with dementia in Japan [in Japanese]. Ministry of Health, Labour, and Welfare website. <https://mhlw-grants.niph.go.jp/project/23685/1>. Published 2015. Accessed July 9, 2021.

4. Jack CR Jr, Knopman DS, Jagust WJ, et al. Hypothetical model of dynamic biomarkers of the Alzheimer's pathological cascade. *Lancet Neurol.* 2010;9:119–128.
5. Evans AC, Janke AL, Collins DL, et al. Brain templates and atlases. *Neuroimage.* 2012;62:911–922.
6. Gispert JD, Pascau J, Reig S, et al. Influence of the normalization template on the outcome of statistical parametric mapping of PET scans. *Neuroimage.* 2003;19:601–612.
7. Della Rosa PA, Cerami C, Gallivanone F, et al. A standardized [^{18}F]-FDG-PET template for spatial normalization in statistical parametric mapping of dementia. *Neuroinformatics.* 2014;12:575–593.
8. Akamatsu G, Ikari Y, Ohnishi A, et al. Automated PET-only quantification of amyloid deposition with adaptive template and empirically pre-defined ROI. *Phys Med Biol.* 2016;61:5768–5780.
9. Lundqvist R, Lilja J, Thomas BA, et al. Implementation and validation of an adaptive template registration method for ^{18}F -flutemetamol imaging data. *J Nucl Med.* 2013;54:1472–1478.
10. Bourgeat P, Villemagne VL, Dore V, et al. Comparison of MR-less PiB SUVR quantification methods. *Neurobiol Aging.* 2015;36(suppl 1):S159–S166.
11. Shimokawa N, Akamatsu G, Kadosaki M, et al. Feasibility study of a PET-only amyloid quantification method: a comparison with visual interpretation. *Ann Nucl Med.* 2020;34:629–635.
12. Iwatsubo T. Japanese Alzheimer's Disease Neuroimaging Initiative: present status and future. *Alzheimers Dement.* 2010;6:297–299.
13. Ikari Y, Nishio T, Makishi Y, et al. Head motion evaluation and correction for PET scans with ^{18}F -FDG in the Japanese Alzheimer's disease neuroimaging initiative (J-ADNI) multi-center study. *Ann Nucl Med.* 2012;26:535–544.
14. Yamane T, Ishii K, Sakata M, et al. Inter-rater variability of visual interpretation and comparison with quantitative evaluation of ^{11}C -PiB PET amyloid images of the Japanese Alzheimer's Disease Neuroimaging Initiative (J-ADNI) multicenter study. *Eur J Nucl Med Mol Imaging.* 2017;44:850–857.
15. Jagust WJ, Bandy D, Chen K, et al. The Alzheimer's Disease Neuroimaging Initiative positron emission tomography core. *Alzheimers Dement.* 2010;6:221–229.
16. Edison P, Carter SF, Rinne JO, et al. Comparison of MRI based and PET template based approaches in the quantitative analysis of amyloid imaging with PIB-PET. *Neuroimage.* 2013;70:423–433.
17. Kang SK, Seo S, Shin SA, et al. Adaptive template generation for amyloid PET using a deep learning approach. *Hum Brain Mapp.* 2018;39:3769–3778.

Interobserver Agreement in the Diagnosis of Parkinson Disease with Cardiac ^{123}I -Metaiodobenzylguanidine Scintigraphy

Robert W. Foley¹, Stewart L. Redman¹, Isabel J. Laurence², Richard N. Graham¹, and David Little¹

¹Department of Radiology, Royal United Hospitals Bath NHS Foundation Trust, Bath, United Kingdom; and ²Department of Radiology, Southmead Hospital, North Bristol NHS Trust, North Bristol, United Kingdom

The aim of this study was to analyze the interobserver agreement of visual and quantitative assessment of cardiac ^{123}I -metaiodobenzylguanidine scintigraphy. **Methods:** Planar images were acquired using a low-energy collimator. The heart-to-mediastinum (HM) ratio was adjusted for the use of a low-energy collimator, using a published formula. Interpretation was undertaken both visually and after the addition of adjusted HM ratios. Image findings were classified as normal, abnormal, or borderline. **Results:** The cohort consisted of 10 patients. On visual interpretation only, there was strong agreement on the interpretation of the scan ($\kappa = 0.82$, $P < 0.01$). Adjusted HM ratios led to a significant increase in mean ratios (1.79 vs. 1.36, $P = 0.02$) and, when utilized in reporting, resulted in perfect agreement ($\kappa = 1.0$, $P < 0.01$). **Conclusion:** The use of quantified HM ratios adjusted for low-energy collimator use improves on visual assessment alone and allowed for excellent interobserver agreement.

Key Words: MIBG cardiac scintigraphy; Parkinson disease; heart-to-mediastinum ratio; collimator

J Nucl Med Technol 2021; 49:262–264

DOI: 10.2967/jnmt.120.258632

Sympathetic input, via noradrenaline, augments the function of the heart as part of the autonomic nervous system. Patients with Parkinson disease display altered noradrenergic function (1). ^{123}I -metaiodobenzylguanidine (^{123}I -MIBG) is a radioactive analog of noradrenaline, which localizes in the myocardial sympathetic nerve terminals and thereby allows this altered function to be imaged (2).

Myocardial sympathetic denervation on cardiac ^{123}I -MIBG scintigraphy has shown great promise in the differential diagnosis of Parkinson disease (3,4) and is included in the Movement Disorder Society diagnostic criteria for Parkinson disease (5). A cardiac ^{123}I -MIBG study can be assessed both visually and quantitatively. The type of quantitative data derived from this test is the heart-to-mediastinum (HM) ratio, which has been demonstrated to be significantly lower in patients with Parkinson disease than in patients with other Parkinsonian syndromes (6).

The use of a low-energy collimator for cardiac ^{123}I -MIBG scintigraphy produces significantly lower HM ratios than those produced by a medium-energy collimator (7). However, correlation between the 2 methods is excellent, and the use of a simple formula allows for the conversion of HM ratios derived from a low-energy collimator cardiac ^{123}I -MIBG study (8).

In the present study, we analyzed the interobserver agreement in the reporting of cardiac ^{123}I -MIBG studies using visual interpretation and quantitative data with HM ratios. We hypothesized that the use of a low-energy collimator conversion formula to calculate adjusted HM ratios will lead to improved interobserver agreement.

MATERIALS AND METHODS

Study Design

A retrospective review was conducted of all patients who underwent cardiac ^{123}I -MIBG scintigraphy at 2 nuclear medicine departments between 2015 and 2019. Patients who underwent the study for a nonneurologic indication were excluded. The institutional review board (Trust Audit Committee) approved this retrospective study, and the requirement to obtain informed consent was waived.

Technical Information

After intravenous injection of 100 MBq (2.7 mCi) of ^{123}I -MIBG, planar images were acquired in the anterior view at both 15 min and 4 h using a dual-head Infinia γ -camera (GE Healthcare) and a low-energy collimator. Photopeak energy was centered on 159 keV with a 10% window and processed on Xeleris software (GE Healthcare). The HM ratio was measured by 2 consultant radiologists on the anterior planar images for image interpretation. A freehand region of interest was drawn around the left ventricle, and a small rectangular region of interest was drawn in the mediastinum, as per Kashiwara et al. (6). The average counts in the left ventricular region of interest were divided by those in the mediastinal region of interest to calculate the HM ratio. Both the early-phase and the delayed-phase images were processed. Normal HM ratios may vary by patient population, and there are no clearly defined normal values for HM ratios using low-energy or medium-energy collimators. However, a normal HM ratio of more than 2.0 has been suggested for both the early and the delayed imaging (6,9), and it has also been demonstrated in healthy controls that a normal early HM ratio is more than 2.07 and a normal delayed HM ratio is more than 1.86 (10). We subsequently recalculated each patient's HM ratio for a medium-energy collimator, using the following published formula: medium energy HM ratio = low-energy HM ratio/(0.41 – 0.63) (8).

Received Oct. 14, 2020; revision accepted Mar. 12, 2021.

For correspondence or reprints, contact Robert W. Foley (rwjfoley@gmail.com).

Published online April 5, 2021.

COPYRIGHT © 2021 by the Society of Nuclear Medicine and Molecular Imaging.

Image Interpretation

Each ^{123}I -MIBG study was visually interpreted by 2 radiology consultants without access to the patient's HM ratio and masked to the clinical information for each patient. Interpretations were classified as normal, abnormal, or borderline for each patient (Fig. 1). Interpretation was then undertaken using the visual analysis and quantitative HM ratio data.

Statistical Analysis

Interobserver agreement was calculated using the Cohen κ . Interobserver agreement for the HM ratio measured by consultants, registrars, and technologists was performed via intraclass coefficient correlation analysis. The mean HM ratio with low-energy collimators and the mean HM ratio after adjustment with the medium-energy formula were compared using the paired t test. Statistical analysis was performed in R software, version 3.3.3.

RESULTS

The cohort consisted of 10 consecutive patients, with an average age of 71 y. There were 7 men and 3 women. The clinical diagnoses were Parkinson disease ($n = 7$), multiple-system atrophy ($n = 2$), and dementia with Lewy bodies ($n = 1$). On visual interpretation of each patient's cardiac ^{123}I -MIBG study, there was strong agreement between the 2 reporters' interpretation of the results ($\kappa = 0.82$; 95% CI, 0.510–1.00; $P < 0.01$). There was disagreement about one patient (Fig. 2), for whom reporter 1 labeled the results as borderline whereas reporter 2 labeled them as abnormal (Table 1).

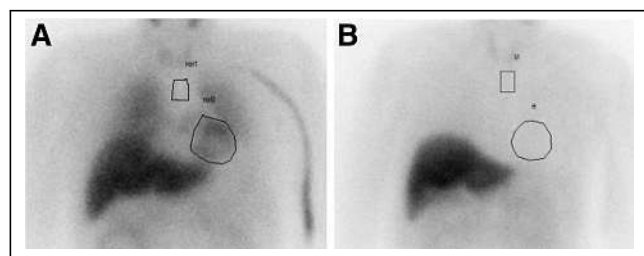


FIGURE 1. Cardiac ^{123}I -MIBG scintigraphy interpreted as normal on visual assessment by both reporters (A), and study interpreted as abnormal by both reporters (B). HM ratios were 2.3 and 1.1, respectively, on delayed-phase images. H = heart; M = mediastinum; ROI = region of interest.

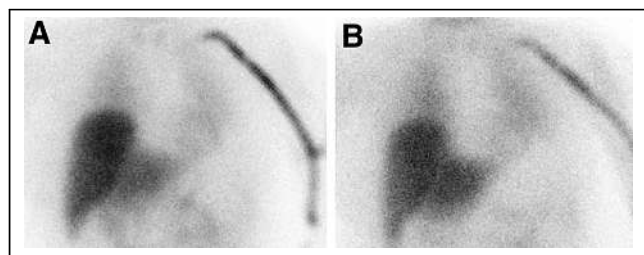


FIGURE 2. Early (A) and delayed (B) cardiac ^{123}I -MIBG scintigraphy images interpreted as borderline by one reporter and abnormal by second reporter on visual assessment. After addition of HM ratios of 1.78 and 1.58, respectively, both reporters interpreted study as abnormal.

TABLE 1
Visual Interpretation of Study Cohort

Reporter 2	Reporter 1		
	Normal	Borderline	Abnormal
Normal	5	1	0
Borderline	0	0	0
Abnormal	0	0	4

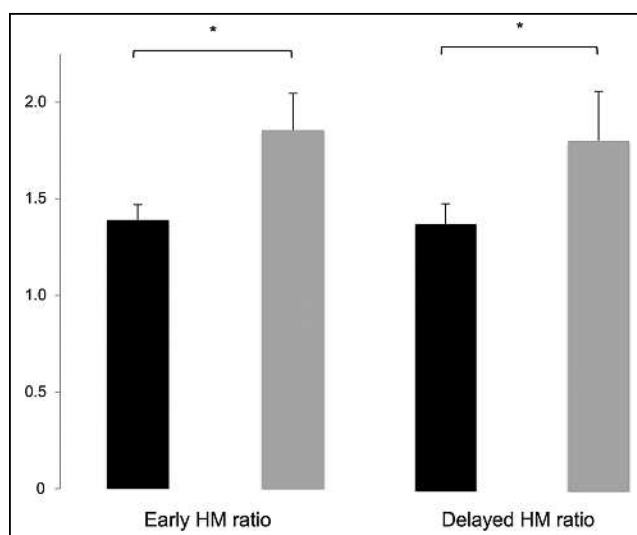


FIGURE 3. There was significant increase in average HM ratio, for both early-phase and delayed-phase imaging after application of linear conversion formula (medium-energy HM ratio = low-energy HM ratio/(0.41 – 0.63)). Original HM ratio is shown in black, with corrected HM ratio in gray. * $P < 0.05$.

The mean HM ratio in this cohort was 1.36 using the low-energy collimators, whereas the mean HM ratio was 1.79 using the medium-energy conversion formula (Fig. 3). This was a statistically significant increase ($P = 0.02$). The interpretation of each cardiac ^{123}I -MIBG study after the addition of the adjusted HM ratios led to perfect agreement between the 2 raters ($\kappa = 1.0$; 95% CI, 1.0–1.0; $P < 0.01$). The patient about whom there was disagreement on the visual assessment demonstrated an HM ratio of 1.78 on early imaging and a ratio of 1.58 on delayed imaging. This patient's results were subsequently labeled as abnormal by both raters after the addition of the quantitative data to their interpretation.

DISCUSSION

The use of cardiac ^{123}I -MIBG scintigraphy in the diagnostic pathway for patients under investigation for Parkinson disease has been well established in the literature. The gold standard for the diagnosis of Parkinson disease is a clinical one; however, in a systematic review of 2016, the overall accuracy of clinical diagnosis is approximately 80%–83% (11). Therefore, imaging retains a core role in attempts to improve this accuracy. Several studies have demonstrated significantly lower HM ratios on cardiac ^{123}I -MIBG scintigraphy in patients

with Parkinson disease (6,12) and in the other Lewy body diseases: dementia with Lewy bodies and pure autonomic failure (6,9,12,13). This finding is in contrast to various patient populations with a normal HM ratio, which includes healthy controls and patients with vascular parkinsonism, drug-induced parkinsonism and the Parkinson-plus syndromes, multiple-system atrophy, progressive supranuclear palsy, and corticobasal degeneration (6,9,12,13).

The results of the present study demonstrate that agreement between 2 experienced readers in the visual interpretation of cardiac ^{123}I -MIBG is strong. The interobserver agreement is further improved by the addition of quantitative data in the form of the HM ratio. Previous research has demonstrated that visual interpretation of cardiac ^{123}I -MIBG studies was equivalent to that of quantitative HM ratios (14,15). In the present study, we demonstrated that the use of quantitative methods in combination with visual assessment in the reporting of ^{123}I -MIBG studies leads to improved agreement between reporters.

Some authors recommend the HM ratio as the primary method of interpretation (16), with visual assessment used as a secondary tool, particularly in borderline cases. This technique would require the normal and abnormal cutoffs for the HM ratio to be defined precisely at each center. However, this is clearly not the case, with normal values demonstrating wide ranges in the literature, varying from 1.38 to 1.94 for early imaging and from 1.34 to 2.40 for delayed imaging (3). Therefore, we recommend a reporting strategy that utilizes both visual interpretation and the quantitative HM ratio data in tandem when interpreting cardiac ^{123}I -MIBG scintigraphy.

The present study utilized a low-energy, high-resolution collimator, as use of such a collimator was our practice for other ^{123}I studies. Inoue et al. found that the average ratio in patients imaged with a medium-energy collimator was 2.66 ± 0.74 , whereas the average ratio with a low-energy collimator was 1.81 ± 0.29 ($P < 0.05$) (7). Therefore, the use of a low-energy collimator makes comparison with established cutoffs in the literature difficult. We have demonstrated that the use of a low-energy collimator for cardiac ^{123}I -MIBG studies can be adjusted via the formula derived by Brumberg et al. (8). If cardiac ^{123}I -MIBG scintigraphy is performed using a low-energy collimator, this formula can be utilized to allow for meaningful comparisons of HM ratios with the published cutoffs in the literature. No such study comparing the clinical interpretation of cardiac ^{123}I -MIBG studies acquired using a medium-energy and a low-energy collimator has been undertaken, and this is a potential area for future research.

We acknowledge several limitations to the present study. This was a relatively small patient cohort under investigation. However, we attempted to remedy this limitation by including 2 nuclear medicine centers. We did not attempt to quantify the overall accuracy of this test in the diagnosis of Parkinson disease. However, as previously discussed, there is myriad evidence for the utility of cardiac ^{123}I -MIBG scintigraphy in the diagnostic pathway for patients under investigation for Parkinson disease.

The present study adds to the body of evidence surrounding the use of cardiac ^{123}I -MIBG scintigraphy in 2 ways. First, we demonstrated that interobserver agreement is improved by the use of visual assessment and HM ratio data. We therefore recommend that a visual and quantitative assessment take place in tandem for the reporting of cardiac ^{123}I -MIBG studies. Second, we demonstrated that the use of a low-energy collimator for cardiac ^{123}I -MIBG studies can be adjusted via a published formula (8) to allow for comparisons with published HM ratios.

CONCLUSION

The use of HM ratios in cardiac ^{123}I -MIBG scintigraphy, adjusted for low-energy collimator use, improves on visual assessment alone and allowed for excellent interobserver agreement in the present study.

DISCLOSURE

No potential conflict of interest relevant to this article was reported.

REFERENCES

- Goldstein DS, Holmes C, Cannon RO, Eisenhofer G, Kopin IJ. Sympathetic cardio-neuropathy in dysautonomias. *N Engl J Med*. 1997;336:696–702.
- Lucio CG, Cuccurullo V, Restuccia A, Tamburrini O, Rotondo A, Mansi L. Neurological applications for myocardial MIBG scintigraphy. *Nucl Med Rev*. 2013;16:35–41.
- Orimo S, Suzuki M, Inaba A, Mizusawa H. ^{123}I -MIBG myocardial scintigraphy for differentiating Parkinson's disease from other neurodegenerative parkinsonism: a systematic review and meta-analysis. *Parkinsonism Relat Disord*. 2012;18:494–500.
- Treglia G, Cason E, Stefanelli A, et al. MIBG scintigraphy in differential diagnosis of Parkinsonism: a meta-analysis. *Clin Auton Res*. 2012;22:43–55.
- Postuma RB, Berg D, Stern M, et al. MDS clinical diagnostic criteria for Parkinson's disease. *Mov Disord*. 2015;30:1591–1601.
- Kashihara K, Ohno M, Kawada S, Okumura Y. Reduced cardiac uptake and enhanced washout of ^{123}I -MIBG in pure autonomic failure occurs conjointly with Parkinson's disease and dementia with Lewy bodies. *J Nucl Med*. 2006;47:1099–1101.
- Inoue Y, Suzuki A, Shirouzu I, et al. Effect of collimator choice on quantitative assessment of cardiac iodine 123 MIBG uptake. *J Nucl Cardiol*. 2003;10:623–632.
- Brumberg J, Blazhenets G, Schröter N, et al. Imaging cardiac sympathetic innervation with MIBG: linear conversion of the heart-to-mediastinum ratio between different collimators. *EJNMMI Phys*. 2019;6:12.
- Kawazoe M, Arima H, Maeda T, et al. Sensitivity and specificity of cardiac ^{123}I -MIBG scintigraphy for diagnosis of early-phase Parkinson's disease. *J Neurol Sci*. 2019;407:116409.
- Roberts G, Lloyd JJ, Kane JPM, et al. Cardiac ^{123}I -MIBG normal uptake values are population-specific: results from a cohort of controls over 60 years of age. *J Nucl Cardiol*. September 16, 2019 [Epub ahead of print].
- Rizzo G, Copetti M, Arcuti S, Martino D, Fontana A, Loggrosino G. Accuracy of clinical diagnosis of Parkinson disease. *Neurology*. 2016;86:566–576.
- Yoshita M. Differentiation of idiopathic Parkinson's disease from striatonigral degeneration and progressive supranuclear palsy using iodine-123 meta-iodobenzylguanidine myocardial scintigraphy. *J Neurol Sci*. 1998;155:60–67.
- Orimo S, Ozawa E, Nakade S, Sugimoto T, Mizusawa H. ^{123}I -metaiodobenzylguanidine myocardial scintigraphy in Parkinson's disease. *J Neurol Neurosurg Psychiatry*. 1999;67:189–194.
- Tiraboschi P, Corso A, Guerra UP, et al. ^{123}I -2- β -carbomethoxy-3- β -(4-iodophenyl)-N-(3-fluoropropyl) nortropane single photon emission computed tomography and ^{123}I -metaiodobenzylguanidine myocardial scintigraphy in differentiating dementia with Lewy bodies from other dementias: a comparative study. *Ann Neurol*. 2016;80:368–378.
- Sakamoto F, Shiraishi S, Tsuda N, et al. ^{123}I -MIBG myocardial scintigraphy for the evaluation of Lewy body disease: are delayed images essential? Is visual assessment useful? *Br J Radiol*. 2016;89:20160144.
- Roberts G, Kane JPM, Lloyd JJ, et al. A comparison of visual and semiquantitative analysis methods for planar cardiac ^{123}I -MIBG scintigraphy in dementia with Lewy bodies. *Nucl Med Commun*. 2019;40:734–743.

⁶⁸Ga-DOTATATE PET/CT for Neuroblastoma Staging: Utility for Clinical Use

Ata Ur Rehman Maaz¹, Jim O'Doherty², and Mehdi Djekidel³

¹Division of Hematology Oncology, Department of Pediatrics, Sidra Medicine, Doha, Qatar; ²Siemens Healthineers, Charleston, South Carolina; and ³Division of Nuclear Medicine and Molecular Imaging, Department of Diagnostic Imaging, Sidra Medicine, Doha, Qatar

Metaiodobenzylguanidine (MIBG) imaging has been the standard for neuroblastoma staging for many decades. Novel agents such as ¹⁸F-DOPA and ⁶⁸Ga-DOTATATE are being used nowadays in academic centers. During the coronavirus disease 2019 (COVID-19) pandemic, procurement of ¹²³I-MIBG has proved particularly challenging, necessitating the use of ⁶⁸Ga-DOTATATE PET. ⁶⁸Ga-DOTATATE is Food and Drug Administration–approved for imaging of somatostatin receptor–positive gastroenteropancreatic neuroendocrine tumors. **Methods:** ⁶⁸Ga-DOTATATE PET/CT imaging was performed for staging of 3 pediatric patients with neuroblastoma at our institution. A review of the literature was also completed. **Results:** ⁶⁸Ga-DOTATATE PET/CT scans were successfully performed on all patients. All patients showed ⁶⁸Ga-DOTATATE–avid disease. PET scans showed an excellent spatial resolution and demonstrated high accuracy in concordance with current European Association of Nuclear Medicine guidelines. **Conclusion:** We have presented ⁶⁸Ga-DOTATATE PET/CT imaging for staging of neuroblastoma and believe it can reliably be used as an alternative to ¹²³I-MIBG. It has technical, clinical, and practical advantages making it an attractive option. Further multicenter studies are required before it can be recommended for standard clinical use.

Key Words: neuroblastoma imaging; MIBG; ⁶⁸Ga-DOTATATE; COVID-19

J Nucl Med Technol 2021; 49:265–268

DOI: 10.2967/jnmt.120.258939

Neuroblastoma, the most common extracranial solid tumor in the pediatric age group, accounts for about 10% of all solid tumors. It varies in presentation from self-resolving disease to the highly malignant variant associated with an extremely poor prognosis. The staging evaluation of neuroblastoma requires both anatomic and nuclear medicine imaging to look for skeletal metastatic deposits (1,2). ¹²³I-metaiodobenzylguanidine (MIBG) can be used for localization of neural crest tumors such as neuroblastoma, pheochromocytoma, and other neuroendocrine tumors. MIBG with ¹³¹I and more recently ¹²³I has been the standard for

neuroblastoma staging since its utility was first reported by Geatti et al. in 1985 (3,4).

The reported sensitivity and specificity of ¹²³I-MIBG are approximately 90% (2,5). However, because 10% of neuroblastomas are not ¹²³I-MIBG–avid, alternate imaging techniques have been investigated, including PET with ¹⁸F-FDG and ¹⁸F-DOPA, as well as PET/CT with DOTA-conjugated peptides such as ⁶⁸Ga-DOTATATE. Early evidence suggests that these modalities may be superior in sensitivity and specificity to MIBG, thus having the potential of replacing MIBG (6–9).

Somatostatin receptors are variably expressed in neuroblastoma (10,11). Somatostatin analogs such as ⁶⁸Ga-DOTATATE have been in clinical use for nearly a decade. Their role is most established in imaging and treatment of adult neuroendocrine tumors and pheochromocytoma but has also been studied in neuroblastoma in limited settings (7,8). ⁶⁸Ga-DOTATATE PET has been studied at the time of recurrence and at the therapeutic planning phase within a theragnostic paradigm. However, there are very few reports of its role at diagnosis for staging (5,12).

Because MIBG production is limited globally, the severe acute respiratory syndrome coronavirus 2 (coronavirus disease 2019 [COVID-19]) pandemic has resulted in unacceptable delays in performing MIBG scans due to interruption in international air traffic. Its availability became particularly challenging at our institution, and we therefore decided to perform ⁶⁸Ga-DOTATATE PET scans for 3 newly diagnosed patients with neuroblastoma. This PET agent is locally produced in a nearby center, obviating the delivery logistics. Here, we report our results and review the literature.

MATERIALS AND METHODS

At the beginning of the COVID 19 pandemic, 3 patients were diagnosed with neuroblastoma at Sidra Medicine. MIBG scintigraphy had to be cancelled for patient 1 when the radiopharmaceutical did not arrive on the scheduled date because of flight cancellations. In a discussion with the clinical team, we decided to perform ⁶⁸Ga-DOTATATE PET/CT imaging instead. For subsequent patients, ⁶⁸Ga-DOTATATE PET was done electively to avoid delays and hazards during the pandemic.

A local ⁶⁸Ge/⁶⁸Ga generator was used to produce ⁶⁸Ga, which was used to radiolabel DOTATATE. Required quality control tests were performed before injecting the patient, in accordance with good manufacturing practices. After radiopharmaceutical injection, an

Received Oct. 20, 2020; revision accepted Feb. 16, 2021.
For correspondence or reprints, contact Mehdi Djekidel (mdjekidel@sidra.org).

Published online April 5, 2021.

COPYRIGHT © 2021 by the Society of Nuclear Medicine and Molecular Imaging.

uptake phase of 45–60 min took place before the patient was scanned. All 3 patients were scanned on a GE Healthcare Discovery 690 PET/CT scanner with an axial field of view of 15.7 cm. A low-dose CT scan (80 kVp, mA dose modulation, adaptive statistical iterative reconstruction, 0.5-s rotation time, 40-mm collimation) was performed for attenuation correction and anatomic localization, followed by a whole-body PET scan at 4 min per bed position with an 11-slice overlap. Images were reconstructed using a time-of-flight iterative reconstruction algorithm with a correction for point-spread function (VUE Point FX [GE Healthcare]: 2 iterations, 28 subsets), and a 3.4-mm postreconstruction gaussian filter. The final pixel size was 1.56×1.56 mm, with a slice thickness of 3.27 mm. All 3 patients were scanned under general anesthesia. The need for sedation was independent of the type of study, as the patients would have required general anesthesia for MIBG as well. The administered activities were weight-based according to the guidelines of the Society of Nuclear Medicine and Molecular Imaging and the European Association of Nuclear Medicine (74 MBq [2 mCi], 101.75 MBq [2.75 mCi], and 45.88 MBq [1.24 mCi] in the first, second, and third patients, respectively) (2).

RESULTS

Patient 1

A 23-mo-old boy presented with lower back pain, ataxia, and leg weakness for 5 d. Physical examination rapidly progressed from normal to lower-limb weakness and frank paraplegia. His work-up included an MRI scan showing a paravertebral mass at the level of the T2–T4 vertebrae, causing spinal cord compression and edema. He underwent emergency laminotomy and laminoplasty by the neurosurgeons and a debulking procedure resulting in return of lower-limb function over the next 48 h.

Patient 2

A 6-y-old girl presented with an intermittent limp over 2 mo. There were no other symptoms. On physical examination, she was unable to stand straight because of pain in the left leg and had mild tenderness on the left side of the abdomen. MRI of her abdomen and pelvis demonstrated a large mass in the left adrenal gland and numerous bony metastatic lesions.

Patient 3

A 3.5-y-old girl presented with weight loss, swelling of the left eye, body aches, and constitutional symptoms over several months. She was severely malnourished and had left-sided proptosis. MRI showed a right-sided adrenal mass, numerous liver metastases, and multiple vertebral lesions.

The clinical and imaging findings are summarized in Table 1, Supplemental Table 1, and Figures 1–4 (supplemental materials are available at <http://jnmmt.snmjournals.org>).

DISCUSSION

The COVID-19 pandemic has posed many unanticipated and unprecedented health-care challenges worldwide, including challenges in the care of cancer patients (13). Before the pandemic, establishing a cancer diagnosis and performing the standard staging investigation were not seen to be a potential problem. Faced with the logistic difficulty of ^{123}I -MIBG procurement, ^{68}Ga -DOTATATE PET scans were performed in the light of limited but compelling evidence of their utility for initial staging of neuroblastoma. Our results will add to the evidence base for future studies.

TABLE 1
Patient Characteristics

Characteristic	Patient 1	Patient 2	Patient 3
Age	23 mo	6 y	3.5 y
Sex	Male	Female	Female
Clinical presentation	Ataxia, irritability, progressing to paraparesis	Limp, discomfort on left side of abdomen	Body pain, swelling of left eye, weight loss, cachexia
Histopathology	Poorly differentiated neuroblastoma	Poorly differentiated neuroblastoma	Not done
Cytogenetics			Not done
N-Myc	Not amplified	Not amplified	
SCA (1p [−] , 11q ⁺ , any other, LOH)	Not seen	1q ⁺ , 11q [−] , 17q ⁺ , X [−] , no LOH	
Alk	No rearrangement	No rearrangement	
NCA	Not seen	Not seen	
Bone marrow	No evidence of infiltration	Infiltrated by nonhematopoietic tumor, neuroblastoma	Infiltrated by nonhematopoietic tumor, neuroblastoma
Urinary catecholamines			
VMA/creatinine ratio	14.1 (0–6.3)	90.7 (0–4.7)	209.8 (0–6.3)
HVA/creatinine ratio	9.9 (0–13.6)	95.6 (0–9.4)	191.0 (0–13.6)

SCA = segmental chromosomal abnormalities; LOH = loss of heterozygosity; NCA = numerical chromosomal abnormalities; 1p[−] = 1 p deletion; 11q[−] = 11q deletion; 17q⁺ = gain of 17q; X[−] = deletion of X-chromosome; N-Myc = N-Myc oncogene; Alk = anaplastic lymphoma kinase; VMA = vanillylmandelic acid; HVA = homovanillic acid.

Data in parentheses represent reference range.

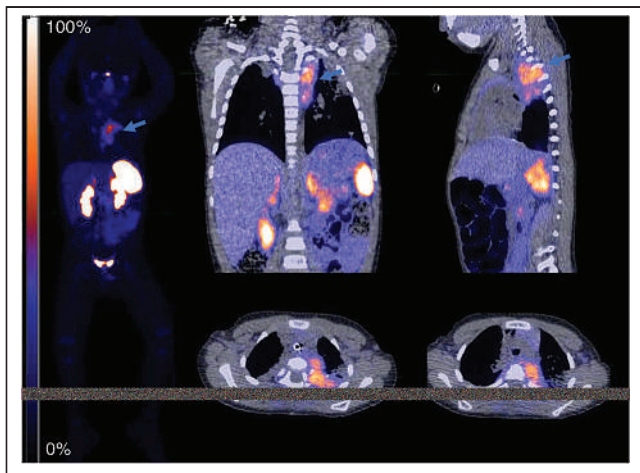


FIGURE 1. Increased uptake in left-sided paravertebral mass and invading the spinal canal and adjacent vertebral body of T3 (blue arrows).

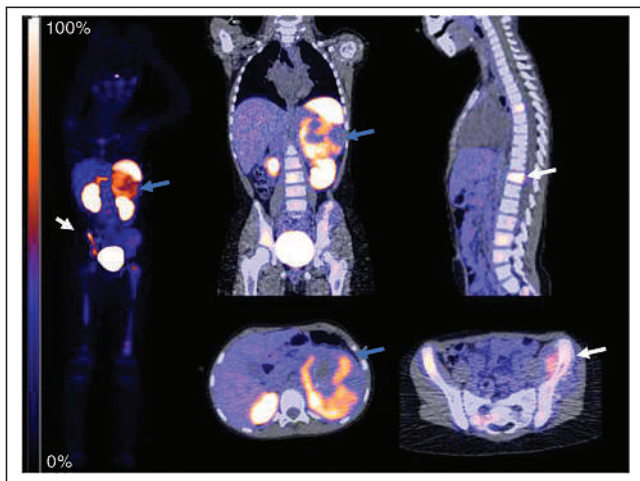


FIGURE 2. Uptake in left suprarenal mass, with areas of necrosis (blue arrows) and evidence of skeletal metastasis (white arrows) and bone marrow infiltration.

^{68}Ga -DOTATATE scans in our patients showed a high spatial resolution and high accuracy in concordance with reports in the literature (5,12,14).

In neuroblastoma management, the role of MIBG scintigraphy is established in staging, prognosis, and response evaluation (15,16). However, several logistic disadvantages make this form of imaging less attractive. These include a lengthy acquisition process, a protracted imaging schedule requiring repeated visits to the nuclear medicine department, and an occasional need for inpatient admission for younger patients. Another disadvantage is the need for thyroid blockade with Lugol solution, as MIBG can result in the accumulation of unbound iodine in the thyroid gland. Finally, MIBG uptake is affected by other medications affecting the sensitivity and accuracy of the study (17,18). On the other hand, ^{68}Ga -DOTATATE can be produced locally using a generator and the patient is injected and imaged on the same day. No special

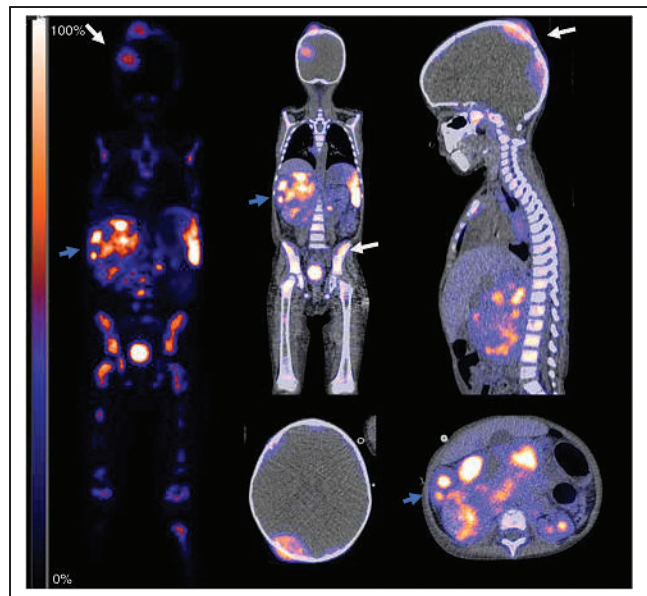


FIGURE 3. Heterogeneous uptake in lobulated right suprarenal mass (blue arrows), with diffuse skeletal metastasis, including in skull and pelvis (white arrows), and diffuse bone marrow infiltration.

preparation is required other than avoiding somatostatin analogs.

The role of ^{68}Ga -DOTATATE PET has previously been studied at the time of recurrence and at the therapeutic planning phase within a theranostic paradigm. However, there are very few reports of its role for staging at diagnosis (5,12). Maurice et al. found that in their series of 15 adults with pheochromocytoma and paraganglioma, ^{68}Ga -DOTATATE was positive in 5 patients in whom MIBG was negative, whereas the converse was true for only 2 patients (19). Similarly Naji et al. found that in adults with neural crest tumors, ^{68}Ga -DOTATATE showed 10 of 12 lesions, versus 5 shown by MIBG (20). Krois et al. compared the sensitivity and specificity of ^{68}Ga -DOTATATE with those of MIBG and morphologic imaging in their series of 11 patients (a mixed pediatric and adult cohort). Although only 5 of 11 patients had a diagnosis of neuroblastoma, ^{68}Ga -DOTATATE had a sensitivity of 97%, versus 90% for MIBG (5). In a case report, Agrawal et al. reported the utility of ^{68}Ga -DOTATATE PET/CT in diagnosis and response evaluation in a 12-y-old child with neuroblastoma (12).

All lesions evaluable on MRI scans were also avid on ^{68}Ga -DOTATATE PET/CT imaging, affirming the hypothesis that it is highly sensitive for neuroblastoma.

The effective radiation doses for ^{123}I -MIBG and ^{68}Ga -DOTATATE are 0.013 mSv/MBq (0.481 mSv/mCi) and 0.021 mSv/MBq (0.777 mSv/mCi), respectively (21). Depending on the activity schedule for a 20-kg pediatric patient using the standardized European Association of Nuclear Medicine weight-based activity calculator (62 MBq [1.7 mCi] for ^{68}Ga -DOTATATE and 136 MBq [3.7 mCi]

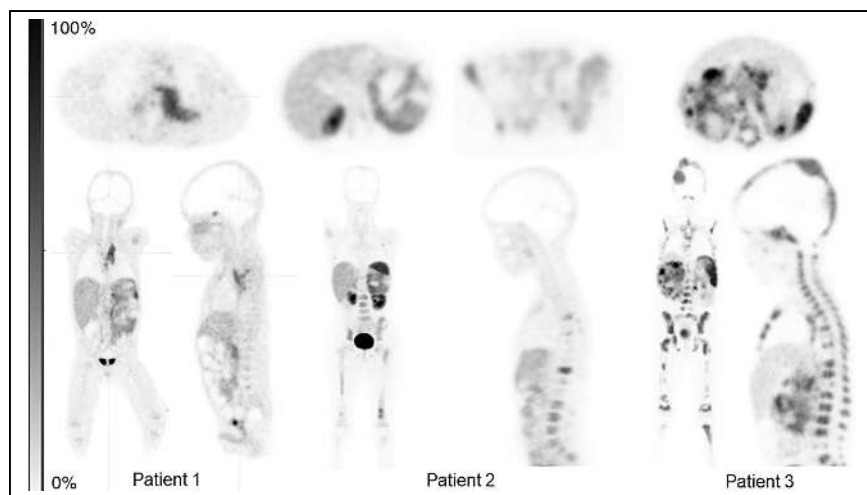


FIGURE 4. Summary of PET images for patients 1–3.

for ^{123}I MIBG), an approximately 25% lower radiation dose is possible with ^{68}Ga -DOTATATE (14,21,22). Reducing the radiation exposure is especially relevant in low-stage tumors for which radionuclide therapy is not required.

Advantages of ^{68}Ga -DOTATATE PET/CT include high image quality and better spatial resolution than with SPECT. Practical advantages also include more rapid imaging requiring less sedation, as well as no specific patient preparation requirements. Considering that ^{68}Ga -DOTATATE has been Food and Drug Administration–approved for use with PET for localization of somatostatin receptor–positive neuroendocrine tumors in pediatric patients, and that it is relatively easy to acquire for clinical use, it should be considered for routine use in staging of neuroblastoma patients.

CONCLUSION

^{68}Ga -DOTATATE PET/CT imaging can reliably be used as an alternative to MIBG for staging evaluation. It has numerous advantages over MIBG, including higher sensitivity, higher spatial resolution from PET, better image contrast, better tumor-to-background ratio, easier patient flow, easier patient preparation, and a more favorable dosimetry profile. Pooled data from multiple institutions may bring forth recommendations for its standard clinical use.

DISCLOSURE

No potential conflict of interest relevant to this article was reported.

ACKNOWLEDGMENTS

We thank Cyclomedica-HMC in facilitating the provision of ^{68}Ga -DOTATATE and Dr. William Mifsud (pathology department at Sidra Medicine) for provision of histopathology images used in the graphical abstract.

REFERENCES

- Monclair T, Brodeur GM, Ambros PF, et al. The International Neuroblastoma Risk Group (INRG) staging system: an INRG Task Force report. *J Clin Oncol*. 2009;27:298–303.
- Bar-Sever Z, Biassoni L, Shulkin B, et al. Guidelines on nuclear medicine imaging in neuroblastoma. *Eur J Nucl Med Mol Imaging*. 2018;45:2009–2024.
- Smets LA, Janssen M, Metwally E, Loesberg C. Extragranular storage of the neuron blocking agent meta-iodobenzylguanidine (MIBG) in human neuroblastoma cells. *Biochem Pharmacol*. 1990;39:1959–1964.
- Geatti O, Shapiro B, Sisson JC, et al. Iodine-131 metaiodobenzylguanidine scintigraphy for the location of neuroblastoma: preliminary experience in ten cases. *J Nucl Med*. 1985;26:736–742.
- Kroiss A, Putzer D, Uprimny C, et al. Functional imaging in pheochromocytoma and neuroblastoma with ^{68}Ga -DOTA-Tyr3-octreotide positron emission tomography and ^{123}I -metaiodobenzylguanidine: a clarification. *Eur J Nucl Med Mol Imaging*. 2012;39:543.
- Bleeker G, Tytgat GA, Adam JA, et al. ^{123}I -MIBG scintigraphy and ^{18}F -FDG-PET imaging for diagnosing neuroblastoma. *Cochrane Database Syst Rev*. 2015;2015:CD009263.
- Kong G, Hofman MS, Murray WK, et al. Initial experience with gallium-68 DOTA-octreotate PET/CT and peptide receptor radionuclide therapy for pediatric patients with refractory metastatic neuroblastoma. *J Pediatr Hematol Oncol*. 2016;38:87–96.
- Gains JE, Bomanji JB, Fersht NL, et al. ^{177}Lu -DOTATATE molecular radiotherapy for childhood neuroblastoma. *J Nucl Med*. 2011;52:1041–1047.
- Shulkin BL, Wieland D, Baro M, et al. Neuroblastoma: positron emission tomography with 2-[fluorine-18]-fluoro-2-deoxy-D-glucose compared with metaiodobenzylguanidine scintigraphy. *Radiology*. 1996;199:743–750.
- O'Dorisio MS, Chen F, O'Dorisio TM, et al. Characterization of somatostatin receptors on human neuroblastoma tumors. *Cell Growth Differ*. 1994;5:1–8.
- Albers AR, O'Dorisio MS, Balster DA, et al. Somatostatin receptor gene expression in neuroblastoma. *Regul Pept*. 2000;88:61–73.
- Agrawal K, Kumar R, Shukla J, Bhattacharya A, Mittal BR. Ga-68 DOTATATE positron emission tomography/computer tomography in initial staging and therapy response evaluation in a rare case of primary neuroblastoma in neck. *Indian J Nucl Med*. 2014;29:175–176.
- Sullivan M, Bouffet E, Rodriguez-Galindo C, et al. The COVID-19 pandemic: a rapid global response for children with cancer from SIOP, COG, SIOP-E, SIOP-PODC, IPSO, PROS, CCI and St Jude Global. *Pediatr Blood Cancer*. 2020;67:e28409.
- Alexander N, Vali R, Ahmadzadehfah H, Shammas A, Baruchel S. Review: the role of radiolabeled DOTA-conjugated peptides for imaging and treatment of childhood neuroblastoma. *Curr Radiopharm*. 2018;11:14–21.
- Suc A, Lumbroso J, Rubie H, et al. Metastatic neuroblastoma in children older than one year: prognostic significance of the initial metaiodobenzylguanidine scan and proposal for a scoring system. *Cancer*. 1996;77:805–811.
- Lewington V, Lambert B, Poetschger U, et al. ^{123}I -MIBG scintigraphy in neuroblastoma: development of a SIOPEN semi-quantitative reporting method by an international panel. *Eur J Nucl Med Mol Imaging*. 2017;44:234–241.
- Van Vickle SS, Thompson RC. ^{123}I -MIBG imaging: patient preparation and technologist's role. *J Nucl Med Technol*. 2015;43:82–86.
- Sharp SE, Trout AT, Weiss BD, Gelfand MJ. MIBG in neuroblastoma diagnostic imaging and therapy. *Radiographics*. 2016;36:258–278.
- Maurice JB, Troke R, Win Z. A comparison of the performance of ^{68}Ga -DOTATATE PET/CT and ^{123}I -MIBG SPECT in the diagnosis and follow-up of pheochromocytoma and paraganglioma. *Eur J Nucl Med Mol Imaging*. 2012;39:1266–1270.
- Naji M, Zhao C, Welsh SJ, et al. ^{68}Ga -DOTA-TATE PET vs. ^{123}I -MIBG in identifying malignant neural crest tumours. *Mol Imaging Biol*. 2011;13:769–775.
- Bombardieri E, Giammarile F, Aktolun C, et al. ^{131}I / ^{123}I -metaiodobenzylguanidine (mIBG) scintigraphy: procedure guidelines for tumour imaging. *Eur J Nucl Med Mol Imaging*. 2010;37:2436–2446.
- Walker RC, Smith GT, Liu E, Moore B, Clanton J, Stabin M. Measured human dosimetry of ^{68}Ga -DOTATATE. *J Nucl Med*. 2013;54:855–860.

Online Learning Strategies and Practical Tips for Nuclear Medicine Instructors

Sara L. Johnson

Nuclear Medicine Technology Certification Board, Tucker, Georgia

As nuclear medicine instructors shift toward online learning, it is imperative to use instructional strategies that align with the program's theoretic foundation. Online learning does not require a complete course redesign, though attention should be paid to careful course design to support learning, promote student engagement, and facilitate competency development. Instructional strategies such as discussions, group projects, and gaming elements support the construction of knowledge and the development of self-efficacy and competency while keeping students engaged in the content. Intentional display and formatting such as content chunking and a variety of materials can also support student learning.

Key Words: online learning; e-Learning; instructional strategies; competency-based education

J Nucl Med Technol 2021; 49:269–274

DOI: 10.2967/jnmt.120.251991

As the recent pandemic forced an abrupt shift into online-only education, nuclear medicine educators rushed to learn technology, adjust instructional and assessment methods, and redesign courses midsemester to support student learning. A sudden transition to online learning can be difficult for instructors and students, particularly if either is inexperienced or uncomfortable with an online format. Nuclear medicine education can be effectively delivered in an online format, though thoughtful modifications to course design and delivery are necessary.

Transitioning to online courses does not require a complete course redesign, but it does require modifications to instructional strategies to best support online learning. Instructional strategies should align with the theoretic foundation of the program or course (1). With the rising popularity of online learning environments, it is imperative for educators to use instructional strategies for student motivation and engagement to maximize authentic learning. This article provides a brief overview of instructional strategies for teaching nuclear medicine technology students online, as well as offering practical tips for delivering quality online education.

Received Jun. 19, 2020; revision accepted Apr. 27, 2021.
For correspondence or reprints, contact Sara L. Johnson (sjohnson@nmtcb.org).

Published online July 9, 2021.

COPYRIGHT © 2021 by the Society of Nuclear Medicine and Molecular Imaging.

THEORETIC FOUNDATIONS

The appropriate choice of educational theory is imperative to program effectiveness, especially regarding career education. Student success in career education programs extends far beyond the classroom. Career education requires the development of knowledge as well as successful, efficient, and repeated demonstration of new skills (2). In short, student success is marked by the ability to perform all entry-level aspects of a job effectively, repeatedly, and efficiently upon graduation. Successful education in career programs require a hybrid theoretic model that includes behaviorism, social cognitive theory, and constructivism. The Joint Review Committee on Educational Programs in Nuclear Medicine Technology (JRCNMT) emphasizes the achievement of technical and professional competencies (3). The technologist section of the Society of Nuclear Medicine and Molecular Imaging (SNMMI-TS) provides a curriculum guide that recommends educational programs adopt competency-based education (CBE) theory (4). Therefore, nuclear medicine education has a heavy emphasis on CBE.

CBE is an educational theory that evolved as a hybrid model with roots in behaviorism, constructivism, experiential learning, and social cognitive theory (5,6). CBE is a hybrid theory that adopted key concepts of existing educational theories to create a method for constructing knowledge and modifying behavior until students achieve mastery in critical technical skills and learning objectives (7). CBE borrows scientifically grounded concepts from existing educational theories to form a hybrid type of educational approach intended to help students construct knowledge and develop critical behavioral outcomes through experience in their chosen profession. Competency-based teaching has 5 major tenets: clear alignment with expected competencies, focus on fostering learning and self-governance, criteria-driven with focus on accountability and competency, connection to real-world experiences, individualized and learner-centered (7).

Behaviorism is evident in career education because the purpose of the program is to teach new skills (2). Behaviorism is rooted in conditioning through stimulus response (8). Educating adults in career education requires the development of behavioral-based outcomes of skills that are needed in that career, which students should be able to perform upon graduation. Researchers note that behavioral learning techniques such as operant learning programs are essential to students

learning new skills and complex procedures in career education programs (9). Aliakbari et al. maintain that operant conditioning can be seen in many career programs because behavior modification and reinforcement are essential for the development of new career skills (10). Behaviorism is evident in the competency-based nature of career education as students must be able to perform entry-level requirements of the career on program completion.

Social cognitive theory is centered on the belief that learning occurs in the social domain and includes learning techniques such as observation and role modeling (2). This is a key component of career education and is seen in activities such as job shadowing, internships, and clinical education. An additional key component of career education is the development of professionalism and professional practices for the career being studied (10). Adults learn by observing others or through role modeling (2). Role modeling is also seen in internships or clinical education in which students can learn from other more experienced professionals in the field. Constructivism is based on the premise that learning is the students' construction of meaning from their experiences (2). Constructivism theory maximizes the students' learning through well-planned and structured experiential learning, enabling them to construct fundamental knowledge and develop needed skills. Constructivism, like social cognitive theory, places importance on the social aspect of learning, which is a key factor in adult education (7). Other well-known theories within constructivism are Vygotsky's theory of the zone of proximal development and scaffolding, which describe the progression of constructing knowledge. These theories specifically describe the development of new, complex knowledge and skills. Scaffolding, in particular, includes working with others who have higher abilities than the student to serve as an apprenticeship (10).

Application of a hybrid model of behaviorism, social-learning theory, and constructivism will support adult learning in competency-based career education programs (7). Behaviorism supports the development of new skills through reinforcement and conditioning in response to stimuli, which helps learners develop new skills needed for their career. Social cognitive theory supports the development of professionalism and career skills and allows the application of knowledge in the real-world setting through the use of observational learning and role modeling. Lastly, constructivism supports the construction of knowledge and the development of new skills by providing structured experiential learning and scaffolding of complex work tasks. When transitioning courses from a live in-person format to online learning, it is imperative to align instructional strategies with educational theory and the theoretic foundations (1).

INSTRUCTIONAL STRATEGIES

Instructional strategies are the techniques instructors use to help students learn or gain a deeper understanding of content (10,11). They are techniques for engaging and motivating

students, as well as supporting learning. Instructional strategies are an essential aspect of course design because they allow the instructor to make purposeful decisions about content delivery and assessment that help keep the course aligned to objectives and outcomes while also helping students gain meaningful knowledge (10,11). Instructional strategies for CBE should be learner-centered and focused on the development of competency and connection to real-world application and allow for self-reflection to foster self-governance and accountability (Table 1) (7). CBE requires both teaching and learning to be purposeful. This section is not an all-inclusive list of instructional strategies for online learning or for CBE, though it provides several examples of effective strategies for CBE in the online format.

Lectures

Lectures can occur in many forms in the online format, though it is not recommended to hold 2- or 3-h live lectures online (12). Students may begin to feel disengaged, and authentic learning is undermined with lengthy lectures. In online learning, lectures work best when using short formats to provide a foundation for a topic or lesson and should not exceed 20 min at a time (7,12). Lectures can be provided as a voice-over PowerPoint, a live presentation, a prerecorded format, or a podcast. Effective online learning uses short lectures to supplement learning in combination with other methods that are student-centered and require participation. Programs such as Storyline (Articulate) and TechSmith Relay allow instructors to create or embed short videos that can serve as an introduction or summary to a topic or a tutorial accompanied by other assignments and resources. If using lectures, Americans with Disabilities Act (ADA) accommodations such as transcripts and closed captioning should be available for all students. Additionally, live lectures can be used as a short supplemental clarification of commonly made student mistakes or a question-and-answer session at the end of an online module.

Case Studies

Case studies tie into several learning theories and support development of critical thinking and competency (12). Although this is often used to present images to students,

TABLE 1
Instructional Strategies for CBE Online

Learning activities	Assessment methods
Short lectures	Exams and quizzes
Case studies	Presentations, student videos
Gaming elements	Case-study analysis
Discussions	Project artifacts (design plan, training manual, etc.)
Group projects	Portfolios

CBE online should include a variety of student-centered instructional strategies to support the construction of knowledge, behavior modification, social learning, and competency development.

case studies do not have to be images. Case studies present a student with a clinical problem but not a clear solution. Case studies may even be combined with small group work that provides opportunities for brainstorming and social learning (12). Some video-conferencing platforms allow for breakout sessions that support this type of instruction. Case studies are beneficial for supporting the development of practical knowledge and helping students think like a technologist. Examples include image analysis or review, a complex clinical case, or an interesting/unusual quality control finding or image.

Gamification

Gamification of courses is defined as the incorporation of gamelike activities or concepts into learning. Gamification is a broad term that could be as complex as creating a virtual game or incorporating game elements into course content. Gaming is increasingly used as an instructional strategy in online courses (13,14). Gamification of online course elements supports constructivism and behaviorism, which contribute to the development of competency through the construction of knowledge and behavior modification (14).

In an online learning environment, gaming has the potential to improve student engagement, motivation, and self-efficacy and support the achievement of behavioral objectives (13,15,16). Research has shown that deep learning in the online learning environment is highly dependent on student engagement, making it necessary for online educators to consider student engagement (13,17). The use of gaming in online courses can assist students in learning new behaviors or encourage the repetitive behavior that leads to habitual performance of an occupational skill (12). Gaming is a method for providing reward or punishment for behavior modification to help students meet behavioral objectives (13). The use of gaming in online courses may be a method of applying operant conditioning to improve student engagement, student motivation, student self-efficacy, and achievement of learning outcomes (14–16,18). Additionally, gaming allows students to learn consequences from their mistakes in a virtually real environment in which the consequences are minimized (14). Instructional games can also strengthen critical thinking and support social learning.

Incorporating gaming into an online course can be a complex and intimidating task for instructors. One method to incorporate gaming into an online course is by hosting a trivia-based game. Some PowerPoint and presentation software programs have free templates for trivia and jeopardy in which the instructor needs only to add the questions and answers while the template tallies the score for each team. Some video-conferencing programs such as Zoom allow for breakout rooms that instructors can use to break classes into more manageable teams. Many Learning Management Systems (LMS) have add-on applications that can be used to award students with badges for successfully completing modules or tasks. Students can be rewarded for collecting badges or scoring points using this method. Some free programs exist that allow instructors to create choose-your-own-adventure

style games that can be embedded into an LMS (13,15). Choose-your-own-adventure games take a bit of time to design and learn the platform. Still, they are beneficial in helping students achieve behavioral outcomes by learning positive and negative consequences for the behaviors they choose (13,15). Choose-your-own-adventure-style games can be useful for teaching students topics such as troubleshooting of equipment, handling a radioactive spill, or other imperfect scenarios encountered as a technologist.

Discussions

Discussions are among the most widely used instructional strategies in online classrooms, and the most effective (12). Effective use of discussion posts appeals to adult learners and supports social learning and construction of knowledge. Discussion posts not only keep students engaged but also they create interactivity (12,19). Discussion posts are beneficial in providing a sense of connectedness and belonging to students, as well as strengthening the connection to the content (19). Discussion prompts that are problem-based also foster critical thinking and the construction of practical knowledge (20).

A recent example prompted students to script how they would explain a nuclear stress test to a patient and take a patient history. Students commented that this prompt made them think critically about the overall process of a stress test and why specific preparation and history questions are performed. Students remarked that it helped them see the bigger picture and put the whole process together. Feedback from peers clarified areas of confusion and boosted their confidence. Using a prompt that ties into a real-world scenario also helps students connect theory to clinical and understand the importance of the assignment. Weaknesses of discussions can be addressed and offset with prior planning. A frequent complaint of students about discussions is that it feels like busywork. A frequent complaint from instructors about discussions is that students do not seem to take them seriously, or they are disappointed by students' lack of effort in discussions or replies to peers (12). Both complaints can be addressed and mitigated with a little prior planning. Effective use of discussions includes setting clear guidelines and expectations for the students, providing a rubric, and aligning the assignment to outcomes and objectives (19). If students are new to discussions, providing a good and a bad example can help students know what is expected of them. A common method of discussion posts requires students to reply to 1 or 2 of their peers. To avoid short replies such as "great job Suzie," instructors can place a minimum word count to the reply and provide students with clear expectations or a template for replies. One method requires each reply to be at least 100 minimum words, with 1 open-ended question and supporting evidence to either agree or disagree with the classmates' original post. Students can find *Journal of Nuclear Medicine Technology* articles or other scientific journals and texts to support a student's post, clarify misunderstandings, or reaffirm that the information is correct. Students may need reminders to make

all posts professional, supporting the development of professional competencies and communication. Caution should be taken in assigning too much weight to discussion posts, which is more likely to lead to redundant or meaningless posts and incidents of plagiarism (12). When discussions are used in a course, it is recommended they account for less than 20 percent of a course's total grade (1).

Group Projects

Group projects can be difficult to facilitate and motivate all students in the online format, though it can be done effectively (1). Some problematic aspects include difficulty in the group being able to meet or communicate effectively due to varied schedules and unequal participation or division of work by individual members. Online group project assignments should be carefully designed to promote individual accountability while maintaining clear interdependence (1,20). Practical tips for incorporating group work are regular self-evaluations and periodic feedback from the group. Group projects support the JRCNMT's professionalism competencies because group projects require interpersonal social skills based on behaviorism, social cognitive theory, and constructivism while improving students' small group social skills and communication.

An example might be a group project on radiation safety in which each small group is given a different scenario requiring students to "think like a technologist" to design a nuclear medicine department, develop a radiation safety plan, and develop the application for accreditation. This project requires the students to apply knowledge from the course, principles of ALARA (as low as reasonably-achievable), and critically examine the regulations and accreditation standards. Projects such as this are an instructional strategy that supports several learning theories including social learning, constructivism, problem-based learning, competency-based learning, and behaviorism. At the end of the project, each group presents their scenario plan to their classmates and submits the written plan. Each student completes a reflection, self-evaluation, and peer evaluation. The instructor should check in with each group on a regular basis to see how students are assigning personal responsibility and dividing the work. Students should feel both accountable and supported knowing there are clearly set expectations and responsibilities. Group projects in which the students present to the class support social-learning theory. Projects such as this also create a competency-based assessment and an artifact that serves as an alternative to testing (1).

Assessments

Assessment of student learning can be difficult in online learning. Many proctoring options exist to protect the integrity of online exams, though students determined to cheat continue to find innovative ways to cheat on exams. Several assessment strategies apply to online learning, which align nicely with various educational philosophies and instructional methods (1). Although quizzes and exams remain an

important aspect of nuclear medicine education, other assessment strategies effectively support competency-based education in the online setting (1,7). Students in online classrooms should be given a variety of assessment methods aligned with a variety of learning assignments. Student digital presentations, student-generated videos, and student presentations are also examples of assessments.

Creation of a project or portfolio in which the student must synthesize information and construct an artifact supports competency-based education and provides a nontesting method for assessing student learning (1). Open-ended projects such as a design plan or training manual help students connect course content to the real world in a way that is meaningful and translates to deep learning. Portfolios and project presentations challenge students to think critically to apply and synthesize content, challenge students to demonstrate higher-order thinking, and foster authentic learning (1,7).

PRACTICAL TIPS FOR QUALITY E-LEARNING

Careful attention and slight changes to course design, organization, and the visual representation of the online course can support quality learning in an online format. Demonstrating technologic competence, communication skills, and feedback skills and providing student support are all important factors in an instructor's ability to deliver quality education online (21).

Additionally, ADA compliance and students' ability to navigate the online content and locate necessary assignments and materials are important indicators of quality online course delivery. Instructors can take some steps in the online organization and presentation of the course to support quality delivery and student learning.

Course Design

The course design refers to the organization of the course in the LMS and the visual presentation. The course should follow a logical flow so students can navigate the course easily (22,23). LMS navigation menus should be as condensed as possible with no unusable options displayed for students. A "Begin Here" module containing links to student resources, the course schedule, and information on how and when to contact the instructor helps students visualize the organization and expectations of the course. Gradebook weighting and due dates available at the onset of the course help students assume responsibility for their own learning and organization (22).

Special attention should be given to course and lesson directions. Course assignment directions should include details of expectations and formatting, how to submit the assignment, alignment to objectives, and grading rubrics (23). Course alignment to assignments and assessments supports adult learning theories and helps students know why the content or assignment is important. A lack of clear instructions, however, can leave students feeling confused and overly anxious and may decrease self-efficacy. Each module should contain the objectives, materials, videos, graphics, assignments, and assessments for that lesson or content so

students can easily access what is needed for that lesson (22,23).

Content Chunking

Content chunking is a way of breaking the content into smaller pieces, making it easier for students to focus in-depth on the topic and prioritize information (24). Content chunking is designed to build on the learners' working memory and ties into both constructivism and competency-based learning. To use content chunking, the instructor can use the LMS to organize lessons into focused modules. Each small module or lesson should include prioritized information, include only relevant information with carefully chosen content and visuals, and take advantage of bulleted and numbered lists to organize concise information. A lesson organized in this way will be divided into several pages of the LMS module so students can progress screen by screen through the lesson (24).

Variety

Varying instructional material supports learning for all learning styles. This can be accomplished by incorporating assigned readings, videos, short live or recorded lectures, graphics, and concise notes (23). Additionally, hands-on activities or experiential learning activities that can be incorporated into the lesson will help kinesthetic learners, as well as support the development of competency. Varying assessment methods to assignments, papers, tests/quizzes, digital presentations, and projects also supports competency development. The application of a variety of instructional strategies and learning materials supports student engagement and helps the instructor reach students with all learning styles (23).

Incorporating Technology

The use of various types of technology in a course can add to the variety of instructional materials and support student engagement with the topic. There are nearly endless options for incorporating instructional technology platforms into an online classroom. Platforms such as Knowmia (TechSmith), Connect (Adobe), and Storyline (Articulate) allow online instructors to create short effective videos and interactive learning resources that engage students and provide valuable learning. Although some nuclear medicine training videos do exist on YouTube, these platforms also provide a tool for instructors to create high-quality videos and lectures that can be uploaded to YouTube or the LMS. Virtual classrooms can also be created through Microsoft Teams or Google Classroom that enable instructors to have video-conferencing and live lecture capabilities and facilitate group work.

Instructor Feedback

Instructor feedback is vitally important to student success in an online environment (19,21,23). Effective online instruction includes frequent, consistent, and constructive feedback. CBE, as well as constructivism and behaviorism, require the educator to act as a facilitator and a mentor, providing

constant feedback so the student can modify behavior. Frequent and productive feedback contributes to students' self-efficacy and motivation (1). Constructive feedback includes a student's strengths and weaknesses as well as suggestions for improvement. Frequent and constructive feedback fosters student learning (1,6,23). It is recommended to set aside time each week to communicate with students and provide personalized feedback.

ADA Compliance

Designing an online course should take the ADA into consideration (23). Consistency in the course design is essential for equal access and ADA compliance. Headers, texts, and fonts should be consistent throughout the course so screen readers can read them (22). Accessibility documents can be created in Word, although documents should also be provided in pdf form. All media should have good sound quality and provide a transcript or closed captioning. Images should contain alternative text (22). Individual institutions may have guidelines available for ensuring the course is ADA compliant.

CONCLUSION

Effective online instruction requires careful course design and implementation, as well as effective communication. Online courses should be modified from traditional face-to-face learning to incorporate effective online learning strategies. All course materials, assignments, and assessments should maintain alignment to learning theory as well as course and program objectives. A variety of instructional strategies, materials, and assessment methods help reach students of all learning styles, support student motivation, and foster student engagement. Instructional strategies for online nuclear medicine education include short lectures, discussions, case studies, course gamification, and group projects. Assessments and feedback should be given frequently so students can modify working knowledge and behavior as they progress toward competency. Thoughtful design and effective course management support student success and the development of competency in the online environment.

REFERENCES

1. Allen S. Applying adult learning principles to online course design. *Dist Learning*. 2016;13:25–32.
2. Merriam SB, Bierema LL. *Adult Learning: Linking Theory to Practice*. Jossey-Bass; 2014.
3. The Joint Review Committee on Educational Programs in Nuclear Medicine Technology (JRCNMT). *Accreditation Standards for Nuclear Medicine Technologist Education*. JRCNMT website. https://jrcnmt.org/sites/jrcnmt/uploads/documents/Accred_Policy_Documents/Final_Standards_rev10_2014.pdf. Accessed June 10, 2020.
4. Alessi AM, Dial J, Gilmore CD, et al. *Nuclear Medicine Technology Competency-Based Curriculum Guide*. 5th ed. Amazonaws website. <https://s3.amazonaws.com/rdcms-snmmt/files/production/public/FileDownloads/Education/SNMMI%20Nuclear%20Medicine%20Technology%20Competency%20Based%20Curriculum%20Guide%20-%205th%20Edition%20docx%20v2.pdf>. Accessed August 12, 2021.
5. Goncz A. Competency-based approaches: linking theory and practice in professional education with particular reference to health education. *Educ Philos Theory*. 2013;45: 1290–1306.

6. Legget T. Competency-based education: a brief overview. *Radiat Ther.* 2018;24: 107–110.
7. Johnston J. Competency perspective on teaching. SiloTips website. <https://silo.tips/download/competency-perspective-on-teaching>. June 14, 2017. Accessed August 12, 2021.
8. Thomas RM. *Comparing Theories of Child Development*. 6th ed. Thomson Wadsworth; 2005.
9. Levy IM, Pryor KW, McKeon TR. Is teaching simple surgical skills using an operant learning program more effective than teaching by demonstration? *Clin Orthop.* 2016; 474:945–955.
10. Aliakbari F, Parvin N, Heidari M, Haghani F. Learning theories application to nursing education. *J Educ Health Promot.* 2015;4:2–9.
11. Wiggins G, McTighe J. *The Understanding By Design Guide To Creating High-Quality Units*. ASCD; 2011.
12. Picciano AG. Theories and frameworks for online education: seeking an integrated model. *Online Learning.* 2017;21:166–190.
13. Bechkoff J. Gamification using a choose your own adventure type platform to augment learning and facilitate student engagement in marketing education. *J for Adv of Mark Educ.* 2019;27:13–30.
14. Cain J, Piascik P. Are serious games a good strategy for pharmacy education? *Am J Pharm Educ.* 2015;79:47 10.5688/ajpe7947.
15. Rick H, Phlypo K. Choose your own adventure: self-directed adult learning and assessment. Paper presented at: 18th European Conference on e-Learning (ECEL 2019); November 7 and 8, 2019; Copenhagen, Denmark.
16. Dicheva D, Dickey C, Agre G, Angelova G. Gamification in education: a systematic mapping study. *J of Ed Tech and Society.* 2015;18:75–83.
17. Abril-Lancheros ME. Motivación del aprendizaje en línea [in Spanish]. *Panorama.* 2018;12:43–56.
18. Buckley P, Doyle E. Gamification and student motivation. *Interact Learn Environ.* 2014;24:1162–1175.
19. Yarbrough JR. Adapting adult learning theory to support innovative, advances, online learning–WVMD model. *Research in H Educ J.* 2018;35:1–15.
20. Stacey E. *A Constructivist Framework for Online Collaborative Learning. Computer Supported Collaborative Learning in Higher Education*. IGI Global; 2005:140–161.
21. Beaudoin MF. Distance education leadership in the context of digital change. *Quart Rev Dist Ed.* 2015;16:33–44.
22. Davis T. *Visual Design for Online Learning*. Jossey-Bass; 2015.
23. Vai M, Sosulski. *Essentials of Online Course Design: A Standard-Based Guide*. 2nd ed. Routledge; 2016.
24. Dickson-Dean C, Philips W. Chunking. In Chen B, deNoyelles A, Thompson K, eds. *Teaching Online Pedagogical Repository*. University of Central Florida Center for Distributed Learning; 2015.

Nuclear Medicine and Molecular Imaging in Nodal Staging and Surveillance of Ocular Melanoma: Case Reports and Review of the Literature

Kenneth S. Zurcher¹, Odette M. Houghton², Joanne F. Shen², Mahesh Seetharam³, Michael C. Roarke¹, and Ming Yang¹

¹Department of Radiology, Mayo Clinic, Scottsdale, Arizona; ²Department of Ophthalmology, Mayo Clinic, Scottsdale, Arizona; and

³Department of Hematology/Oncology, Mayo Clinic, Scottsdale, Arizona

Ocular melanoma (OM) is a rare noncutaneous malignancy and consists of 2 different subtypes based on the anatomic location in the eye: uveal melanoma and conjunctival melanoma. Like cutaneous melanoma, OM benefits from nuclear medicine and molecular imaging in nodal staging and clinical management. Through the illustration of 2 distinctive cases, we aim to demonstrate the complementary roles of standard lymphoscintigraphy, advanced SPECT/CT, ¹⁸F-FDG PET/CT, and ¹⁸F-FDG PET/MRI in accurate nodal staging and surveillance of OM. We also review the epidemiology, existing staging guidelines, and management of uveal melanoma and conjunctival melanoma.

Key Words: conjunctival melanoma; ¹⁸F-FDG/PET; lymphoscintigraphy; SPECT; uveal melanoma

J Nucl Med 2021; 49:275–280

DOI: 10.2967/jnmt.120.260539

Ocular melanoma (OM) represents the most common form of rare noncutaneous melanoma and the most common primary ocular tumor in adults (1). There are 2 subtypes of OM based on anatomic location in the eye: uveal melanoma (UM), which involves the choroid, retina, iris, or ciliary body and accounts for 95% of OM cases, and the rarer conjunctival melanoma (CM), which involves mainly the bulbar conjunctiva and comprises only about 5% of OM cases. The clinical manifestations of, and treatment approaches toward, OM vary between UM and CM, and accurate staging outside the eyes is crucial in the assessment of treatment response and surveillance (2–4).

Given the differences in lymphatic drainage and potential sites of metastases between UM and CM, distinct considerations must be made with regard to tumor staging strategies. Nuclear medicine and molecular imaging (i.e., ^{99m}Tc-sulfur colloid lymphoscintigraphy-guided sentinel lymph node biopsy [SLNB] and whole-body ¹⁸F-FDG PET/CT) have proven of value in staging melanoma in the discovery of tracer-avid locoregional nodal and visceral metastases (5–8). Although limited data exist on the optimal imaging modality for staging CM, which has a lymphatic spread pattern similar to that of cutaneous melanoma, ^{99m}Tc-sulfur colloid lymphoscintigraphy and SPECT/CT-guided SLNB have emerged as valuable tools. Given the technical skill required for

subconjunctival radiotracer injection, these 2 tools have been used at only some specialized eye institutions (9–12). ¹⁸F-FDG PET/MRI systems have become increasingly available and allow for combined whole-body molecular imaging and high-resolution, targeted, diagnostic MRI in a 1-stop imaging examination model. ¹⁸F-FDG PET/MRI enables diagnosis of hepatic and brain metastasis and evaluation of tumor burden and assists in clinical management of OM (13).

In this study, we present 2 distinct cases to demonstrate the clinical utility of standard and advanced nuclear medicine imaging modalities in OM, followed by a review of OM epidemiology and existing guidelines on staging and management. Specifically, we aim to underscore the importance of ¹⁸F-FDG PET/CT or ¹⁸F-FDG PET/MRI in the staging or restaging of OM and the use of ^{99m}Tc-sulfur colloid lymphoscintigraphy and SPECT/CT in CM. This study complied with institutional review board policy.

CASES

Case 1

A 74-y-old man presented with visual changes in his left eye. On ophthalmologic examination, the patient was found to have retinal detachment with a large pigmented uveal mass, consistent with a diagnosis of ciliochoroidal melanoma. Staging CT and MRI of the liver demonstrated multiple hepatic lesions. Metastatic ciliochoroidal melanoma was confirmed after ultrasound-guided biopsy of a liver lesion revealed stage T4bN0M1 disease. The patient underwent γ -knife radiotherapy to the left-eye lesion and began systemic therapy with pembrolizumab. To evaluate response to therapy, ¹⁸F-FDG PET/MRI was performed on a GE Healthcare Signa 3-T PET/MRI system. The customized PET/MRI protocol consisted of 2 parts. The first part was a whole-body ¹⁸F-FDG PET/MRI survey scan with 370 MBq of ¹⁸F-FDG injected intravenously, a 60-min uptake time, and 6–8 bed positions covering the whole body (an imaging time of ~4 min at each bed position). Simultaneous T1-weighted Dixon LAVA Flex (GE Healthcare; water, fat, in-phase, and out-of-phase) sequences were acquired for attenuation correction and localization. The second part was a focused contrast-enhanced liver MRI scan. The whole-body ¹⁸F-FDG PET/MRI demonstrated a recurrent or residual tracer-avid primary left eye lesion on a survey scan, with progression of hepatic metastases (Fig. 1). The patient did not respond to chemotherapy and died 15 mo after the initial diagnosis of UM.

Case 2

A 64-y-old woman with a history of primary acquired melanosis (PAM) presented with a rapidly enlarging mobile lesion of the right

Received Nov. 19, 2020; revision accepted Mar. 1, 2021.

For correspondence or reprints, contact Ming Yang (yang.ming@mayo.edu).

Published online April 5, 2021.

COPYRIGHT © 2021 by the Society of Nuclear Medicine and Molecular Imaging.

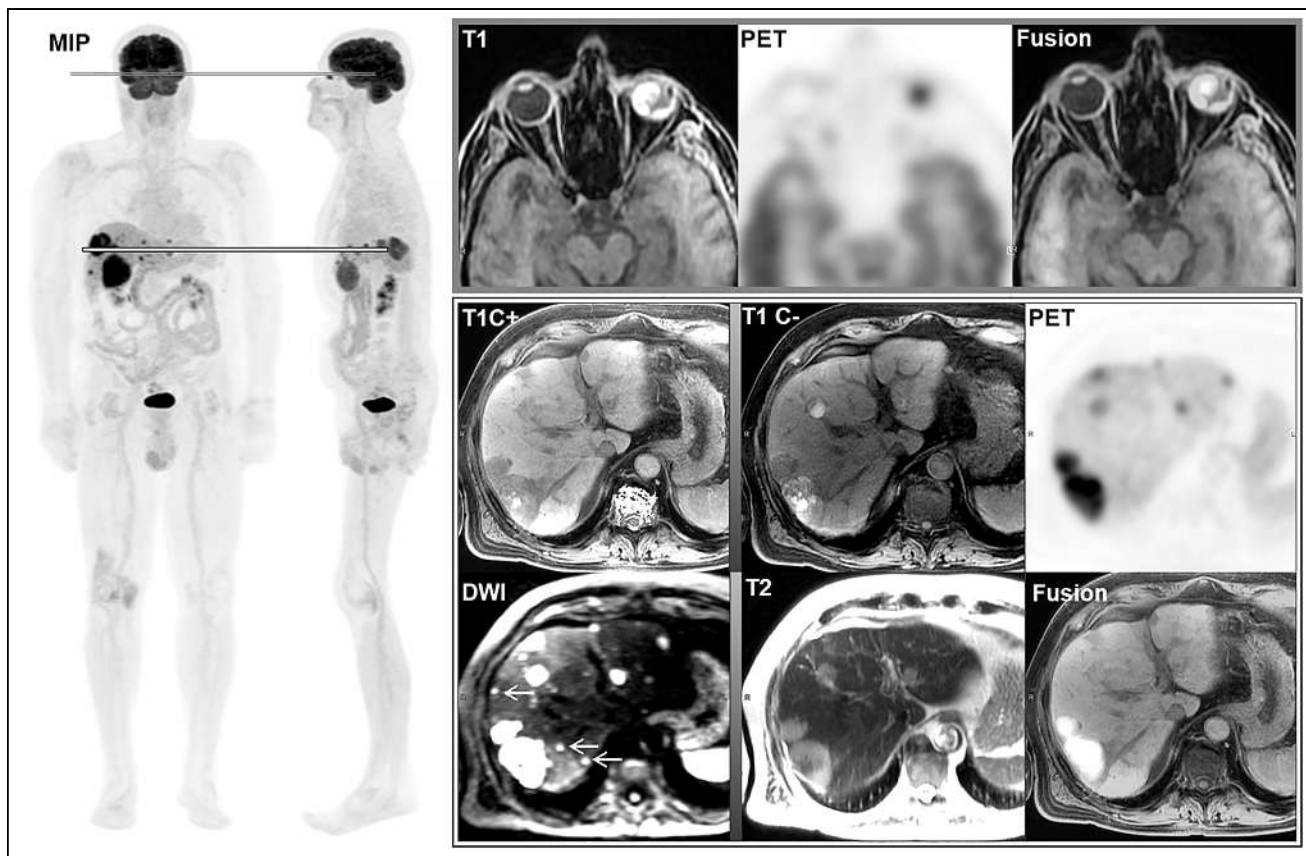


FIGURE 1. Whole-body ^{18}F -FDG PET/MRI study in surveillance of UM (case 1). Whole-body maximal-intensity-projection (MIP) images exhibit tracer-avid left eye lesion and numerous tracer-avid lesions in liver. Axial ^{18}F -FDG PET/MRI of left eye demonstrates high T1-signal lesion in left globe with increased tracer uptake, with SUV_{max} of 8.3 (top line on MIP image; top row of images). On representative layer of liver (bottom line on MIP image; bottom 2 rows of images), multiple liver lesions with variable low and high T1 signals show increased uptake, with SUV_{max} of 4.0–11.7. In addition, diffusion-weighted imaging (DWI) shows more small metastases with restricted diffusion (arrows) than does contrast-enhanced T1-weighted MRI (T1C+) or PET. T1C– = non-contrast-enhanced T1-weighted MRI; T2 = T2-weighted MRI. Color version of this figure is available as supplemental file at <http://tech.snmjournals.org>.

eye. On examination, a mobile pigmented lesion involving the right superior temporal conjunctiva was noted, with surrounding melanosis and without scleral invasion. The patient underwent excisional biopsy and cryotherapy. Pathologic examination revealed invasive bulbar CM with a 2.6-mm depth of invasion. Nasal and temporal margins were positive for residual PAM with atypia only. A further staging workup was performed, including whole-body ^{18}F -FDG PET/CT (same dosage and uptake time as for whole-body ^{18}F -FDG PET/MRI) and MRI of the brain and neck, both of which were negative for a recurrent lesion or metastatic disease. Lymphoscintigraphy for the purposes of SLNB was also performed. Subconjunctival radiotracer injection was performed by an ophthalmologist with a valid authorized-user status. In detail, 4% lidocaine was topically administered with a cotton tip applicator to the injection site of the right eye following a dedicated sterile preparation protocol. With the patient's eyelids manually held open by the ophthalmologist, the patient was instructed to look in the opposite direction from the injection site, and two 0.2-mL aliquots of normal saline containing 11.1 MBq of $^{99\text{m}}\text{Tc}$ -filtered sulfur colloid were successfully injected in the subconjunctival space in separate locations in the area of the excised melanoma. Dynamic and static planar scintigraphy images of the head and neck were obtained, followed by SPECT/CT images,

to localize the sentinel node. Both planar and SPECT images identified a right parotid sentinel node, which was resected through a superficial parotidectomy and was negative for metastasis on final pathologic examination (Fig. 2). The disease was staged as T1cN0M0. The patient remained negative for tumor recurrence or metastasis on repeated biopsy and multimodality image studies,

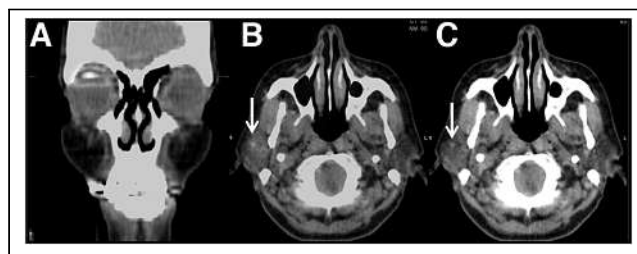


FIGURE 2. $^{99\text{m}}\text{Tc}$ -filtered sulfur colloid SPECT/CT (case 2). (A) Coronal PET/MR image demonstrating successful radiotracer injection to right-eye subconjunctival region by ophthalmologist. (B) Axial PET/MR image. (C) Axial low-dose CT image. Tiny sentinel lymph node (arrows) was identified in right fossa of parotid gland. Node was negative for metastasis on biopsy. Color version of this figure is available as supplemental file at <http://tech.snmjournals.org>.

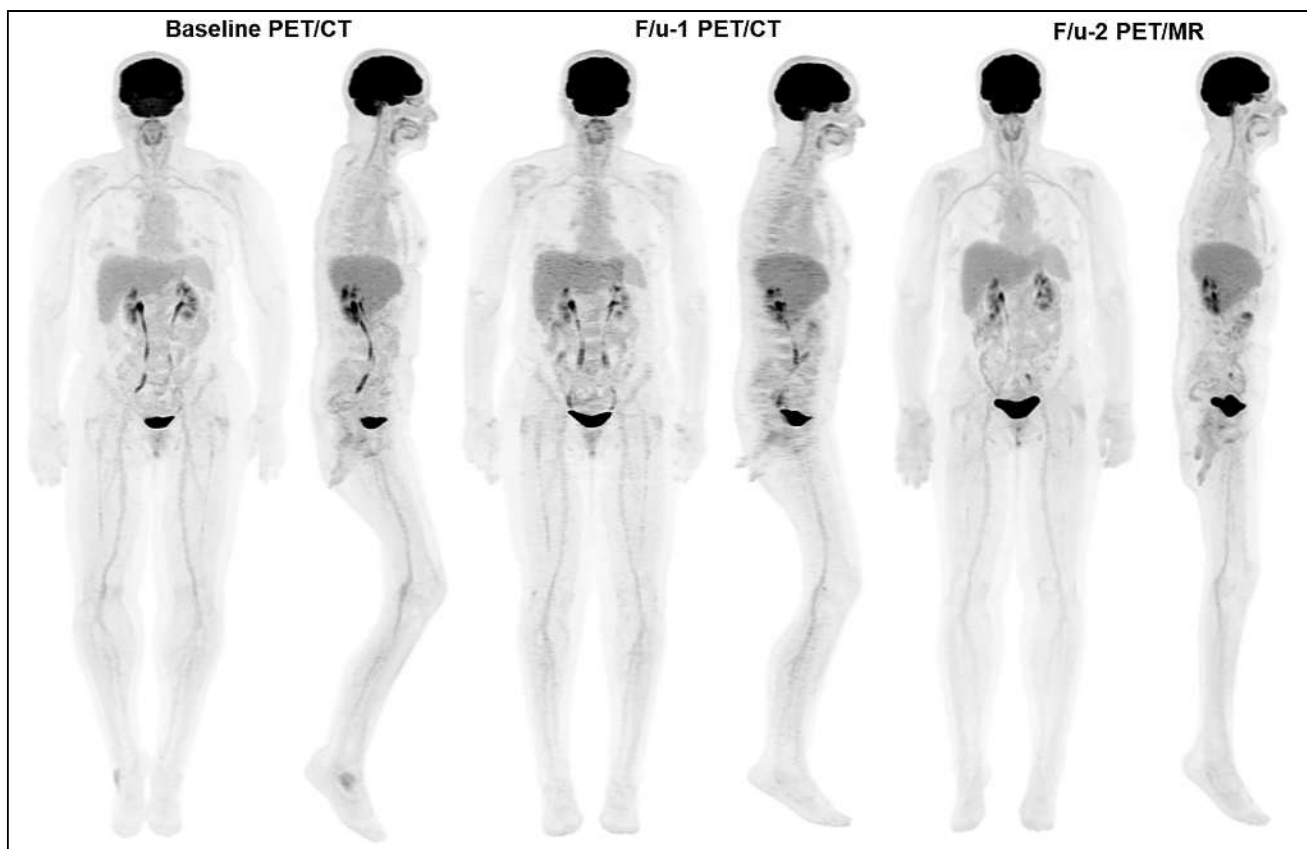


FIGURE 3. Whole-body maximum-intensity-projection ^{18}F -FDG PET/CT and ^{18}F -FDG PET/MRI in surveillance of CM (case 2). Consecutive anterior and right lateral views do not demonstrate hypermetabolic metastasis or recurrence at baseline or at the first (12 mo) or second (16 mo) follow-up (F/u-1 and F/u-2, respectively).

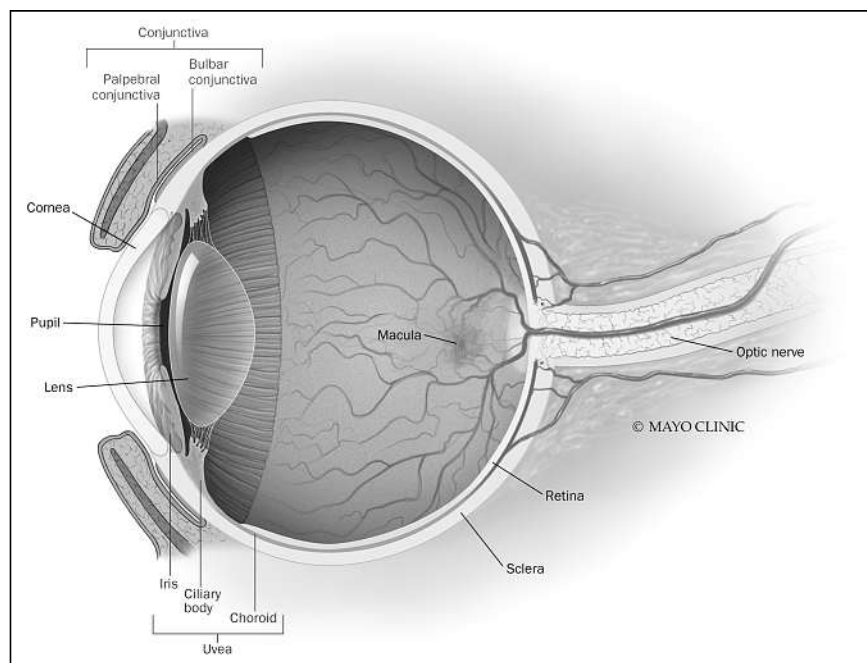


FIGURE 4. Illustration of eye anatomy. UM occurs at iris, ciliary body, and choroid. CM occurs at palpebral and bulbar conjunctiva. (Reprinted with permission of (38).) Color version of this figure is available as supplemental file at <http://tech.snmjournals.org>.

including whole-body ^{18}F -FDG PET/CT and ^{18}F -FDG PET/MRI (Fig. 3).

DISCUSSION

OM is a rare type of noncutaneous melanoma and the second most common melanoma after cutaneous melanoma (1). On the basis of its anatomic location, OM is categorized as UM or CM (Fig. 4). There are distinctive differences in epidemiology, pathophysiology, and clinical management between these 2 subtypes. Accurate staging and appropriate clinical surveillance may guide clinical management and ultimately improve prognosis in UM and CM, similarly to their cutaneous melanoma counterpart. From SLNB to whole-body ^{18}F -FDG PET/CT, nuclear medicine and molecular imaging have a well-established role in staging and surveillance of cutaneous melanoma. Given the complex anatomy of the eye and the rarity of OM, we present these 2 cases to demonstrate that the variety of nuclear medicine and molecular imaging modalities provides excellent imaging tools in staging and surveillance of OM.

UM

Epidemiology and Pathophysiology. UM represents the most common primary intraocular malignancy in adults, with a mean age-adjusted incidence of 5.1 per million population (1,14–16). On the basis of Surveillance, Epidemiology, and End Results data collected in the United States between 1973 and 2008, UM represented approximately 3.1% of all melanoma cases, with 5- and 15-y survival rates of 81.6% and 45%, respectively (15,16). UM develops from melanocytes along the uveal tract and most frequently arises from the choroid (85%), with retinal, iris, and ciliary body involvement comprising the remainder of cases (14,17). Increased rates of UM are seen in white populations.

Staging. Because of a relative lack of lymphatics within the eye, metastatic spread of UM occurs predominantly in a hematogenous manner. Although metastases can be found in several organ systems, UM demonstrates a notorious propensity for liver metastasis. Although this mechanism is not well understood, an estimated 71%–95% of patients with metastatic disease demonstrate hepatic lesions; other metastatic sites include bone, lung, skin, and other organ systems (14,18,19).

Staging of OM is guided by the American Joint Committee on Cancer, with imaging playing a vital role in identifying metastatic disease (16). Consensus-based guidelines on staging workup of UM were proposed by Weis et al. (16) in 2016 and recommend that one of the following be obtained: CT of the chest and abdomen (liver protocol for abdomen), whole-body ^{18}F -FDG PET/CT, or liver MRI with chest CT.

Recent studies have highlighted the sensitivity and positive predictive value of both ^{18}F -FDG PET/CT and MRI in assessing metastatic UM. A 2012 study by Freton et al. (20) highlighted ^{18}F -FDG PET/CT as an effective screening modality for hepatic and extrahepatic metastasis, with a 100% positive predictive value. Of 333 consecutive patients with UM who underwent screening with ^{18}F -FDG PET/CT, 7 demonstrated biopsy-proven liver metastases, and 2 of those 7 (29%) had multiorgan involvement. In a 2005 study by Kurli et al. (19), 20 patients with suspected metastatic UM underwent ^{18}F -FDG PET/CT to identify metastatic disease. Of 8 patients positive for metastasis, 8 (100%) demonstrated liver metastasis and 6 (75%) showed multiorgan involvement, resulting in a sensitivity of 100%. Klingenstein et al. (21), in 2010, further established ^{18}F -FDG PET/CT as an effective tool in imaging staging and follow-up of metastatic UM.

In specifically determining the presence of isolated hepatic metastatic disease, a 2010 study by Servois et al. (22) reported the sensitivity and positive predictive value of liver MRI to be 67% and 95%, respectively, compared with 41% and 100% for ^{18}F -FDG PET/CT. This increased sensitivity of MRI over ^{18}F -FDG PET/CT in detecting liver lesions was further corroborated in a 2012 study by Orcurto et al. (23), in which MRI outweighed ^{18}F -FDG PET/CT in detecting small lesions (<1.2 cm). Importantly, in that study, ^{18}F -FDG PET/CT identified at least one metastatic liver lesion per patient as well as changes in ^{18}F -FDG uptake not related to size change, suggesting a potential role in determining early therapy response.

Although a single optimal imaging modality has not yet been determined in the staging of UM, benefits exist for both ^{18}F -FDG PET/CT (identifying extrahepatic disease with good sensitivity and positive predictive value for hepatic lesions) and MRI (improved sensitivity for identifying hepatic lesions). In case 1, ^{18}F -FDG PET/MRI was chosen as the optimal surveillance modality, which demonstrated excellent performance in delineating both

the primary lesion and the hepatic metastases in the advantageous 1-stop imaging pattern. The hybrid diagnostic liver ^{18}F -FDG PET/MRI demonstrated its unique advantage in combining morphologic and molecular imaging information in the diagnosis of liver metastasis in melanoma. If available or feasible, ^{18}F -FDG PET/MRI may represent an alternative that combines the described advantages of both modalities, with a reduced radiation dose compared with whole-body ^{18}F -FDG PET/CT.

Management. Management of UM is highly specialized and requires multidisciplinary support. With regard to surgical management, enucleation remains the preferred treatment for lesions more than 10 mm thick or more than 18 mm in diameter (16). Local resection can be considered in select ciliary body or iris lesions. Lesions best suited for brachytherapy include those less than 10 mm thick and less than 18 mm in maximal diameter, as well as high-risk indeterminate lesions.

The appropriate imaging surveillance strategy for patients with metastatic UM remains to be fully established. However, annual follow-up with ^{18}F -FDG PET/CT or liver MRI, or with liver ultrasonography and chest radiography, is recommended. Although a prospective study of 188 high-risk UM patients showed that semiannual liver MRI detected metastases in 92% of patients before symptoms manifested, whether such a regimen has a survival benefit remains to be established (24).

CM

Epidemiology and Pathophysiology. CM represents a considerably rarer entity than UM, occurring approximately one fortieth as often, with an estimated annual incidence of 0.2–0.8 cases per million (25–29). CM is predominantly seen in middle-aged to older white populations, without a definite sex predilection. Five- and 8-y mortalities have been most recently estimated at 7% and 13%, respectively (30). Although risk factors commonly associated with cutaneous melanoma have not been demonstrated in CM (e.g., family history, ultraviolet light exposure, or fair skin and hair), an association between PAM and CM has been well established. Of CM cases, 57%–76% are thought to be attributable to PAM—with PAM with severe atypia transforming into CM at a high frequency (30,31). CM results from malignant proliferation of melanocytes—specifically from the conjunctiva. Anatomically, the conjunctiva represents a clear mucous membrane that lines the posterior surface of the eyelids (palpebral conjunctiva), the anterior portions of the globe, and the superior and inferior fornices (bulbar and forniceal conjunctiva, respectively) (25). However, there is no particular quadrant prediction, with the following quadrant incidence ranges reported: 16%–34% in the superior quadrant, 22%–39% in the inferior quadrant, 17%–34% in the nasal quadrant, and 26%–63% in the temporal quadrant (30,32).

Staging. Because the conjunctiva is supplied by both blood vessels and lymphatics, metastatic spread can occur hematogenously or via lymphatic drainage to regional lymph nodes. Initial lymphatic spread is estimated to occur in up to 41%–62% of patients, with distant metastases in the absence of local nodal involvement occurring in 26%–50% (3,30,33). Reported risk factors for regional nodal spread include nonlimbal location, tumor thickness greater than 2 mm, large basal diameter, positive resection margins, and orbital extension (34). The lymphatic spread of CM seems to be associated with the location of the primary tumor, with nasal conjunctiva appearing to drain to the submandibular lymph nodes (9%) whereas tumors of the rest of the conjunctiva drain primarily to the

preauricular nodes (73%) and deep cervical lymph nodes (18%) (3). Currently, no strict imaging guidelines exist for systemic staging workup or restaging of CM (4,31). Existing recommendations include CT or MRI of the brain, chest, and abdomen/liver or ^{18}F -FDG PET/CT. In contrast to UM, a paucity of data exists assessing the utility of ^{18}F -FDG PET/CT in CM. The largest case series was reported by Kurli et al. (35), who investigated the performance of ^{18}F -FDG PET/CT in 14 CM patients: 7 for preoperative staging and 7 for restaging after treatment (surgical removal with adjuvant cryotherapy or chemotherapy). Among the small cohort of patients, one (T4 stage) had multisite distant metastases, with involvement of the liver, lung, peritoneal cavity, lumbar spine, and other sites. The remaining 13 patients (T3 stage) were negative for either locoregional or distant metastasis. This study indicated a limited role for ^{18}F -FDG PET/CT in initial T and N staging but value for restaging of CM. Damian et al. reported a case presenting with a hypermetabolic primary left-eye CM lesion and an ipsilateral preauricular node on restaging ^{18}F -FDG PET/CT, without evidence of distant metastasis (36).

Because of the similarity in the pattern of lymphatic spread between CM and cutaneous melanoma, lymphoscintigraphy with SLNB has arisen as a safe and viable staging tool in the last 1–2 decades and has been supported in several small case series (11,34,36). Preoperative SLNB allows for potential detection of otherwise clinically undetectable systemic spread and is performed during or after removal of the primary lesion (31). The success of SLNB requires a sophisticated subconjunctival injection of filtered $^{99\text{m}}\text{Tc}$ -sulfur colloid near the existing tumor or site of resection at the nuclear medicine laboratory (37). Dynamic planar images are obtained with a γ -camera to identify a sentinel lymph node. The skin is marked in this region, with use of SPECT/CT for further localization. Intraoperatively, a handheld γ -probe and methylene blue injection are also used to localize the sentinel node, followed by surgical dissection, excision, and histologic processing.

Ultimately, further trials are required to fully identify the role and survival benefit of lymphoscintigraphy with SLNB in this population. Given the rarity of CM, existing data remain limited, with a cohort of 18 patients from Cohen et al. (34) remaining the largest studied population.

Management. Again, because of the rarity of CM, management of this malignancy is based on case reports and series. The current standard of care includes wide local excision with double freeze–thaw cryotherapy to the resection margins (4,31). Enucleation may be required in advanced cases in which wide local excision is not feasible. Topical chemotherapy and brachytherapy have been explored as adjuvant therapy. Unfortunately, 5-y recurrence rates are high, currently estimated at 36%–45% after surgical resection (31). Like UM, CM currently has no optimal or well-researched method of imaging surveillance for restaging, with ^{18}F -FDG PET/CT often being used.

CONCLUSION

Nuclear medicine and molecular imaging have an established role in the staging and surveillance of OM. Because of differences in metastatic pathways between UM and CM, imaging strategies for both entities also differ. In patients with UM, whole-body ^{18}F -FDG PET/CT may represent mainstays of initial staging and surveillance. The role of emerging hybrid ^{18}F -FDG PET/MRI is promising, especially in the diagnosis and assessment of metastasis in the liver and brain, but it is limited by lack of availability and needs to be better defined

by greater clinical application. Data on the staging and surveillance of CM remain sparse and are based on limited case series. Since CM may spread to locoregional lymph nodes via the lymphatic drainage channel, there is a rationale for performing SLNB and SPECT/CT in the staging of CM to predict recurrence and survival. Collaboration with ophthalmology at a clinical nuclear medicine practice is crucial to successfully perform the sophisticated subconjunctival radio-tracer injection.

DISCLOSURE

No potential conflict of interest relevant to this article was reported.

REFERENCES

- McLaughlin CC, Wu XC, Jemal A, Martin HJ, Roche LM, Chen VW. Incidence of noncutaneous melanomas in the U.S. *Cancer*. 2005;103:1000–1007.
- Aronow ME, Topham AK, Singh AD. Uveal melanoma: 5-year update on incidence, treatment, and survival (SEER 1973–2013). *Ocul Oncol Pathol*. 2018;4:145–151.
- Esmali B, Wang X, Youssef A, Gershenwald JE. Patterns of regional and distant metastasis in patients with conjunctival melanoma: experience at a cancer center over four decades. *Ophthalmology*. 2001;108:2101–2105.
- Vora GK, Demirci H, Marr B, Mruthyunjaya P. Advances in the management of conjunctival melanoma. *Surv Ophthalmol*. 2017;62:26–42.
- Fuster D, Chiang S, Johnson G, Schuchter LM, Zhuang H, Alavi A. Is ^{18}F -FDG PET more accurate than standard diagnostic procedures in the detection of suspected recurrent melanoma? *J Nucl Med*. 2004;45:1323–1327.
- Morton DL, Wen DR, Wong JH, et al. Technical details of intraoperative lymphatic mapping for early stage melanoma. *Arch Surg*. 1992;127:392–399.
- Steinert HC, Huch Böni RA, Buck A, et al. Malignant melanoma: staging with whole-body positron emission tomography and 2-[F-18]-fluoro-2-deoxy-D-glucose. *Radiology*. 1995;195:705–709.
- Wong SL, Faries MB, Kennedy EB, et al. Sentinel lymph node biopsy and management of regional lymph nodes in melanoma: American Society of Clinical Oncology and Society of Surgical Oncology clinical practice guideline update. *Ann Surg Oncol*. 2018;25:356–377.
- Balasubramanya R, Selvarajan SK, Cox M, et al. Imaging of ocular melanoma metastasis. *Br J Radiol*. 2016;89:20160092.
- Esmali B. Sentinel lymph node mapping for patients with cutaneous and conjunctival malignant melanoma. *Ophthalm Plast Reconstr Surg*. 2000;16:170–172.
- Esmali B, Eicher S, Popp J, Delpassand E, Prieto VG, Gershenwald JE. Sentinel lymph node biopsy for conjunctival melanoma. *Ophthalm Plast Reconstr Surg*. 2001;17:436–442.
- Reddy S, Kurli M, Tena LB, Finger PT. PET/CT imaging: detection of choroidal melanoma. *Br J Ophthalmol*. 2005;89:1265–1269.
- Buchbender C, Heusner TA, Lauenstein TC, Bockisch A, Antoch G. Oncologic PET/MRI, part 2: bone tumors, soft-tissue tumors, melanoma, and lymphoma. *J Nucl Med*. 2012;53:1244–1252.
- Kalemaki MS, Karantanas AH, Exarchos D, et al. PET/CT and PET/MRI in ophthalmic oncology. *Int J Oncol*. 2020;56:417–429.
- Singh AD, Turell ME, Topham AK. Uveal melanoma: trends in incidence, treatment, and survival. *Ophthalmology*. 2011;118:1881–1885.
- Weis E, Salopek TG, McKinnon JG, et al. Management of uveal melanoma: a consensus-based provincial clinical practice guideline. *Curr Oncol*. 2016;23:e57–e64.
- Vora GK, Demirci H, Marr B, Mruthyunjaya P. Advances in the management of conjunctival melanoma. *Surv Ophthalmol*. 2017;62:26–42.
- Bakalian S, Marshall JC, Logan P, et al. Molecular pathways mediating liver metastasis in patients with uveal melanoma. *Clin Cancer Res*. 2008;14:951–956.
- Kurli M, Reddy S, Tena LB, Pavlick AC, Finger PT. Whole body positron emission tomography/computed tomography staging of metastatic choroidal melanoma. *Am J Ophthalmol*. 2005;140:193–199.
- Fretton A, Chin KJ, Raut R, Tena LB, Kivelä T, Finger PT. Initial PET/CT staging for choroidal melanoma: AJCC correlation and second nonocular primaries in 333 patients. *Eur J Ophthalmol*. 2012;22:236–243.
- Klingenstein A, Haug AR, Nentwich MM, Tiling R, Schaller UC. Whole-body F-18-fluoro-2-deoxyglucose positron emission tomography/computed tomography imaging in the follow-up of metastatic uveal melanoma. *Melanoma Res*. 2010;20:511–516.

22. Servois V, Mariani P, Malhaire C, Petras S, Piperno-Neumann S, Plancher C. Preoperative staging of liver metastases from uveal melanoma by magnetic resonance imaging (MRI) and fluorodeoxyglucose-positron emission. *Eur J Surg Oncol*. 2010;36:189–194.
23. Orcurto V, Denys A, Voelter V, et al. ¹⁸F-fluorodeoxyglucose positron emission tomography/computed tomography and magnetic resonance imaging in patients with liver metastases from uveal melanoma: results from a pilot study. *Melanoma Res*. 2012;22:63–69.
24. Marshall E, Romaniuk C, Ghaneh P, et al. MRI in the detection of hepatic metastases from high-risk uveal melanoma: a prospective study in 188 patients. *Br J Ophthalmol*. 2013;97:159–163.
25. Brownstein S. Malignant melanoma of the conjunctiva. *Cancer Control*. 2004;11:310–316.
26. Shildkrot Y, Wilson MW. Conjunctival melanoma: pitfalls and dilemmas in management. *Curr Opin Ophthalmol*. 2010;21:380–386.
27. Triay E, Bergman L, Nilsson B, All-Ericsson C, Seregard S. Time trends in the incidence of conjunctival melanoma in Sweden. *Br J Ophthalmol*. 2009;93:1524–1528.
28. Tuomaala S, Eskelin S, Tarkkanen A, Kivelä T. Population-based assessment of clinical characteristics predicting outcome of conjunctival melanoma in whites. *Invest Ophthalmol Vis Sci*. 2002;43:3399–3408.
29. Yu GP, Hu DN, McCormick S, Finger PT. Conjunctival melanoma: is it increasing in the United States? *Am J Ophthalmol*. 2003;135:800–806.
30. Shields CL, Shields JA, Gunduz K, et al. Conjunctival melanoma: risk factors for recurrence, exenteration, metastasis, and death in 150 consecutive patients. *Arch Ophthalmol*. 2000;118:1497–1507.
31. Wong JR, Nanjp AA, Galor A, Karp CL. Management of conjunctival malignant melanoma: a review and update. *Expert Rev Ophthalmol*. 2014;9:185–204.
32. Shields CL, Markowitz JS, Belinsky I, et al. Conjunctival melanoma: outcomes based on tumor origin in 382 consecutive cases. *Ophthalmology*. 2011;118:389–395.e1–2.
33. Tuomaala S, Kivelä T. Metastatic pattern and survival in disseminated conjunctival melanoma: implications for sentinel lymph node biopsy. *Ophthalmology*. 2004;111:816–821.
34. Cohen VML, Tsimpida M, Hungerford JL, Jan H, Cerio R, Moir G. Prospective study of sentinel lymph node biopsy for conjunctival melanoma. *Br J Ophthalmol*. 2013;97:1525–1529.
35. Kurli M, Chin K, Finger PT. Whole-body ¹⁸F-FDG PET/CT imaging for lymph node and metastatic staging of conjunctival melanoma. *Br J Ophthalmol*. 2008;92:479–482.
36. Damian A, Gaudio J, Engler H, Alonso O. ¹⁸F-FDG PET-CT for staging of conjunctival melanoma. *World J Nucl Med*. 2013;12:45–47.
37. Wainstein AJ, Drummond-Lage AP, Kansaon MJ, et al. Sentinel lymph node biopsy for conjunctival malignant melanoma: surgical techniques. *Clin Ophthalmol*. 2014;9:1–6.
38. Bakri SJ, ed. *Mayo Clinic Guide to Better Vision*. Mayo Foundation for Medical Education and Research; 2014:11.

Imaging Biomarkers in Lung Cancer with ^{68}Ga -DOTATATE, ^{18}F -Fluoride, and ^{18}F -FDG PET/CT Scans and the Theranostics Paradigm

Mehdi Djekidel¹, Ghulam Syed², and Aladdin Kanbour³

¹NCCCR, Division of Oncology, Hamad Medical Corporation, Doha, Qatar; ²Department of Radiology, Division of Nuclear Medicine, Hamad Medical Corporation, Doha, Qatar; and ³Department of Radiology, Division of Nuclear Medicine, Sidra Medicine, Doha, Qatar

Lung cancer is the number 1 cause of cancer deaths in the United States. The prognosis is quite grim with the exception of stage 1. When faced with several failed therapeutic regimens and rapid progression of the disease, considering alternative therapies such as radiopharmaceutical therapies may be an option. We describe the case of a 36-y-old man with lung adenocarcinoma who had imaging molecular characterization of his disease with ^{18}F -FDG, ^{68}Ga -DOTATATE, and ^{18}F -fluoride PET/CT scans that were able to shed some light on molecular characterization of his disease and serve as a guide to potential targeted or personalized radiopharmaceutical therapeutic options.

Key Words: lung cancer; lung adenocarcinoma; ^{18}F -FDG; ^{68}Ga -DOTATATE; ^{18}F -fluoride; theranostics

J Nucl Med Technol 2021; 49:281–283

DOI: 10.2967/jnmt.120.258343

Lung cancer is the number 1 cause of cancer deaths in the United States. The overall 5-y survival is 12% (1). The adenocarcinoma subtype is the most common primary lung cancer. The prognosis is quite grim with the exception of stage 1 (1,2). Somatostatin receptor expression has been described in lung cancer in general and also specifically in lung adenocarcinomas (3–6). Today, β - and α -emitters are available for treatment clinically. The Food and Drug Administration and the European Medicines Agency have approved ^{177}Lu -DOTATATE and ^{223}Ra for the treatment of gastroenteropancreatic neuroendocrine tumors and metastatic castration-resistant prostate cancers, respectively. However, these agents have also been used off-label, such as in neuroblastoma, pheochromocytoma, paraganglioma, and thyroid cancer patients. When faced with several failed therapeutic regimens and rapid progression of the disease, exploring alternative therapies such as radiopharmaceutical therapies may be an option. In a theranostic approach, the choice of the radiopharmaceutical used for treatment is important and

will depend on the distribution of the disease and on uptake of the specific companion diagnostic agent.

CASE REPORT

We present the case of a 36-y-old man who quickly progressed to advanced, stage IV, moderately differentiated lung adenocarcinoma with metastasis to the liver and bone. Initial staging CT scans on May 12, 2019, showed an irregular right-upper-lobe mass and a few small sub-centimeter mediastinal lymph nodes. Biopsy revealed a moderately differentiated lung adenocarcinoma that was anaplastic large cell lymphoma-negative, had PD-L1 expression in 35% of the tumor, and had a next-generation sequencing EGFR mutation in exon 20 and a JAK mutation in exon 14. The initial staging ^{18}F -FDG scan showed uptake in the primary right-upper-lobe lesion and mediastinal lymph nodes, with no distant metastases (Fig. 1). Brain MRI findings were unremarkable. Right upper lobectomy and mediastinal lymph node dissection were performed, revealing invasive adenocarcinoma, mainly of the acinar subtype, and micropapillary components; there was a grade 1, well-differentiated single tumor measuring $4.2 \times 2.8 \times 2.5$ cm (R0). Spread of the tumor through air spaces was present. Visceral pleural invasion was also present, as well as extensive lymphovascular invasion. Twelve of 16 regional lymph nodes were involved, with extranodal extension. The patient at initial surgery had stage IIIA disease (T2b N2 M0). Surgery was followed by 4 cycles of adjuvant cisplatin/vinorelbine tartrate and adjuvant radiotherapy. About 1 mo after completion of adjuvant chemoradiation, the patient presented with generalized bone pain, and an ^{18}F -fluoride PET scan showed widespread bony metastasis (Fig. 2). This rapid progression of disease required an inpatient hospital stay and several narcotics for pain control. These findings prompted consideration of palliation with radionuclide-based treatments and bone-seeking agents such as ^{153}Sm , ^{89}Sr , ^{186}Re , ^{188}Re , or even ^{223}Ra . However, bearing in mind that the patient might also have additional soft-tissue disease, a ^{68}Ga -DOTATATE scan was performed to assess whether the disease was predominantly in the bones or also in the soft tissues (Fig. 3). This scan showed mostly bony lesions, slightly

Received Oct. 11, 2020; revision accepted Jan. 27, 2021.
For correspondence or reprints, contact Mehdi Djekidel (mdjekidel@sidra.org).

Published online March 15, 2021.

COPYRIGHT © 2021 by the Society of Nuclear Medicine and Molecular Imaging.

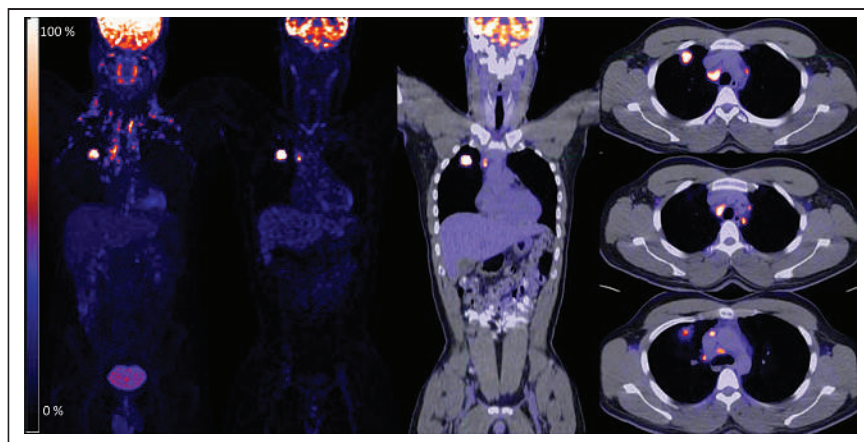


FIGURE 1. ^{18}F -FDG PET/CT scan. Initial staging showing intensely ^{18}F -FDG-avid right-upper-lobe mass with additional ^{18}F -FDG-avid mediastinal lymph nodes. From right to left maximum-intensity-projection PET, coronal PET, coronal PET/CT, and axial PET/CT images.

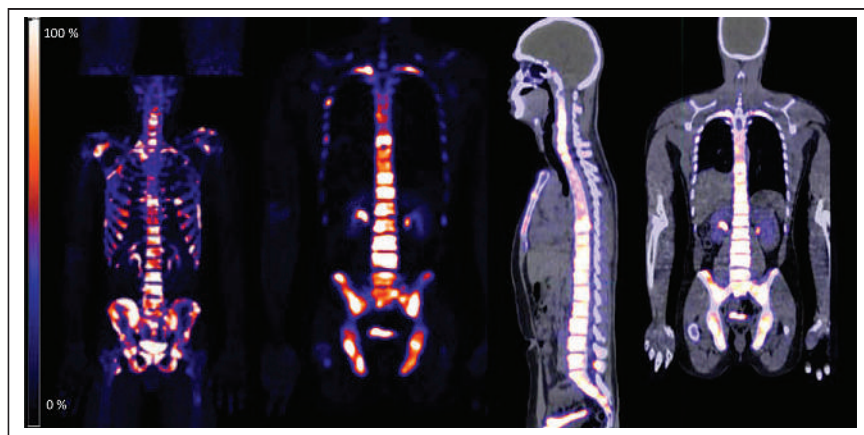


FIGURE 2. ^{18}F -fluoride PET/CT scan. Diffuse bony metastasis with intense ^{18}F -fluoride uptake is seen. From right to left maximum-intensity-projection PET, coronal PET, sagittal PET/CT, and coronal PET/CT images.

less prominent than on the ^{18}F -fluoride scan, and minimal uptake in the pleura, best appreciated retrospectively. Restaging ^{18}F -FDG PET done within a few days showed not only bony disease but also right-sided pleural disease and fewer than 5 subcentimeter liver deposits, also not appreciated on the ^{68}Ga -DOTATATE scan (Fig. 4). The progression of disease and molecular characterization are summarized in Figure 5.

DISCUSSION

^{223}Ra , an α -emitter selectively targeting bone metastasis, improved overall survival in the ALSYMPCA trial in castration-resistant metastatic prostate cancer (7,8). ^{177}Lu -DOTATATE, a β -emitter, also improved overall survival, progression-free survival, and quality of life in patients with midgut neuroendocrine tumors from the NETTER-1

study (9). Although radiopharmaceutical therapies are seldom used in lung cancer, there is a growing interest in use in a variety of cancers. ^{177}Lu -DOTATATE-based radiopharmaceutical therapies were also shown to improve overall and progression-free survival in bronchopulmonary carcinoids (10–13). Reports have also discussed the ^{177}Lu -DOTATATE treatment paradigm in small cell lung cancer (14–17). Additionally, some reports and clinical trials are evaluating the benefit of ^{223}Ra in non-small cell lung cancer (18–20). One of the prerequisites for ^{177}Lu treatment is somatostatin receptor expression demonstrated on a companion diagnostic ^{177}Lu -DOTATATE PET scan such as in our case. Positive bone scan results are the companion diagnostic for ^{223}Ra . ^{18}F -fluoride and ^{177}Lu -DOTATATE PET scans offer a road map to assess the eligibility of a patient for a therapeutic option. This, of course, is currently limited to situations in which all conventional treatments have been exhausted. In our patient, we considered palliative treatment with radiopharmaceutical therapies with bone-seeking agents such as ^{153}Sm , ^{89}Sr , or even ^{223}Ra . ^{177}Lu -DOTATATE treatment was considered within a theranostic approach in the context of the patient's also having some soft-tissue disease in the pleura and liver. Bone-seeking radiopharmaceuticals may be preferred in bone-predominant disease, and ^{177}Lu -DOTATATE-based

therapeutic radiopharmaceuticals may be preferred for non-bone-predominant disease. After declining any additional chemotherapy or immunotherapy and complete molecular characterization of the patient's disease with PET, the patient then traveled to his home country and passed away shortly thereafter.

CONCLUSION

Considering that lung cancer patients frequently have a poor prognosis, radiopharmaceutical therapies should be kept in mind even if only for palliation of disease. In the era of theranostics, it becomes feasible to assess targets by pretherapy imaging such as, in our patient, with ^{18}F -fluoride and ^{68}Ga -DOTATATE. Further studies and clinical trials are needed for validation in lung cancer and other types of cancer.

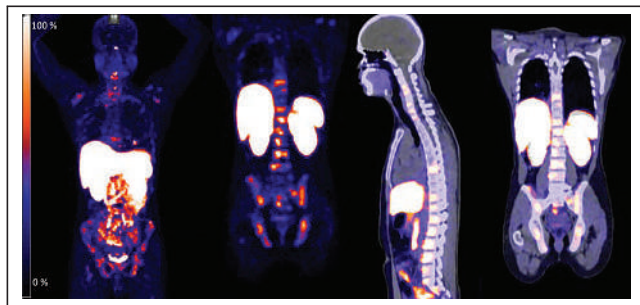


FIGURE 3. ^{68}Ga -DOTATATE PET/CT scan. Diffuse bony metastasis is noted; uptake of ^{68}Ga -DOTATATE is less prominent than that of ^{18}F -fluoride in Figure 2. Liver and pleural involvement seen on subsequent ^{18}F -FDG scan 1 wk later is not clearly appreciated with ^{68}Ga -DOTATATE. From right to left maximum-intensity-projection PET, coronal PET, sagittal PET/CT, and coronal PET/CT images.

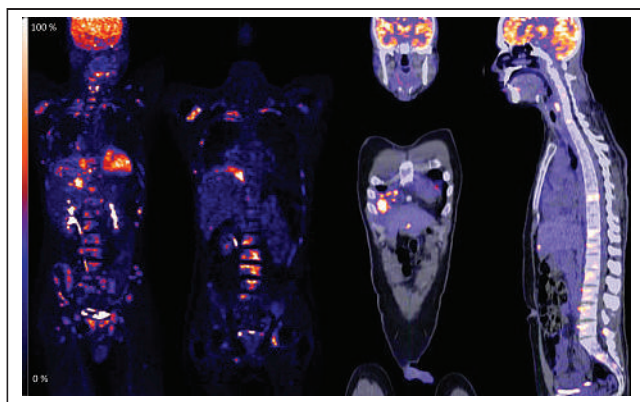


FIGURE 4. ^{18}F -FDG PET scan showing diffuse bony lesions but also detecting pleural and very minimal subtle liver disease not visualized on ^{68}Ga -DOTATATE scan. From right to left maximum-intensity-projection PET, coronal PET, coronal PET/CT, and sagittal PET/CT images.

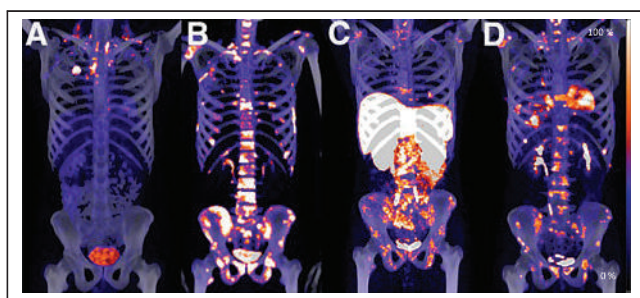


FIGURE 5. (A) Initial staging ^{18}F -FDG PET/CT scan. (B) Seven months later, ^{18}F -fluoride PET/CT scan shows diffuse bony metastasis. (C) Additional ^{68}Ga -DOTATATE PET/CT scan 2 wk later shows bony lesions less prominently than on ^{18}F -fluoride scan, somewhat similar to follow-up ^{18}F -FDG PET/CT scan. (D) Follow-up ^{18}F -FDG PET/CT scan 1 wk later shows bony lesions and pleural and liver disease.

DISCLOSURE

No potential conflict of interest relevant to this article was reported.

REFERENCES

- Myers DJ, Wallen JM. Lung adenocarcinoma. StatPearls website. <https://www.statpearls.com/ArticleLibrary/viewarticle/24486>. Updated June 26, 2021. Accessed August 2, 2021.
- Li C, Lu H. Adenosquamous carcinoma of the lung. *Onco Targets Ther*. 2018;11:4829–4835.
- Stumpf C, Kaemmerer D, Neubauer E, et al. Somatostatin and CXCR4 expression patterns in adenocarcinoma and squamous cell carcinoma of the lung relative to small cell lung cancer. *J Cancer Res Clin Oncol*. 2018;144:1921–1932.
- Petito LC, García-Albéniz X, Logan RW, et al. Estimates of overall survival in patients with cancer receiving different treatment regimens: emulating hypothetical target trials in the Surveillance, Epidemiology, and End Results (SEER)-Medicare linked database. *JAMA Netw Open*. 2020;3:e200452.
- Bombardieri E, Grippa F, Cataldo I, et al. Somatostatin receptor imaging of small cell lung cancer (SCLC) by means of ^{111}In -DTPA octreotide scintigraphy. *Eur J Cancer*. 1995;31A:184–188.
- Traub T, Petkov V, Ofluoglu S, et al. ^{111}In -DOTA-lanreotide scintigraphy in patients with tumors of the lung. *J Nucl Med*. 2001;42:1309–1315.
- Parker C, Nilsson S, Heinrich D, et al. Alpha emitter radium-223 and survival in metastatic prostate cancer. *N Engl J Med*. 2013;369:213–223.
- Taneja SS. Re: alpha emitter radium-223 and survival in metastatic prostate cancer [editorial]. *J Urol*. 2014;191:657.
- Strosberg JR, Wolin EM, Chasen BA, et al. First update on overall survival, progression-free survival, and health-related time-to-deterioration quality of life from the NETTER-1 study: ^{177}Lu -Dotatate vs. high dose octreotide in progressive midgut neuroendocrine tumors [abstract]. *J Clin Oncol*. 2018;36(suppl):4099.
- Escala Cornejo RA, García-Talavera P, Navarro Martin M, et al. Large cell neuroendocrine carcinoma of the lung with atypical evolution and a remarkable response to lutetium Lu 177 dotatate. *Ann Nucl Med*. 2018;32:568–572.
- Filoso PL, Ruffini E, Oliaro A, et al. Large-cell neuroendocrine carcinoma of the lung: a clinicopathologic study of eighteen cases and the efficacy of adjuvant treatment with octreotide. *J Thorac Cardiovasc Surg*. 2005;129:819–824.
- Mariniello A, Bodei L, Tinelli C, et al. Long-term results of PRRT in advanced bronchopulmonary carcinoid. *Eur J Nucl Med Mol Imaging*. 2016;43:441–452.
- Naraev BG, Ramirez RA, Kendi AT, et al. Peptide receptor radionuclide therapy for patients with advanced lung carcinoids. *Clin Lung Cancer*. 2019;20:e376–e392.
- Lewin J, Cullinane C, Akhurst T, et al. Peptide receptor chemoradionuclide therapy in small cell carcinoma: from bench to bedside. *Eur J Nucl Med Mol Imaging*. 2015;42:25–32.
- Schmitt A, Bernhardt P, Nilsson O, et al. Biodistribution and dosimetry of ^{177}Lu -labeled [DOTA⁰,Tyr³]octreotate in male nude mice with human small cell lung cancer. *Cancer Biother Radiopharm*. 2003;18:593–599.
- Schmitt A, Bernhardt P, Nilsson O, et al. Differences in biodistribution between $^{99\text{m}}\text{Tc}$ -depreotide, ^{111}In -DTPA-octreotide, and ^{177}Lu -DOTA-Tyr³-octreotate in a small cell lung cancer animal model. *Cancer Biother Radiopharm*. 2005;20:231–236.
- Lapa C, Hänscheid H, Wild V, et al. Somatostatin receptor expression in small cell lung cancer as a prognostic marker and a target for peptide receptor radionuclide therapy. *Oncotarget*. 2016;7:20033–20040.
- Taber AM, Riley D, Olszewski AJ, et al. Radium-223 following front-line chemotherapy for patients with non-small cell lung cancer and bone metastases [abstract]. *J Clin Oncol*. 2018;36(suppl):e21211.
- Geva R, Lopez J, Danson S, et al. Radium-223 in combination with paclitaxel in cancer patients with bone metastases: safety results from an open-label, multicenter phase Ib study. *Eur J Nucl Med Mol Imaging*. 2019;46:1092–1101.
- Reck M, Mileham KF, Clump DA, et al. 1420TiP A phase I/II trial of radium-223 (Ra-223) in combination with pembrolizumab in patients (pts) with stage IV non-small cell lung cancer (NSCLC) [abstract]. *Ann Oncol*. 2020;31(suppl 4):S897–S898.

Effect of COVID-19 on ^{18}F -FDG PET/CT: Is There a Need to Consider COVID-19 Status Before Planning ^{18}F -FDG PET/CT for Oncologic Evaluation?

Anwin Joseph Kavanal¹, Santosh Ranjan Jena¹, Rajender Kumar¹, Chandan Krushna Das², Sunil Kumar¹, and Bhagwant Rai Mittal¹

¹Department of Nuclear Medicine, Postgraduate Institute of Medical Education and Research, Chandigarh, India; and ²Medical Oncology OPD, Department of Radiotherapy, Postgraduate Institute of Medical Education and Research, Chandigarh, India

Incidental detection of coronavirus disease 2019 (COVID-19)-related lung changes on ^{18}F -FDG PET/CT images of oncology patients has been increasingly reported. Most of the case reports or series have stressed the retrospective diagnosis of COVID-19 with the help of ^{18}F -FDG PET/CT lung findings. In this case report, we introduce a different aspect of COVID-19-related lung changes on ^{18}F -FDG PET/CT, interfering with the evaluation of metastatic lung lesions in a patient with renal cell carcinoma.

Key Words: COVID-19; ^{18}F -FDG PET/CT; lung metastasis; response evaluation; renal cell carcinoma

J Nucl Med Technol 2021; 49:284–285

DOI: 10.2967/jnmt.121.262145

Various lung involvement patterns have been reported on ^{18}F -FDG PET/CT scans of coronavirus disease 2019 (COVID-19) patients undergoing workup for various malignancies. The patterns range from ^{18}F -FDG-avid diffuse ground-glass opacities to ^{18}F -FDG-avid patchy consolidatory changes, with or without ^{18}F -FDG-avid mediastinal lymph nodes, depending on the imaging time from the onset of infection and other unknown factors (1–4). COVID-19 infection was a retrospective diagnosis in most reported cases, after the typical findings were seen on the ^{18}F -FDG PET/CT images (3–7). Here, we present a different aspect of COVID-19 on ^{18}F -FDG PET/CT, in which there was interference with response assessment in a patient receiving chemotherapy for pulmonary metastasis from renal cell carcinoma.

CASE REPORT

A 45 y-old man with a known case of metastatic renal cell carcinoma underwent cytoreduction nephrectomy followed by first-line chemotherapy with pembrolizumab and axitinib because of multiple cannonball metastases in the lungs. ^{18}F -FDG PET/CT at the end of treatment showed disease progression in the form of an increase in the number and size of lung nodules. The patient was then started on second-line chemotherapy with oral lenvatinib (18 mg daily) and everolimus (5 mg daily). His interim ^{18}F -FDG PET/CT scan (Fig. 1) showed a favorable response ($>30\%$ reduction in size and ^{18}F -FDG avidity compared with baseline PET/CT) to second-line therapy, and he was continued on the same treatment. He was diagnosed with COVID-19 in May 2020 on evaluation for malaise and chills. He was managed conservatively with antibiotics, antipyretics, and multivitamins in a local hospital. He had no symptoms or signs suggestive of pneumonia and never required oxygen support during the 11-d course in the hospital. He was discharged from the hospital after a negative nucleic acid test 1 wk before

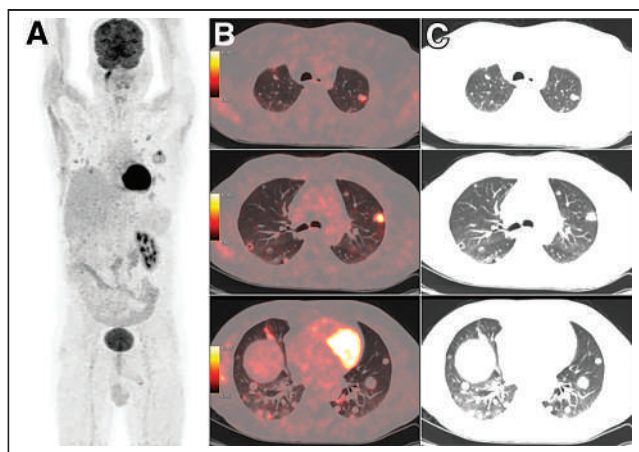


FIGURE 1. ^{18}F -FDG PET/CT whole-body maximum-intensity-projection image (A), axial PET/CT images (B), and corresponding CT images (C) showing variably ^{18}F -FDG-avid random nodules in both lung fields (SUV_{max} of hottest nodule, 9.9).

Received Feb. 16, 2021; revision accepted Mar. 26, 2021.
For correspondence or reprints, contact Bhagwant Rai Mittal (brmittal@yahoo.com).
Published online July 9, 2021.
Immediate Open Access: Creative Commons Attribution 4.0 International License (CC BY) allows users to share and adapt with attribution, excluding materials credited to previous publications. License: <https://creativecommons.org/licenses/by/4.0/>. Details: <http://jnmsnmjournals.org/site/misc/permission.xhtml>.
COPYRIGHT © 2021 by the Society of Nuclear Medicine and Molecular Imaging.

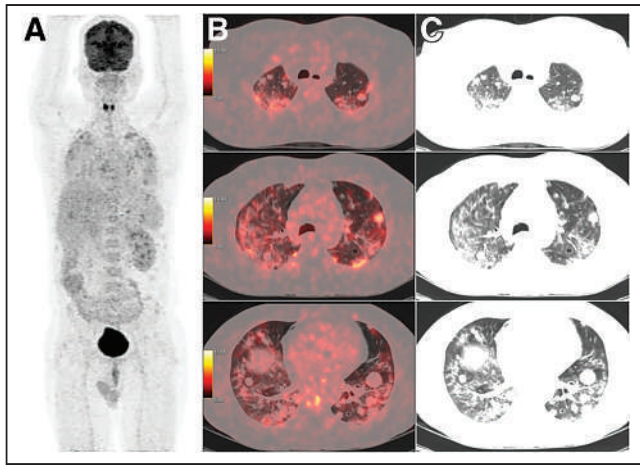


FIGURE 2. ¹⁸F-FDG PET/CT whole-body maximum-intensity-projection image (A), axial PET/CT images (B), and corresponding CT images (C) showing ¹⁸F-FDG-avid diffuse ground-glass opacities/patchy consolidatory changes bilaterally in lung fields from apex to base, obscuring details of metastatic lesions (SUV_{max} of hottest nodule, 7.8; SUV_{max} of ground-glass opacities, 7.3).

he was scheduled for an ¹⁸F-FDG PET/CT scan at 6 mo of chemotherapy to determine the response. The ¹⁸F-FDG PET/CT scan (Fig. 2) showed ¹⁸F-FDG-avid diffuse ground-glass opacities/patchy consolidatory changes bilaterally in the lung fields from apex to base, obscuring the metastatic lesions. The COVID-19-related lung changes obscured both the anatomic and the metabolic features of the metastatic lesions, leading to difficulty in assessing the response to treatment.

DISCUSSION

¹⁸F-FDG uptake in ground-glass opacities in the background may add spill-in counts to metastatic lesions, causing a falsely

high uptake in metastatic lesions (8). For this reason, an accurate assessment of the metabolic response was not possible in this patient. The patient was advised to repeat the nucleic acid test because of ¹⁸F-FDG avidity in the ground-glass opacities/consolidatory changes and was found to be positive. The patient was then advised to remain home in isolation again.

CONCLUSION

During the COVID-19 pandemic phase, we have to consider sources of possible interference such as described in this report before scheduling patients for ¹⁸F-FDG PET/CT scans for various oncologic purposes.

DISCLOSURE

No potential conflict of interest relevant to this article was reported.

REFERENCES

1. Ajuria-Illarramendi O, Martinez-Lorca A, Orduna-Diez MDP. [¹⁸F]FDG-PET/CT in different COVID-19 phases. *IDCases*. 2020;21:e00869.
2. Charters PFP, Little D, Rodrigues JCL, et al. ¹⁸F-FDG-PET/CT findings in COVID-19: a single centre retrospective radiological review. *BJR Case Rep*. 2020;6:20200091.
3. Liu C, Zhou J, Xia L, et al. ¹⁸F-FDG PET/CT and serial chest CT findings in a COVID-19 patient with dynamic clinical characteristics in different period. *Clin Nucl Med*. 2020;45:495–496.
4. Colandrea M, Gilardi L, Travaini LL, et al. ¹⁸F-FDG PET/CT in asymptomatic patients with COVID-19: the submerged iceberg surfaces. *Jpn J Radiol*. 2020;38:1007–1011.
5. Deng Y, Lei L, Chen Y, et al. The potential added value of FDG PET/CT for COVID-19 pneumonia. *Eur J Nucl Med Mol Imaging*. 2020;47:1634–1635.
6. Doroudinia A, Tavakoli M. A case of coronavirus infection incidentally found on FDG PET/CT scan. *Clin Nucl Med*. 2020;45:e303–e304.
7. Martineau P, Kidane B. FDG PET/CT findings in an asymptomatic case of confirmed COVID-19. *Clin Nucl Med*. 2020;45:647–648.
8. Akerele MI, Wadhwa P, Silva-Rodriguez J, et al. Validation of the physiological background correction method for the suppression of the spill-in effect near highly radioactive regions in positron emission tomography. *EJNMMI Phys*. 2018;5:34.

Reactive Axillary Lymphadenopathy to COVID-19 Vaccination on ^{18}F -FDG PET/CT

Mathew V. Smith and Ming Yang

Department of Radiology, Mayo Clinic, Scottsdale, Arizona

In this report, we present ^{18}F -FDG PET/CT findings of reactive left axillary and supraclavicular hypermetabolic lymphadenopathy, as well as ipsilateral deltoid muscle injection site radiotracer uptake, related to recent coronavirus disease 2019 (COVID-19) vaccination in a patient with osteosarcoma. With the growing number of patients receiving COVID-19 vaccine, recognition of benign characteristic ^{18}F -FDG PET/CT image findings will ensure staging and restaging accuracy and avoid unnecessary biopsy.

Key Words: COVID-19; vaccination; lymphadenopathy

J Nucl Med Technol 2021; 49:286–287

DOI: 10.2967/jnmt.121.262008

Reactive lymphadenopathy is a recognized side effect related to vaccination. With messenger RNA–based coronavirus disease 2019 (COVID-19) vaccines, efficacy depends on the activation of dendritic cells after administration. These activated antigen-presenting cells must then migrate to the draining lymph nodes and present the translated protein to the node-based B and T cells in order to create robust humoral and cell-mediated adaptive immunity (1). As more oncologic patients start to receive COVID-19 vaccines, it is important to recognize the benign ^{18}F -FDG PET/CT imaging features immediately after vaccination to ensure staging accuracy and prevent unnecessary biopsy.

CASE REPORT

A 40-y-old woman with a history of metastatic left proximal tibia osteosarcoma underwent surveillant ^{18}F -FDG PET/CT. There was no radiotracer uptake suggestive of tumor recurrence. However, multiple morphologically benign-appearing hypermetabolic lymph nodes were visualized at the left axillary and supraclavicular regions, as well as focal uptake in the left deltoid muscle (Fig. 1). On further interview, the patient revealed receiving her second dose of the BNT162b2 vaccine (Pfizer/BioNTech) against SARS-CoV-2 the day before the ^{18}F -FDG PET/CT scan. She also stated that she had experienced pain at the left-upper-arm injection site, intense body aches, headaches, and a slight fever. Combined with inoculation history and characteristic imaging

features, as well as exclusion of tracer injection at ipsilateral arm, a diagnosis of reactive lymphadenopathy secondary to COVID-19 vaccination was achieved.

Reactive lymphadenopathy is one of the well-documented reactions after intramuscular injection of COVID-19 vaccine and is likely secondary to a robust vaccine-elicited immune response (2,3). The efficacy of messenger RNA COVID-19 vaccine depends on encoding dendritic cell migration to draining lymph nodes in order to kickstart the complex humoral and cell-mediated response and, ultimately, to establish immunity (2). There are rich draining lymph nodes at the axillary region that may show an immediate response after vaccination (4,5). ^{18}F -FDG is a glucose analog and is nonspecifically trapped in metabolically active tumor cells and benign conditions such as infection and inflammation, potentially leading to false-positive interpretations on oncologic ^{18}F -FDG PET/CT scans (6). Among the most common etiologies of hypermetabolic axillary lymph nodes on ^{18}F -FDG PET/CT scans are malignancies, reactive changes, and lymphatic drainage of radiotracer extravasation.

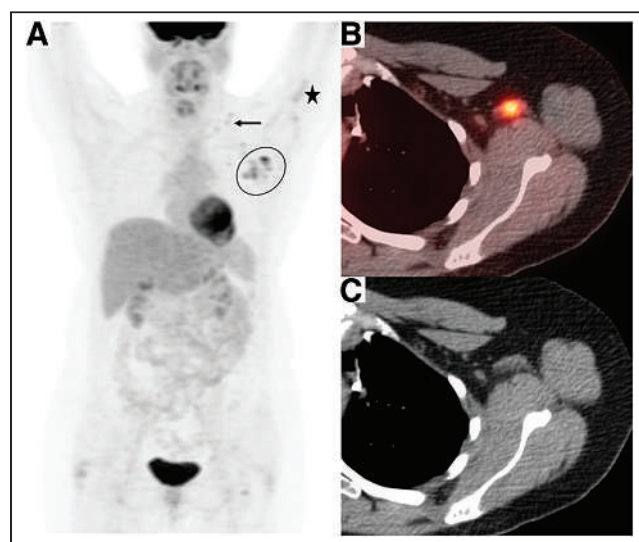


FIGURE 1. (A) Maximum-intensity-projection image demonstrating cluster of hypermetabolic left axillary lymph nodes (encircled), cluster of hypermetabolic supraclavicular lymph nodes (arrow), and faint intramuscular radiotracer uptake (star). (B and C) Representative left axillary lymph node that appears benign on axial CT image (C) but demonstrates increased uptake (SUV_{max} , 7.1) on axial ^{18}F -FDG PET/CT image (B).

Received Jan. 26, 2021; revision accepted Mar. 9, 2021.
For correspondence or reprints, contact Ming Yang (yang.ming@mayo.edu).
Published online April 5, 2021.
COPYRIGHT © 2021 by the Society of Nuclear Medicine and Molecular Imaging.

CONCLUSION

With more oncologic patients receiving messenger RNA COVID-19 vaccines, it is important for nuclear radiologists to recognize the characteristic benign ^{18}F -FDG uptake after vaccination. A detailed COVID-19 vaccination history, including the inoculation time, which arm was injected, and any side effects, should be acquired before the ^{18}F -FDG PET/CT scan to ensure the accuracy of staging or restaging and to avoid an unnecessary biopsy.

DISCLOSURE

No potential conflict of interest relevant to this article was reported.

REFERENCES

1. Lindsay KE, Bhosle SM, Zurla C, et al. Visualization of early events in mRNA vaccine delivery in non-human primates via PET-CT and near-infrared imaging. *Nat Biomed Eng.* 2019;3:371–380.
2. Polack FP, Thomas SJ, Kitchin N, et al. Safety and efficacy of the BNT162b2 mRNA Covid-19 vaccine. *N Engl J Med.* 2020;383:2603–2615.
3. Baden LR, El Sahly HM, Essink B, et al. Efficacy and safety of the mRNA-1273 SARS-CoV-2 vaccine. *N Engl J Med.* 2021;384:403–416.
4. Coates EE, Costner PJ, Nason MC, et al. Lymph node activation by PET/CT following vaccination with licensed vaccines for human papillomaviruses. *Clin Nucl Med.* 2017;42:329–334.
5. Thomassen A, Lerberg Nielsen A, Gerke O, Johansen A, Petersen H. Duration of ^{18}F -FDG avidity in lymph nodes after pandemic H1N1v and seasonal influenza vaccination. *Eur J Nucl Med Mol Imaging.* 2011;38:894–898.
6. Stumpe KD, Dazzi H, Schaffner A, von Schulthess GK. Infection imaging using whole-body FDG-PET. *Eur J Nucl Med.* 2000;27:822–832.

Follicular Thyroid Carcinoma with Unusual Radioiodine-Refractory Breast Metastasis Mimicking Primary Breast Malignancy

Tarun Kumar Jain¹, Venkata Subramanian Krishnaraju¹, Bhagwant Rai Mittal¹, Ashwani Sood¹, Rajender Kumar¹, Rashi Garg², and Sunil Kumar¹

¹Department of Nuclear Medicine, Postgraduate Institute of Medical Education and Research, Chandigarh, India; and ²Cytopathology, Postgraduate Institute of Medical Education and Research, Chandigarh, India

The breast is an unusual site for metastasis from malignant tumors, although it may be the first manifestation of an extramammary primary malignancy typically arising in the lung, skin (melanoma), ovary, or lymph nodes (lymphoma). Breast metastasis from thyroid carcinoma is extremely rare and may take years to develop, as differentiated thyroid carcinoma is usually indolent and slow-growing and metastasizes to the lymph nodes, lungs, and bones. Here, we present the case of a middle-aged woman (after subtotal thyroidectomy for multinodular goiter 24 y previously) showing discordant ¹⁸F-FDG and iodine avidity in proven metastatic disease involving the lymph nodes, bones, spleen, and breast on whole-body ¹³¹I and ¹⁸F-FDG scans due to tumor heterogeneity.

Key Words: follicular thyroid carcinoma; iodine scan; ¹⁸F-FDG; PET/CT; breast metastasis

J Nucl Med Technol 2021; 49:288–289

DOI: 10.2967/jnmt.120.259259

Metastatic involvement of the breast is unusual, with an incidence of 0.5%–2.0%, when the primary tumor is a lung malignancy, a melanoma, or a hematologic malignancy, apart from the contralateral breast (a primary tumor in one breast that metastasizes to the other breast) (1). Separate primary malignancies may occur in thyroid and breast in a synchronous or metachronous fashion (2). However, breast metastasis arising from a thyroid primary is very uncommon.

CASE REPORT

A 55-y-old woman, who 24 y previously had undergone subtotal thyroidectomy for multinodular goiter and had been on levothyroxine replacement treatment since that time, presented with a low backache of 10-mo duration. MRI of the spine showed a large soft-tissue mass at the level of the L5–S1 vertebrae, and the histopathologic diagnosis on a fine-needle aspiration sample was metastatic follicular

thyroid carcinoma. The biochemical profile showed a normal serum level of thyroid-stimulating hormone (0.9 μ IU/mL; reference range, 0.5–4.5 μ IU/mL) and elevated levels of thyroglobulin (>1,000 ng/mL; reference range, 0–55 ng/mL) and antithyroglobulin (938.6 IU/mL; reference range, 0–125 IU/mL). A diagnostic radioiodine planar scan of the whole body and a SPECT/CT scan of the neck and thorax were done after administration of an oral dose of 74 MBq (\sim 2 mCi) of ¹³¹I. Iodine-avid widespread metastatic disease and a non-iodine-avid right-breast lesion were seen on the planar, SPECT/CT, and CT images (Fig. 1).

In view of the presence of both iodine-avid and non-iodine-avid lesions and the markedly elevated thyroglobulin levels, ¹⁸F-FDG whole-body PET/CT (Fig. 2) was done to identify the disease extent and characterize the lesions. This scan showed—in the right breast, the spleen, the skeleton, and the cervical lymph nodes—¹⁸F-FDG-avid lesions that were non-avid on the iodine scan. Mammography revealed a lesion in the parenchyma of the right breast (category 4 in the Breast Imaging Reporting and Data System), without involvement of the contralateral breast. A fine-needle aspiration sample from the breast lesion revealed metastatic follicular carcinoma of the thyroid based on cytopathologic features and thyroglobulin levels from the washout sample (Fig. 3). The patient received 7,400 MBq (\sim 200 mCi) of radioiodine therapy in view of the iodine-avid widespread metastatic disease, though the breast lesion remained non-tracer-avid on the posttherapy iodine scan, confirming its radioiodine-refractory nature.

DISCUSSION

Metastasis of differentiated thyroid cancer to the breast is extremely rare, with only a few isolated cases being reported in the literature (3,4). There are no clinical or mammographic parameters that can indicate whether a malignant breast lesion is a secondary manifestation of a separate primary tumor. As in our patient, heterogeneity in iodine and ¹⁸F-FDG uptake may correspond to varied degrees of differentiation, as glucose metabolism is inversely related to iodine uptake, and ¹⁸F-FDG PET/CT has an established role in the detection of iodine-negative recurrent or metastatic disease. Cytologic or histopathologic examination of fine-needle aspiration

Received Oct. 26, 2020; revision accepted Jan. 27, 2021.
For correspondence or reprints, contact Ashwani Sood (sood99@yahoo.com).

Published online March 15, 2021.

COPYRIGHT © 2021 by the Society of Nuclear Medicine and Molecular Imaging.

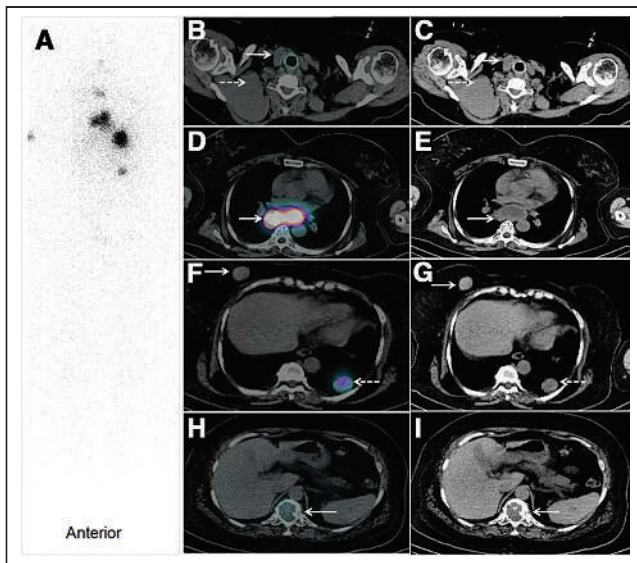


FIGURE 1. Whole-body radioiodine planar (A), transaxial SPECT/CT (B, D, F, and H), and CT (C, E, G, and I) images showing iodine-avid residual tissue in thyroid bed (B and C, solid arrows), multiple cervical and mediastinal lymph nodes (D and E, arrows), bilateral lung nodules (F and G, dashed arrows), and a few non-tracer-avid cervical lymph nodes (B and C, dashed arrows), right-breast lesions (F and G, solid arrows), and skeletal lesions (H and I, arrows).

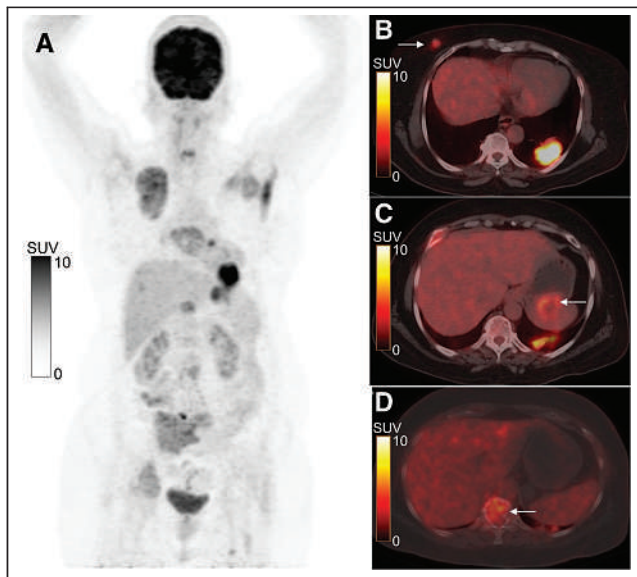


FIGURE 2. Maximum-intensity-projection PET image (A) and transaxial PET/CT images (B, C, and D) showing ^{18}F -FDG-avid lesions in right breast (B, arrow; SUV_{max} , 3.6), spleen (C, arrow), and D12 vertebra (D, arrow) (nonavid on whole-body iodine scan).

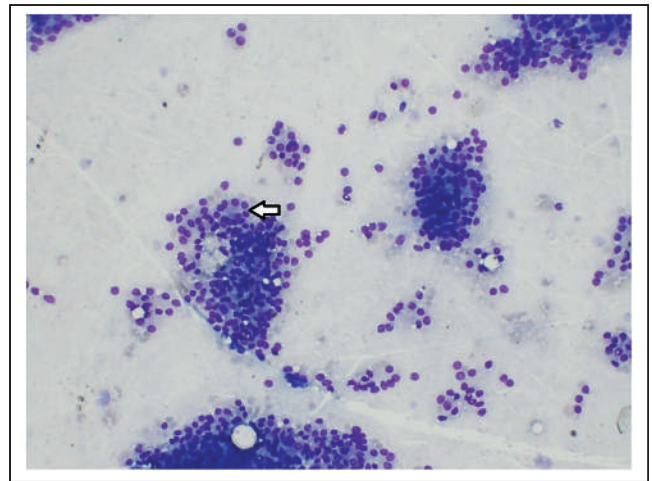


FIGURE 3. Photomicrograph of sample from fine-needle aspiration of right-breast lesion showing monomorphic tumor cells arranged in microfollicles (May-Grünwald-Giemsa stain, $\times 100$; arrow), suggestive of metastatic follicular carcinoma from thyroid.

samples of the breast lesion after immunohistochemistry is the mainstay for diagnosis and for differentiating primary from secondary lesions (5).

CONCLUSION

Management of primary breast lesions is entirely different from that of secondary breast lesions arising from thyroid carcinoma. The widespread disease with tumor heterogeneity in this index case was appreciated on 2 different functional imaging modalities, though precise sampling was essential for diagnosis and appropriate therapy.

DISCLOSURE

No potential conflict of interest relevant to this article was reported.

REFERENCES

- McIntosh IH, Hooper AA, Millis RR, Greening WP. Metastatic carcinoma within the breast. *Clin Oncol*. 1976;2:393–401.
- Nio Y, Iguchi C, Itakura M, et al. High incidence of synchronous or metachronous breast cancer in patients with malignant and benign thyroid tumor or tumor-like disorders. *Anticancer Res*. 2009;29:1607–1610.
- Tanriverdi O, Avci A, Yugunt I, Polat M. A case report of breast and liver metastases of thyroid follicular carcinoma. *J Cancer Res Ther*. 2015;11:652.
- Cristallini EG, Ascani S, Nati S, Liberati F, Farabi R. Breast metastasis of thyroid follicular carcinoma. *Acta Oncol*. 1994;33:71–73.
- Sneige N, Zachariah S, Fanning TV, Dekmezian RH, Ordóñez NG. Fine-needle aspiration cytology of metastatic neoplasms in the breast. *Am J Clin Pathol*. 1989;92:27–35.

Antiseptic-Mediated Colloid Labeling as a Potential Source of Abnormal Liver and Spleen Uptake with ^{99m}Tc -Dimercaptosuccinic Acid

Veronica Krull, Madison R. Kocher, and William J. Rieter

Department of Radiology, Medical University of South Carolina, Charleston, South Carolina

Altered biodistribution can be a source of diagnostic error in the interpretation of nuclear medicine studies. This case reports an instance of increased liver and spleen uptake with ^{99m}Tc -dimercaptosuccinic acid believed to be a result of chlorhexidine-mediated colloid labeling. This finding underscores the principle that certain constituents of antiseptics may adversely affect the purity of radiopharmaceuticals during their preparation.

Key Words: ^{99m}Tc -DMSA; antiseptic; chlorhexidine; colloid; liver-spleen

J Nucl Med Technol 2021; 49:290–291

DOI: 10.2967/jnmt.120.258020

^{99m}Tc -dimercaptosuccinic acid (DMSA) is a renal cortical binding agent used for the evaluation of renal parenchymal abnormalities such as renal cortical scarring. It has been suggested that certain constituents of antiseptics used during preparation of ^{99m}Tc -DMSA, including chlorhexidine, may interact with the DMSA molecules to form ^{99m}Tc -labeled colloid particles (1). The colloid particles are subsequently extracted by the reticuloendothelial system, leading to increased hepatic and splenic uptake. Yet, to our knowledge, there has been only a single case report illustrating this phenomenon since it was first described over 2 decades ago (2). Herein, this case presents diffusely increased liver and spleen ^{99m}Tc -DMSA uptake likely secondary to chlorhexidine-mediated colloid labeling. Recognition of this pattern of activity with ^{99m}Tc -DMSA is important not only to provide an accurate clinical impression but also to emphasize that improper technique with antiseptics may be a source of radiochemical impurity.

CASE REPORT

The patient was initially diagnosed with grade II left vesicoureteral reflux via a fluoroscopic voiding

cystourethrogram at 5 mo old after multiple renal cysts were incidentally noted on spine MRI. There was no reported history of urinary tract infections, and laboratory values at the time were within normal limits. One year later, a follow-up voiding cystourethrogram showed resolution of the vesicoureteral reflux. A subsequent ^{99m}Tc -DMSA scan showed a small left kidney with multiple areas of probable renal cortical scarring (Figs. 1A and 1B). Annual ultrasounds continued to show a size discrepancy between the kidneys. When the patient was 13 y old, a repeat ^{99m}Tc -DMSA scan was ordered because of a transfer of care to reevaluate this size discrepancy. The repeat scan showed a similar pattern of renal cortical uptake in the small left kidney; however, mild diffuse activity throughout the liver and spleen was also observed (Figs. 1C and 1D). At the time of the scan, the patient was asymptomatic; laboratory values were normal, with a creatinine of 0.7 mg/dL; and the only reported medication was polyethylene glycol (GlycoLax; SRZ Properties, Inc.), as needed, which prompted us to further investigate the etiology of abnormal uptake. The institutional review board approved this study, and the requirement for informed consent was waived.

DISCUSSION

Increased hepatic and splenic activity with ^{99m}Tc -DMSA has been shown to occur in the setting of several disease processes, including acute renal failure, mononucleosis, and hepatic steatosis (3). Impurities should also be considered a potential source of altered biodistribution, particularly when the patient is otherwise healthy and laboratory values are normal (2,4). While investigating the source of altered biodistribution in this case, we discovered that the technologist failed to let the antiseptic used to sterilize the rubber stopper on the supplied DMSA vial dry completely before reconstituting it with ^{99m}Tc . We believed contamination with chlorhexidine was the likely source of altered distribution when considering the constellation of otherwise normal clinical findings, medication review, and lot verification of DMSA with the manufacturer.

Received Oct. 4, 2020; revision accepted Jan. 27, 2021.
For correspondence or reprints, contact William J. Rieter (rieter@musc.edu).
Published online March 15, 2021.
COPYRIGHT © 2021 by the Society of Nuclear Medicine and Molecular Imaging.

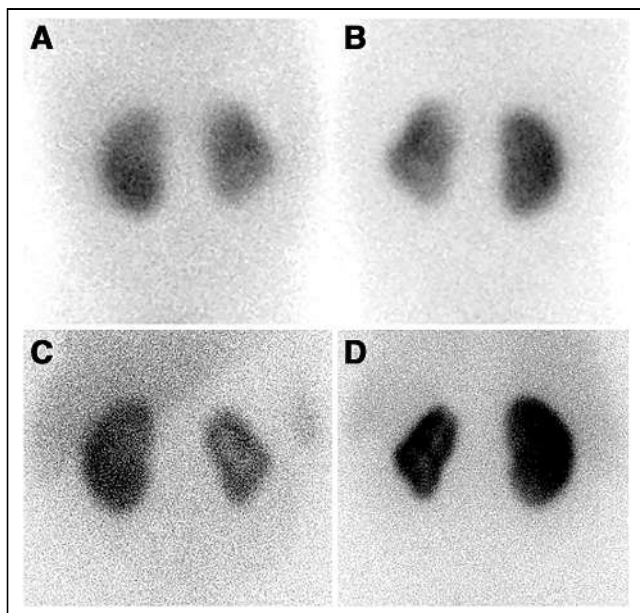


FIGURE 1. (A and B) Anterior (A) and posterior (B) ^{99m}Tc -DMSA images obtained in a 20-mo-old child showing a small left kidney with probable areas of superior and inferior pole scarring. A dromedary hump is also seen on the left kidney, and is most consistent with an anatomic variant based on correlation with ultrasound. (C and D) Anterior (C) and posterior (D) scintigraphic images obtained in the same patient at 13 y old, showing a similar appearing small left kidney, but now with mild diffuse radiotracer activity throughout the liver and spleen.

CONCLUSION

As new antiseptic formulations are introduced for clinical use, it is important for technologists and nuclear medicine practitioners to be aware that certain constituents may adversely affect the purity of radiopharmaceuticals and, subsequently, result in an atypical biodistribution of the radiotracer. When preparing DMSA, ethanol could be considered an alternative antiseptic if not routinely used in a clinical practice.

DISCLOSURE

No potential conflict of interest relevant to this article was reported.

REFERENCES

1. Murray T, Hilditch TE, Whateley TL, Elliott AT. Formation of labelled colloid in ^{99m}Tc -DMSA due to the presence of bactericidal fluid. *Nucl Med Commun*. 1986;7: 505–510.
2. Firuzyar T, Ghaedian T. The effect of antiseptic on ^{99m}Tc -DMSA scans. *Clin Nucl Med*. 2017;42:237–238.
3. Fakhari A, Mamaghani FF, Gharepapagh E, Dabiri S. Dos and don'ts that are issued through radiolabeling process of DMSA (dimercaptosuccinic acid) by $^{99m}\text{TcO}_4^-$ and ^{99m}Tc -DMSA(III)DMSA (III), the gold standard radiopharmaceutical for renal cortical scintigraphy. *J Nucl Med Radiat Ther*. 2018;9:1–7.
4. Vallabhajosula S, Killeen R, Osborne J. Altered biodistribution of radiopharmaceuticals: role of radiochemical/pharmaceutical purity, physiological, and pharmacologic factors. *Semin Nucl Med*. 2010;40: 220–241.

Regarding “Waxing and Waning Presentation of Isolated Cardiac Sarcoidosis on Sequential ¹⁸F-FDG PET Exams”

TO THE EDITOR: I read with interest the article by Ostwani et al. (1) and, for 3 reasons, am concerned that the patient does not have cardiac sarcoidosis (CS). First, because of the lack of a positive biopsy result, the patient does not meet guideline criteria for the diagnosis of CS (2). Second, corticosteroid-refractory sarcoidosis is considered very rare (3). Third, accumulating data suggest that there may not be a pathophysiologic entity of truly isolated CS. It is clear that there are many patients with manifest CS who have no clinically apparent disease in other organs—that is, who have what can be termed *clinically* isolated CS. However, sarcoidosis is, by definition and biology, a systemic disease. Hence, a key starting point to understand isolated CS is to agree on a standardized definition. The 2017 version of the Japanese CS guidelines tackled, for the first time, the definition of and criteria for the diagnosis for isolated CS (4). They included the following 3 criteria: no clinical findings characteristic of sarcoidosis are observed in any organs other than the heart; ⁶⁷Ga scintigraphy or ¹⁸F-FDG PET reveals no abnormal tracer accumulation in any organs other than the heart; and a chest CT scan reveals no shadowing along the lymphatic tracts in the lungs or no hilar and mediastinal lymphadenopathy (minor axis > 10 mm).

Using a similar definition, my group found *imaging*-isolated CS in only 1 in 31 patients (5). However, other data suggest that even these apparent isolated cases are unlikely to be truly isolated. Petek et al. investigated 10 patients with presentations and cardiac imaging consistent with the Japanese definition of isolated CS. Four of these 10 had granulomas on bronchial biopsy (6). Hence,

these data suggest that there is a small subset of patients who at the moment of ¹⁸F-FDG PET imaging have PET-detectable inflammation only in their heart. However, it also follows that additional or interval investigation will likely reveal extracardiac disease.

This debate is more than just semantics, as the overdiagnosis of “imaging-isolated CS” can, as in this case (1), lead to unnecessary immunosuppression or a missed alternative diagnosis.

REFERENCES

1. Ostwani W, Hanna C, Brice AE, Wymer DC, . Waxing and waning presentation of isolated cardiac sarcoidosis on sequential ¹⁸F-FDG-PET exams. *J Nucl Med Technol*. June 9, 2020 [Epub ahead of print].
2. Birnie DH, Sauer WH, Bogun F, . HRS expert consensus statement on the diagnosis and management of arrhythmias associated with cardiac sarcoidosis. *Heart Rhythm*. 2014;11: 1305–1323.
3. Goldman C, Judson MA, . Corticosteroid refractory sarcoidosis. *Respir Med*. 2020; 171:106081.
4. Terasaki FYK, . New guidelines for diagnosis of cardiac sarcoidosis in Japan. *Ann Nucl Cardiol*. 2017;3:42–45.
5. Juneau D, Nery P, Russo J, . How common is isolated cardiac sarcoidosis? Extracardiac and cardiac findings on clinical examination and whole-body ¹⁸F-fluorodeoxyglucose positron emission tomography. *Int J Cardiol*. 2018;253:189–193.
6. Petek BJ, Rosenthal DG, Patton KK, . Cardiac sarcoidosis: diagnosis confirmation by bronchoalveolar lavage and lung biopsy. *Respir Med*. 2018;144(suppl):S13–S19.

David H. Birnie

University of Ottawa Heart Institute

40 Ruskin St.

Ottawa, ON, K1Y 4W7

E-mail: dbirnie@ottawaheart.ca

Published online September 4, 2021.
DOI: 10.2967/jnmt.120.254276

Pharmacology Primer for Medications in Nuclear Medicine and Medical Imaging

Geoffrey Currie

Society of Nuclear Medicine and Molecular Imaging, 2020, 248 pages, \$109

The new *Pharmacology Primer for Medications in Nuclear Medicine and Medical Imaging* is a timely and much-needed book for nuclear medicine technologists and students. The author of this book, Geoffrey Currie, BPharm, MMedRadSc(NucMed), MAppMngt(Health), MBA, PhD, AM, has an impressive curriculum vitae. Dr. Currie is a nuclear medicine professor at Charles Stuart University in Wagga Wagga, Australia.

This book is ideal for those in the practice of nuclear medicine technology. It is a useful textbook for new learners and a valuable reference for the shelf of every nuclear medicine department.

Modern medicine continues to become more technologically complex. Pharmacology has always been an integral part of nuclear medicine and molecular imaging as a tool to evaluate the physiology of various organs and organ systems. The use of different medications to create a physiologic response allows evaluation through functional imaging. Nuclear medicine professionals should understand these processes, be competent in administering these medications, and know what to look for when monitoring patients after administration.

The timing of the publication of this book is ideal. Technologists need to understand the pharmacodynamics and pharmacokinetics of medications used in nuclear medicine exams. Although pharmacology has always been included in the recommended nuclear medicine technology curriculum and scope of practice, there is a debate on the competency of technologists to administer these medications. This book, written specifically for those practicing nuclear medicine technology, is important in assisting them in advocating for this function within the practice.

As an educator, Dr. Currie listed learning outcomes at the beginning of the book and specific learning outcomes and objectives for each chapter. This is especially useful for educators who choose to incorporate this book into their course.

This book is organized into 17 chapters. The first chapter is an introduction to pharmacology. The following 2 chapters break down pharmacology into pharmacodynamics and pharmacokinetics. Chapters 4 and 5 include dose forms and administration, followed by pharmacology variations for different populations (pediatric, geriatric, and female). Chapters 6–9 discuss pharmaceuticals used in specific nuclear medicine procedures. Chapters 10 and 11 cover contrast media used in CT and MRI. Chapters 12–16 cover crash cart medications, pain medications, chemotherapy, over-the-counter medications, and lifestyle and sports drugs. The final chapter covers known interactions with radiopharmaceuticals.

Most pharmaceuticals used in nuclear medicine are included in this book. A separate chapter is dedicated to renal, biliary, and

cardiac medications. Another chapter covers the other interventional medications. A few pharmaceuticals used in nuclear medicine are not included (acid-citrate-dextrose solution, Lugol solution, and recombinant human thyroid-stimulating hormone). Atropine is discussed in the crash cart chapter, not the cardiology chapter. Insulin is reviewed in the lifestyle and sports chapter, which may be because no chapter specific to PET or nuclear medicine therapy (i.e., octreotide, amino acid solutions, or antiemetics) is included.

Including CT and MRI contrast agents in this book is crucial for nuclear medicine professionals. These 2 chapters introduce the contrast agents and then describe their properties, mechanism of action, pharmacokinetics, contraindications, precautions, and adverse reactions. They also highlight concerns associated with extravasation. The MRI chapter includes a brief discussion of nephrogenic systemic fibrosis, which poses a small but significant risk to patients with a history of renal dysfunction.

What makes this textbook comprehensive are the final 5 chapters. As imaging professionals, we will encounter many situations outside the routine scenarios in the nuclear medicine department. The chapter on the crash cart (emergency trolley) includes the many drugs found in a crash cart; their indications, doses (including pediatric doses), and frequencies of administration; and any precautions or contraindications. The chapter on pain management summarizes many medications our patients may be taking when they come to us. The chapter on chemotherapy describes the mode of action, pharmacokinetics, risks, precautions, contraindications, adverse effects, interactions, and dosage of chemotherapeutic agents. The chapters on over-the-counter medications and lifestyle and sports drugs cover many pharmaceuticals that our patients may be taking.

One of this book's many strengths is its figures and tables. The figures are in color and are truly worth a thousand words. Each chapter includes multiple figures to illustrate many of this book's complex concepts. The tables allow for quick reference of the many pharmaceuticals covered.

Overall, this book is an excellent addition to any library. This book helps one quickly identify a medication and discover the most important and relevant information needed. It is also helpful as a comprehensive textbook for students entering the nuclear medicine profession. I would recommend it to nuclear medicine technologists, students, and other professionals (e.g., nursing professionals) working in nuclear medicine or medical imaging departments.

Cybil Nielsen, CNMT, NMTCB(RS), FSNMMI-TS

Indiana University

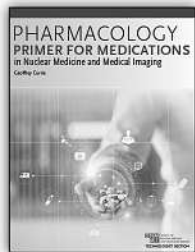
Indianapolis, Indiana

E-mail: cybniels@iupui.edu

Published online April 5, 2021.
DOI: 10.2967/jnmt.121.262380

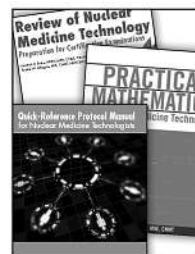
Essential Learning Tools for Nuclear Medicine Technologists

SNMMI's best-selling books and comprehensive online learning programs are designed to support you at all stages of your career as a nuclear medicine technologist.



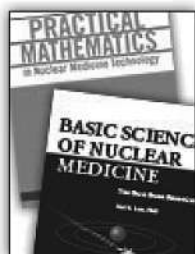
NEW! Pharmacology Primer for Medications in Nuclear Medicine and Medical Imaging

This practice-oriented text provides a concise overview of the basic principles of pharmacology that will help you thoroughly understand indications, contraindications, warnings, precautions, proper use, drug interactions, and adverse reactions for each medication used in medical imaging.



NEW! Technologist Study and Reference Combo

New! Save 10% when you purchase Review of Nuclear Medicine Technology, 5th Edition, Practical Mathematics in Nuclear Medicine Technology, 2nd Edition, and the Quick Reference Protocol Manual for Nuclear Medicine Technologists together as part of this new Technologist Study and Reference Combo.



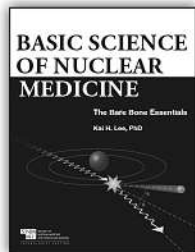
Technologist Math and Science Combo

Save 10% when you purchase *Practical Mathematics in Nuclear Medicine Technology, 2nd Edition* and *Basic Science of Nuclear Medicine: The Bare Bone Essentials* together as part of this new Technologist Math and Science combo.



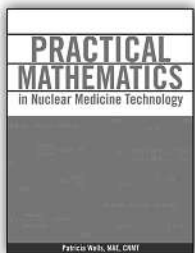
Technologist Reference and Review Combo

Save 10% when you purchase *Quick Reference Protocol Manual for Nuclear Medicine Technologists* and *Review of Nuclear Medicine Technology, 5th Edition* together as part of this new Technologist Reference and Review combo.



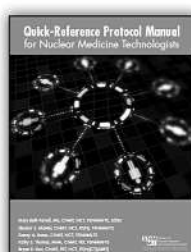
Basic Science of Nuclear Medicine: The Bare Bone Essentials

Basic Science of Nuclear Medicine: The Bare Bone Essentials is a great tool for nuclear medicine technologist students looking to better comprehend the fundamentals of the physics and technologies of modern-day nuclear medicine.



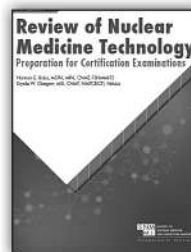
Practical Mathematics in Nuclear Medicine Technology, 2nd Edition

Informative word problems and explanations throughout *Practical Mathematics in Nuclear Medicine Technology* help you or your students prepare for the CNMT exam and real-life situations. Purchase together with the *Review of Nuclear Medicine Technology* and save 10%.



Quick Reference Protocol Manual for Nuclear Medicine Technologists

The *Quick Reference Protocol Manual for Nuclear Medicine Technologists* features protocols for 71 common nuclear medicine procedures. Each protocol lists the essential information for the procedure, including clinical indications and contraindications, patient preparation, and more.



Review of Nuclear Medicine Technology, 5th Edition

The best-selling *Review of Nuclear Medicine Technology, 5th Edition*, gives you a detailed overview of nuclear medicine technology—covering patient care, instrumentation, radiopharmaceuticals, federal regulations, imaging of ten systems within the body, and radionuclide therapy—complemented by hundreds of self-evaluation questions and answers mirroring the structure of national certification examinations.

ONLINE LEARNING PROGRAMS

CT+ Review and Essentials

CT+ Review and Essentials provides you with the comprehensive didactic education you need to succeed, whether you're looking to build your general CT knowledge, or preparing to sit for the ARRT (CT) and/or NMTCB (CT) exam(s). Includes post-course mock exam.

Quality in Nuclear Medicine Program

The nuclear medicine role now requires technologists to demonstrate appropriate patient assessment skills, practice appropriate safety procedures with regards to staff and patients, provide necessary patient education and instruction and provide physicians with pertinent information to assist with the interpretation and outcome of the study. This course was designed to assist you in understanding the skill requirements that are vital to your quality of practice.

Radiation Safety+ Review and Essentials

The Radiation Safety+ Review and Essentials program provides a comprehensive overview of all aspects of radiation safety for nuclear medicine technologists preparing to take the NMTCB's Radiation Safety Certification Examination. Includes post-course mock exam.

Technologist Student Review & Mock Exam Bundle

Sharpen your skills on radiation safety, instrumentation, clinical procedures, radiopharmacy, and more in this course designed to prepare you for the NMTCB and ARRT examinations. Includes post-course mock exam.

Already certified? Use this course as a refresher to brush up on basic concepts.

*Free shipping available on book orders within the continental United States.

www.snmmi.org/TechTools

SNMMI Value Initiative
TECHNOLOGIST SECTION

SNMMI TECHNOLOGIST SECTION PRESENTS AWARDS, ELECTS NEW OFFICERS AT 2021 VIRTUAL ANNUAL MEETING

More than 6,300 physicians, technologists, physicists, scientists, and exhibitors gathered at the Society of Nuclear Medicine and Molecular Imaging (SNMMI) 2021 Virtual Annual Meeting, held June 11–15. The meeting had 189 scientific oral presentations and 1,000 scientific posters, as well as sessions on new tracers and applications, emerging technologies, updates on appropriate use criteria and coding and reimbursement and the impact of COVID-19 on nuclear medicine and molecular imaging. A new Nuclear Medicine Technology Student Program was launched at the meeting and focused on specific topics of interest for students pursuing a career in nuclear medicine and molecular imaging. The Technologist Section also celebrated its 50th anniversary at the meeting with special events and speakers.

During the meeting, SNMMI Technologist Section (SNMMI-TS) inducted new officers, who will serve through June 2022. A number of technologists were also recognized for their outstanding contributions to nuclear medicine, molecular imaging, and the society.

2021–2022 SNMMI-TS OFFICERS

SNMMI-TS introduced a new slate of officers during the Annual Meeting. **Dusty M. York, MAEd, CNMT, PET, ARRT(N)(CT)**, has been elected as the 2021–22 president for the SNMMI-TS. York is an associate professor and clinical coordinator of the nuclear medicine program at Chattanooga State Community College in Chattanooga, Tennessee. “As a nuclear medicine and molecular imaging educator, I am committed to promoting the field and am excited to represent the members of the SNMMI-TS,” noted York. “I would like the SNMMI-TS to be the first place technologists look for continuing education, patient resources and advocacy support. In this ever-changing world, we will continue to make every effort to meet our members’ needs.”

During the meeting, SNMMI-TS also announced **Krystle W. Glasgow, MIS, CNMT, NMTCB(CT), NMAA, FSNMMI-TS**, as president-elect. Glasgow is a teacher and clinical coordinator at the University of Alabama at Birmingham (UAB) in Birmingham, Alabama, and is currently pursuing her doctorate degree in health services administration with a concentration in health informatics at UAB. “As SNMMI-TS president-elect, I plan to be laser-focused on membership,” stated Glasgow. “Membership is the lifeline



Dusty M. York

for the society, and we must continue to retain and gain in our numbers. Having served as the Technologist Section Membership Committee chair for two years, I have seen a lot of excitement from our members. We need to continue to bring individuals into our great society, get them involved, and help them succeed in our profession.”

Other newly elected individuals include:

- Secretary: Kelli E. Schlarbaum, MBA, CNMT, PET, CT
- Executive Board Members at Large:
 - Dori L. Nelson, BS, CNMT, NCT
 - Lance Burrell, MS, CNMT, PET, RT(CT)
- Finance Committee: Sarah R. Gibbons, MBA, CNMT, NMTCB(CT)
- Specialty Area Representatives:
 - Tricia L. Peters, BS, CNMT, PET, RT(CT) – Manager
 - Marcia L. Hess Smith, Med, CNMT, FSNMMI-TS – Industry



Krystle W. Glasgow

SNMMI-TS FELLOWS

The following three individuals were named SNMMI-TS Fellows. These are members of SNMMI-TS who have demonstrated leadership and have made a significant contribution to the profession of nuclear medicine technology at the national level. SNMMI-TS selects Fellows based on exemplary contributions in the following areas: participation in professional activities, education, professional experience, professional contributions, and civic activities. New SNMMI-TS Fellows receive a memorial plaque and pin signifying their Fellow status.



Barbara J. Grabher

- **Barbara J. Grabher, BS, CNMT, RT(N), NCT, FSNMMI-TS**
Greater New York Chapter Member Since 1986
- **Cheryl Rickley, CNMT, FSNMMI-TS**
Greater New York Chapter Member Since 1989



Cheryl Rickley

- **Leesa Ann Ross, MA, CNMT, PET, RT(N), RT(CT), FSNMMI-TS**
Southeastern Chapter Member Since 1995

OUTSTANDING JNMT ARTICLES

The Editor's Choice Awards for the best JNMT articles published in 2020 were selected by JNMT editor Kathy S. Thomas, MHA, CNMT, PET, FSNMMI-TS, and the journal's editorial board. Awards include:

- **Editors' Choice Award – 1st Place:** Paul E. Christian, Simon-Peter Williams, Lance Burrell, Paulo Castaneda, Justin Albiani, Nicholas Sandella, Andrei Iagaru, John M. Hoffman, Alex de Crespigny, and Sandra Sana-bria Bohorquez, Genentech, Inc., South San Francisco, California, for "Optimization of 89Zr PET Imaging for Improved Multisite Quantification and Lesion Detection Using an Anthropomorphic Phantom." *J. Nucl. Med. Technol.* 2020; 48:54–57.
- **Editors' Choice Award – 2nd Place:** Shirin Hatami, Sarah Frye, Anna McMunn, Crystal Botkin, Razi Muzaffar, Kara Christopher, and Medhat Osman Doisy, College of Health Sciences, Saint Louis University, St. Louis, Missouri, for "Added Value of Digital over Analog PET/CT: More Significant as Image Field of View and Body Mass Index Increase." *J. Nucl. Med. Technol.* 2020; 48:354–360.
- **Editors' Choice Award – 3rd Place:** Krista Wolfe, Jonathan Baldwin, Vesper Grantham, and Wendy Galbraith, College of Allied Health, University of Oklahoma Health Sciences Center, Oklahoma City, Oklahoma, for "⁹⁰Y-Labeled Resin Microsphere Spills: A Pilot Study to Determine Efficient Cleanup Practices." *J. Nucl. Med. Technol.* 2020; 48:274–277.
- **Editors' Choice Award – Best Continuing Education Article:** Barbara J. Grabher, Grabher Consulting and Specialty Services, Forest Hill, Maryland, for "Breast



Leesa Ann Ross



Paul E. Christian



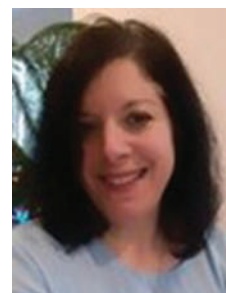
Shirin Hatami



Krista Wolfe

Cancer: Evaluating Tumor Estrogen Receptor Status with Molecular Imaging to Increase Response to Therapy and Improve Patient Outcomes." *J. Nucl. Med. Technol.* 2020; 48:191–201.

- **Editors' Choice Award — Best Educator's Forum Article:** Gail A. McFarland, Richard G. Hoylman, Jennifer L. Prekeges, and Vanessa R. Bennett,



Gail A. McFarland

Nuclear Medicine Technology Program, Bellevue College, Bellevue, Washington, for "Teaching Professional Behavior." *J. Nucl. Med. Technol.* 2020; 48:317–325.

SNMMI-TS OUTSTANDING TECHNOLOGIST AWARD

Sarah R. Gibbons, BS, CNMT, NMTCB(CT), a nuclear medicine technologist, at Indiana University Health Bedford in Bedford, Indiana, received the 2021 SNMMI-TS Outstanding Technologist award. The award recognizes SNMMI-TS members who have demonstrated outstanding service and dedication to the field of nuclear medicine technology. Gibbons has worked effortlessly over the last several years at the chapter and national level to encourage students and technologists to join the Technologist Section and to get involved with the society.



Sarah R. Gibbons

SNMMI-TS KATHY E. THOMPSON-HUNT OUTSTANDING EDUCATOR AWARD

Jennifer L. Prekeges, MS, CNMT, FSNMMI-TS, program chair of nuclear medicine technology at Bellevue College in Bellevue, Washington, was awarded the 2021 SNMMI-TS Kathy E. Thompson-Hunt Outstanding Educator Award. The award is presented to members who have exhibited commitment to advancing the field in their workplace and through their involvement with the society. In 2020, the SNMMI-TS changed the name of this award to recognize the late Kathy E. Thompson-Hunt, who served as president of the Technologist Section from 2010–2011. Prekeges received the award in recognition for her work in converting the Educator's Forum and Student Review Course to virtual programming in 2020.



Jennifer L. Prekeges

SNMMI-TS ADVOCATE(S)-OF-THE-YEAR AWARD

The SNMMI-TS Advocate(s)-of-the-Year Award was presented to **Tricia L. Peters, BS, CNMT, PET, RT(CT)**, director of nuclear medicine at Ridley-Tree Cancer Center at Samsom Clinic in Santa Barbara, California, and **Dmitry D. Beyder, MPA, CNMT**, nuclear medicine clinical supervisor at Barnes-Jewish Hospital in St. Louis, Missouri. This award recognizes an individual or individuals who have made significant contributions to advancing advocacy efforts at the state and federal level. In the midst of the pandemic, both Peters and Beyder were influential in ensuring that technologists were recognized as front-line workers. They also advocated on behalf of SNMMI for the FIND Act in Congress.



Trisha L. Peters



Dmitry D. Beyder

SNMMI-TS LIFETIME ACHIEVEMENT AWARD

The 2021 SNMMI-TS Lifetime Achievement Award was presented to **Frances L. Neagley, BA, CNMT, FSNMMI-TS**. This award is reserved for individuals who have made significant contributions to the field of nuclear medicine and the SNMMI-TS and its chapters. Neagley has been a staple within the SNMMI-TS and has served on the National Council of Representatives for decades, in a variety of positions. She also served as editor to the *Journal of Nuclear Medicine Technology* where she successfully embarked on several improvements to the journal, including reducing article turnaround time from submission to publication, publishing procedure guidelines, adding case studies and invited commentaries, and encouraging submissions from chapter presidents.



Frances L. Neagley

SNMMI-TS PRESIDENTIAL DISTINGUISHED SERVICE AWARD

The 2021 Presidential Distinguished Service Award winners are given to individuals who made a significant impact during the presidential tenure of Tina Buehner, PhD, MS, CNMT, NMTCB(CT)(RS), RT(N)(CT), FSNMMI-TS. The individuals being recognized this have shown exceptional leadership and have provided strategic guidance in the areas of education and research.

The SNMMI-TS Presidential Distinguished Service Award was presented to:

- **Norman E. Bolus, MSPH, CNMT, FSNMMI-TS; Crystal Botkin, PhD, MPH, CNMT, PET; C. David Gilmore, EdD, CNMT, FSNMMI-TS; and Cybil J. Nielsen, MBA, CNMT, FSNMMI-TS**, for their outstanding contributions on the SNMMI-TS Educators Committee and, more specifically, for the development of the career pathways document and revisions to the entry level curriculum.
- **Bital Savir-Baruch, MD**, for her research mentorship as SNMMI-TS president Tina Buehner, PhD, CNMT, FSNMMI-TS, worked through her PhD thesis and for her friendship and guidance over the past year as Buehner served as SNMMI-TS president.
- **Mark H. Crosthwaite, MEd, CNMT, PET, FSNMMI-TS**, for his leadership as 2019–2020 SNMMI-TS president as the society transitioned to 100 percent virtual, and his leadership as chair of the SNMMI-TS COVID-19 Task Force, which worked tirelessly to provide additional resources for SNMMI-TS members to ensure that they were protected front-line workers in all aspects of their jobs.



Norman E. Bolus



Bital Savir-Baruch



Mark H. Crosthwaite

SNMMI-TS PRESIDENT'S PLAQUE

Tina M. Buehner, PhD, MS, CNMT, NMTCB(CT)(RS), RT(N)(CT), FSNMMI-TS, was awarded the SNMMI-TS president's plaque and gavel for her service as 2020–2021 SNMMI-TS president. Buehner has nearly 20 years of experience as a nuclear medicine technologist. She worked as the manager of the nuclear medicine/nuclear cardiology at Loyola University Health System's Gottlieb Memorial Hospital in Melrose Park, Illinois, for five years and as a staff technologist and clinical educator at Northwestern



Tina M. Buehner

Memorial Hospital in Chicago for 14 years before taking her current position.

She has been actively involved with SNMMI-TS for many years. Currently a director-at-large on the SNMMI Board of Directors, Buehner has served as a director-at-large on the SNMMI Board of Directors, as a delegate on the SNMMI House of Delegates, on the SNMMI-TS National Council of Representatives, and on the SNMMI-TS Awards, Grants, and Scholarships Committee. Very active within the Central Chapter of SNMMI, Buehner serviced as chair of the Membership and Programs committees, on the technologist Educator's Task Force, and as technologist chapter president from 2014 to 2016.

SNMMI-TS ABSTRACT AWARD WINNERS 2021

Technologist Best Abstract Award Winners

First Place

Kristin McBride, Radiology University of California Davis, Sacramento, California: "Blanching defects at the pressure points: a potential pitfall in dynamic total-body PET/CT studies."

Second Place

Anne Ellis, Michigan Medicine, Ann Arbor, Michigan: "Comparison of four infusion methods for Lutathera peptide radionuclide receptor therapy."

Third Place

Katie Moses, Radiology, University of Colorado Hospital, UCHealth, Aurora, Colorado: "Advanced PET imaging simultaneously improves image noise and patient throughput in ^{68}Ga DOTATATE scans."

SNMMI-TS/PET CoE Technologist Best PET Abstract Award

Kristin McBride, Radiology University of California Davis, Sacramento, California: "Blanching defects at the pressure points: a potential pitfall in dynamic total-body PET/CT studies."

SNMMI-TS/Therapy CoE Technologist Best Therapy Abstract Award

Anne Ellis, Michigan Medicine, Ann Arbor, Michigan: "Comparison of four infusion methods for Lutathera peptide radionuclide receptor therapy."

ERF/SNMMI-TS Best COVID-19 Abstract

Anne Ellis, Michigan Medicine, Ann Arbor, Michigan: "Comparison of four infusion methods for Lutathera peptide radionuclide receptor therapy."

SNMMI-TS Technologist Poster Awards

First Place

Amer Pierret, Radiology, University of Colorado Hospital, UCHealth, Aurora, Colorado: "Effects of image matrix on quantitative metrics in ^{68}Ga DOTATATE studies: Changes in SUV and signal-to-noise ratio in modern digital PET detectors."

Second Place

Heather Hunt, University of California Davis Medical Center; Sacramento, California: "Tranquility scoring to optimize pediatric imaging and reduce radiation on total-body PET scanners."

Third Place

C. David Gilmore, Massachusetts College of Pharmacy & Health Sciences University, Boston, Massachusetts: "Co-teaching in nuclear medicine technology."

SNMMI-TS/Cardiovascular Council Best Poster Awards

First Place

Alan Stuckey, University of Tennessee Graduate School of Medicine, Knoxville, Tennessee: "Synthesis of $^{99\text{m}}\text{Tc}$ -labeled peptide p5 + 14 for detection of cardiac amyloidosis - Preclinical studies in a mouse model."

Second Place

Sarah Frye, Saint Louis University, Saint Louis, Missouri: "Seeing the big picture: The importance of reviewing the entire field of view in myocardial perfusion imaging and the role of the nuclear medicine technologist."

Third Place

Yoko Kaimoto, Tokyo Women's Medical University, Tokyo, Japan: "Optimization of injected dose for myocardial flow quantification in ^{13}N ammonia PET with time-of-flight scanner. Noise equivalent count rate analysis."

ANZSNM/SNMMI-TS Best Abstract Award 2021

Brylee Thomson, Austin Health: "16 vs 8 bin evaluation of left ventricle ejection fraction in myocardial perfusion imaging."

ANZSNM/SNMMI-TS Best Abstract Award 2020

Sarah Thomas, Department of Molecular Imaging and Therapy, Austin Health, Australia: "Interobserver variability in interpretation of ventilation-perfusion lung scans (VQ scans)."

Technologist Student Abstract Award Winners

First Place

Robin L. Schroeder, Northwestern Memorial Hospital, Chicago, Illinois: "Simulating reduced dose PET imaging to determine impacts on diagnostic image quality."

Second Place

Gabriela Feliciano, Rhode Island Hospital, North Providence, Rhode Island: " ^{177}Lu -Dotatate therapy for inoperable or metastasized gastroenteropancreatic neuroendocrine tumors: How often do patients discontinue treatment early and why?"

Third Place

Fatimah Almuallim, Indiana University School of Medicine, Indianapolis, Indiana: "The effects of temperature change on Tc-99m MAA radiochemical purity."

SNMMI-TS Career Advancement Grants

The 2021 SNMMI-TS Career Advancement Grants were awarded to Nickie Beaulieu, CNMT; Samar El Khatib, CNMT; Sarah Frye, MBA, CNMT, PET, CCRP; Derrick Gillan, ARRT(N)(MR)(CT)PET; Jeremy Heinrich, CNMT,

NMTCB(CT), RT; Clifford Liguori, CNMT; Marcy McCarty, MBA, RT (R)(N); Patricia O'Neal, CNMT, NMT; Alexandria Pleshek, CNMT; Diane Soulek, CNMT, NCT, PET, RT(N); Sara Vandehey, MBA CNMT RT(N)(CT); and Cheyenne Waters, CNNT.



2022
Mid-Winter
Meeting

ACNM
ANNUAL MEETING

Save
THE
Date



www.snmmi.org/MWM2022

January 27-29
2022
SNMMI MID-WINTER &
ACNM ANNUAL MEETING

**HILTON ORLANDO
LAKE BUENA VISTA
ORLANDO, FLORIDA**

VISIT SNMMI'S "Radiopharmaceutical Therapy Central"

YOUR SOURCE FOR THE LATEST RADIOPHARMACEUTICAL
THERAPY NEWS, EDUCATION, AND RESOURCES FROM SNMMI.



www.snmmi.org/Therapy



MIRION
TECHNOLOGIES

Customize Your Lab for Safety and Efficiency



Biodex™ Lead-Lined Laboratory Furniture Versatile, Safe, Modular and Secure

Designed specifically for practical, secure storage of radioactive inventory, Biodex Lead-Lined Laboratory Furniture can be configured to meet your storage, decay and workbench requirements.

Key Features

- Install units individually, or in any combination
- Cabinets support up to 1500 lbs.
- Fully encased in steel - no exposed lead
- Includes key-lock doors and brackets for seismic anchoring
- Injection and Disposal Supplies

Let us Help

A product specialist is available to provide laboratory furniture design and technical assistance at **no cost or obligation**.



BIODEX
Part of Mirion Technologies



**Learn more about
Lead-Lined Laboratory
Furniture**

sales@biodex.com • 1-800-224-6339



Join our TechJobsSep2019 Project